Bayesian Methods for Inverse Problems

Lian Duan
St Anne's College
University of Oxford

A thesis submitted for the degree of
Doctor of Philosophy
Michaelmas 2013

Acknowledgements

This thesis is supported in part by Award No KUK-C1-013-04, made by King Abdullah University of Science and Technology (KAUST)

I would like to express my gratitude to my supervisors, Dr. Chris Farmer, Prof. Ben Hambly and Dr. Irene Moroz whose expertise, understanding, and patience, added significantly to my graduate experience. I appreciate their knowledge and skills in many areas (e.g., vision, literature, ethics, and interaction with others), and their assistance in writing reports and papers on occasions when I have been puzzled. I have greatly enjoyed working with them and learning from them.

In addition, I wish to thank Dr. Ibrahim Hoteit at KAUST and Dr. Xiaodong Luo at International Research Institute of Stavanger for hosting my research visit in KAUST between November 2010 to February 2011. There has been some very interesting, important, innovative and inspired discussion between us.

I want to thank my colleagues at the Oxford Center for Collaborative Applied Mathematics for making it fun to go to work.

And last, but not least, I would like to thank my wife, Yiying Shi, for providing me such a wonderful life outside my research and support and encouragement during my D.Phil..

Abstract

This thesis describes two novel Bayesian methods: the Iterative Ensemble Square Filter (IEnSRF) and the Warp Ensemble Square Root Filter (WEnSRF) for solving the barcode detection problem, the deconvolution problem in well testing and the history matching problem of facies patterns.

For the barcode detection problem, at the expanse of overestimating the posterior uncertainty, the IEnSRF efficiently achieves successful detections with very challenging real barcode images which the other considered methods and commercial software fail to detect. It also performs reliable detection on low-resolution images under poor ambient light conditions.

For the deconvolution problem in well testing, the IEnSRF is capable of quantifying estimation uncertainty, incorporating the cumulative production data and estimating the initial pressure, which were thought to be unachievable in the existing well testing literature. The estimation results for the considered real benchmark data using the IEnSRF significantly outperform the existing methods in the commercial software.

The WEnSRF is utilised for solving the history matching problem of facies patterns. Through the warping transformation, the WEnSRF performs adjustment on the reservoir features directly and is thus superior in estimating the large-scale complicated facies patterns. It is able to provide accurate estimates of the reservoir properties robustly and efficiently with reasonably reliable prior reservoir structural information.

Contents

List of Units

cf

Cubic feet (unit of gas volume).

cP

centipoise (unit of fluid viscosity).

D

Days (unit of time).

°F

Fahrenheit (unit of temperature).

hrs

Hours (unit of time).

Mscf

Thousand standard cubic feet (unit of gas volume).

Psi

Pound per square inch (unit of gauge pressure).

Psia

Pound per square inch (unit of absolute pressure).

rb

Reservoir barrels (unit of oil volume).

scf

Standard cubic feet (unit of gas volume).

stb

Stock tank barrels (unit of oil volume).

List of Abbreviations

DTC

Derivative Type Curve.

EAN

European Article Number.

EKF

Extended Kalman Filter.

EnKF

Ensemble Kalman Filter.

EnSRF

Ensemble Square Root Filter.

ETKF

Ensemble Transform Kalman Filter.

FP

Flow Period.

FR

Flow Rate.

FS

Full-Size.

FWI

Full Waveform Inversion.

GLVQ

Generalized Learning Vector Quantization.

GMRES

Generalised Minimal Residual.

IBF

Iterative Bayesian Filter.

IDM

Iterative Deconvolution Method.

IEnSRF

Iterative Ensemble Square Root Filter.

IMS

Imperfect Model Scenario.

IPF

Interacting Particle Filter.

KF

Kalman Filter.

LLDTC

Log-Log Derivative Type Curve.

LR

Low-Resolution.

MAP

Maximum A Posterior.

MECPD

Measurements Excluding the Cumulative Production Data.

MICPD

Measurements Including the Cumulative Production Data.

MLP

Mean of the estimated Log Permeability fields found using the analysed ensemble.

MTX/MTY

Mean of the Transformations in the X/Y direction of the analysed ensemble.

pdf

Probability Density Function.

PMS

Perfect Model Scenario.

PTC

Pressure Type Curve.

SD

Standard Deviation.

SDLP

Standard Derivation of the estimated Log Permeability fields found using the analysed ensemble.

SDTX/SDTY

Standard Derivation of the Transformations in the X/Y direction of the analysed ensemble.

SVD

Singular Value Decomposition.

UPC

Universal Product Code.

WEnSRF

Warp Ensemble Square Root Filter.

Chapter 1

Introduction

Inverse problems involve inferring the physical properties of systems from measurements. Often the properties being inferred are different from those being measured.

In many cases the 'obvious' formulation of an inverse problem leads to an ill-posed problem [79] because (i) a solution may not exist; (ii) the solution may not be unique; and (iii) the solution does not depend continuously on the data.

A key theme of the following thesis is that, by formulating an inverse problem as a problem in Bayesian inference, one can obtain a well-posed formulation. The Bayesian approach requires (i) a model of the system of interest; (ii) a model for the measuring instrument; and (iii) a prior assessment of the probability density of the system state. The model of the system might be stochastic or deterministic and the model of the measuring apparatus will generally involve some measurement noise.

Almost all mathematical modelling has an associated inverse problem. Inverse problems in reservoir engineering have been among the most interesting and challenging topics for many researchers and are indeed the primary focus of this thesis:

- **Barcode Detection**

Barcodes are ubiquitous in our lives. Yet, using a fix-focus-lens camera, the barcode image is often blurred, leading to misdetection or undetectability using conventional methods. Can we develop a Bayesian method to detect the barcode?

- **Deconvolution Problem in Well Testing**

  Well testing is a branch of reservoir engineering. A test well is drilled (e.g. Fig. 2.2 on page 12) soon after the discovery of a field to answer questions about productivity, fluid properties, composition, pressure, and temperature during exploration and appraisal, and to prove reservoir potential, confirm well performance, and improve field productivity during development to production.

  Well testing is operated at various flow rates. While the wellbore pressure and the flow rates are recorded in time, the wellbore pressure response with respect to the unit flow rate (known as the impulse response), in which the answers to the well test questions are embedded, is required. Using the noise-polluted pressure and the potentially biased flow rate data, is it possible to find a physical interpretation that describes the underlying reservoir/well physics? Is it possible to assign a certainty level to the estimated model for reservoir operation and risk management?

- **History Matching Problem of Facies Pattern**

  The history matching problem is an important and long-standing problem in reservoir engineering. 'Facies' are a body of rock with specified characteristics [127]. History matching of facies patterns[1] is commonly used to describe a calibration process for the reservoir (geological) model (of the facies patterns) carried out using historical data from reservoir production[2]. Once the reservoir model has been history matched, it can perhaps be used to predict the reservoir behaviour and plan strategies to maximise the production and enhance the production at late-life of old wells.

  Can we find an automatic history matching algorithm to calibrate the reservoir model

---

[1] Ideally, a facies is a distinctive rock type that forms under certain conditions of sedimentation, reflecting a particular process or environment.

[2] For old or marginally economic wells where production data are often used for well test analysis, the deconvolution problem in well testing is also categorised as a history matching problem [45, 75].

in real time? Is it possible to predict and quantify the reservoir production uncertainty using the history matched model?

With the aim of solving inverse problems in real-world situations, ensemble-based filtering techniques, a special class of Bayesian method, appear to offer several powerful capabilities. These can be relatively easy to implement without the need for adjoint or tangent-linear models, and come naturally with uncertainty estimation. However, these are unable to explore the exact posterior density of a high-dimensional nonlinear system using the current implementation and computational resources.

For the prior construction part of Bayesian inference, the key idea in this thesis involves the introduction and application of a novel[3] parameterisation technique: the B-spline. It is argued that this newly-developed approach, using ensemble-based filtering methods and priors constructed based on the B-spline parameterisation, are computationally superior to existing approaches and (in some cases) provide better ways for including prior information. The full estimation approaches are explained in detail for each problem in the body of the thesis, and their success is evaluated through real and synthetic experiments.

The outline of this thesis is as follows. Chapter 2 presents mathematical modelling of the forward problems and statements of the inverse problems using the state-space formulation. Based on the Ensemble Square Root Filter (EnSRF), Chapter 3 derives and discusses the Iterative Ensemble Square Root Filter (IEnSRF) and the Warp Ensemble Square Root Filter (WEnSRF), which are utilised as the Bayesian methods for solving the considered inverse problems. In Chapter 4, our prior information and some novel options for the corresponding parameterisation of each inverse problem and the WEnSRF are reviewed. Chapter 5 combines the IEnSRF with a level-set parameterisation to develop an efficient method for solving the barcode detection problem. Chapter 6 utilises the IEnSRF with a B-spline parameterisation to develop

---

[3] In the the context and applications of this thesis.

a framework for solving real deconvolution problems in well testing. In Chapter 7, the performance and potential of the WEnSRF are tested and illustrated for the history matching problems of facies patterns. Conclusions of this thesis, possible future research directions and other possible applications of our proposed filtering methods are presented in Chapter 8.

My original contributions described in this thesis are as follows. In Chapter 2: the real out-of-focus barcode image model (2.7) along with the modified well-test model (2.33) in the log-log space. In Chapter 3: the formulation and derivation of the IEnSRF and WEnSRF. Although, a similar work to IEnSRF has been published by Lorentzen *et.al* [109] in May 2011, the research on IEnSRF was carried out independently from February to November 2010. Results have been presented in both internal and external meetings and conferences between November 2010 to October 2011. The research content in the Chapters 4 to 8 is entirely my own work. In these chapters, when comparing against existing methods, the work or results of other researchers will be indicated by explicit references. In particular, in Chapter 6, the nonlinear convolution simulator for the modified Duhamel's principle (2.33) in C++[4] is released in commercial well-test-analysis software, Interpret$^{\mathrm{TM}}$ 2010, which was programmed and integrated during my internship at Paradigm. To my knowledge, the work in Chapter 6 is the first work that formulates and solves the deconvolution problem in well testing in the Bayesian framework. In addition, I am a contributor to four published and two unpublished papers related to this thesis [48, 49, 50, 51, 52, 110].

---

[4] The Matlab version of this simulator is utilised in this thesis.

Chapter 2

Mathematical Modelling and Inverse Problems

2.1 Introduction

Inverse problems infer the physical properties of a system from indirect and noise-polluted measurements. In contrast, the problem of simulating measurements using system properties and parameters is known as the forward problem/modelling.

In most situations, the mathematical models and the corresponding forward modelling are only used for the forecast of the system state and for the prediction of the measurements, respectively. However, because inference of the physical properties using the measurements must be based on the (state-space system of the) forward modelling, to a certain extent, the success of solving inverse problems is highly dependent on the adequacy and complexity of the forward model.

In this chapter, we introduce the state-space system as the mathematical framework first and then the special cases: (i) the Gaussian convolution equation for modelling the blurry barcode image, (ii) Duhamel's principle for the study of transient-flow phenomena and (iii) two-phase flow equations for simulating oil reservoir production.

2.2 The State-Space System

Many mathematical models have two parts: a system model and a measurement model. In the engineering literature, this is known as the state-space system [98].

Throughout this thesis, our state-space system includes additive noise as follows:

$$\begin{aligned} \text{the state equation:} \qquad x_k &= f(x_{k-1}); && (2.1a) \\ \text{the measurement equation:} \qquad s_k &= Hx_k + v_k. && (2.1b) \end{aligned}$$

Here, the subscript k is a nonnegative integer and denotes the time index; $x_k \in \mathcal{R}^{n_x}$ is called the state vector; the function $f(\cdot)$ is the nonlinear model of the physical process; $s_k \in \mathcal{R}^{n_s}$ is the output of the state-space system and is called the measurement vector; H is the measurement operating matrix; and $v_k \in \mathcal{R}^{n_s}$ is the measurement noise, which is assumed to be independent and drawn from a Gaussian distribution with mean of 0 and covariance of $R \in \mathcal{R}^{n_s \times n_s}$.

In the forward problem, the state-space system is used to simulate the state and/or the measurements with a given (exact) input. The forward problem is well-posed, because the simulated states and measurements exist and are unique. However, in the inverse problem, the state x_k must be inferred using the measurement s_k with uncertainty R, which often leads to non-existence, non-uniqueness or a non-continuously-dependent solution. Hence, the inverse problem is almost always ill-posed.

2.3 The Inverse Problem of Barcode Detection

The performance of barcode detection systems is being challenged by increasing demands from the military and internet retailers. Traditional scanners use analog edge detectors [93]. Once the strength of the reflected intensity crosses over a given threshold, an edge is detected and considered to correspond to a bar/space boundary.

Nowadays, with hand-held devices, detection is required on blurry barcode images, where edge detection often leads to errors. By modelling the blurred image as a Gaussian convolution process [118, 128, 142], extended from the modelling of the conventional barcode laser scanning, the barcode detection problem can be formulated as a classical inverse problem: the deconvolution problem.

Figure 2.1: The UPC and EAN barcodes for a 1TB external hard drive.

We first derive the convolution model for barcode laser scanning in §2.3.1 and then extend its physical principle to model blurry barcode images in §2.3.2. The forward problem, which simulates a blurry barcode image, and the barcode detection problem in a deconvolution formulation, are summarised in §2.3.3 and §2.3.4, respectively.

2.3.1 Mathematical Models of Barcode Laser Scanning

The history and stories regarding the invention of the first barcode and laser bardcode scanner since the late 1950's is provided in [177]. Here, we consider a one-dimensional barcode[1] with parallel (black) 'bars' and separated by (white) 'spaces' (as shown in Fig. 2.1) and begin the modelling of the reflection of a single scan of a laser barcode scanner with the following key assumptions:

Assumption 1. *The bar or space consists of identical unit width (white or black) barcode stripes. Its width only varies with the number of consecutive duplicated stripes.*

Assumption 2. *The barcode is printed on a white background with sufficient white spaces on either side and can be clearly identified from any other feature.*

---

[1] A barcode image is normally two dimensional, but the information of the barcode is only coded in the direction perpendicular to the barcode stripes.

Assumption 3. *The barcode scan is taken in an environment where the light sources emit uniform and almost white light and are sufficiently far from the barcode. The barcode is placed in a plane and its scan is taken at some point perpendicular to this plane without any influence of obstacles or shadows along the layer beam path.*

Assumption 4. *During a single scan, after focusing by the optical train, the optical beam moves over the barcode in the direction perpendicular to all boundaries of the barcode with uniformly speed at* v *and an intensity profile,* $\Gamma(x)$*, that is approximated by a Gaussian kernel of amplitude* α *and (rescaled) standard deviation* $\sigma > 0$*:*

$$\Gamma(x) = \alpha \exp\left(-\frac{x^2}{\sigma^2}\right). \tag{2.2}$$

Here, we set up the coordinate system with the $x-$*axis perpendicular to the barcode edge and the origin and scale 1 are located at the first edge at the beginning and the last edge at the end of the barcode, respectively*[2]*. Both the amplitude* α *and standard deviation* σ *depend on the distance of the scanner to the barcode [55, 93, 94, 143, 174]. Thus, the further the distance between the scanner and the barcode is, the smaller the amplitude and the larger the standard deviation becomes.*

A monochrome printing notation is utilised to denote the black and white of the barcode stripes, that is logic 1 and 0 indicate a black and a white stripe, respectively. Using assumptions 1 and 2, the nondimensionalised barcode, $u(x) : [0, 1) \to \{0, 1\}$, can be characterised using a two-level piecewise constant function, as follows:

$$u(x) = \sum_{j=1}^{J} U^j \mathbf{1}_{F_j}(x) \tag{2.3}$$

where $u(x) = 0$ for $x \notin [0, 1)$. Here, J is the total number of stripes[3], $U^j \in \{0, 1\}$ denotes the logic of the j^{th} barcode stripe, and $\mathbf{1}_{F_j}$ is an indicator function of the

---

[2] i.e. the (nondimensionalised) one-dimensional barcode is defined to be between 0 and 1.

[3] It can be seen that we have assumed the unit width of the barcode strip is $1/J$.

space interval $F_j = [(j-1)/J, j/J)$ of the j^{th} stripe, as follows:

$$\mathbf{1}_{F_j}(x) = \begin{cases} 1; & \text{if } x \in F_j, \\ 0; & \text{if } x \notin F_j. \end{cases} \tag{2.4}$$

Using assumptions 2 and 4, the total energy reflected by the barcode, $\Lambda(t)$, can be modelled as the convolution of the optical beam profile (2.2) with the barcode (2.3):

$$\Lambda(t) = \int_{-\infty}^{+\infty} u(x)\Gamma(x - vt)dx = \alpha \sum_{j=1}^{J} \int_0^1 U^j \mathbf{1}_{F_j}(x) \exp\left(-\frac{(x - vt)^2}{\sigma^2}\right) dx. \tag{2.5}$$

This model was first introduced in 1984 and was confirmed to capture the underlying physics behind barcode laser scanning through several experiments [14].

2.3.2 Mathematical Modelling of Blurry Barcode Imaging

Many researchers have investigated the possibility of replacing the conventional laser scanning equipment with compact camera-based detection systems. The fixed-lens camera is cost effective, but often leads to out-of-focus blurry images. It is also claimed that the blurry image of a poorly printed barcode taken with a correctly-adjusting lens, has the same effect as the out-of-focus blurry image [55, 174].

Here, we model the one-dimensional blurry barcode image (signal) using the same notations and assumptions as for barcode laser scanning in §2.3.1. As in [55, 93, 94, 143, 174], under assumptions 1, 2 and 4, by considering the displacement of the optical beam, vt, as a single spatial variable, eq. (2.5) can be extended further for modelling the blurry barcode image:

$$\Lambda(x) = \alpha \sum_{j=1}^{J} \int_0^1 U^j \mathbf{1}_{F_j}(x') \exp\left(-\frac{(x - x')^2}{\sigma^2}\right) dx'. \tag{2.6}$$

Here, the amplitude and standard deviation of the Gaussian kernel in Assumption

4 now depend on the distance between the camera and the barcode, the difference between the shooting focus and the correct focus, or the quality of the barcode print.

In real situations, unlike a barcode scan, images can only be taken with some ambient light. Using Assumption 3, modified from eq. (2.6), we introduce the model equation for the blurry barcode image to be used throughout this thesis, as follows:

$$\Lambda(x) = E^s + \alpha \sum_{j=1}^{J} \int_0^1 U^j \mathbf{1}_{F_j}(x') \exp\left(-\frac{(x-x')^2}{\sigma^2}\right) dx', \tag{2.7}$$

where $\Lambda(x)$ is the intensity of the barcode image and $E^s \in [0,1]$ is a scalar, denoting the image brightness due to ambient light[4]. $E^s = 0$ indicates an ideal environment with absolutely uniform white light emission on the barcode surface. In this case, the ideal model equation (2.6) is recovered. On the other hand, when modelling a dark ambient light with E^s close to 1, the barcode image is darkened overall as expected.

2.3.3 The Forward Problem

Although in eq. (2.7), the mathematical model of the blurry barcode image is analytical and has continuous-spatial dependence, in real-world situations, the images are digital and sampled pixel-by-pixel. Our goal in the forward problem is to simulate such a blurry signal with a given barcode, ambient light and focus parameters.

For the k^{th} pixel at location $x_k \in [0,1]$, by transforming the continuous convolution in eq. (2.7) to the discrete form, its intensity can be expressed as follows:

$$\Lambda^k = \gamma^k(E^s, \alpha, \sigma, U^1, \ldots, U^J) = E^s + \alpha \sum_{j=1}^{J} \sum_{k'=1}^{N} U^j \mathbf{1}_{F_j}(x_{k'}) \exp\left(-\frac{(x_k - x_{k'})^2}{\sigma^2}\right), \tag{2.8}$$

where N denotes the total number of sample pixels, γ^k denotes the discrete approximation of the convolution process (2.7) evaluated at position x_k.

---

[4] As the monochrome printing notation defined on page 8, logic 1 and 0 denote the black and white ambient light, respectively.

Hence, a typical input of the state-space system in the form of eqs (2.1a,b) for the blurry barcode image can be written as: $x_0 = [\mathbf{m}_0, \mathbf{o}_0]^T = [E_0^s, \alpha_0, \sigma_0, U_0^1, \ldots, U_0^J, \Lambda_0^1, \ldots, \Lambda_0^N]^T \in \mathcal{R}^{n_x}$, where the superscript T denotes matrix transpose; the subscript 0 denotes the prior stage to simulation, $\mathbf{m} = [E^s, \alpha, \sigma, U^1, \ldots, U^J]^T$ denotes the model variables and $\mathbf{o} = [\Lambda^1, \ldots, \Lambda^N]^T$ denotes the observation variables. The observation variables are used to match the form of the state-space system and to be filled with output from the mathematical model. The state-space system is summarised:

$$x_1 = f(x_0) = [\mathbf{m}_0, \gamma^1(\mathbf{m}_0), \ldots, \gamma^N(\mathbf{m}_0)]^T, \tag{2.9a}$$

$$s_1 = Hx_1 + v, \tag{2.9b}$$

where the subscript 1 denotes the posterior stage.

$$H = [0^{N\times(n_x-N)}, I^N] \tag{2.9c}$$

is the measurement operator, $0^{N\times(n_x-N)}$ is an $N\times(n_x-N)$ zero matrix, I^N is an $N\times N$ identity matrix and v is the measurement noise, which is assumed to be independent and drawn from a Gaussian distribution with mean 0 and standard derivation $\sigma_s \in \mathcal{R}$:

$$v \sim \mathcal{N}(0, \sigma_s^2 I^N). \tag{2.9d}$$

2.3.4 The Inverse Problem: Barcode Detection

Almost all hand-held devices[5] are equipped with fixed-lens cameras, which lead to the barcode images often being blurred. While the state-space system (2.9a,b) is a useful tool for simulating the blurry image ($s_1 = [\gamma^1(\mathbf{m}_0), \ldots, \gamma^N(\mathbf{m}_0)]^T$) using a given barcode ($[U^1, \ldots, U^J]$) and shooting parameters (E^s, α, σ), the inverse problem, considered in this thesis, is to estimate the underlying barcode ($[U^1, \ldots, U^J]$) and the

---

[5] For example, the standard iphone 4s has 8 and 0.3 megapixel fixed lens cameras installed at rear and front of the phone, respectively.

shooting parameters (E^s, α, σ) from the blurry image s_1. This inverse problem is also known as a deconvolution problem. In the real world, the underlying physical process can be more complicated than our model (e.g. a nonuniform ambient lighting in §5.4.3), which provides additional challenges to the detection methods.

2.4 The Inverse Problem in Well Testing

Once hydrocarbons are found in rock formations, the first process in production is to drill a test well. While drilling, the well is cased with metal tubes cemented into the well with cement on the outside of the casing and are said to be "completed" at places where the casing is perforated to allow flow between the well and the reservoir. This is the most common form of completion: the cased hole completion. In order to examine the reservoir zone of interest, some 'packers', downhole devices that can be placed to expand to seal the wellbore, isolate the zone to be tested from the drilling fluid column. Pressure-recording devices are placed in the well and on the surface. A valve (or port), a device that can adjust the flow rate (FR) by opening and closing it, is finally installed and operates from the surface by a platform or a (mobile) laboratory as in Fig. 2.2.

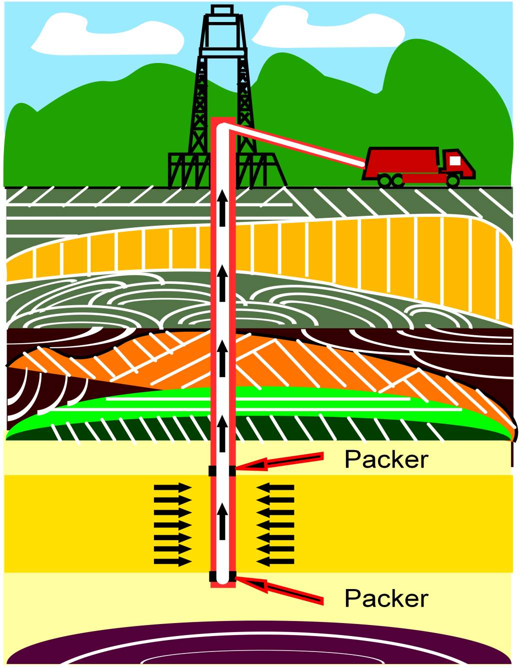

Figure 2.2: Well testing using a platform and a mobile laboratory.

During the well test, the valves are operated over a range of flowing conditions in which the wellbore pressure (at the bottomhole) and FRs are monitored. While the bottomhole pressure and temperature are monitored by downhole gauges[6], the FRs are (conventionally) monitored by single-phase flow meters[7] installed on each of the gas, oil and water outlets of the separators and tanks at the surface.

Using these bottomhole pressure and FR data, the well test is conducted to meet the following objectives: (i) To evaluate the characterisation of the reservoir/well in a large volume. (ii) To estimate the reservoir parameters under in-situ[8] conditions. (iii) To investigate the producing zones along the well length. (iv) To estimate the near-wellbore condition[9]. Beside the most obvious applications in exploration, with information about the conditions and characteristics of the reservoir/well system, improved analysis of reservoir performance and forecasting of future production can be achieved by the reservoir engineer, while the reservoir performance can be optimised by the production engineer [28, 29].

There are many ways to approach the well test objectives from the earliest semi-log straight line analyses in 1935 [154] to the more recent deconvolution methods in 2001 [163] and using single-test-wells up to multiple-test-well systems. However, the fundamental theme is unchanged over its long history which is to extract the well bottomhole pressure behaviour in response to unit-rate flows, in which the described reservoir/well system configuration and characteristics are included. Estimating this response function is a classical inverse problem, known as the deconvolution problem.

In this section, Duhamel's principle modelling the wellbore pressure of a single test well with respect to the FRs and type curves is first derived in §2.4.1. The forward problem which simulates the well test measurements based on a given Log-Log Derivative Type Curve (LLDTC) is introduced in §2.4.2 before a summary of the deconvolution problem in well testing in §2.4.3.

---

[6] Downhole gauges are normally electronic or fibre optic sensors (e.g. the Sapphire sensor in Schlumberger's WellWatcher Gauges) which provide real-time reservoir and production monitoring on working bottomhole pressure and temperature.

[7] A single-phase flow meter is a measuring device which measures only one type of fluid.

[8] A recovery technique which apply heat (stem) or solvents to oil or bitumen reservoirs.

[9] i.e. drilling- and completion-related damage to a well.

2.4.1 Mathematical Models of Wellbore Pressures

In this subsection, we derive Duhamel's principle (2.26) first by modelling a single test well in an oil reservoir. It is then shown to be also valid for gas reservoirs under the pseudo-pressure transformation.

Mathematical Modelling of the Wellbore Pressure of a Single Test Well in an Oil Reservoir

We start with the general oil flow modelling in the porous medium (reservoir) before restricting our attention to the fluid condition at the surface of the well. We set up the cartesian coordinate $\underline{x} = (x, y, z)$ with origin located at the center of the wellbore at the ground surface with $x-$, $y-$ and $z-$ axes pointing east, north and vertically upwards, respectively. We denote the reservoir domain and the surface of the well by Ω and D, respectively, and begin modelling of liquid flow in the reservoir with the following key assumptions:

Assumption 5. *The fluid flow is single phase.*

Assumption 6. *Gravitational forces are negligible.*

Assumption 7. *Darcy's law for Laminar flow is applicable.*

Assumption 8. *The reservoir is an homogeneous and isotropic porous medium of uniform thickness.*

Assumption 9. *The spatial pressure gradients are small compared to the second order spatial pressure variation [113].*

Assumption 10. *The viscosity and compressibility of the liquid are constant*[10].

---

[10] The viscosity and compressibility of gas are pressure dependent.

The governing equations for the flow inside a small volume are given by mass conservation (2.10), Darcy's law (2.11) and the fluid compressibility law (2.12):

$$\phi\frac{\partial\rho}{\partial t} + \nabla\cdot(u\rho) = 0, \tag{2.10}$$

$$u = -\frac{\kappa}{\mu}\nabla p, \tag{2.11}$$

$$\frac{d\rho}{dp} = c\rho. \tag{2.12}$$

Here, ρ and p are continuous space-and-time-dependent scalar functions called the density and pressure, respectively; u is continuous space-and-time-dependent vector function called the Darcy flux; and c, κ, ϕ and μ are positive constant scalars called the oil compressibility coefficient, the permeability, porosity and fluid viscosity, respectively. The boundary conditions include the outer boundary conditions[11] at the reservoir boundary $\delta\Omega$, and the linear time-dependent inner boundary condition at the well (i.e. the wellbore pressure variation due to FR):

$$p = p_D(t) \qquad \text{on} \qquad \underline{x} = D. \tag{2.13}$$

Constant initial reservoir pressure and fluid density are assumed:

$$p = p^0 \quad \text{and} \quad \rho = \rho^0 \qquad \text{at} \qquad t = 0. \tag{2.14a,b}$$

Substituting eq. (2.11) into eq. (2.10) using the chain rule and eq. (2.12), we have:

$$\frac{\partial\rho}{\partial t} = \frac{\kappa}{\phi\mu c}\nabla^2\rho. \tag{2.15}$$

Solving eq. (2.12) with the initial conditions (2.14a,b) and neglecting higher order

---

[11] This is often used in deriving the analytical solution for a specified reservoir/well configuration (e.g. [19]), but not used explicitly in deriving Duhamel's principle.

terms, the reservoir density can be expressed in terms of pressure as follows:

$$\rho = \rho^0 e^{c(p-p^0)} \approx \rho^0[1 + c(p - p^0) + \frac{1}{2}c^2(p - p^0)^2], \tag{2.16}$$

Substituting eq. (2.16) into eq. (2.15), we have:

$$[1 + c(p - p^0)]\frac{\partial p}{\partial t} = \frac{\kappa}{\phi\mu c}\left\{\left[1 + c(p - p^0)\right]\nabla^2 p + c\nabla p \cdot \nabla p\right\}. \tag{2.17}$$

Using Assumption 9[12] and eq. (2.17), we find the hydraulic diffusivity equation:

$$\frac{\partial p}{\partial t} = \frac{\kappa}{\phi\mu c}\nabla^2 p. \tag{2.18}$$

We define the pressure drop within the reservoir and at the well surface D as:

$$P = p^0 - p \quad \text{and} \quad P_D = p^0 - p_D, \tag{2.19a,b}$$

respectively. We nondimensionalise the full problem by defining $t = (m^2)c\phi\mu t^*/\kappa$. In nondimensional form (dropping the asterisk), the model system becomes:

$$\frac{\partial P}{\partial t} = \nabla^2 P, \tag{2.20a}$$

$$P\Big|_{t=0} = 0, \tag{2.20b}$$

$$P\Big|_{\underline{x}=D} = P_D. \tag{2.20c}$$

Using the boundary condition (2.20b) and taking the Laplace transform of P with $\tilde{P}(\underline{x}, s) = \int_0^\infty e^{-st}P(\underline{x}, t)\, dt$ in eq. (2.20a), our model equations become:

$$\nabla^2\tilde{P} = s\tilde{P}, \tag{2.21a}$$

$$\tilde{P}\Big|_{\underline{x}=D} = \tilde{P}_D(s), \tag{2.21b}$$

---

[12] The second term of eq. (2.17) is much smaller than the first one on the right hand side.

for which the solution (in the Laplace domain) is given by:

$$\tilde{P}(\underline{x}, s) = s\tilde{P}_D(s)\tilde{P}_1(\underline{x}, s), \tag{2.21c}$$

where, $\tilde{P}_1(\underline{x}, s)$ is a solution to system (2.21a,b) and satisfies all outer boundary conditions and inner boundary condition: $\tilde{P}_1(\underline{x}, s)\big|_{\underline{x}=D}=1/s$.

We establish the link between the wellbore pressure and the FR $q_D(t)$ through the well surface D by differentiating eq. (2.21c) with respect to the normal direction to D, n_D, multiplying by $-\kappa/\mu$ and integrating over the entire surface D:

$$\tilde{q}_D(s) = s\tilde{P}_D(s)\left(-\frac{\kappa}{\mu}\int \frac{\partial \tilde{P}_1}{\partial n_D} dD\right). \tag{2.22}$$

Under the same modelling system (2.21a,b), we denote the wellbore pressure drop due to a time-invariant constant flow with FR $q_D^{\mathbf{c}}$ as $P_D^{\mathbf{c}}$. The pressure type curve (PTC), the unit-rate pressure response, is thus defined as:

$$p_D^u = \frac{P_D^{\mathbf{c}}}{q_D^{\mathbf{c}}}. \tag{2.23}$$

In this constant flow regime, the relationship of wellbore pressure and FR as described in eq. (2.22) also holds:

$$\tilde{q}_D^{\mathbf{c}}(s) = s\tilde{P}_D^{\mathbf{c}}(s)\left(-\frac{\kappa}{\mu}\int \frac{\partial \tilde{P}_1}{\partial n_D} dD\right). \tag{2.24}$$

Substituting eq. (2.24) into eq. (2.22) and performing the inverse Laplace transformation of P with $P(\underline{x}, t)=\int_{c-i\infty}^{c+i\infty} e^{st}\tilde{P}(\underline{x}, s)\, ds$ gives:

$$\int_0^t q_D(t-\hat{\tau})\frac{dP_D^{\mathbf{c}}(\hat{\tau})}{d\hat{\tau}}d\hat{\tau} = \int_0^t q_D^{\mathbf{c}}(t-\hat{\tau})\frac{dP_D(\hat{\tau})}{d\hat{\tau}}d\hat{\tau}, \tag{2.25}$$

where $\hat{\tau}$ is a dummy variable for integration propose called the pseudo time. Substituting eqs (2.23) and (2.19b) into eq. (2.25), Duhamel's principle

$$p_D = p^0 - \int_0^T q_D(t - \hat{\tau}) \frac{dp_D^u(\hat{\tau})}{d\hat{\tau}} d\hat{\tau}, \tag{2.26}$$

which is fundamental to the study of transient-flow phenomena and must be satisfied by the wellbore pressure regardless of the reservoir boundary is derived. Here, T is the well test duration and the FR $q_D(t)$ is assumed to be equal to 0 for $t \leq 0$. Note that in the well testing literature, the derivatives of the PTC with respect to the pseudo-time ($dp_D^u/d\hat{\tau}$) and logarithmic pseudo-time ($dp_D^u/d\ln\hat{\tau}$) are know as the impulse function and Derivative Type Curve (DTC), respectively [19, 74, 75, 103][13] .

Mathematical Modelling of the Wellbore Pressure of a Single Test Well in a Gas Reservoir

As stated in Assumption 10, the viscosity and compressibility of oil are independent of pressure. However, in a gas reservoir, the viscosity and compressibility depend on pressure, so that the gas law relating the gas pressure and density must be applied. This subsection, by using a pseudo pressure transformation (2.31), shows that Duhamel's principle (2.26) also holds for gas reservoirs.

For the wellbore pressure in the single test well of a gas reservoir, we set up the same coordinate system as for the oil reservoir in the last subsection and again denote the 3-dimensional reservoir domain and the surface of the well by Ω and D, respectively. We assume assumptions 5 to 8 are valid and begin modelling the gas flow with the following additional assumptions:

Assumption 11. *The gas is isothermal and the ideal gas law holds.*

---

[13] In fact, the name type curve is used, because, in the late 1970s [3, 114], petroleum engineers would plot the estimated unit-rate pressure responses using the measured data and compare and match it against the theoretically calculated pressure responses (set of type curves) with different reservoir models and parameter sets to identify the reservoir/well model and parameters for the reservoir under investigation. This process is known as type curve analysis.

Assumption 12. *The dependency of permeability on the pressure is negligible [8, 9, 10]. Hence, the permeability κ is taken to be a pressure-independent constant.*

Assumption 13. *Viscosity and the gas law derivative factor change slowly with pressure.*

The governing equations for the flow inside a small volume element are given by mass conservation (2.27a), Darcy's law (2.27b), the gas law (2.27c) and the isothermal compressibility of gas (2.27d), as follows:

$$\phi\frac{\partial\rho}{\partial t} + \nabla\cdot(u\rho) = 0, \tag{2.27a}$$

$$u = -\frac{\kappa}{\mu}\nabla p, \tag{2.27b}$$

$$\rho = \frac{M}{RT}\frac{p}{Z}, \tag{2.27c}$$

$$\frac{d\rho}{dp} = c\rho. \tag{2.27d}$$

Here, ρ and p are continuous space-and-time-dependent scalar functions called the density and pressure, respectively; u is continuous space-and-time dependent vector function called the Darcy flux; c, ϕ, κ, M, R and T are positive scalar constants called the compressibility coefficient, porosity, permeability, gas molecular weight, gas constant and absolute temperature, respectively; and μ and Z are pressure-dependent scalar functions called the gas viscosity and (compressibility) Z-factor, respectively. The linear time-dependent inner boundary condition and the initial condition for the reservoir pressure and gas density are the same as in eqs (2.13, 2.14a,b) for oil reservoirs. Substituting eqs (2.27b,c) into eq. (2.27a), we have:

$$\phi\frac{\partial}{\partial t}\left(\frac{p}{Z}\right) = \nabla\cdot\left(\frac{\kappa p}{\mu Z}\nabla p\right). \tag{2.28}$$

Substituting eq. (2.27c) into eq. (2.27d), we obtain:

$$\frac{\partial}{\partial t}\left(\frac{p}{Z}\right) = \frac{cp}{Z}\frac{\partial p}{\partial t}. \tag{2.29}$$

Substituting eq. (2.29) into eq. (2.28) gives:

$$\frac{pc\phi}{Z\kappa}\frac{\partial p}{\partial t} = \nabla \cdot \left(\frac{p}{\mu Z}\nabla p\right). \tag{2.30}$$

In order to transform eq. (2.30) into a similar form as the hydraulic diffusivity equation (2.18), a scale change in pressure must be made to deal with the change of gas properties. The concept of pseudo pressure[14] φ is developed in [4] as follows:

$$\varphi = 2\int_{p_l}^{p} \frac{p}{\mu Z}dp, \tag{2.31}$$

where p_l is a low base pressure. One may note that p_l can be chosen as any arbitrary number, but it is preferable to chose it as 0 for ease of calculation[15]. Substituting eq. (2.31) into eq. (2.30), we have: $\partial\varphi/\partial t = \kappa\nabla^2\varphi/\phi\mu c$, where the diffusivity, $\kappa/\phi\mu c$, is a nonlinear function of pressure, even for a perfect gas. However, when the pressure is not varied significantly (as in the real experiments considered in this thesis), it can be taken to be a constant. As a result, the transformation using the pseudo pressure does not only eliminated nonlinearity of the flow equation, but also enables the use of Duhamel's principle (2.26) to model the pseudo wellbore pressure of the single test well in a gas reservoir. Note that throughout this thesis and in almost all real applications, the pseudo pressures data are provided for well tests in gas reservoirs.

2.4.2 The Forward Problem

In the well testing and reservoir engineering literature, the type curves are normally presented in a log-log plot not only because reservoir information can be better interpreted using DTC, but also the properties of both the PTC and the DTC can be better compared. It is thus desirable to formulate our forward problem for the wellbore pressure simulation based on the Log-Log DTC (LLDTC).

---

[14] The unit of the pseudo pressure is pressure-squared per centipoise.

[15] In practice, the pseudo pressure is often evaluated numerically using trapezoidal rule.

First of all, to transform the model equation (2.26) into the log-log domain for the DTC, we introduce the logarithmic pseudo time $\tau = \ln \hat{\tau}$, and the LLDTC

$$z(\tau) = \ln\left(\frac{dp_D^u(\hat{\tau})}{d\ln\hat{\tau}}\right) = \ln\left(\hat{\tau}\frac{dp_D^u(\hat{\tau})}{d\hat{\tau}}\right) = \ln\left(e^{\tau}\frac{p_D^u(e^{\tau})}{de^{\tau}}\right). \tag{2.32}$$

Substituting eq. (2.32) into eq. (2.26), Duhamel's principle can be rewritten as a nonlinear Volterra equation of the first-kind, as follows: $p_D(t) = p_0 - \int_{-\infty}^{\ln T} q_D(t - e^{\tau})e^{z(\tau)}d\tau$. Or more practically usefully as,

$$p_D(t) = p_0 - q_D(t - t_{\min})p_{\min}^u - \sum_{j=1}^{J}\int_{\ln t_{\min}}^{\ln T} Q^j \mathbf{1}_{F^j}(t - e^{\tau})e^{z(\tau)}d\tau, \tag{2.33}$$

Here, $t \in [t_{\min}, T]$, $t_{\min} \geq 0$ and $p_{\min}^u = p_D^u(t_{\min}) = \int_{-\infty}^{\ln t_{\min}} e^{z(\tau)}d\tau$. In deriving eq. (2.33), we assume the well testing is operated with a constant FR in each flow period (FP) and modelling the FR using a piecewise constant function: $q_D(t) = \sum_{j=1}^{J} Q^j \mathbf{1}_{F^j}(t)$, where Q^j is the FR of the j^{th} FP; $F^j = [F_e^{j-1}, F_e^j)$ is the time interval of the j^{th} FP, the subscript e indicates the end time of the FP, $F_e^0 = 0$ and $F_e^J = T$ are assumed, $\mathbf{1}_{F_j}$ is an indicator function of F^j as defined in eq. (2.4).

For practical purposes, we further extend the analytical modelling in eq. (2.33) using discrete pressure and LLDTC samples. The LLDTC is normally provided and required with total N' discrete samples. For the k^{th} pressure measurement at time t_k, Duhamel's principle (2.33) in the discrete form can be summarised as:

$$\begin{aligned} p^k = \gamma^k(p^0, \tau^1, z^1, \ldots, \tau^{N'}, z^{N'}, Q^1, \ldots, Q^J) &= p^0 - p_{\min}^u \sum_{j=1}^{J} Q^j \mathbf{1}_{F^j}(t_k - t_{\min}) \\ -\frac{1}{2}\sum_{j=1}^{J}\sum_{k'=2}^{k'=N}(\tau^{k'} - \tau^{k'-1})&[e^{z^{k'}}Q^j\mathbf{1}_{F^j}(t_k - e^{\tau^{k'}}) - e^{z^{k'-1}}Q^j\mathbf{1}_{F^j}(t_k - e^{\tau^{k'-1}})], \end{aligned} \tag{2.34}$$

where the superscript k' is the LLDTC sample index, γ^k denotes the discrete trapezoidal approximation of the convolution process (2.33) evaluated at time t_k with initial pressure p^0, FR $(Q^1, \ldots, Q^J)$ and the LLDTC samples $(\tau^1, z^1, \ldots, \tau^{N'}, z^{N'})$,

$[z^1 = z(\tau^1), \ldots, z^{N'} = z(\tau^{N'})]$ and $\tau^1 = \ln t_{\min}$ and $\tau^{N'} = \ln T$ are assumed.

Hence, a typical input of the state-space system in the form of eqs (2.1a,b) is $x_0 = [\mathbf{m}_0^z, p_0^0, \mathbf{Q}_0, \mathbf{p}_0]^T = [\mathbf{m}_0^z, p_0^0, Q_0^1, \ldots, Q_0^J, p_0^1, .., p_0^N]^T \in \mathcal{R}^{n_x}$, where, the superscript T denotes the matrix transpose, N is the total number of pressure measurements, $\mathbf{m}^z = [\tau^1, z^1, \ldots, \tau^{N'}, z^{N'}]^T$ denotes the model variables for the LLDTC, $\mathbf{Q} = [Q^1, \ldots, Q^J]^T$ denotes the FRs in all FPs and $\mathbf{p} = [p^1, .., p^N]^T$ denotes the exact pressure simulations at all sample times. The state-space system can be summarised as follows:

$$x_1 = f(x_0) = [\mathbf{m}_0^z, p_0^0, \mathbf{Q}_0, \gamma^1(p_0^0, \mathbf{m}_0^z, \mathbf{Q}_0), \ldots, \gamma^N(p_0^0, \mathbf{m}_0^z, \mathbf{Q}_0)]^T \tag{2.35a}$$

$$s_1 = Hx_1 + v. \tag{2.35b}$$

Here, the subscripts 0 and 1 denote the prior and posterior stages of the simulation, respectively; The measurement operator

$$H = [0^{(N+J+1)\times(n_x-N-J-1)}, I^{N+J+1}], \tag{2.35c}$$

where $0^{(N+J+1)\times(n_x-N-J-1)}$ is an $(N+J+1) \times (n_x-N-J-1)$ zero matrix and I^{N+J+1} is an $(N+J+1)\times(N+J+1)$ identity matrix; and v is the measurement noise, which is assumed to be drawn from a Gaussian distribution with mean 0 and covariance

$$R = \begin{pmatrix} \sigma_{p^0}^2 & 0 & 0 \\ 0 & \sigma_Q^2 \mathcal{D}^J & 0 \\ 0 & 0 & \sigma_p^2 I^N \end{pmatrix}, \tag{2.35d}$$

where σ_{p^0}, σ_Q and σ_p are the standard deviations of the initial pressure, the FR, the wellbore pressure noises, respectively; and $\mathcal{D}^J$ is the $J \times J$ diagonal matrix with most diagonal entries equal to 1 and 0 entries denoting the exact knowledge of the corresponding FRs when the well is shut, as follows:

$$\mathcal{D}^J = \operatorname{diag}(1, 1, \ldots, 0, 1, 0, \ldots, 1). \tag{2.36}$$

Note that the state-space formulation of the wellbore pressure simulation is almost identical to the formulation of the blurry barcode image (2.9a,b,c,d).

As the core of the forward simulator, equation (2.34) is evaluated with a piecewise linear LLDTC with constant logarithmic spacing. The Matlab version of the forward simulator is utilised in this thesis, while the optimized C version has been utilised in the commercial software: Interpret™ 2010.

2.4.3 The Inverse Problem: Deconvolution

As shown in many well/reservoir modelling references within the field [3, 17, 19, 74, 77], information regarding the well/reservoir characterisation, near-wellbore effect and reservoir boundaries is embedded in the LLDTC and PTC. While the state-space system (2.35a,b,c,d) is a useful tool for simulating the measurements s_1, the considered inverse problem is to estimate the underlying LLDTC ($\mathbf{m}_0^z$) and (in some cases) well operational parameters (p_0^0 and $\mathbf{Q}_0$) using the measurements, and hence to extract the well/reservoir key information in the LLDTC.

Note that the LLDTC cannot be directly measured, but must be calculated using PTC. Measuring the PTC directly does not normally provide reliable estimates, not only because controlling the exact FR though a perforation is very challenging, but also because the pressure measurements are sensitive and do not yield good quality during production. For these reasons, the well tests are multi-rate and the LLDTC must be extracted. Since Duhamel's principle is a convolution process, the described inverse problem is first formulated by Hutchinson and Sikora within the field in 1959 [84] and is known as a deconvolution problem.

2.5 The Inverse Problem in Reservoir Production

After the prediction of productivity and estimation of reservoir properties through well testing, the reservoir will be operated to produce hydrocarbons. The uncertainty in production forecasts for guiding operational and development plans can be reduced if the uncertainty in the spatial reservoir model and the descriptions of geological formations and their flow-related properties is first reduced.

Although, several data acquisition techniques, such as core rock sample characterisations[16], well logging[17], and seismic surveys[18], can be carried out to provide the distribution of geological facies[19] and rock properties, the amount of useful and interpretable data is greatly limited in practice by the cost and operational constraints. Hence, an interpolation of the available data is made in order to infer information about the unobserved regions, in which assumptions regarding the structure of geological formation are necessary. These assumptions involve a significant level of uncertainty [41]. Consequently, finding improved reservoir descriptions with reduced uncertainties is required and can be achieved by adjusting the model parameters to improve the match between the simulated and observed production data [71, 121]. This is a typical inverse problem and is known as the 'history matching problem' in the reservoir engineering literature. In this section, we first derive the two-phase (oil and water) flow model system for water flooding experiment in §2.5.1. Based on the numerical solution using an Implicit Finite Volume Scheme (Appendix A), the forward problem, to simulate the reservoir states and the measurements in the wells,

---

[16] The use of core samples taken from the borehole during drilling (e.g. trapped with a sampling chamber) to give information on strata age, composition, and porosity, and the presence of hydrocarbons or water along the length of the borehole.

[17] A well log is a detailed record of the geologic formations penetrated by a borehole. The log may be based either on visual inspection of samples brought to the surface or on physical measurements of the rock and their contained fluids made by instruments lowered into the hole.

[18] A method explores the large-scale surface structure by propagating elastic waves through the earth and measuring the time duration and amplitude of the echo.

[19] In geology, facies are a body of rock with specified characteristics such as permeability, porosity, etc [127]. Ideally, a facies is a distinctive rock type that forms under particular conditions of sedimentation, reflecting a particular process or environment.

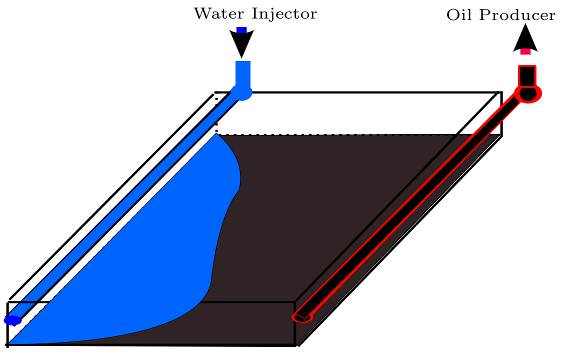

Figure 2.3: Three-dimensional view of oil secondary recovery using water flooding as presented in [23].

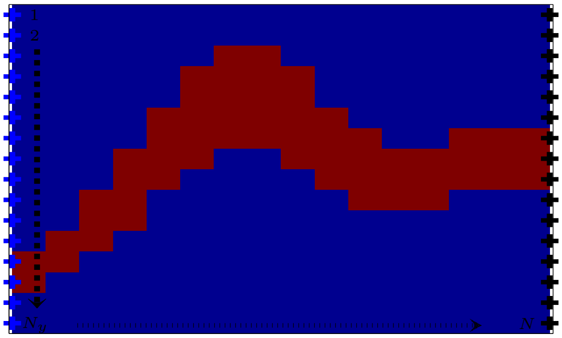

Figure 2.4: The facies of the reservoir model, blue cells (shale), red cells (sandstone), blue pluses (injectors) and black pluses (producers).

is summerised in §2.5.2, while an introduction and a summary of key aspects of the history matching problem of facies patterns concludes this section in §2.5.3.

2.5.1 Mathematical Models of Two-phase Flow in an Oil Reservoir

Here, we consider a two dimensional horizontal, rectangular oil reservoir with isotropic permeability, constant thickness and no-flow outer boundaries as shown in Fig. 2.4. Using the water flooding experiment in [23], secondary oil recovery is performed by injecting water into the western boundary and oil is produced from the eastern boundary of the reservoir as shown in Fig. 2.3.

We denote the reservoir domain and boundary by Ω and $\partial\Omega$, respectively, and begin modelling the two phase (oil-water) flow with the following assumptions:

Assumption 14. *The reservoir is formed from two types of rock: a large shale area with low permeability* κ_l *and a small amount of sandstone with high permeability* κ_h.

Assumption 15. *The reservoir is fully saturated with water and oil.*

Assumption 16. *Gravitational forces are negligible.*

Assumption 17. *Darcy's Law is applicable.*

Assumption 18. *Oil and water are incompressible and immiscible*[20].

Assumption 19. *Capillary pressure,* P_c*, which describes the difference in pressure across the interface between oil and water is assumed to be 0.*

Assumption 20. *The total water injection rate in all injection wells is constant and denoted by* Q_I *in mass and* q_I *in volume, while the bottomhole pressure at all the production wells is held constant and denoted by* p_P*.*

We set up the coordinate system with the origin located at the south-west corner of the reservoir, the x-axis is pointing east and the y-axis is pointing north. The reservoir domain is defined as $\underline{x} = (x, y) \in \Omega : \{0 \leq x \leq l_x; 0 \leq y \leq l_y\}$, where l_x and l_y denote the length of the reservoir in the x and y directions, respectively.

Using assumptions 16, 17, 18 and 20, the governing equations are given by mass conservation (2.37a,b) and Darcy's law (2.37c,d) for each fluid phase [12, 112]:

$$\rho_o \phi \frac{\partial S_o}{\partial t} + \nabla \cdot (\rho_o \underline{u}_o) = \sum_{\omega=1}^{W} Q_{\omega,P,o} \delta(\underline{x} - \underline{\varsigma}_{\omega,P}), \tag{2.37a}$$

$$\rho_w \phi \frac{\partial S_w}{\partial t} + \nabla \cdot (\rho_w \underline{u}_w) = \sum_{\omega=1}^{W} Q_{\omega,I,w} \delta(\underline{x} - \underline{\varsigma}_{\omega,I}) + \sum_{\omega=1}^{W} Q_{\omega,P,w} \delta(\underline{x} - \underline{\varsigma}_{\omega,P}), \tag{2.37b}$$

$$\underline{u}_o = -\frac{\kappa \kappa_{ro}}{\mu_o} \nabla p_o, \tag{2.37c}$$

$$\underline{u}_w = -\frac{\kappa \kappa_{rw}}{\mu_w} \nabla p_w. \tag{2.37d}$$

Here, the subscripts o, w, I and P denote the 'oil', 'water', 'injection wells' and 'production wells', respectively; the subscript ω is the well index; W is the total number of injection and production well pairs; ϕ, κ, ρ_o (or ρ_w), μ_o (or μ_w) are positive constant scalars called the the porosity, permeability, oil (or water) density and oil (or water) viscosity, respectively; p_o (or p_w) and s_o (or s_w) are continuous space-and-time dependent scalar functions called the pressure and saturation[21] for oil (or water),

---

[20] Two or more fluids do not mix with each other.

[21] A measure (within 0 to 1) of the gross void space in a reservoir rock that is occupied by a fluid.

respectively; $\underline{u}_o$ (or $\underline{u}_w$) is continuous space-and-time dependent vector function called the Darcy flux for oil (or water); κ_{ro} and κ_{rw} are continuous saturation dependent functions called the relative permeability[22] of oil and water, respectively; $Q_{\omega,P,w}$, $Q_{\omega,I,w}$ and $Q_{\omega,P,o}$ denote the external water mass FR at the production and injection wells and the external oil mass FR at the production wells, respectively; and $\underline{\varsigma}$ denotes the position of the well.

Using assumptions 15, 19 and 20, the boundary conditions imposed are:

$$S_o + S_w = 1, \tag{2.37e}$$

$$p_o = p_w = P, \tag{2.37f}$$

$$p_o|_{\underline{x}=\underline{\varsigma}_{\omega,P}} = p_w|_{\underline{x}=\underline{\varsigma}_{\omega,P}} = p_P, \tag{2.37g}$$

$$\sum_{\omega=1}^{W} Q_{\omega,I,w} = -\left(\sum_{\omega=1}^{W} Q_{\omega,P,o} + \sum_{\omega=1}^{W} Q_{\omega,P,w}\right) = Q_I. \tag{2.37h}$$

Substituting eqs (2.37c,f) into eq. (2.37a) and (2.37d,f) into eq. (2.37c), respectively, model system (2.37a-h) can be written as:

$$\phi\frac{\partial S_o}{\partial t} - \nabla\cdot(\kappa\lambda_o\nabla P) = \sum_{\omega=1}^{W} q_{\omega,P,o}\delta(\underline{x} - \underline{\varsigma}_{\omega,P}), \tag{2.38a}$$

$$\phi\frac{\partial S_w}{\partial t} - \nabla\cdot(\kappa\lambda_w\nabla P) = \sum_{\omega=1}^{W} q_{\omega,I,w}\delta(\underline{x} - \underline{\varsigma}_{\omega,I}) + \sum_{\omega=1}^{W} q_{\omega,P,w}\delta(\underline{x} - \underline{\varsigma}_{\omega,P}), \tag{2.38b}$$

$$S_o + S_w = 1, \tag{2.38c}$$

$$P|_{\underline{x}=\underline{\varsigma}_{\omega,P}} = p_P, \tag{2.38d}$$

$$\sum_{\omega=1}^{W} q_{\omega,P,o} + \sum_{\omega=1}^{W} q_{\omega,P,w} = -\sum_{\omega=1}^{W} q_{\omega,I,w} = -q_I, \tag{2.38e}$$

where $q_{\omega,P,w}$, $q_{\omega,I,w}$ and $q_{\omega,P,o}$ are the external water volumetric FRs at the production and injection wells and the external oil FR at the production wells, respectively; and

---

[22] The Corey models for calculating the relative permeabilities are summarised in eqs (7.1a,b).

the continuous space-and-time dependent mobilities are:

$$\lambda_o(\underline{x}, t) = \frac{\kappa_{ro}(S_o)}{\mu_o} \qquad \text{and} \qquad \lambda_w(\underline{x}, t) = \frac{\kappa_{rw}(S_w)}{\mu_w}. \tag{2.38f,g}$$

For a given set of model parameters $(\phi, \kappa, \lambda_o, \lambda_w)$, reservoir controls (boundary condition) (p_P, q_I, $\underline{\varsigma}_{\omega,P}$ and $\underline{\varsigma}_{\omega,I}$) and initial conditions $(S_o(\underline{x}, 0), S_w(\underline{x}, 0), P(\underline{x}, 0))$, a solution for the unknown state variables, P, S_o, S_w, $q_{\omega,P,o}$ and $q_{\omega,P,w}$, can be determined using the reservoir system (2.38a-e). However, a closed form solution can only be achieved under rare circumstances with highly simplifying assumptions. In practice, an approximate solution is found on a discrete grid using either a Finite Element or Finite Volume numerical method at desired times.

In Appendix A, we provide a detailed derivation of an implicit Finite Volume scheme which is used throughout this thesis in seeking a numerical solution of the reservoir system (2.38a-e). We write the Finite Volume approximation of the reservoir system (2.38a-e) using the function ϖ in the form:

$$\varpi\left(\mathbf{P}^k, \mathbf{S}_w^k, \mathbf{P}^{k+1}, \mathbf{S}_w^{k+1}, \mathbf{\Phi}, \mathbf{K}, \mathbf{\Lambda}\right) = 0, \tag{A.9}$$

where the subscript k denotes the time step index; $\mathbf{P}$, $\mathbf{S}_w$, $\mathbf{\Phi}$, $\mathbf{K}$, $\mathbf{\Lambda}$ denote the discretised pressure, water saturation, porosity, absolute permeability and mobility in all cells on the standard grid in a vector form, respectively; these are all of dimension $N \times 1$, where N is the total number of cells in the reservoir domain.

With the known reservoir model $(\mathbf{\Phi}, \mathbf{K}, \mathbf{\Lambda})$ and state ($\mathbf{P}^k$, $\mathbf{S}_w^k$) at time t_k, to determine the reservoir state at time t_{k+1} $(\mathbf{P}^{k+1}, \mathbf{S}_w^{k+1})$, we minimise the cell residues of system (A.9) by applying Newton iteration in which the Generalised Minimal RESidual (GMRES) method is adapted as the linear solver at each time step. For ease of presentation, we denote the reservoir solver of the described process as:

$$\left[\mathbf{P}^{k+1}, \mathbf{S}_w^{k+1}\right]^T = \varpi_s\left(\mathbf{P}^k, \mathbf{S}_w^k, \mathbf{\Phi}, \mathbf{K}, \mathbf{\Lambda}\right). \tag{2.39}$$

Note that the reservoir model system (2.38a-e) is rather simple with ignored gravitational effects and capillary pressure. The actual flow equations are much more complicated than these in commercial software. We have chosen such a model, because the aim of this thesis is to investigate methods for solving the inverse problem related to reservoir flow, and not to find the optimal reservoir model equations.

2.5.2 The Forward Problem

A typical input of the state-space system in the form of eqs (2.1a,b) is:

$$x_k = [\mathbf{\Phi}^k, \mathbf{K}^k, \mathbf{\Lambda}^k, \mathbf{P^k}, \mathbf{S}_w^k]^T \in \mathcal{R}^{n_x} = \mathcal{R}^{5N}, \tag{2.40}$$

where the superscript T denotes a matrix transpose. The state-space system which describes the simulation of the pressure and saturation fields and the production data in the wells can be summarised as follows:

$$x_k = f(x_{k-1}) = [\mathbf{\Phi}^{k-1}, \mathbf{K}^{k-1}, \mathbf{\Lambda}^{k-1}, \varpi_s\left(\mathbf{P}^{k-1}, \mathbf{S}_w^{k-1}, \mathbf{\Phi}^{k-1}, \mathbf{K}^{k-1}, \mathbf{\Lambda}^{k-1}\right)]^T, \tag{2.41a}$$

$$s_k = Hx_k + v_k. \tag{2.41b}$$

Here, H is a $2N_y \times 5N$ measurement matrix:

$$H = \begin{pmatrix} 0^{N_y \times (n_x - 2N)} & I^{N_y} & 0^{N_y \times (2N - 2N_y)} & 0^{N_y \times N_y} \\ 0^{N_y \times (n_x - 2N)} & 0^{N_y \times N_y} & 0^{N_y \times (2N - 2N_y)} & I^{N_y} \end{pmatrix}, \tag{2.42}$$

where N_y denotes the number of discrete cells along the $y-$direction on the standard grid, $0^{N_y \times (n_x - 2N)}$ is an $N_y \times (n_x - 2N)$ zero matrix, I^{N_y} is an $N_y \times N_y$ identity matrix. The first and second identity matrices take measurements of the pressure in the injection wells and the water saturation in the production wells[23]. The measurement

---

[23] Some research papers adapt the mass or volumetric FRs of the fluids in the production wells as the observation variables and measurements in the state-space system. According to our FR modelling in eq (A.8) and definition of fluid mobility in eqs. (2.38f,g) and using the inverse problem prior information, this is the same as making the measurements directly on the water saturation in

noise v_k is assumed to be independent and drawn from a Gaussian distribution with mean 0 and covariance matrix

$$R = \begin{pmatrix} \sigma_P^2 I^{N_y} & 0 \\ 0 & \sigma_S^2 I^{N_y} \end{pmatrix}, \tag{2.43}$$

where σ_P and σ_S are the standard deviations of the pressure and saturation measurement noises, respectively.

2.5.3 The Inverse Problem: History Matching of Facies Patterns

In real-world situations, many sources of error can lead to unreliable model prediction, including oversimplified reservoir geometry and inaccurate well locations and rock properties. In addition, the mathematical model must closely capture all the important physical processes present in the actual reservoir to avoid introducing bias during the prediction. These concerns not only introduce uncertainties into the prediction, but also alert the reservoir engineers to the importance of calibrating reservoir models through history matching processes.

The quantities $\phi, \kappa, \lambda_o, \lambda_w$ are reservoir properties and are not accessible through direct measurements except at the wells. While the state-space system (2.41a,b) is a useful tool for predicting the reservoir behaviour based on the prior information of the exact $\phi, \kappa_h, \kappa_l, \lambda_o, \lambda_w$ and a prior permeability field, the inverse problem being considered in this thesis is to update the structure of the facies pattern (κ) using the pressure measurements at the injection wells and the saturation measurements at the production wells. This special class of the history matching problem is known as the history matching problem of facies patterns, and has become an important area of study in a number of research projects [27, 44, 107, 108, 117].

---

the production wells.

Chapter 3

Nonlinear Filtering Methods

3.1 Overview

While the state-space system is widely-accepted and utilised as a mathematical tool for simulating model states and predicting measurements, it is also used in the inverse problem framework for model estimation using measurements.

Generally speaking, all inversion methods can be categorised as Bayesian or non-Bayesian methods with the same aim to find estimates which, in some sense, minimise the misfit between the observations and prediction in some specific norm. Most of the non-Bayesian methods adopt optimisation procedures with an introduced norm, which is often known as 'regularisation', to provide a single deterministic solution, while the Bayesian methods generally seek the posterior probability density (conditioned on the measurement) through sampling by a Monte Carlo Method[1].

In many cases, the solution of the non-Bayesian method can be interpreted as a quantitative estimate of one of the modes of the posterior density or the mean of the posterior density if the posterior is Gaussian or nearly Gaussian. The solution provided by Bayesian methods is thus more comprehensive and complete compared

---

[1] Either only at the beginning as in the Ensemble Square Root Filter or at each time step as in the bootstrap Particle Filter.

to the non-Bayesian methods. For this reason, the inversion methods considered in this thesis are all Bayesian. Because the uncertainty of the model reduces when incorporating reasonable measurements compared to the uncertainty description prior to any measurements incorporation (initial prior pdf), the Bayesian inversion methods are also known as filtering methods or filters[2].

For state-space systems with linear state equations and Gaussian measurement noise, the corresponding inverse problem is completely solved by the legendary Kalman Filter (KF) [97]. Although there exists a general optimal filter theory [91, 96], both theoretical analysis and practical applications meet with the fundamental problem that optimal filters for the inverse problem with nonlinear state-space systems are generally infinite dimensional, which makes them difficult to approximate [102]. Consequently, applications rely on suboptimal[3] approximations to the optimal filter.

We begin with the derivation of the Recursive Bayesian Filters (RBF), which provides the exact solution of the posterior pdf in §3.2. For practical proposes, the Ensemble Square Root Filter (EnSRF), one of the most well-studied approximations of the RBF using an ensemble of realisations, is introduced in §3.3. As the number of realisations increases, EnSRF do not converge to the exact solutions of RBF but to their Gaussian approximations, which makes it suboptimal and less rigorous compared to the Interacting or Regularised Particle Filters (IPF or RPF) [46, 73, 132]. On the other hand, this design avoids the curse of dimensionality[4] in particle filters [37, 38] and offers relative ease of implementation and practicable computational cost which are very useful for our problems.

Based on the formulation of the EnSRF and to overcome specified implementation

---

[2] In the traditional engineering or signal processing definition, a filter is a device algorithm which removes the unwanted component (e.g. a frequency band-pass filter) or feature (or measurement noise) and is not necessarily an estimator as in this thesis.

[3] Finite-dimensional and optimal.

[4] Simulation-based methods suffer from slow convergence in the large-dimensional system and exponential growth of the posterior sample number according to the problem dimension for a fixed level of accuracy.

difficulties using EnSRF to the considered inverse problems, the Iterative Ensemble Square Root Filter (IEnSRF) is introduced and derived based on the Iterative Bayesian Filter (IBF) for the barcode detection problem and the deconvolution problem in well testing in §3.4 and the Warp Ensemble Square Root Filter (WEnSRF) is introduced for solving the history matching problem of facies patterns in §3.5.

3.2 The Recursive Bayesian Filter

For the considered inverse problems, the state-space systems (2.9a,b), (2.35a,b) and (2.41a,b) can be summarised in a general form as follows:

$$x_k = f(x_{k-1}); \tag{2.1a}$$

$$s_k = Hx_k + v_k. \tag{2.1b}$$

Here, the subscript k denotes the time index, the function $f(\cdot)$ is the time-varying nonlinear mathematical model for each of the considered problem, s_k is the measurements, which depends upon state vector x_k through the measurement operating matrix, H, and v_k is the measurement noise, which is assumed to be independent and drawn from a Gaussian distribution with mean 0 and variance R:

$$v_k \sim \mathcal{N}(0, R). \tag{3.1}$$

The dimensions of x_k and f are both n_x and the dimensions of s_k and v_k are both n_s. For the barcode detection problem and deconvolution problem in the well testing, the state-space system is a special nonrecursive case of this general formulation (2.1a,b) ($k = 1$) with state vector consist of time independent model parameters and observation variables, where only one set of measurements is available for assimilation[5].

---

[5] We can thus find solutions of the barcode detection problem and the deconvolution problem in well testing by restricting the solution for the general formulation to the first time step.

Throughout this thesis, we denote the time sequence of observations $\{s_1, ..., s_m\}$ by S_m, and define the conditional pdf, $\pi(x_k|S_k)$, as 'the pdf of state x_k, given all the observations s_k up to and including time step k'. It is defined by the expression $\pi(x_k, S_k) = \pi(x_k|S_k)\pi(S_k)$ such that $\pi(x_k|S_k) = \pi(x_k, S_k)/\pi(S_k)$, where the marginal density is $\pi(S_k) = \int_{\mathcal{R}^{n_x}} \pi(x_k, S_k)\ dx_k$.

With the assumption that an initial prior pdf, $\pi(x_0)$, for x_0 has been provided at $t = 0$, the focal problems of this thesis are the prediction problem (i.e. predicting the future reservoir states based on all the measurement up until the current time) and the filtering problem (i.e. estimating the current reservoir state based on all the measurements up to and including the current time):

The Prediction Problem

Suppose that at time $k-1$, a solution $\pi(x_{k-1}|S_{k-1})$ has been found. From the previous definitions and the modelling assumptions, we are aiming for the prior pdf $\pi(x_k|S_{k-1})$:

$$\begin{aligned}\pi(x_k|S_{k-1}) &= \int_{\mathcal{R}^{n_x}} \pi(x_k, x_{k-1}|S_{k-1}) dx_{k-1} = \int_{\mathcal{R}^{n_x}} \pi(x_k|x_{k-1}, S_{k-1})\pi(x_{k-1}|S_{k-1}) dx_{k-1} \\ &= \int_{\mathcal{R}^{n_x}} \pi(x_k|x_{k-1})\pi(x_{k-1}|S_{k-1}) dx_{k-1}, \qquad (3.2)\end{aligned}$$

where the pdf of $\pi(x_k|x_{k-1})$ is found by using eq. (2.1a).

The Filtering Problem

In this case, we are aiming for the posterior pdf. Using Bayes' rule, the independence of S_{k-1} and s_k, the previous definitions and the modelling assumptions, we have:

$$\pi(x_k, s_k|S_{k-1}) = \pi(s_k|x_k, S_{k-1})\pi(x_k|S_{k-1}) = \pi(s_k|x_k)\pi(x_k|S_{k-1}). \qquad (3.3a)$$

By Bayes' rule, the posterior pdf $\pi(x_k|S_k)$ satisfies:

$$\pi(x_k|S_k) = \frac{\pi(x_k, s_k|S_{k-1})}{\pi(s_k)} = \frac{\pi(s_k|x_k)\pi(x_k|S_{k-1})}{\pi(s_k)} = \frac{\pi(s_k|x_k)\pi(x_k|S_{k-1})}{\int_{\mathcal{R}^{n_x}} \pi(s_k|x_k)\pi(x_k|S_{k-1})\ dx_k}. \qquad (3.3b)$$

Here, $\pi(s_k|x_k)$ is known as the likelihood function (where s_k is fixed and x_k can vary) and $\pi(s_k|S_{k-1})$ is known as the evidence probability density.

In summary, the RBF for the state-space model (2.1a,b) is

1. Assuming that the pdf of the initial state $\pi(x_0)$ is known, the initial prior is $\pi(x_0|s_0) = \pi(x_0)$. As by convention, we assume the initial state is not observed.

2. For $k = 1, 2, \cdots$, proceed using the following steps:

   Forecasting step:

   (a) Generate the prior pdf $\pi(x_k|S_{k-1})$ using eq. (3.2).

   Analysis step:

   (b) Compute the likelihood probability density $\pi(s_k|x_k)$ using eq. (2.1b) and update the posterior $\pi(x_k|S_k)$ using eqs (3.3a,b).

3.3 The Ensemble Square Root Filter

It can be seen that the RBF provides the exact solutions of the prior and posterior pdfs and thus the optimal state estimation in the inverse problem. If the state equation (2.1a) is linear and the initial prior $\pi(x_0)$ is Gaussian, using theorems of probability theory, representing and reconstructing the prior and posterior pdfs using their means and variances is adequate and completely captures all the information. It is in this setting, the KF is proven to be equivalent to the RBF and is thus optimal. However, as considered, when the state equation is nonlinear, even starting with a Gaussian initial prior, the prior and posterior pdfs at each time step are non-Gaussian and require adequate approximation and representation.

Instead of using the mean and variance only, the EnSRF approximates the pdfs using an ensemble of r realisations, $X^a_{k-1} = \{x^a_{k-1,1}, \ldots, x^a_{k-1,r}\} \in \mathcal{R}^{n_x \times r}$, via:

$$\pi(x_{k-1}|S_{k-1}) = \frac{1}{r}\sum_{i=1}^{r} \delta(x_{k-1} - x^a_{k-1,i}). \tag{3.4}$$

Here, $r > 1$, the subscript i denotes the realisation index; the superscript a denotes 'analysed'; $1/r$ is the weight associated with the i^{th} realisation representing the likelihood (i.e. equally likely) and δ denotes the Dirac delta function.

Suppose that at time $k-1$, the posterior pdf $\pi(x_{k-1}|S_{k-1})$ in the form of eq. (3.4) has been found. Substituting eq. (3.4) into eq. (3.2) and using the properties of the Dirac delta function, the predictive prior pdf $\pi(x_k|S_{k-1})$ at time step k satisfies:

$$\pi(x_k|S_{k-1}) = \sum_{i=1}^{r} \frac{1}{r} \int_{\mathcal{R}^{n_x}} \delta(x_k - f(x_{k-1}))\delta(x_{k-1} - x^a_{k-1,i})dx_k = \sum_{i=1}^{r} \frac{1}{r}\delta(x_k - x^f_{k,i}), \quad (3.5)$$

where the realisations in the forecast ensemble, $x^f_{k,i} = f(x^a_{k-1,i})$, are generated by propagating the realisations in the analysed ensemble through the state eq. (2.1a).

Rigorous methods, such as IPF or RPF [13], are designed to approximate the prior pdf based on the Glivenko-Cantelli theorem [26]. In this case, substituting eq. (3.5) into eq. (3.3b) and using eqs (2.1b, 3.1), the posterior pdf can be approximated as:

$$\pi(x_k|S_k) = \sum_{i=1}^{r} \frac{e^{-(s_k - Hx_k)^T R^{-1}(s_k - Hx_k)/2}}{(2\pi)^{n_s/2} r \pi(s_k)|R|^{1/2}} \delta(x_k - x^f_{k,i}), \quad (3.6)$$

where the realisation weight depends on the likelihood function (i.e. the 'distance' between the observed and simulated measurements and covariance). Theoretically, the approximate pdfs in the form of eq. (3.5) and (3.6) converge to the exact prior and posterior as the number of realisations increases. However, due to the widely realised curse of dimensionality [37, 38], the described pdf approximation via ensemble using Monte Carlo method may fail in large scale systems. That is the maximum of the realisation weights converges to one as both the number of realisations and the dimension of the considered system tends to infinity [15]. In this case, without special devices (e.g. resampling), for a fixed accuracy, the number of realisations is required grows exponentially to provide a meaningful approximation of pdfs [37, 78]. This makes the application of particle filters difficult in practice. Instead, the EnSRF approximates the predictive prior pdf in eq. (3.5) as a Gaussian distribution as this assists the choice of more practical algorithms:

$$\pi(x_k|S_{k-1}) \approx \frac{e^{-(x_k-\hat{x}_k^f)^T P_k^{f^{-1}}(x_k-\hat{x}_k^f)/2}}{(2\pi)^{n_x/2}|P_k^f|^{1/2}} \tag{3.7a}$$

where the ensemble average and covariance matrix are given by

$$\hat{x}_k^f = \frac{1}{r}\sum_{i=1}^{r} x_{k,i}^f \quad \text{and} \quad P_k^f = \frac{1}{r-1}\sum_{i=1}^{r}(x_{k,i}^f - \hat{x}_k^f)(x_{k,i}^f - \hat{x}_k^f)^T = A_k^f A_k^{f^T}. \tag{3.7b,c}$$

Here, $A_k^f = [A_{k,1}^f, ..., A_{k,r}^f] \in \mathcal{R}^{n_x \times r}$ is the ensemble of ‘anomalies’ and

$$A_{k,i}^f = \frac{1}{\sqrt{r-1}}(x_{k,i}^f - \hat{x}_k^f). \tag{3.7d}$$

Furthermore, using eqs (2.1b,c, 3.7a), the likelihood probability density

$$\pi(s_k|x_k) = \frac{e^{-(s_k-Hx_k)^T R^{-1}(s_k-Hx_k)/2}}{(2\pi)^{n_s/2}|R|^{1/2}}, \tag{3.8a}$$

and the evidence probability density,

$$\pi(s_k) = \frac{e^{-(s_k-H\hat{x}_k^f)^T(HP_k^fH^T+R)^{-1}(s_k-H\hat{x}_k^f)/2}}{(2\pi)^{n_s/2}|HP_k^fH^T+R|^{1/2}}, \tag{3.8b}$$

respectively. Substituting eqs (3.7a, 3.8a,b) into eq. (3.3b) with some algebra (and patience), the posterior pdf, $\pi(x_k|s_k)$, can be written as:

$$\pi(x_k|s_k) = \frac{e^{-(x_k-\hat{x}_k^a)^T P_k^{a^{-1}}(x_k-\hat{x}_k^a)/2}}{(2\pi)^{n_x/2}|P_k^a|^{1/2}} \tag{3.9}$$

where the matrices $K_k \in \mathcal{R}^{n_x \times n_s}$ and $P_k^a \in \mathcal{R}^{n_x \times n_x}$ are known as the Kalman Gain Matrix and analysed error variance, respectively, and are defined as follows:

$$\hat{x}_k^a = \hat{x}_k^f + K_k(s_k - H\hat{x}_k^f), \tag{3.10a}$$

$$\begin{aligned} P_k^a &= (I^{n_x} - K_k H) P_k^f, && (3.10b) \\ K_k &= P_k^f H^T (H P_k^f H^T + R)^{-1}, && (3.10c) \end{aligned}$$

and I^{n_x} is an $n_x \times n_x$ identity matrix. The deduction of eq. (3.9) can be found in many references [146, 147]. Equations (3.10a,b,c) are the update step of the KF.

For completeness of the update, the analysed ensemble in the form of (3.4) must be drawn from the posterior pdf in eq. (3.9). It can be seen that the simplest scheme for generating such an analysed ensemble of realisations is to use the mean and variance of the posterior in eqs (3.10a,b) and perform stochastic (re)sampling of the (Gaussian) posterior. This is indeed the concept of the traditional Ensemble Kalman Filter (EnKF) [56, 57], which is derived in detail in Appendix B. However, as shown in [25], the (stochastic resampling in) EnKF only provides the mean and variance of the posterior approximately in a statistical sense and is systematically an $O(r^{-1/2})$ sampling error. Particularly for small ensembles, it tends to underestimate the analysed covariance and can cause ensemble collapse[6].

The EnSRF is designed to drawn samples from the posterior with the exact mean and variance in eqs (3.10a,b) through an ensemble correction in eq. (3.14) while avoiding the described systematic sampling error [172]. Using the positive-definiteness and symmetry properties of the matrices P_k^f and R, the theoretical error covariance in eq. (3.10b) can be writen as:

$$P_k^a = P_k^f - P_k^f H^T (H P_k^f H^T + R)^{-1} H P_k^f. \tag{3.11}$$

Substituting eq. (3.7c) into eq. (3.11), we have:

$$P_k^a = A_k^a A_k^{aT} = A_k^f [I^{n_x} - {A_k^f}^T H^T (H P_k^f H^T + R)^{-1} H A_k^f] {A_k^f}^T. \tag{3.12}$$

---

[6] The ensemble spread reduces too rapidly in the analysis step in one time step, which leads to poor pdf approximations in the subsequent time step [25].

Hence, using the positive-definiteness and symmetry properties of the matrices P_k^f and R, it can be deduced that the analysed anomalies A_k^a are required to satisfy:

$$A_k^a = A_k^f[I^{n_x} - (HA_k^f)^T(HP_k^fH^T + R)^{-1}(HA_k^f)]^{1/2}. \tag{3.13}$$

Here, $\mathcal{M}^{1/2}$ denotes a specific unique square root of a matrix $\mathcal{M}$ [167]:

Definition 1. *For a matrix $\mathcal{M} \in \mathcal{R}^{m\times n}$ and its singular value decomposition (SVD) $\mathcal{M} = \mathcal{V}_L\mathcal{D}\mathcal{V}_R^T$, $\mathcal{M}^{1/2} = \mathcal{V}_L\mathcal{D}^{1/2}\mathcal{V}_R^T$, where $\mathcal{V}_L \in \mathcal{R}^{m\times m}$ and $\mathcal{V}_R \in \mathcal{R}^{n\times n}$ are unitary matrices with columns of left- and right-singular vectors of $\mathcal{M}$, respectively and $\mathcal{D} \in \mathcal{R}^{m\times n}$ is a diagonal matrix with the non-zero singular values of $\mathcal{M}$.* ☐

Using the definition of the ensemble anomalies (3.7d), for all $i = 1, ..., r$, to achieve the exact covariance in eq. (3.10b), the realisations of the analysed ensemble is required to satisfy: $x_{k,i}^a = \hat{x}_k^a + A_{k,i}^a$. In matrix form, this is

$$X_k^a = \hat{x}_k^a \cdot \mathcal{U}^{1\times r} + A_k^a, \tag{3.14}$$

where $\mathcal{U}^{1\times r}$ denotes a $1 \times r$ unit matrix (matrix of 1s).

In most of the inverse problems which the EnSRF is applied to, the feasible number of realisations is much smaller than the dimension of the state vector. Hence, the ensemble covariance matrix in eq. (3.7c) is actually a low-rank approximation (of the $n_x \times n_x$ full covariance matrix) with a maximum rank of $r-1$. Hence, SVD must be applied in seeking a stable pseudo-inverse of the matrix $(HP_k^fH^T+R)$ in eqs (3.10c, 3.13) and the matrix square root in eq. (3.13) [59, 60]. This subsection provides the outline of the EnSRF without a very formal derivation and implementation detail. Particularly satisfying EnKF (EnSRF) derivations are provided in [64, 149]. Throughout this thesis, the EnSRF scheme on page 555 of [59] are implemented.

One may notice in eq. (3.13) that the ensemble transform matrix is on the right hand side of the forecast anomalies and has dimension of $r \times r$, which normally has a much lower dimensionality compare to the $n_x \times n_x$ ensemble transform matrix in some of the earlier versions of the EnSRF [5, 157, 172]. It thus overcomes the earlier implementation limitation on the computational memory in seeking a matrix square root (or inversion) via a matrix decomposition or by solving a system of linear equations using an iterative method for large-scale inverse problems.

The EnSRF scheme introduced here is first derived by Bishop *et al.* [18] and is sometime more specifically named as the Ensemble Transform Kalman Filter (ETKF) to distinguished to earlier versions of the EnSRF operating with less-practicable $n_x \times n_x$ ensemble transform matrix. However, since it is a small variation of the EnSRF, throughout this thesis, we use the term EnSRF for consistency.

Summary

In summary, throughout this thesis, the EnSRF for our state-space model (2.1a,b) has the structure (Only outlines are provided here. The detailed implementation is the same as the scheme on page 555 of [59]):

Initialization step:

1. The pdf $\pi(x_0)$ of the initial state and model parameters is assumed given and is approximated statistically by an ensemble $X_0^a = \{x_{0,1}^a, \ldots, x_{0,r}^a\} \in \mathcal{R}^{n_x \times r}$.
2. For every filtering step $k = 1, 2, \cdots$, proceed as follows:

   Forecasting step

   (a) Integrate the available analysed ensemble $X_{k-1}^a = \{x_{k-1,1}^a, \ldots, x_{k-1,r}^a\}$ forward with the state equation to the time of the next available observation and compute the forecast ensemble $X_k^f = \{x_{k,1}^f, \ldots, x_{k,r}^f\}$ as $x_{k,i}^f = f(x_{k-1,i}^a)$ for $i = 1, \ldots, r$, where the superscripts f and a denote forecast and analysed, respectively.

   (b) Compute the forecast ensemble mean $\hat{x}_k^f$, anomalies $A_k^f = [A_{k,1}^f, ..., A_{k,r}^f]$ and error covariance matrix P_k^f:

$$\hat{x}_k^f = \frac{1}{r}\sum_{i=1}^{r} x_{k,i}^f, \quad A_{k,i}^f = \frac{1}{\sqrt{r-1}}(x_{k,i}^f - \hat{x}_k^f) \quad \text{and} \quad P_k^f = A_k^f (A_k^f)^T. \quad (3.15\text{a,b,c})$$

Analysis step

(c) Compute the Kalman Gain Matrix K_k:

$$K_k = P_k^f H^T (H P_k^f H^T + R)^{-1}. \tag{3.16}$$

(d) Calculate the analysed ensemble mean $\hat{x}_k^a$ using the Kalman analysis equation:

$$\hat{x}_k^a = \hat{x}_k^f + K_k (s_k - H\hat{x}_k^f). \tag{3.17}$$

(e) Perform singular value decomposition on $I^{n_x} - (HA_k^f)^T (HP_k^f H^T + R)^{-1} (HA_k^f)$, such that $I^{n_x} - (HA_k^f)^T (HP_k^f H^T + R)^{-1}(HA_k^f) = \mathcal{V}_L \mathcal{D} \mathcal{V}_R^T$, where $\mathcal{V}_L$ and $\mathcal{V}_R$ are unitary matrices and $\mathcal{D}$ is a diagonal matrix.

(f) Generate a new analysed ensemble $X_k^a = \hat{x}_k^a \cdot \mathcal{U}^{1\times r} + A_k^a$ using a transform matrix $\mathcal{T} = \mathcal{V}_L \mathcal{D}^{1/2} \mathcal{V}_R^T$ and the analysed ensemble anomalies $A_k^a = A_k^f \mathcal{T}$, where $\mathcal{U}^{1\times r}$ denotes an $1 \times r$ unit matrix (matrix of 1s).

3.4 The Iterative Ensemble Square Root Filter

As summarised in §3.2, the state-space system of the barcode detection problem and the deconvolution problem in well testing is a special nonrecursive case of the general state-space system (2.1a,b). Restricting the ensemble approximation of the exact posterior in RBF derived in eq. (3.6) for assimilating only one set of measurements, the exact posterior pdf for both considered problems can be approximated as:

$$\pi(x_1|S_1) = \sum_{i=1}^{r} \frac{e^{-(s_1 - Hx_1)^T R^{-1} (s_1 - Hx_1)/2}}{(2\pi)^{n_s/2} r \pi(s_1) |R|^{1/2}} \delta(x_1 - f(x_{0,i}^a)), \tag{3.18}$$

the structure of which depends on both the initial prior and the measurement quality.

We first highlight the important feature of measurement quality. As shown in Fig 5.2 on page 83 and Fig. 5.6 on page 88, for the barcode detection problem, the (high-frequency) measurement noises are generally insignificant compare to the barcode signal to be processed, because (i) the noise is greatly attenuated when we generate the barcode signal by averaging the measured barcode image[7] and (ii) most of the cost-efficientive shooting devices nowadays generally provide excellent Signal-To-Noise (STN) ratio[8]. Similarly, as shown in Figs. 6.2, 6.5 and 6.7, for the deconvolution problem in well testing, the data in the well shut-in periods has better quality than in the production periods and is normally preprocessed to a good STN ratio prior to the deconvolution stage[9]. Hence, for both considered problems, the measurement covariance R can be assumed quite small.

On the other hand, the initial priors for the considered problems generally contain significant uncertainty. This is because (i) no prior information regarding the product number or shooting-related parameters should be assumed for general application in solving the barcode detection problem, and (ii) for the deconvolution problem in well testing, the conventional way of generating the initial prior adapts the estimate from pressure transient analysis which normally contains large uncertainty at the late-time.

With the described features of a quite informative set of measurements and a less-informative or even biased initial prior, constructing the approximate posterior using an ensemble of realisations in eq. (3.18) is challenging, because using a feasible number of realisations representing the uncertainty in the initial prior, only a few or even none of these realisations in the forecast ensemble would actually be ‘close enough’ to the actual measurement to gain a considerable likelihood weight. Therefore, the posterior

---

[7] More generally, a high-frequency cut filter is normally applied as a industry standard.

[8] A measure compares the level of a desired signal to the level of noise.

[9] Generally speaking, as an industry standard, before the deconvolution, the pressure data are passed through a high-frequency cut filter and the single-value flow rate data in each flow period are the average of all the reasonable observed rate measurements within this flow period. There is thus still significant uncertainty inherent in the flow rate measurement.

Experiment	5.4.1	6.4.1.1	6.4.1.2	6.4.2.1	6.4.2.2	6.4.3.1	6.4.3.2
Condition number ($\times 10^{15}$)	52.6	3.05	2.18	3.67	6.37	2.29	18.3

Table 3.1: The conditional number of the forecast ensemble measurement covariance matrix ($HP_1^f H^T$) generated using the initial ensemble in all numerical experiments.

approximation is no longer adequate using these realisations.

As an empirical observation, we propagate the realisations of the initial ensemble[10] in the numerical experiments for both the barcode detection problem and the deconvolution problem in well testing and compute the likelihood weight associate with each realisation. With the standard 32-bits variable precision offered in Matlab, the likelihood weights are all zeros which verifies our described challenges and earlier comments for adapting the particle filters. We also compute the conditional number of the forecast ensemble measurement covariance matrix ($HP_1^f H^T$) for each experiment. The result is summarised in table 3.1[11] and indicates that the rank of the ensemble covariance matrix are unpreserved through the considered nonlinear convolution process. Direct implementation of EnSRF is thus not practicable, because the matrix inversion in generating the Kalman Gain matrix in eq. (3.16) can not be achieved precisely using a poorly conditioned forecast ensemble measurement error covariance matrix and small measurement variance (R).

In this section, we introduce an Iterative Ensemble Square Root Filter (IEnSRF) to overcome the described challenge. We begin with the derivation of the Iterative Bayesian Filter (IBF), a special case of the RBF, in §3.4.1 and demonstrate that repeatedly assimilating the same measurement has the same effect on the posterior estimation compare to assimilating this measurement only once with a reduced measurement uncertainty. Based on the conclusion and formulation of the IBF, IEnSRF is developed in §3.4.2 and summarised in §3.4.3.

---

[10] The generation of the initial priors are summarised in §5.3 for the barcode detection problem and §6.4.1, §6.4.2 and §6.4.3 for the deconvolution problem in well testing.

[11] The initial ensemble in the synthetic experiment 5.4.1 and real experiments 5.4.2 and 5.4.3 are generated using the same procedure and parameters as discussed in §5.3. Hence, only the result for experiment 5.4.1 is presented.

3.4.1 The Iterative Bayesian Filter

In this subsection, we derive the IBF, a special case of the RBF in §3.2 , which explores the exact posterior pdf resulted by repeatedly assimilating the measurements from our considered system (2.9a,b) or (2.35a,b). It forms the theoretical background of the IEnSRF. We first reformulate the state-space system (2.9a,b) or (2.35a,b) in an iterative form as follows:

$$
\begin{aligned}
x_{\mathrm{K}} &= f(x_{\mathrm{K}-1}); && (3.19\mathrm{a})\\
s_{\mathrm{K}} &= Hx_{\mathrm{K}} + \mathrm{v}; && (3.19\mathrm{b})\\
\mathrm{v} &\sim \mathcal{N}(0, R_I). && (3.19\mathrm{c})
\end{aligned}
$$

Here, the subscript K is the iteration index and the independent random noise $\mathrm{v} \in \mathcal{R}^{n_x}$ is drawn from a Gaussian distribution with mean 0 and variance R_I. Using Bayes' rule in eq. (3.3b), the posterior at the K^{th} iteration is:

$$
\begin{aligned}
\pi(x_{\mathrm{K}}|S_{\mathrm{K}}) = &\frac{e^{-(s_{\mathrm{K}}-Hx_{\mathrm{K}})^T R_I^{-1}(s_{\mathrm{K}}-Hx_{\mathrm{K}})/2}}{(2\pi)^{n_s/2}|R_I|^{1/2}\pi(S_{\mathrm{K}})}\int_{R^{n_x}}\delta(x_{\mathrm{K}}-f(x_{\mathrm{K}-1}))\ldots\Big[\frac{e^{-(s_2-Hx_2)^T R_I^{-1}(s_2-Hx_2)/2}}{(2\pi)^{n_s/2}|R_I|^{1/2}}\\
&\int_{R^{n_x}}\delta(x_2-f(x_1))\Big(\frac{e^{-(s_1-Hx_1)^T R_I^{-1}(s_1-Hx_1)/2}}{(2\pi)^{n_s/2}|R_I|^{1/2}}\\
&\int_{R^{n_x}}\delta(x_1-f(x_0))\pi(x_0)dx_0\Big)dx_1\Big]\ldots dx_{\mathrm{K}-1}, \qquad (3.20)
\end{aligned}
$$

where $S_{\mathrm{K}} = [s_1, \ldots, s_{\mathrm{K}}]$ denotes all the measurements up to the K^{th} iteration and $\pi(S_{\mathrm{K}})$ is the evidence pdf. Because the considered state equation (2.9a) and (2.35a) only compute the observation variables without modifying the model parameters of the state variable (i.e. $f(f(x)) = f(x)$), eq. (3.20) can be simplified as:

$$
\begin{aligned}
\pi(x_{\mathrm{K}}|S_{\mathrm{K}}) = &\frac{e^{-(s_{\mathrm{K}}-Hx_{\mathrm{K}})^T R_I^{-1}(s_{\mathrm{K}}-Hx_{\mathrm{K}})/2}}{(2\pi)^{n_s/2}|R_I|^{1/2}\pi(S_{\mathrm{K}})}\int_{R^{n_x}}\delta(x_{\mathrm{K}}-f(x_0))\frac{e^{-(s_{\mathrm{K}-1}-Hf(x_0))^T R_I^{-1}(s_{\mathrm{K}-1}-Hf(x_0))/2}}{(2\pi)^{n_s/2}|R_I|^{1/2}}\\
&\ldots\frac{e^{-(s_1-Hf(x_0))^T R_I^{-1}(s_1-Hf(x_0))/2}}{(2\pi)^{n_s/2}|R_I|^{1/2}}\pi(x_0)dx_0. \qquad (3.21)
\end{aligned}
$$

Using properties of the Gaussian distribution and the Dirac delta function, we have

$$\pi(x_{\mathrm{K}}|S_{\mathrm{K}}) = \frac{e^{-\mathrm{K}(\bar{S}_{\mathrm{K}}-Hx_{\mathrm{K}})^T R_I^{-1}(\bar{S}_{\mathrm{K}}-Hx_{\mathrm{K}})/2}}{(2\pi)^{n_s/2}|R_I/\mathrm{K}|^{1/2}\pi(S_{\mathrm{K}})} \int_{R^{n_x}} \delta(x_{\mathrm{K}}-f(x_0))\pi(x_0)dx_0, \tag{3.22}$$

where $\bar{S}_{\mathrm{K}}$ denotes the mean of the all the measurements up to the K^{th} iteration, S_{K}. Since the evidence pdf $\pi(S_{\mathrm{K}})$ only normalise the posterior pdf, eq. (3.22) indicate that assimilating the measurements (not necessary the same measurement) from the considered system (depends on the model variables only) in the IBF is equivalent to assimilating a single measurement with a (iteration-related) reduced measurement uncertainty using BF.

3.4.2 The Iterative Ensemble Square Root Filter

With the derived IBF for the considered problems, our aim to overcome the practical difficulty of obtaining an adequate ensemble approximation of the posterior when the initial prior is less informative or even biased and a single set of measurements with small uncertainty (R) is assimilated can be achieved by assimilating this measurement ($s_{\mathrm{K}}=s_1$ for all K in IBF) repeatedly with an invariant but inflated measurement uncertainty (R_I) over a specific number of iterations (where ensemble approximation of the posterior using the inflated measurement uncertainty (R_I) is practicable).

For the ensemble approximation of the posterior in each iteration of the proposed method, the EnSRF is utilised and thus the name of IEnSRF. When applying the IEnSRF to the considered problems, we first propagate the ensemble of realisations representing the initial prior to generate the forecast ensemble measurement error covariance matrix ($HP_1^f H^T$) and perform a sensitivity analysis to find a minimum positive integer K_I such that the matrix ($HP_1^f H^T + R_I$) is well conditioned and thus can be precisely inverted, where $R_I = K_I R$. Based on eq. (3.22) of the IBF, (take the posterior in the last iteration as the prior for the current iteration,) the IEnSRF adapts the forecast and analysis steps of the EnSRF to assimilate the same measurement using the inflated measurement uncertainty R_I in each iteration. The desired ensemble approximation of the posterior is obtained at the end of ${K_I}^{th}$ iterations.

Because of the Gaussian approximations (eq. (3.7a)) made in deriving the EnSRF, the IEnSRF is an approximation to the IBF. In particular, assuming perfect measurement is assimilated and there is more than one state x that satisfies $s_1 = Hf(x)$, the estimated posterior is a single Dirac function using IEnSRF, as opposed to a sum of Dirac delta functions in the IBF.

Remark

In the nonlinear filtering literature, the described practical difficulty can also be identified more generally as the inconsistency between the analysed observed variable and the simulation of the analysed model variable: $x_1^a \neq f_1(x_1^a)$.

This problem, first identified and studied in [91], was at first attacked by iterating the Extended Kalman Filter (EKF) globally. The EKF is the nonlinear version of the KF, which adapts the linearised state-space system in the forecast and analysis steps of the KF. Recently, Krymskaya *et al.* [99] introduced a modified scheme which is called the Iterative Ensemble Kalman Filter (IEnKF). The estimated model variable found using the posterior pdf at the end of the filtering steps is used as the mean of the model variable with a specific covariance matrix (invariant over iterations) for the next iteration to process the same measurement. However, a detailed explanation of the initialisation in each iteration, stopping criterion and convergence property can improve the rigorous content of this scheme[12]. Lorentzen *et al.* [109] have also formulated a new improved IEnKF. Their formation is similar to our proposed IEnSRF and their derivation of convergence directly in the EnSRF formulation establishes the same conclusion as in IBF[13]. However, the design and approach of the IEnKF in [109] are more from an engineer's point of view without a rigorous exploration of stopping

---

[12] Another non-iterative method for obtaining an ensemble which is claimed to improve the representation of the state distribution can be found in [169].

[13] Independent work and derivations are presented here.

criterion and targeting a good state estimation rather than an accurate posterior estimate from a Bayesian point of view as in our proposed IEnSRF. It is also noted that running the proposed IEnSRF exceeds the designed K_I iterations is equivalent to over-fitting the data using the IEnKF as described in [109].

3.4.3 Summary

Throughout this thesis, the IEnSRF for our state-space model (2.9a,b) or (2.35a,b) has the structure:

Initialization step:

1. The initial pdf $\pi_0(x_0) = \pi_0(\mathbf{m}_0, \mathbf{o}_0)$ of the initial state and model parameters is assumed to be given and is represented statistically by an ensemble: $X_0^a = \{x_{0,1}^a, \ldots, x_{0,r}^a\} = \{[\mathbf{m}_{0,1}^a, \mathbf{o}_{0,1}^a]^T, \ldots, [\mathbf{m}_{0,r}^a, \mathbf{o}_{0,r}^a]^T\} \in \mathcal{R}^{n_x \times r}$.
2. Integrate the initial ensemble X_0^a forward with the state equation and compute the forecast ensemble $X_1^f = \{x_{1,1}^f, \ldots, x_{1,r}^f\}$ as $x_{1,i}^f = f(x_{0,i}^a)$ for $i = 1, \ldots, r$, where the superscripts f and a denote forecast and analysed, respectively.
3. Calculate the forecast ensemble mean $\hat{x}_1^f = 1/r \sum_{i=1}^{r} x_{1,i}^f$ and measurement error covariance matrix $HP_1^f H^T = HA_1^f (A_1^f)^T H^T$ using the anomalies $A_{1,i}^f = 1/\sqrt{r-1}(x_{1,i}^f - \hat{x}_1^f)$ respectively; and then perform a sensitivity analysis to find a minimum positive integer K_I such that the matrix $(HP_1^f H^T + R_I)$ is well-conditioned and can be precisely inverted, where $R_I = K_I R$.

Reformulation Step:

4. Reformulate the state-space model (2.9a,b) or (2.35a,b) into the iterative setting as in eqs (3.19a,b).

Iteration step:

5. For each iteration K = 1, ..., K_I, proceed with the forecast and analysis step in

the EnSRF as in §3.3 with the time index k replaced by the iteration index K, measurement uncertainty R replaced by the inflated measurement uncertainty R_I and s_K replaced by the actual measurement s_1.

3.5 The Warp Ensemble Square Root Filter

Both the EnSRF and the IEnSRF are based on the Kalman analysis update (3.17), which requires the state vector to be a continuous variable. In the history matching problem of facies patterns in §2.5.3, when incorporating the exact facies permeability (i.e. κ_h and κ_l), the permeability field $\mathbf{K}$ becomes a discrete variable and the estimation is thus incompatible with the introduced filtering methods[14].

To overcome this problem, as well as taking the advantages of the ensemble approximation, the Warp Ensemble Square Root Filter (WEnSRF) combines an image warping process and the introduced EnSRF and is designed to estimate the permeability field through a 'warping' transformation using some prior permeability fields.

In digital image processing, image warping is a transformation which maps all positions in one image plane to positions in a second plane [24, 175, 176]. Its applications arises in many diverse areas, almost all of which require the location and orientation of the image to be adjusted [43]. As a result, the parameterisation variable of the warping transformation is continuous and to be estimated by the EnSRF.

3.5.1 Derivation

The RBF in eqs (3.2, 3.3b) provides the exact solution of the prior and posterior pdfs, while the EnSRF derived in §3.3 is its practical ensemble approximation. The proposed WEnSRF essentially adds a warping transformation step prior to the forecast step of the introduced EnSRF formulation, in which, the prior permeability field and

---

[14] In other words, even if the realisations are initialised with permeabilities containing only κ_h and κ_l, after the ensemble update, the permeability in each realisation does not contain only κ_h and κ_l.

the warping transformation parameterisation are used to construct the uncertainties of the permeability field for the data assimilation.

Warping Transformation

We begin with the introduction and definition of the warping process first in the continuous formulation as in the image processing literature and then in the discrete formulation which is used in the inverse problem application and the WEnSRF.

Traditionally, in image processing, the warping process for a 2-dimensional image bounded by a normalised rectangle Ω:$\{0 \leq x \leq 1; 0 \leq y \leq 1\}$ using Cartesian coordinates with the origin at the bottom left of the image and the x- and y-axis pointing rightwards and upwards, respectively, is defined as follows:

Definition 2. *Given an image κ^0 and spatial-coordinate transformation function, $\mathcal{T}$, which maps spatial coordinates $(x, y) \in \Omega$ to new spatial coordinates (x', y'), such that $(x', y') = (x, y) + \mathcal{T}(x, y)$, warping is a process that generates a transformed image, κ^w:*

$$\kappa^w(x, y) = \kappa^0((x, y) + \mathcal{T}(x, y)) = \kappa^0(x + \mathcal{T}^x(x, y), y + \mathcal{T}^y(x, y)), \tag{3.23a}$$

where $\mathcal{T}^x$ and $\mathcal{T}^y$ are the single-valued functions for the x and y components of the spatial coordinates, respectively, subject to:

$$x + \mathcal{T}^x(x, y) = \begin{cases} 1; x + \mathcal{T}^x(x, y) > 1 \\ 0; x + \mathcal{T}^x(x, y) < 0 \end{cases} \quad \textit{and } y + \mathcal{T}^y(x, y) = \begin{cases} 1; y + \mathcal{T}^y(x, y) > 1 \\ 0; y + \mathcal{T}^y(x, y) < 0 \end{cases}. \tag{3.23b,c}$$

The warping process defined in Definition 2 is known as inverse warping in contrast to forward warping: $\kappa^0(x, y) = \kappa^w((x, y) - \mathcal{T}^{-1}(x, y))$ and is more desirable in practice[15]. Here, the explicit assumptions (3.23b,c) assume boundaries of the original

---

[15] For the forward mapping, $\mathcal{T}^{-1}$ must be carefully chosen to avoid multiple to one mapping and the warped image domain may not be fully-covered without introducing explicit assumptions in the warped image domain [24]. Such problems are avoidable by adapting the inverse mapping process in Definition 2 which samples exactly in the warped image domain and requires explicit assumptions in

image extending to span the $\mathcal{R}^2$ space in each of their limit directions[16].

Adapting the warping process described in the considered problem, a prior permeability field κ^0 (e.g. the top left panel of Fig. 3.1) which consists of a known number of facies types with specific permeability (in this case, shale rock and sandstone with permeabilities κ_l and κ_h, respectively) is assumed available and is processed through a warping transformation to generate the warped permeability field κ^w. Furthermore, both prior and warped permeability fields are required in discrete forms for the numerical reservoir simulator, which are assumed to be constant inside cells on the standard grid[17]. Here, we use the same notation as in Appendix A and denote the discrete prior and warped permeability fields as $\mathbf{K}^0 = [\kappa_1^0, \ldots, \kappa_N^0]$ and $\mathbf{K}^w = [\kappa_1^w, \ldots, \kappa_N^w]$, where $N = N_x N_y$ is the total number of cells and N_x and N_y are the number of cells along the x and y directions, respectively. The warping transformation functions $\mathcal{T}^x$ and $\mathcal{T}^y$ are consistently discretised on the standard grid and denoted as $\mathbf{T}^x = [\mathcal{T}_1^x, \ldots, \mathcal{T}_N^x]$ and $\mathbf{T}^y = [\mathcal{T}_1^y, \ldots, \mathcal{T}_N^y]$, respectively. The warping process for the permeability field in the discrete form based on Definition 2 is:

Definition 3. *Given a prior permeability field* $\mathbf{K}^0$ *and warping transformation,* $(\mathbf{T}^x, \mathbf{T}^y)$*, the warped permeability field* $\mathbf{K}^w$ *is generated using inverse mapping as follows:*

$$\mathbf{K}^w = [\kappa_1^w, \ldots, \kappa_N^w]^T = [\kappa^w_{1+\mathcal{I}_1^x, 1+\mathcal{I}_1^y}, \ldots, \kappa^w_{N_x+\mathcal{I}_N^x, N_y+\mathcal{I}_N^y}]^T = W_t(\mathbf{K}^0, \mathbf{T}^x, \mathbf{T}^y). \quad (3.24)$$

Here, $\mathbf{I}^x = [\mathcal{I}_1^x, \ldots, \mathcal{I}_N^x] = \lfloor [\mathcal{T}_1^x, \ldots, \mathcal{T}_N^x]/h_x + 0.5 \rfloor$ *and* $\mathbf{I}^y = [\mathcal{I}_1^y, \ldots, \mathcal{I}_N^y] = \lfloor [\mathcal{T}_1^y, \ldots, \mathcal{T}_N^y]/h_y + 0.5 \rfloor$ *are the discrete warping transformations associated with cell indices in the* x *and* y *directions, respectively, where* $\lfloor \cdot \rfloor$ *denotes the floor function and* h_x *and* h_y *are constant spacings between the nodes of two consecutive cells in the* x *and* y *directions, respectively. Function* $W_t(\cdot)$ *denotes the described discrete warping transformation.*

---

the original image domain. The inverse mapping process is thus desirable in practise [175], because it is simpler in implementation and computationally superior to the forward mapping [176].

[16] Or the references $(x + \mathcal{T}^x(x,y), y + \mathcal{T}^y(x,y))$ outside the image boundaries are moved to the boundaries which are closest to them.

[17] The grid setup and spatial discretisation detail can be found in Appendix A.

For all $i \in [1, N_x]$, $j \in [1, N_y]$ *and* $I = (i-1)N_y + j (\in [1, N])$, *it is assumed*

$$i + \mathcal{I}_I^x = \begin{cases} N_x; & i + \mathcal{I}_I^x > N_x \\ 1; & i + \mathcal{I}_I^x < 1 \end{cases} \quad \textit{and } j + \mathcal{I}_I^y = \begin{cases} N_y; & \textit{if } j + \mathcal{I}_I^y > N_y \\ 1; & \textit{if } j + \mathcal{I}_I^y < 1 \end{cases} . \qquad (3.25\text{a,b})$$

An example of the warping process is demonstrated in Fig. 3.1 with $\mathbf{K}^0$, $\mathbf{K}^w$, $\mathbf{T}_x$ and $\mathbf{T}_y$ presented in the top left, top right, bottom left and bottom right panels, respectively. Through this demonstration, we wish to highlight two key properties of the warping process: (i) Permeability values not appearing in the prior permeability

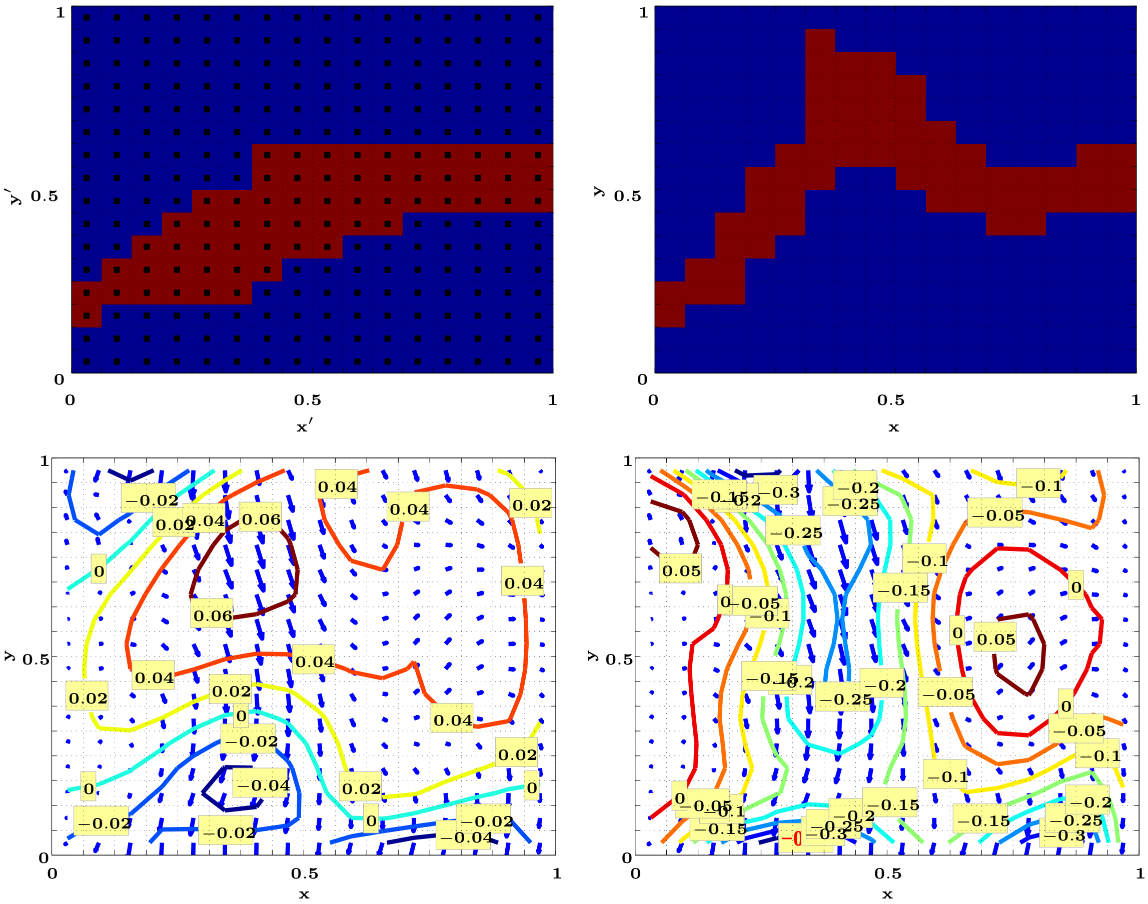

Figure 3.1: A warping process using Definition 3. The prior permeability field ($\mathbf{K}^0$, top left panel) indicates the cell centres (black dots); the contour plot of the discrete transformation functions $\mathbf{T}^x$ (bottom left panel) and $\mathbf{T}^y$ (bottom right panel) in the background of the Quiver plot; and the warped permeability ($\mathbf{K}^w$, top right panel) resulted with the presented prior permeability field and transformation functions.

field will never be created in the warped permeability field. (ii) The uncertainty of the warped permeability field can be specified indirectly using the uncertainty of the warping transformation. In the history matching problem of facies patterns, property (i) brings us the possibility of incorporating the information of the exact facies types and values using the prior permeability field while property (ii) lies at the core of the WEnSRF. Instead of estimating the (discrete) permeability (values) directly (which is incompatible with the EnSRF), WEnSRF is designed to estimate the (continuous) warping transformation using EnSRF and then the permeability indirectly.

WEnSRF

To achieve the design purpose of the WEnSRF, we must modify the input and the formulation of the state-space system for the history matching problem of facies patterns in (2.41a,b). The modified input should replace the permeability parameters $\mathbf{K}$ by the prior permeability field $\mathbf{K}^0$ (consisting of a known number of facies types with the specified permeability) and the warping transformation $[\mathbf{T}^{xk}, \mathbf{T}^{yk}]^T$: $x_k = [\mathbf{\Phi}^k, \mathbf{\Lambda}^k, \mathbf{K}^0, \mathbf{T}^{xk}, \mathbf{T}^{yk}, \mathbf{P^k}, \mathbf{S}_o^k]^T$, where the superscript T denotes a matrix transpose. The state-space system, which describes the simulation of the pressure and saturation in every cell and the measurements in the wells, is modified to consist of an additional warp transformation stage prior to the propagation:

$$x_k = f(x_{k-1}) = [\mathbf{\Phi}^{k-1}, \mathbf{\Lambda}^{k-1}, \mathbf{K}^0, \mathbf{T}^{xk-1}, \mathbf{T}^{yk-1}, \varpi_s\big(\mathbf{P}^{k-1}, \mathbf{S}_o^{k-1}, \mathbf{\Phi}^{k-1}, \mathbf{K}^{k-1}, \mathbf{\Lambda}^{k-1}\big)]^T \tag{3.26a}$$

$$s_k = Hx_k + v_k. \tag{3.26b}$$

Here, $\mathbf{K}^{k-1} = W_t(\mathbf{K}^0, \mathbf{T}^{xk-1}, \mathbf{T}^{yk-1})$ denotes the permeability field after the warping transformation in the warping transformation stage as defined in Definition 3,

$$H = \begin{pmatrix} 0^{n_y \times 5N} & I^{N_y} & 0^{n_y \times (2N - Ny)} & 0^{N_y \times Ny} \\ 0^{n_y \times 5N} & 0^{N_y \times Ny} & 0^{n_y \times (2N - Ny)} & I^{N_y} \end{pmatrix} \tag{3.27}$$

is a $2N_y \times 7N$ measurement matrix, where $0^{n_y \times 5N}$ is an $n_y \times 5N$ zero matrix, I^{N_y} is an $N_y \times N_y$ identity matrix, the first and second identity matrices I^{N_y} take the measurements on the pressure in the injection wells and the water saturation in the production wells. The measurement noise v_k is assumed to be independent and drawn from a Gaussian distribution with mean 0 and covariance matrix R as specified in eq. (2.43). It is noted that although the prior permeability $\mathbf{K}^0$ is included in the input, it is assumed exact in all time steps and not to be estimated.

WEnSRF utilises EnSRF to estimated the warping transformation function $(\mathbf{T}^x, \mathbf{T}^y)$ when measurements become available at each time step. At the end of each data assimilation cycle, the warped permeability field ensemble must be reconstructed using the analysed warping transformation ensemble and the prior permeability field to quantify the uncertainty of the permeability field estimation.

Note that compared to the original state-space formulation in (2.41a,b), the input for WEnSRF has $2N$ additional dimensions due to the (additional) warping transformation, which is not practically desirable. In §4.4.1, by introducing parameterisation for the warping transformation, the dimension of input for WEnSRF can be reduced to a similar dimension as the input of the original state-space formulation.

3.5.2 Summary

Throughout this thesis, WEnSRF for our (modified) state-space system (3.26a,b) for solving the history matching problem of facies patterns has the structure:

Initialization step:

1. The prior permeability field $\mathbf{K}^0$, which consisting of a known number of facies

types with the exact permeability, is assumed to be provided (by the geophysicists). The pdf $\pi_0\big(\mathbf{\Phi}^0, \mathbf{\Lambda}^0, \mathbf{T}^{x0}, \mathbf{T}^{y0}, \mathbf{P}^0, \mathbf{S}_w^0\big)$ of the initial state and model parameters is assumed to be given and represented statistically using an ensemble $X_0^a = \{x_{0,1}^a, \ldots, x_{0,r}^a\} = [(\mathbf{\Phi}_{0,1}^a, \mathbf{\Lambda}_{0,1}^a, \mathbf{K}_{0,1}^a, {\mathbf{T}^{xa}}_{0,1}, {\mathbf{T}^{ya}}_{0,1}, \mathbf{P}_{0,1}^a, \mathbf{S}_{w,0,1}^a, \mathbf{Q}_{o,0,1}^a, \mathbf{Q}_{w,0,1}^a)^T, \ldots,$ $(\mathbf{\Phi}_{0,r}^a, \mathbf{\Lambda}_{0,r}^a, \mathbf{K}_{0,r}^a, {\mathbf{T}^{xa}}_{0,r}, {\mathbf{T}^{ya}}_{0,r}, \mathbf{P}_{0,r}^a, \mathbf{S}_{w,0,r}^a, \mathbf{Q}_{o,0,r}^a, \mathbf{Q}_{w,0,r}^a)^T] \in \mathcal{R}^{n_x \times r}$.

2. For every filtering step $k = 1, 2, \cdots$, proceed as follows:

   Forecast step:

3. Perform the forecast step of the EnSRF in §3.3 using the state equation (3.26a) consisting of a warping transformation (in eq. (3.24)) step and a propagation step.

   Analysis step:

4. Perform the analysis step of the EnSRF in §3.3.

   Permeability field reconstruction step:

5. The posterior of the estimated permeability is reconstructed using the density reconstruction scheme in Appendix D with realisations of warped permeability fields generated using the prior permeability field $\mathbf{K}^0$ and each realisation of the analysed warping transformation $\{{\mathbf{T}^{xa}}_{k,1} \ldots, {\mathbf{T}^{xa}}_{k,r}\}$ and $\{{\mathbf{T}^{ya}}_{k,1} \ldots, {\mathbf{T}^{ya}}_{k,r}\}$.

3.6 Summary

In my opinion, every filtering method has its advantages and disadvantages when applied to particular problems. For example, for real (high-dimensional) nonlinear systems, the IPF and RPF are rigorous, but computationally infeasible. In comparison, the ensemble-base Kalman filtering methods are not rigorous because of further assumptions on the approximate predictive prior and posterior, but computationally superior. One should choose an appropriate method that best suits each individual problem to achieve the goals using various engineering heuristics, tuning of the process noise, different coordinate systems, various factorisations of the covariance matrix, and so on. This opinion is also evidenced by several reviews and books on the current nonlinear filtering techniques via several angles [11, 13, 32, 47, 65, 147].

The EnSRF, IEnSRF and WEnSRF are all variations of EnKF, the theory and history of which is reviewed in [58]. The EnKF is an easily-implemented and computationally-affordable suboptimal filter[18]. It has the properties given by the KF and the capability of computing the measurements in real time, but the true posterior will not be recovered with an increasing number of realisations.

For the barcode detection problem and the deconvolution problem in well testing, the direct reconstruction of the analytical posterior is challenging due to the practical difficulties in combining the likelihood pdf with a small uncertainty and the predictive prior pdf, which is integrated from a highly-nonlinear model system using a less informative or even biased initial prior. Through an iterative formulation and ensemble approximation (i.e. EnSRF), the newly-developed IEnSRF yields a suboptimal approximation of the IBF and is designed to overcome the described difficulty by repeatedly assimilating the same measurement with an inflated uncertainty. IEnSRF is also adaptable to any general problem with the described practical difficulty in a recursive formulation.

The newly-developed WEnSRF combines the image warping idea [24, 175, 176] and the EnSRF. It is designed to overcome the incompatibility of estimating the discrete model variables (e.g. the permeability of the facies) using the ensemble-based filtering methods through an indirect estimation of the continuous transformation mapping. Although, we have formulated the WEnSRF in particular for the considered history matching problem of facies patterns, it is also adaptable to any general estimation problem with discrete or multilevel spatial model variables as in the remote sensing and radar and medical imaging applications.

---

[18] EnKF is optimal for Linear and Gaussian state-space model, but is an uncontrolled approximation in general.

Chapter 4

Prior Constructions

4.1 Overview

Ill-posedness in real-world problems is often caused by model nonlinearity, small measurement dimension (compared to the dimension of the state vector) and (sometimes) presence of measurement noise. In this situation, several solutions can be found that give satisfactory and essentially indistinguishable fits to the measurements. This is, indeed, the challenge for solving the inverse problems. Replacing the original set of unknowns (the model variables) with a smaller (lower dimensional) group of unknowns that still capture the most important physical features is commonly employed to make the inverse problems better posed by reducing redundancy. This is called parameterisation and is a process of constructing prior information in the Bayesian framework. Some of these constructed priors are classified as dogmatic priors, because assumptions regarding the underlying physical system using everyday knowledge, previous data or prior belief must be made[1]. While helping to ease the non-uniqueness of the inverse problem, if assumptions are unreliable or falsely describe the true physics, a dogmatic prior that assigns zero probability to a reliable model may never be

---

[1] The dogmatic prior is thus a prior with small variance or a reduced prior, where many variables and parameters are assumed known.

revised. Likewise, a false model with prior probability of one may never be updated by the new data. In such situations, these dogmatic priors can lead to inconclusive and incomprehensive results. In contrast, a nondogmatic prior makes no or very few assumptions on the physical system and covers a wider range of hypotheses.

In this chapter, we introduce our prior information, which is dogmatic but constructed with some reasonable assumptions on the physical system for each of the inverse problems considered, and review some novel options for the corresponding parameterisations using a binary level set method and B-splines.

4.2 Barcode Stripe Prior for Barcode Detection

In the barcode detection problem introduced in §2.3.4, we aim to estimate the underlying barcode and the shooting parameters using the blurry image, and thus enable machine readable detections. In this section, we introduce the prior incorporated to parameterise the barcode in solving the described inverse problem using the Iterative Ensemble Square Root Filter (IEnSRF) in Chapter 5.

4.2.1 Prior Construction using a Binary Level Set Method

As derived in modelling of the blurry barcode images in §2.3.2, the barcode to be estimated is presented by a logic array of J barcode stripes, $[U^1, \ldots, U^J]$, where $U^j \in \{0, 1\}$ for all $j \in [1, J]$. In other words, using Assumptions 1, 2 and 4 on page 7, the prior of the logic of the barcode stripes being only 1 (black) or 0 (white) needs to be incorporated. However, such prior information makes the barcode stripe variable discrete and incompatible with the formulation of the IEnSRF in §3.4, which is designed to work only with continuous variables.

To go around this problem, one needs to introduce a parameterisation that transforms the discrete variables representing the logic of the barcode stripes into continuous variables and then use the latter in the estimation process. Here, we propose to achieve this using a one-dimensional binary level set modelling of the logic of the barcode stripes [139, 152, 158]. Suppose two subregions, D and its complement, D^C, form the domain of the logic of the barcode stripe, the level set modelling is:

$$U^j(m^j) = 1, \ \ \forall m^j \in D; \qquad U^j(m^j) = 0, \ \ \forall m^j \in D^C. \tag{4.1}$$

With the logic of the barcode stripe being a one-dimensional variable and the barcode stripes are equally probable to be logic 0 and 1 (without prior information regarding the digits). We define the domain of the binary level set modelling to be the real number set $\mathcal{R}$ with two subsects of domain being $D=(0,+\infty)$ and $D^C=(-\infty,0]$.

4.2.2 Summary

Throughout this thesis, a typical input for solving the barcode detection problem is $x_0 = [\mathbf{m}_0, \mathbf{o}_0]^T = [E_0^s, \alpha_0, \sigma_0, m_0^1, \ldots, m_0^J, \Lambda_0^1, \ldots, \Lambda_0^N]^T \in \mathcal{R}^{n_x}$, where the superscripts T and N denote the matrix transpose and the total number of discrete pixel samples, respectively; the subscript 0 denotes the prior stage of the simulation; $\mathbf{m} = [E^s, a, \sigma, m^1, \ldots, m^J]^T$ denotes the model variables and $\mathbf{o} = [\Lambda^1, \ldots, \Lambda^N]^T$ denotes the observation variables. The state-space system (modified from the state-space system (2.9a,b) on page 11) can be summarised as follows:

$$\begin{aligned} x_1 &= f(x_0) = [\mathbf{m}_0, \gamma^1(E_0^s, \alpha_0, \sigma_0, U^1(m_0^1), \ldots, U^J(m_0^J)), \\ &\qquad \ldots, \gamma^N(E_0^s, \alpha_0, \sigma_0, U^1(m_0^1), \ldots, U^J(m_0^J))]^T, && \text{(4.2a)} \\ s_1 &= Hx_1 + v, && \text{(4.2b)} \end{aligned}$$

where the logic of the j^{th} barcode stripe $U^j(m^j)=1, \forall m^j>0$, and $U^j(m^j)=0, \forall m^j \leq 0$, the function γ^k is introduced in eq. (2.8) and denotes the discrete approximation of the convolution process (2.7) evaluated at position x_k with the ambient light effect E^s, the barcode stripes $(U^1, \ldots, U^J)$ and the Gaussian convolution kernel with amplitude α and (rescaled) standard deviation σ, the subscript 1 denotes the posterior stage, H and v are the the measurement operator and noise as introduced in eqs (2.9c) and (2.9d) on page 11, respectively.

4.3 Type Curve Priors for the Deconvolution Problem in Well Testing

The most important goal of the deconvolution problem in well testing is to estimate the Log-Log Derivative Type Curve (LLDTC) for the given data and compare it against the analytical LLDTCs to identify the reservoir characteristics and boundaries [75, 76]. Hence, appropriate prior construction for parameterising the LLTDC is crucial to the success of deconvolution and pressure transient analysis.

The most common parameterisation uses a uniform piecewise linear approximation for the LLDTC directly [52, 103, 104, 163, 164], and is utilised in many commercial software applications, such as Fekete, Interpret$^{\text{TM}}$, Saphir and TLSD. From a Bayesian point of view, this corresponds to imposing a prior knowledge of uniform structure and first order smoothness, which is not very realistic and normally insufficient if a small number of nodes is used [76]. Indeed, it was suggested to use a minimum of 70 nodes for smooth and interpretable estimates [103, 104].

An indirect parameterisation with a higher order of smoothness was first proposed in [85]. The impulse function (the natural derivative of the Pressure Type Curve (PTC), see eq. (2.26)) is parameterised as a second order non-parametric B-spline function[2] with uniform logarithmically spaced knots using which the LLDTC and PTC can be computed. From a Bayesian point of view, this parameterisation

---

[2] A B-spline is a piecewise polynomial function which is defined on subintervals connected by points called knots with the property of continuity (of the function and its derivatives).

corresponds to imposing a prior knowledge of uniform structure and second order smoothness on the LLDTC, which offers a better potential to approximate the actual LLDTC with the same accuracy but fewer knots compared to the previous linear parameterisation. Indeed, the authors of [85] suggested that the number of knots should be on the order of at least 2 to 6 knots per log cycle.

In general, it would be more appropriate and useful to constrain the dimension of model parameters which could lead to a lower-dimensional estimation problem while still capturing the important features of the LLDTC with acceptable accuracy. In this section, the unclamped parametric B-spline curve is first introduced and proposed to parameterise the LLDTC in §4.3.1. §4.3.2 compares the performance of the proposed parameterisation against the two described existing methods, based on which conclusions and remarks for applying the proposed parameterisation are made. In §4.3.3, the state-space system based on the proposed parameterisation is summarised.

4.3.1 Prior Construction using Unclamped Parametric B-splines

The B-spline is a spline function that has minimal support with respect to a given degree, smoothness, and domain partition. A fundamental theorem states that every spline function of a given degree, smoothness, and domain partition, can be represented as a linear combination of B-splines of the same degree and smoothness, and over that same partition [39]. The method is mainly used for curve fitting [129], image registration [160] and oceanography [16]

In the deconvolution problem in well testing, with the aim of estimating the LLDTC for the comparison against the analytical LLDTCs in the reservoir characterisation analysis, the parameterisation of the LLDTC is desirable to provide an approximation of the analytical LLDTC with low-dimensional unknowns while still able to preserve the key feature, smoothness and complexity of the analytical LLDTC.

This helps ease the high non-uniqueness of the inverse problem and provides an improved estimate. For these purposes, a particularly useful parameterisation approach is the unclamped B-spline function which is a generalisation of a Bézier curve.

Definition 4. *We propose to approximate the LLDTC, $z(\tau)$, using a two-dimensional parametric unclamped B-spline function as follows [33, 125]:*

$$\underline{z}(\chi, \mathbf{a}, \mathbf{b}) = [\tau, z(\tau)]^T = \sum_{c=0}^{n} N_{c,d}(\chi)[a^c, b^c]^T. \tag{4.3a}$$

Here, both the subscript and superscript $c \in [0, n]$ is the index of the $n+1$ control points; the subscript d is the degree of the curve; $\chi \in [\log t_{min}, \log T]$ is a reference point; $a^c \in [\log t_{min}, \log T]$ and b^c the position along the logarithmic well test duration axis and the weight of the control point, respectively; and $\underline{z}(\chi, \mathbf{a}, \mathbf{b})$ is a parametric evaluation point at reference point χ using control points located at $\mathbf{a} = [a^0, \ldots, a^n]$ with heights $\mathbf{b} = [b^0, \ldots, b^n]$. The $N_{c,d}(\chi)$ are the B-spline basis functions and are recursively constructed as a function of $n+d+1$ knots τ_m in the standard open uniform fashion:

$$\tau_m = \begin{cases} \log t_{min}, & 0 \le m \le d \\ \log t_{min} + \frac{(m-d)(\log T - \log t_{min})}{n+1-d}, & d+1 \le m \le n \\ \log T, & n+1 \le m \le n+d+1 \end{cases} . \tag{4.3b}$$

The recursive definition of the B-spline functions starts from the basis function

$$N_{c,0}(\chi) = \begin{cases} 1, & \tau_c \le \chi \le \tau_{c+1} \\ 0, & \textit{otherwise} \end{cases} \tag{4.3c}$$

for $0 \le c \le n+d$. The functions are then computed recursively as

$$N_{c,l}(\chi) = \frac{\tau - \tau_c}{\tau_{c+l} - \tau_c} N_{c,l-1}(\chi) + \frac{\tau_{c+l+1} - \tau}{\tau_{c+l+1} - \tau_{c+1}} N_{c+1,l-1}(\chi) \tag{4.3d}$$

for $1 \le l \le d$ and $0 \le c \le n+d-l$.

For demonstration and comparison purposes, the prior information of LLDTC with uniform structure is adopted[3] (i.e. $\mathbf{a}$ is known and uniformly spaced on the logarithmical well test duration axis $[\log t_{\min}, \log T]$).

Furthermore, for an accurate approximation of the analytical LLDTC, the degree of the B-spline is normally required to be large, which makes its computation time-consuming [77]. Throughout this thesis, the prior knowledge of the cubic B-spline (with $d = 3$) is imposed to capture the most important feature of the complexity and smoothness of the LLDTC with consideration of the computational effort.

4.3.2 Comparison Against Parameterisations in Existing Methods

Numerical Experiments

Four numerical experiments are carried out to compare the approximations of analytical LLDTCs using linear [163], nonparametric [85] and the proposed parametric B-spline parameterisation methods. The corresponding oil reservoir models and boundary conditions for the analytical LLDTCs are summarised in table 4.1. The reservoir details and the oil properties of all experiments are all set to be the same and are summarised in table 4.2. The acquisition detail is summarised in table 4.3. The exact analytical functions for these LLDTCs are not specified explicitly, but can be found in the references provided in table 4.1 for the corresponding reservoir models.

In each experiment, 121 data points (20 uniform-logarithmically spaced samples per log cycle) are sampled from the analytical LLDTC in the time interval $[10^{-3}, 10^{3}]$ (hrs). The estimated LLDTCs, which best fit the data points[4], using the described parameterisation methods are found. The average absolute misfit (i.e. the L1

---

[3] This is not essential in real applications, for which nonuniform structures can be easily identified from the initial prior information.

[4] Using the nonlinear regression solver, lsqnonlin, in Matlab with the Trust-Region-Reflective Algorithm [35].

No.	Near-Wellbore Effects	Reservoir Behaviours	Boundary Effects [77]
1	Wellbore storage and skin [3]	Homogeneous [3]	Single boundary
2	Uniform flux vertical fracture [19]	Homogeneous	Channel boundary
3	Finite conductivity vertical fracture [19]	Double porosity, restricted interporosity flow [74]	Channel boundary
4	Uniform flux, horizontal well [77]	Multi-layer, cross-flow [17]	Infinite lateral extent

Table 4.1: Reservoir models for each numerical experiment.

Well direction	Wellbore radius	Formation volume factor	Net reservoir thickness	Matrix porosity	Total compressibility	Viscosity
Vertical	4.25 ft	1 rb/stb	100 ft	30%	10^{-5}/psi	1.0 cP

Table 4.2: The well, reservoir and oil properties for experiments in §4.3.2.

Durations	Initial pressure	Reservoir temperature
1000 hr	5000 psia	150 °F

Table 4.3: The well testing acquisition parameters for experiments in §4.3.2.

norm) between the analytical and estimated data points is employed to quantify the performance of the parameterisation.

Fig. 4.1 presents the analytical LLDTCs and the curves of the average misfit using the described parameterisations with increasing numbers of knots or nodes. Note that the number of knots represents especially the number of unduplicated knots.

The parametric B-spline parameterisation has at least 1 decimal point precision and outperforms the two existing parameterisation methods when the number of the knots is between 3 and 10. Using the suggested range of knot number (12 to 36 knots) for a non-parametric B-spline parameterisation [85], both parametric and non-parametric B-spline parameterisations outperform the linear parameterisation by one decimal precision on the average absolute misfit, which is hardly noticeable in real-world applications. Indeed, in [122], consistent deterministic estimates are found using linear and non-parametric parameterisations for three synthetic and one real-world deconvolution problems. In practice, the inconsistent estimates are caused by

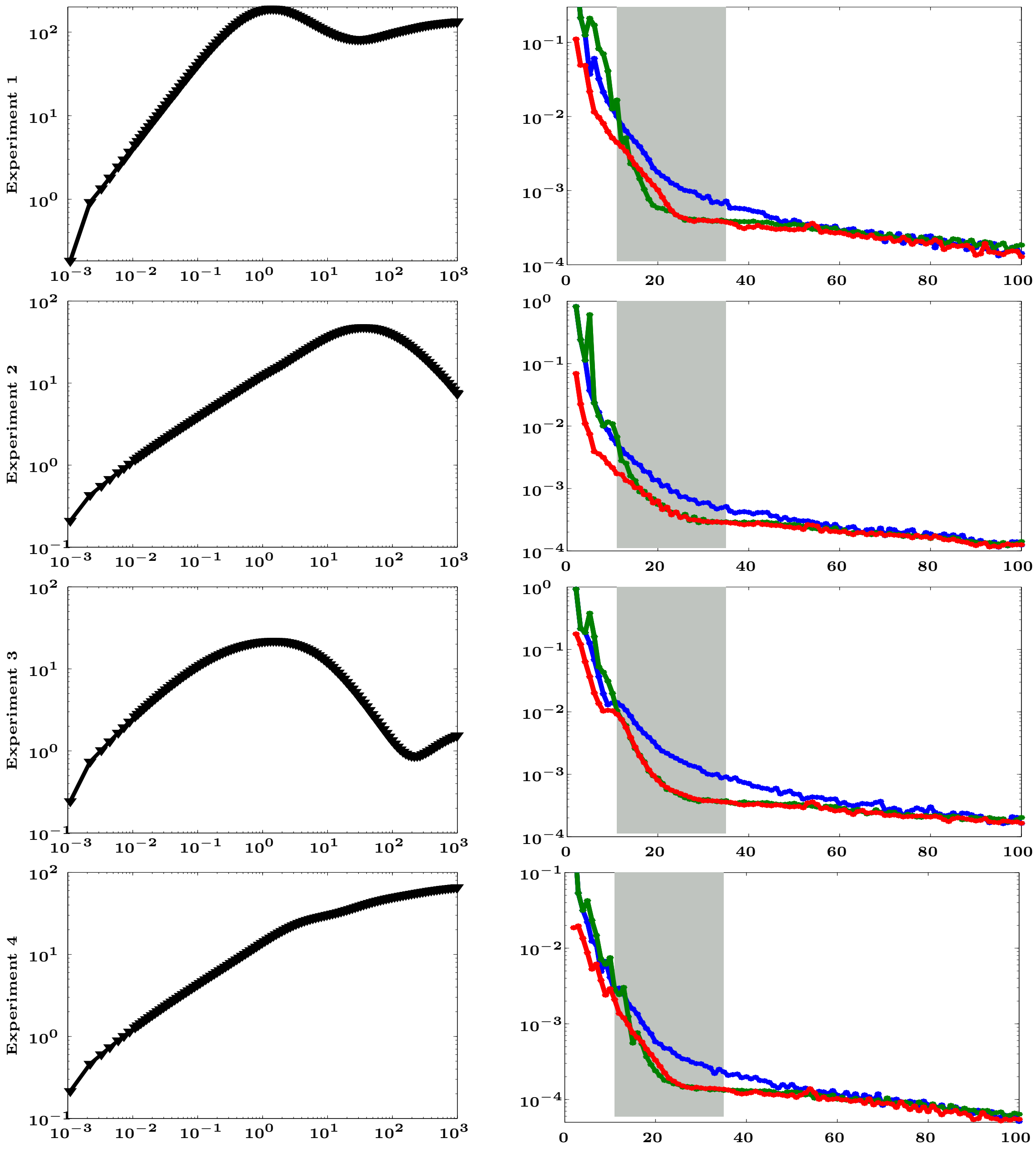

Figure 4.1: The analytical LLDTCs (left column) and the average absolute misfit using different parameterisation methods (right column) for the four experiments (each row) described in table 4.1. The analytical LLDTC plots present the analytical LLDTC curves (line) and sample points (triangles). The average absolute misfit plots present misfit between the analytical and estimated data points using the linear (blue), non-parametric B-spline (green) and parametric B-spline (red) parameterisations and the suggested range of knot number [85] for using non-parametric B-spline parameterisation (gray block).

different regularisations, not the parameterisations. With more than 50 nodes or knots, as we expected, the performance of all three parameterisation methods are almost identical and converges to the analytical LLTDC as the number of nodes or knots increases.

Conclusion and Remarks

The proposed parametric B-spline parameterisation method for the LLDTC naturally ensures strict positivity of the PTC at the expense of rendering the problem nonlinear. However, zeros of DTC cannot be prevented using this parameterisation. Through four numerical experiments, with a negligible additional computational effort (compared to the linear and nonparametric parameterisations) and using 3 to 10 knots, the proposed parameterisation is capable of providing an approximation to the analytical LLDTCs with acceptable accuracy and outperforms the existing linear and non-parametric B-spline parameterisations.

Throughout this thesis, the parametric cubic B-spline parameterisation is utilised for the estimation of the LLDTCs with 5 to 12 (uniform-logarithmically spaced[5]) control points (equivalently 3 to 10 knots) to give enough flexibility for reservoir characterisation without increasing the chances of having different parameter sets producing a comparable fit to the available measurements.

4.3.3 Summary

Throughout this thesis, a typical input for solving the deconvolution problem in well testing is $x_0 = [\mathbf{a}_0, \mathbf{b}_0, p_0^0, \mathbf{Q}_0, \mathbf{p}]^T \in \mathcal{R}^{n_x \times 1}$, where the superscript T denotes the matrix transpose, $\mathbf{a} = (a^0, ..., a^{n_z-1})^T$ and $\mathbf{b} = (b^0, ..., b^{n_z-1})^T$ are vectors of model parameters consisting of the n_z control point positions and weights for the LLDTC

---

[5] A non-uniform structure of the type curves can be adapted with non-uniform control points in the proposed parameterisation based on prior knowledge.

parameterisation, respectively, and $n_z \in [5, 12]$. The state-space system (modified from the state-space system (2.35a,b) on page 22) is:

$$x_1 = f(x_0) = [\mathbf{a}_0, \mathbf{b}_0, p_0^0, \mathbf{Q}_0, \gamma^1(p_0^0, \mathbf{m}_0^z(\mathbf{a}_0, \mathbf{b}_0), \mathbf{Q}_0), \cdots, \gamma^N(p_0^0, \mathbf{m}_0^z(\mathbf{a}_0, \mathbf{b}_0), \mathbf{Q}_0)]^T, \tag{4.4a}$$

$$s_1 = Hx_1 + v. \tag{4.4b}$$

Here, the subscripts 0 and 1 denote the prior and posterior stages of the simulation, respectively; N is the total number of pressure measurements;

$$\mathbf{m}^z(\mathbf{a}, \mathbf{b}) = [\tau^1, z^1, \cdots, \tau^{N'}, z^{N'}]^T = [\underline{z}(\chi^1, \mathbf{a}, \mathbf{b}), \cdots, \underline{z}(\chi^{N'}, \mathbf{a}, \mathbf{b})]^T \tag{4.4c}$$

denotes the B-spline parameterisation in eq. (4.3a), where $\chi^{k'} = \log t_{\min} + (k' - 1)(\log T - \log t_{\min})/(N' - 1)$ for all $k' \in [1, N']$ and denotes the uniformly-placed reference points on the logarithmic well test duration axis, γ^k is introduced in eq. (2.34) and denotes the discrete trapezoidal approximation of the convolution process (2.33) evaluated at time t_k with initial pressure p^0, flow rate $(Q^1, \ldots, Q^J)$ and the LLDTC samples $(\tau^1, z^1, \ldots, \tau^{N'}, z^{N'})$, H and v are the measurement operator and noise as introduced in eqs (2.35c) and (2.35d) on page 22, respectively.

4.4 Prior for the Transformation Mapping in the Warp Ensemble Square Root Filter

After the process of well testing, the uncertainty of the reservoir characterisation and boundaries is reduced, but not for the uncertainty in the spatial description of the permeability. Other than the use of expensive time-lapse seismic surveys, carrying out a history matching process during the production phase is the only hope to reduce such uncertainties. This process can also increase the accuracy and usefulness of model predictions if a reasonable description of the true field is estimated.

When the permeability field is modelled using a fine discretisation, given the limited amount of data and the reservoir complexity, the solutions of the history matching problem is often highly non-unique. This is why many engineers prefer to assign a dogmatic prior and adjust relatively small number of parameters ("global parameters"). For instance, large scale permeability trends, like barriers and channels, have a large impact on the fluid flow (i.e. reservoir production). This indeed is the reason why accurate knowledge of the number of facies types and the permeability of each facies is assumed and the geological structure is the goal of the history matching problem of facies patterns.

In this thesis, this goal is achieved by adapting the Warp Ensemble Square Filter (WEnSRF) in §3.5 to estimate the warp transformation mapping between the prior and warped permeability fields. However, the dimension of the unknowns for the transformation map is twice as large compared to the dimension of the unknown permeability if they are defined on the same grid. We propose to parameterise the transformation mapping using the parametric B-spline surface to reduce the dimension of the unknowns to be estimated and constrain the transformation between the prior and warped permeability fields in a reasonable and reliable manner.

4.4.1 Priors Construction using B-spline Surfaces

We consider a two-dimensional (rectangular) reservoir with a complicated channel feature as shown in the right panel of Fig. 4.2. Prior to the history matching process, a prior permeability field in the left panel of Fig. 4.2 is provided[6]. As expected, it does not provide the exact feature, but yields a reasonable approximation to the coarse-scale structure. The goal of the WEnSRF is to estimate the transformation mapping, $\mathcal{T} = (\mathcal{T}_x, \mathcal{T}_y)$ as defined in definition 2 on page 49, which maps the spatial coordinate, x and y in the domain of the estimated (warped) permeability field, to

---

[6] Methods to generate this prior permeability field is discussed and explained in [36, 63, 150, 151]

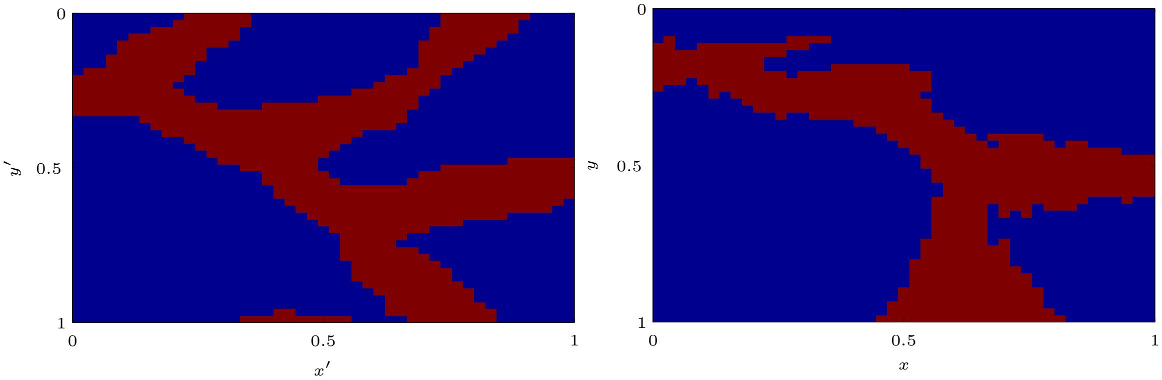

Figure 4.2: An areal plot of permeability fields with complicated features before and after the warping transformation. Plots show the prior (left) and warped (right) permeability fields, high permeability sandstone (red), low permeability shale (blue).

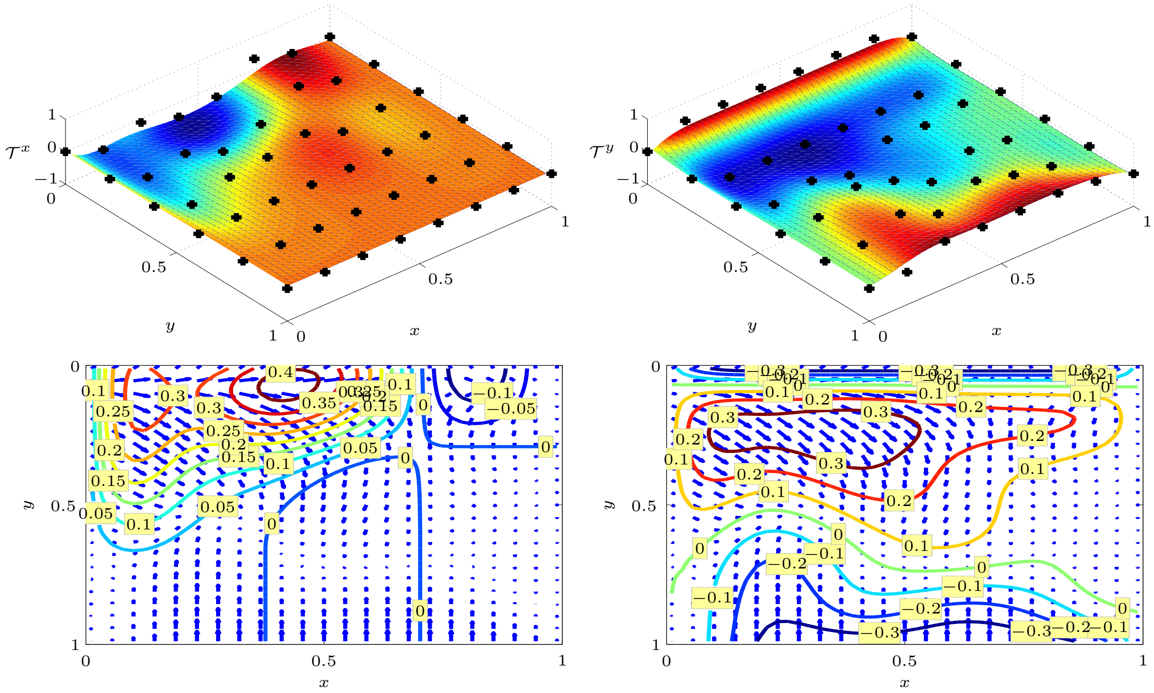

Figure 4.3: The B-spline surfaces (top row) of the single-valued transformation mapping, $\mathcal{T}^x$ (left) and $\mathcal{T}^y$ (right), with the uniform control net of 8×6 control points (black pluses in the plane) and the contour plots (bottom row) of $\mathcal{T}^x$ (left) and $\mathcal{T}^y$ (right), in the backgrounds of the Quiver plot.

new spatial coordinates x' and y' in the domain of the prior permeability field.

In digital image processing, there is a large literature regarding spatial transformation mapping, from the earliest affine transformations including image translation, rotation, scale and shear to more recent global spline transformations using basis functions and regularisations [24, 175, 176]. A particulary efficient and important transformation mapping is the B-spline transformation. It was first proposed in [138] where a bivariate cubic B-spline tensor product is used to define the free-form deformation function of solid geometric models. A sufficient condition for a 2-dimensional cubic B-spline surface to be one-to-one is also presented in the same paper.

Definition 5. *Using the same formulation in the WEnSRF, we assume the transformation is smooth and propose to parameterise it by B-spline surfaces based on the tensor product of nonparametric unclamped B-spline functions as follows [33, 125, 144]:*

$$\mathcal{T}^x(x,y) = B_s(x,y,\mathbf{b}^{s_x}) = \sum_{c_x=0}^{m_x-1}\sum_{c_y=0}^{m_y-1} N_{c_x,d_x}(x)N_{c_y,d_y}(y)b^{c_x,c_y}. \tag{4.5a}$$

Here, $\mathcal{T}^x$ is the single-valued transformation mapping in the x direction; subscripts and superscripts x and y denote the x and y directions, respectively; both the subscripts and superscripts $c_x \in [0, m_x–1]$ and $c_y \in [0, m_y–1]$ are the indices of the two-dimensional uniform control net consisting of $m_x \times m_y$ control points of the transformation mappings; the subscripts d_x and d_y denote the degrees of the smoothness of the B-spline surface in x and y directions, respectively; b^{c_x,c_y} is the weight of the control point which is located at the c_xth place in the x direction and the c_yth place in the y direction of the control net; $N_{c_x,d_x}(x)$ and $N_{c_y,d_y}(y)$ are the B-spline basis functions, which are recursively constructed as in eqs (4.3b,c,d) with open uniform knots, respectively; $\mathbf{b}^{s_x} = [b^{0,0}, \ldots, b^{m_x,m_y}]$ denotes the array of control point heights, and $B_s(x,y,\mathbf{b}^{s_x})$ denotes the proposed B-spline parameterisation using the two-dimensional uniform control net consisting of $m_x \times m_y$ control points with heights $\mathbf{b}^{s_x}$.

Similarly, the single-valued transformation mapping in the y direction, $\mathcal{T}^y$, is proposed to be parameterised using a B-spline surface $B_s(x,y,\mathbf{b}^{s_y})$ with uniform control *net consisting of* $\mathrm{m}_x \times \mathrm{m}_y$ *control points and heights* $\mathbf{b}^{s_y} = [\mathrm{b}^{0,0}, \ldots, \mathrm{b}^{\mathrm{m}_x,\mathrm{m}_y}]$*, as follows:*

$$\mathcal{T}^y(x,y) = B_s(x,y,\mathbf{b}^{s_y}) = \sum_{\mathrm{c}_x=0}^{\mathrm{m}_x-1} \sum_{\mathrm{c}_y=0}^{\mathrm{m}_y-1} N_{\mathrm{c}_x,\mathrm{d}_x}(x) N_{\mathrm{c}_y,\mathrm{d}_y}(y) \mathrm{b}^{\mathrm{c}_x,\mathrm{c}_y}. \tag{4.5b}$$

Definition 6. *In discrete form, the warping transformation mapping is assumed to be constant* $(\mathbf{T}^x_{i,j}, \mathbf{T}^y_{i,j})$ *inside each cell of the standard grid defined in Appendix A with cell* (i,j) *centered at* $((i-1)h_x, (j-1)h_y)$*, where* $i \in [1, N_x]$ *and* $j \in [1, N_y]$*. The proposed B-spline parameterisation,* $\mathbf{B}_s$ *, for the warping transformation functions in eqs (4.5a,b) in the discrete form can be summarised as:*

$$\begin{aligned} \mathbf{T}^x = \mathbf{B}_s(\mathbf{b}^{s_x}) = [\mathbf{T}^x_{1,1}, \ldots, \mathbf{T}^x_{i,j} \ldots \mathbf{T}^x_{N_x,N_y}]^T \\ = [B_s(0,0,\mathbf{b}^{s_x}), \ldots, B_s((i-1)h_x, (j-1)h_y, \mathbf{b}^{s_x}), \ldots, B_s(1,1,\mathbf{b}^{s_x})]^T, \quad (4.6a) \\ \mathbf{T}^y = \mathbf{B}_s(\mathbf{b}^{s_y}). \quad (4.6b) \end{aligned}$$

As a demonstration, the true (warped) reservoir permeability field on a uniform 45 × 45 grid in the right panel of Fig. 4.2 could be recovered by warping the prior permeability field in the left panel with transformation mappings in Fig. 4.3 (another example is presented in Fig. 3.1). The number of unknowns is reduced from $2 \times 45 \times 45$ to $2 \times 8 \times 6$ by adapting the B-spline parameterisation.

4.4.2 Summary

Throughout this thesis, a typical input for solving the history matching problem of facies patterns using the WEnSRF is:

$$x_k = [\mathbf{\Phi}^k, \mathbf{\Lambda}^k, {\mathbf{K}^0}^k, {\mathbf{b}^{s_x}}^k, {\mathbf{b}^{s_y}}^k, \mathbf{P}^\mathbf{k}, \mathbf{S}^k_w]^T \in \mathcal{R}^{5N + m_x m_y + \mathrm{m}_x \mathrm{m}_y}, \tag{4.7}$$

where the superscript T denotes a matrix transpose, N is the total number of cells in the reservoir domain on the standard grid, $\mathbf{P}$, $\mathbf{S}_w$, $\mathbf{\Phi}$, $\mathbf{\Lambda}, \mathbf{K}^0$ are all of dimension N

and denote the discretised pressure, water saturation, porosity, mobility and the prior facies pattern consisting of a known number of facies types with specified permeability in all cells in a vector form, respectively, $\mathbf{b}^{s_x} \in \mathcal{R}^{m_x m_y}$ and $\mathbf{b}^{s_y} \in \mathcal{R}^{\mathrm{m}_x \mathrm{m}_y}$ are the height arrays of the control points of the uniform control net for the warping transformation mapping in the x and y directions, respectively. The state-space system (modified from the state-space system (3.26a,b) on page 52) can be summarised as follows:

$$
\begin{aligned}
x_k &= f(x_{k-1}) \\
&= [\mathbf{\Phi}^{k-1}, \mathbf{\Lambda}^{k-1}, {\mathbf{K}^{0}}^{k-1}, {\mathbf{b}^{s_x}}^{k-1}, {\mathbf{b}^{s_y}}^{k-1}, \varpi_s\left(\mathbf{P}^{k-1}, \mathbf{S}_w^{k-1}, \mathbf{\Phi}^{k-1}, \mathbf{K}^{k-1}, \mathbf{\Lambda}^{k-1}\right)]^T, \quad (4.8a) \\
s_k &= H x_k + v_k. \quad (4.8b)
\end{aligned}
$$

Here, $\mathbf{K}^{k-1} = W_t({\mathbf{K}^{0}}^{k-1}, \mathbf{B}_s^{k-1}({\mathbf{b}^{s_x}}^{k-1}), \mathbf{B}_s^{k-1}({\mathbf{b}^{s_y}}^{k-1}))$ denotes the permeability field after the warping transformation as introduced in definition 3 on page 50, where $\mathbf{B}_s$ denotes the proposed B-spline surface parameterisation as introduced in definition 6 on page 70, H and v_k are the measurement operator and noises as introduced in eqs (2.42) and (2.43) on page 30, respectively. Although the prior permeability $\mathbf{K}^0$ is included in the input vector, it is a constant not to be estimated.

4.5 Summary

A quotation from Henri Poincaré [7]

> "La physique ne nous donne pas seulement l'occasion de résoudre des problèmes ..., elle nous fait pressentir la solution."

underlines this chapter. That is, by constructing realistic and improved prior information based on the model physics, we help ease the ill-posedness of the inverse problems. Hence, improved posterior density and estimates can be achieved [61, 120, 168].

---

[7] Cited by [79] at the beginning of the paper in which he defined well-posed problems.

For the barcode detection problem, by assuming the barcode is printed in black and white only, a level set method is used to parameterise the color of the barcode stripes and makes the modified state-space system compatible with the IEnSRF.

A large part of the prior construction methods introduced in this chapter are based on the application of B-splines [39]. For the deconvolution problem in well testing, a two-dimensional parametric unclamped B-spline function is used to parameterise the LLDTC. The prior information, which has been incorporated by this parameterisation, is that the smoothness, complexity and structure of the exact underlying LLDTC can be approximated by the degree of the B-spline, and the number and weights of the control points, respectively. In particular, in §4.3.2, the parameterisation method is compared against two existing methods, namely (piecewise) linear and nonparametric B-spline parameterisations. Through numerical experiments, the proposed parameterisation method has demonstrated improved approximation to the analytical LLDTC compared to the existing methods and is able to provide reasonable approximations with only a few control points.

In history matching of facies patterns, the WEnSRF is designed to adjust the shape and location of the reservoir features indirectly using warping transformations on some prior permeability field. Incorporating the ideas in the image warping, we propose to parameterise the transformation mapping using B-spline surfaces. Our prior information incorporated by this parameterisation is that the smoothness and direction of the transformation mapping can be approximated by the degree of the B-spline surfaces and the weights of the control points, respectively. However, in the WEnSRF, our prior information regarding the structure and complexity of the feature is unable to be incorporated using the transformation mapping and must be included in the prior permeability field.

Chapter 5

The Barcode Detection Problem

5.1 Introduction

Barcodes are a technology for presenting data in a machine-readable format. They are inexpensive, fast to produce and normally detected quickly and optically with simple hardware. Barcodes were invented by Bernard Silver and Norman Woodland as part of the system to automatically read product information during checkout in 1949 [67]. This became the biquitous Universal Product Code (UPC) barcode as shown in Fig. 2.1. It was patented in 1952 and first used commercially in 1974 [69].

The 12-digit UPC barcode is one of the most widely used linear barcodes, whilst the 13-digit "European Article Number" (EAN) barcode, another linear barcode (also presented in Fig. 2.1), is widely used in Europe. Both standards are based on similar ideas: (i) A dark bar denotes a logic 1, and a bright space denotes a logic 0. (ii) Barcodes begin and end with bits 101 and with the five bits 01010 in the middle separating the left and right side of the code. These bits are called "guard bars" and used for synchronizing the decoder. (iii) Each digit begins and ends with known bits (i.e. code on the left side begins with logic 0 and ends with logic 1 and code on the right side begins with logic 1 and ends with logic 0[1]). These bits are called 'code

---

[1] The code on the right is the exact inverse logic to the code on the left side.

indicators' and used to ease the detection difficulties. These highlighted facts for the UPC standard can be identified in Table 5.1. The first and last digits of the UPC barcodes are the product type and check digit[2]. The two standards only differ on the digit code standards and total number of digits.

Digit	UPC Barcode	
	Left Side	Right Side
0	0001101	1110010
1	0011001	1100110
2	0010011	1101100
3	0111101	1000010
4	0100011	1011100
5	0110001	1001110
6	0101111	1010000
7	0111011	1000100
8	0110111	1001000
9	0001011	1110100

Table 5.1: The digit codes for the UPC standard.

Conventionally, the barcode is detected with a scanner. When the scanning is performed close enough, the traditional methods, which detect the bar edges (e.g. through the first or second order derivative of the input signal) and intensity [21, 80, 141], works well. Nowadays, with the popularity of hand-held devices with fixed-focus-lens cameras, an improved method for detecting the (often out-of-focus) blurry images is needed by the retail industry and the military.

Recent detection methods for blurry images can be summarised into three main categories:

The Edge Detection-Based Approach [92, 93, 94, 143]

Using the principle that the peaks are more immune to blurring, the early detection methods [93, 94] are based on detecting edges using the peaks of the first or second derivative of the brightness across the barcode. With the presence of measurement noise, these methods very often misdetect edges. They are improved further in [143] with an Otsu's threshold[3] [123], which acted as a filter to attenuate the noise. The improved method has worked reasonably well with quality input, but often fails [165] because of the smeared out brightness and edges when the images are very blurred

---

[2] A built-in engineering error correction number being place at the last digit. Denoting the sums of the digits at odd-numbered and even-numbered places (excluding the check digit) as Σ_O and Σ_E respectively, the check digit is obtain by $10 - (\mathrm{mod}(3\Sigma_O + \Sigma_E, 10))$, where $\mathrm{mod}(a, b)$ denotes the operation in seeking the remainder of a divided by b.

[3] In computer vision and image processing, Otsu's method is used to automatically perform histogram shape-based image thresholding or the reduction of a graylevel image to a binary image.

or in low resolution.

The Inverse-Problem-Based Approach [55, 159, 174]

The barcode detection problem is first formulated as an inverse problem by Turin *et al.* [159]. Using the forward model (2.6), the expectation-maximisation algorithm is used to calculate the maximum likelihood solution of the Gaussian kernel and barcode. In [174], Wittman formulated the inverse problem into a minimisation problem of the total 'energy' which consists of: (i) the misfit energy between the observed and predicted signals , and (ii) the total variation energy of the predicted signal[4]. This method was reported to process each signal in about 6 minutes in Matlab on a Celeron with 2.4 GHz clock rate[5].

At the same time, Selim Esedoglu, proposed a more rigorous and computationally superior deconvolution method using the same model and total variational approach [55]. He adapted a level-set type regularisation term in the total energy function and implemented a gradient descent method in the Fourier space for the optimisation. Using the associated Matlab code at [54], the method was shown through experiments to provide consistent estimation results in a reasonable time. However, as will be demonstrated in §5.4.4 , this method is inapplicable to real-world problems.

The Statistical Machine Learning Approach [165, 166]:

Based on a database of over 1100 contaminated barcode images captured using a specified device, a feature vector classification method is proposed in [165] to extract the characters of a barcode image. The characters with the smallest recognition distance are selected as the estimates, while the training of the statistical classifier is based on the modified Generalized Learning Vector Quantization (GLVQ) method. These authors later improved their earlier method by incorporating a wavelet transformation and character segmentation (based on the zero crossings of the second derivative of

---

[4] The latter energy part can be seen as a 0^{th}-order Tikhonov regularisation term [95, 156]

[5] According to our experiments using the available code on their website [173], the process time for all signals can take as long as 12-15 minutes in Matlab on an Intel Quad Core I3 (2.4 GHz clock rate each core) with 3 gigabytes of memory.

the brightness values) to locate the barcode [166]. However, the system maintenance cost for this method is usually an issue because of the effort in building the training image database and potential restrictions for using a particular database with only the specified capturing devices.

In this chapter, we introduce a new method for blurry UPC barcode (image) detection by solving the deconvolution problem using the Iterative Ensemble Square Root Filter (IEnSRF) with a one-dimensional binary level set parameterisation of the barcode stripes. Using the proposed approach, we demonstrate that the blurry UPC barcode images under both synthetic and real conditions can be detected mostly within 10 seconds of Matlab computational time and present the comparison of the test results against existing methods and commercial software.

This chapter is organised as follows. §5.2 recalls the state-space formulation and discusses the detailed implementation of our proposed method. §5.3 states the typical form of filter realisations and specifies the prior knowledge incorporated and the scheme for generating the initial ensemble used in the numerical experiments. §5.4 presents and discusses the results of numerical experiments on both synthetic and real barcode images. A summary and a discussion conclude the work in §5.5.

5.2 The State-Space System and Practical Implementation

When taking a barcode image with a fix-focus-lens camera as installed on many hand-held devices, the barcode image is often very blurred, which often leads to misdetection and undetectability using conventional methods. Indeed, as defined in Chapter 1, developing a Bayesian method with improved performance to find out the product information from a blurry barcode image is the goal of this chapter.

5.2.1 The State-Space System

The barcode detection problem is a typical inverse problem which must be tackled by mathematical modelling based on the underlying physics, measurement uncertainties, and information summarising our prior knowledge. In §2.3, by modifying the existing mathematical model for laser barcode scanning with additional real-world shooting environment parameters, the blurry barcode images due to both the out-of-focus shooting equipment (with clear barcode print) and poorly-printed barcode print (with correctly-focused shooting equipment) are modelled as the convolution of a Gaussian (type) kernel with the exact barcode logic signal in eq. (2.7)[6].

In §4.2, the assumption that the underlying barcode consists of equal-width black and white barcode strips is proposed and incorporated in the constructed prior for the state-space formulation. In particular, to make the formation compatible with the requirements of the newly-developed Bayesian method, IEnSRF, in §3.4, a binary level set parameterisation of the barcode stripes is introduced.

We recall that the state-space system for solving the barcode detection problem using IEnSRF is summarised in eqs. (4.2a,b) in §4.2.2 based on the constructed prior in §4.2. It is used to estimate the barcode stripe parameterisation $(m^1, \ldots, m^J)$ and the shooting parameters (E^s, a, σ) using the the measured barcode signal (s_1).

5.2.2 Implementation for Real-World Detection Problems

To compare existing methods with our proposed method, we adapted the simulator in [54, 55, 173, 174] as our forward simulator with spatial samples of a one-dimensional barcode signal, $\mathbf{\Lambda}$, positioned uniformly across the barcode: $x_k = k/(MJ)-1/(2MJ)$, where M is a positive integer and denotes the sample rate (i.e. the number of uniformly-spaced samples) in each barcode stripe. Based on this assumption, both the

---

[6] The blending process of the neighbouring pixels of the out-of-focus blurry image is known to the photographers since the invention of the first camera and is commonly called ‘Gaussian Blur’ which corresponds to the convolution kernel used in our model [118, 128, 142].

Gaussian kernel and the barcode stripe can be evaluated at this uniform sample gird prior to the forward simulator to provide an efficient way of computing the discrete convolution function γ^k in eq. (2.8)[7] and simulating the barcode signal.

Note that the reduction of the sample rate can improve the computational time, but is an artifact of the described simulator, because it must compensate by increasing the amplitude and (rescaled) standard deviation (SD) of the Gaussian kernel which should only depend on the experimental setup and image equipment, not the measurement resolution. This artifact was not reported in the original publications [54, 55, 173, 174], because these authors were aiming for the development of the method not the real-world practicality. We set $M = 4$ to be the default value in our forward simulator for both realistic modelling and computational efficiency[8].

To accommodate the described forward simulator, a two-dimensional barcode image must be preprocessed to give a compatible one-dimensional uniformly sampled barcode signal. For a given barcode image, we manually select[9] and crop an area of it, the left and right borders of which should yield a good approximation of the beginning and end of the barcode. This selected area of the original image is defined as the full-size (FS) (barcode) image. It is then averaged along the direction of the barcode stripes and resampled using the averaging resampling algorithm in Appendix C to generate the measured barcode signal as the measurement vector s_1.

5.3 Barcode Estimation using the IEnSRF

The barcode detection method we propose is to update the continuous parameterisation of the logic of the barcode stripes using the IEnSRF (in §3.3). To adapt the IEnSRF, the state-space system (4.2a,b) is transformed into the iterative formation as

---

[7] I.e. using Matlab built-in command ‘conv’.

[8] The default value of the sample rate per barcode stripe in [54, 55, 173, 174] is set to be $M = 8$.

[9] The goal of this chapter is to find a Bayesian method for solving the barcode detection problem, not to locate the barcode feature in a image.

in eq. (3.19a,b,c) of §3.4.3. A typical realisation is: $x_{K,i}=\{E^s_{K,i},\alpha_{K,i},\sigma_{K,i},m^1_{K,i},\ldots,m^J_{K,i},\Lambda^1_{K,i},\ldots,\Lambda^N_{K,i}\}^T\in\mathcal{R}^{n_x}$, where K and i denote the iteration and realisation indices, respectively. As discussed in §5.1, for a 12-digit UPC code with digit codes summarised in Table 5.1, the realisation must satisfy the following exact information: (i) Total number of barcode stripes[10] (J) and samples is 95 and $95M$, respectively. (ii) For guard bars: $[m^1,m^2,m^3]=[1,0,1]$, $[m^{46},m^{47},m^{48},m^{49},m^{50}]$=$[0,1,0,1,0]$ and $[m^{93},m^{94},m^{95}]$=$[1,0,1]$, respectively. (iii) For code indicators: $m^{7d-3}=0$, $m^{3+7d}=1$, $m^{44+7d}=1$ and $m^{50+7d}=0$ for $d=1,\ldots,6$.

The initial priors for the image brightness due to ambient light (E^s), amplitude (α) and SD (σ) of the Gaussian kernel and barcode stripe parameterisation ($\mathbf{m}^U$) are constructed as Gaussian distributions with mean at $\mu_{E^s}\in[0,1]$, $\mu_a\in\mathcal{R}^+$, $\mu_\sigma\in\mathcal{R}$ and $\mu_{\mathbf{m}^U}\in\mathcal{R}^J$ and (scalar) SDs of σ_{E^s}, σ_α, σ_σ and σ_m, respectively, as follows:

$$\begin{pmatrix} E^s_0 \\ \alpha_0 \\ \sigma_0 \\ \mathbf{m}^U_0 \end{pmatrix} \sim \mathcal{N}\left(\begin{pmatrix} \mu_{E^s} \\ \mu_\alpha \\ \mu_\sigma \\ \mu_{\mathbf{m}^U} \end{pmatrix}, \begin{pmatrix} \sigma^2_{E^s} & 0 & 0 & 0 \\ 0 & \sigma^2_\alpha & 0 & 0 \\ 0 & 0 & \sigma^2_\sigma & 0 \\ 0 & 0 & 0 & \sigma^2_m\mathcal{D}^J \end{pmatrix}\right). \tag{5.1}$$

Here, $\mathcal{D}^J=\text{diag}(0,0,0,0,1,\ldots,1,0,0,0,0,0,0,0,1,\ldots,1,0,0,0,0)$ is the $J\times J$ diagonal matrix with entries mostly equal to 1 and the entry 0 is at the places corresponding to the exact information regarding both the guard bars and code indicators. Correspondingly, to incorporate this exact information, the entries of the barcode stripe parameterisation mean $\mu_{\mathbf{m}^U}$ are setting to be the logic of these barcode stripes.

For the barcode stripe, the mean ($\mu_{\mathbf{m}^U}$) at places where exact information is absent, is set to be 0, and the SD (σ_m) is set to be 0.5 to optimise the convergence and performance of the IEnSRF[11]. The means and SDs of the initial prior are kept

---

[10] 7×12 stripes for the product digits and 11 stripes for the guard bars.

[11] When the SD is too large, some of the generated random numbers of the barcode stripe parameterisation may be far away from zero, the sign of which may not be changed in the analysis step of IEnSRF in the first few iterations. This means unnecessary delay to the detection time. Likewise,

		α	σ	E_s
Exact		0.08	0.175	N/A
Initial Prior	Mean	0.02	0.85	0.175
	SD	0.002	0.085	0.025

Table 5.2: Exact model parameters and the mean and Standard Deviation (SD) of the initial prior for all experiment.

consistent for all experiments and are summarised in Table 5.2. To reflect the lack of initial prior information for the model parameters, they are chosen deliberately to be quite different to the exact parameters used to generate the barcode signal in §5.4.1 and the barcode prints in §5.4.2. To mitigate the potential problem of ensemble collapse, an ensemble with 500 realisations is used in the experiments [59, 135, 136]. At initialisation requirement for the IEnSRF, we propagate the realisations in the initial ensemble to generate the forecast ensemble measurement error covariance matrix ($HP_1^f H^T$) and conduct a sensitivity analysis for the inflated measurement uncertainty. The inflated measurement SD σ_I is found to be 0.05 and used to assimilated the measurement in each iteration of the IEnSRF.

In the conventional setting of the IEnSRF, the total number of iterations must agree with the inflated scale of the measurement uncertainty and the solution is the ensemble approximation of the posterior pdf. With the principal aim of testing the applicability of the IEnSRF in extracting the barcode information from a blurry image in real applications, we refine the stopping criterion of the IEnSRF to be the matching of the barcode check digit. At the end of each iteration, the ensemble mean of the logic of the barcode stripe is inversely mapped to product digit using the digit barcode Table 5.1. The detection is successful and iteration is terminated, if the last product digit matches with the calculated result using the checking algorithm with the first 11 product digits (see footnote 2 on page 74). In this setting, the IEnSRF ensures efficiency and estimation accuracy at the expense of overestimating the posterior uncertainty (in our numerical experiments)[12].

---

when the SD is too small, the sign change are easily-adjusted which lead to the sensitivity estimation in the first few iterations and unnecessary delay.

[12] The estimated posterior uncertainty is underestimated if the terminating iteration is more than the designed number of iterations (i.e. overfitting the data).

5.4 Numerical Experiments

One synthetic and two real-world numerical experiments are performed to test the proposed barcode detection method and to evaluate its performance. The UPC code in Fig. 2.1, which has product digits ‘093053772246’, is used in all experiments.

In the synthetic experiment, we simulate the ‘true’ barcode image using the forward simulator. Synthetic measurements are then extracted from the true states and perturbed with (known) random noise to test the method in the Perfect Model Scenario (*PMS*). In the real experiments, the IEnSRF is performed under the Imperfect Model Scenarios (*IMS*) with inadequate information on the measurement noises and mathematical model. The mean and SD of the image brightness due to ambient light, the amplitude and SD of the Gaussian kernel and the logic of the barcode stripe ensemble are used to quantify their estimates and uncertainty.

In the real experiments, the barcode is placed in a simple frame between three red folders as shown in Fig. 5.1. The image is taken with a single-lens reflex digital camera with the resolution set to be 3888×2592 pixels. An area of this image, whose left and right borders yield the beginning and end of the barcode is cropped to be the FS image and then preprocessed to generate the measured barcode signal.

In each experiment, in order to test the performance and applicability of the proposed method in overcoming the challenges in detecting low-resolution (LR) barcode images, a test is also performed on an LR image which is generated by selecting a single pixel out of several consecutive pixels of the FS image without any smoothing or averaging. Both the FS and LR images for generating the measured signals are summarised in Fig. 5.2. where, as we expected, the LR image is more noisy compared to the FS image on its left.

To rigorously quantify the computational time and iterations required using the proposed method, 100 detection trials are performed. The computational time and iterations for each trial are recorded and analysed using Matlab on a laptop with an

Intel Quad Core I3 (2.4 GHz clock rate each core) with 4 gigabytes of memory.

5.4.1 Synthetic Barcode Detection

Using the parameters summarised in Table 5.2, to deliberately make the experiment difficult and to correspond to the real-world situation, the true barcode image (Fig. 5.2) is generated using the forward simulator and perturbed by random noise with SD $\sigma_s = 0.001$, while a very poor initial prior has been deliberately assigned.

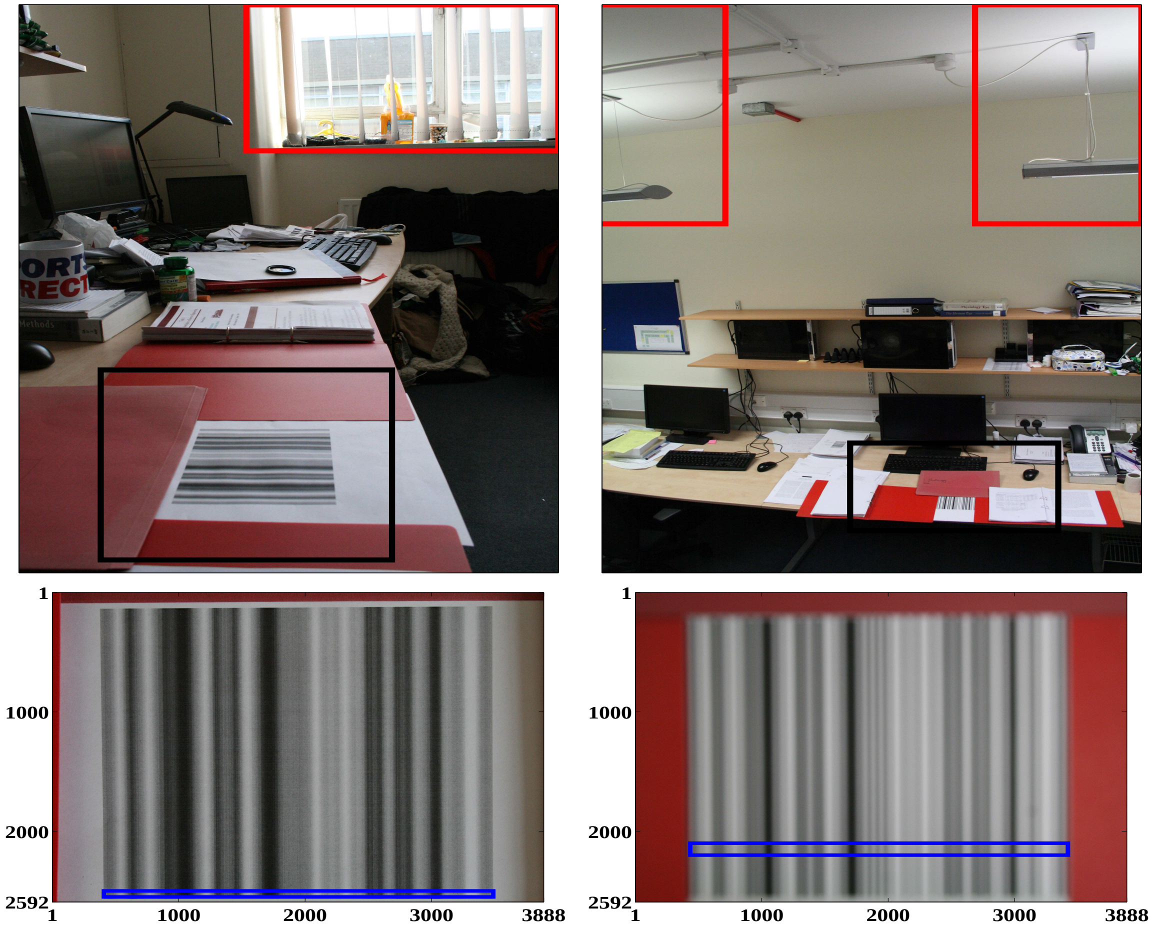

Figure 5.1: The experimental setup and the corresponding original barcode images for real experiments 5.4.1 (left column) and 5.4.2 (right column). The experimental setup figures (top row) show the ambient light sources (red rectangles) and the barcode print in a simple frame (black rectangles). The original images (bottom row) show the barcode feature (blue rectangles) which is cropped and selected to generate the full-size and low resolution barcode images in Fig. 5.2.

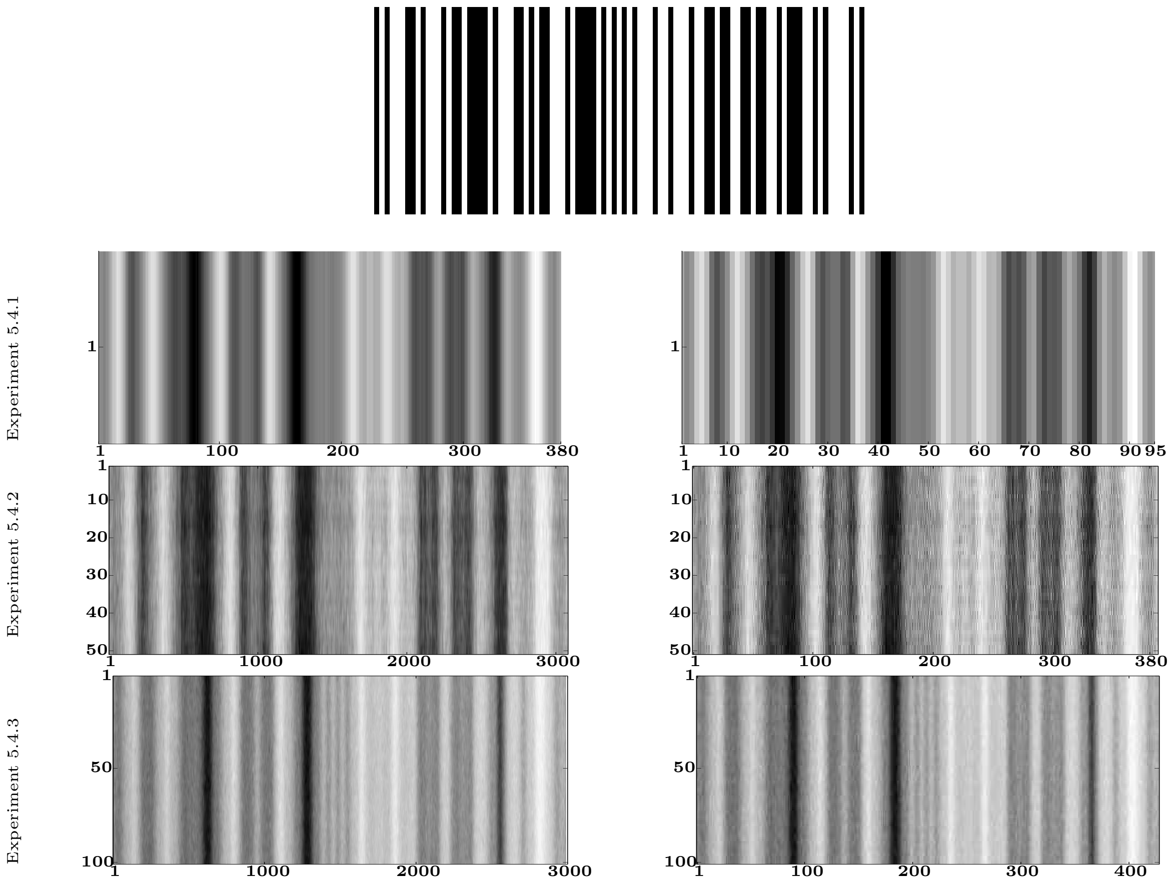

Figure 5.2: The idealised (top), full-size (left column) and low-resolution (right column) barcode images for synthetic experiment 5.4.1 (second row) and real experiments 5.4.2 (third row) and 5.4.3 (bottom row).

For a fair comparison[13], the image brightness due to ambient light, E^s, is taken as 0. Detections are performed using both the FS and LR images (second row of Fig. 5.2). With the default setting of the forward simulator ($M=4$), the FS image has dimension of 380×1 (left). The LR image (right) with dimension 95×1 is generated by selecting the first sample in every 4 consecutive samples of the FS image, where the 'aliased' effect is clearly identified. To correspond to the selection process for the LR image, we modify the measurement operator H in eq. (2.9c) to:

$$H = [0^{N\times(n_x-N)}, D^N], \tag{5.2a}$$

---

[13] The image brightness due to ambient light is not considered in [55]. $\mu_{E^s}=0$ and $\sigma_{E^s}=0$ are thus set in the initial ensemble generation for IEnSRF.

where $0^{N\times(n_x-N)}$ is (again) an $N\times(n_x-N)$ zero matrix and $\mathcal{D}^N$ is a diagonal matrix:

$$\mathcal{D}^N = \mathrm{diag}(1, 0, 0, 0, \ldots, 1, 0, 0, 0) \tag{5.2b}$$

with entry 1 placed at the first entry of every 4 consecutive entries.

The results of estimating the barcode using IEnSRF with the FS and LR images are summarised in Figs 5.3 and 5.4, respectively, while the results of estimating the Gaussian kernel parameters are summarised in Fig. 5.5 and Table 5.3.

Because of the deliberately-built poor initial kernel information and lack of prior barcode digits information, the initial realisations in the top left plane of Fig. 5.3 are quite different from the true barcode and the initial signal matching is quite poor with simulations providing unrealistic negative reflected energy (due to realisations with negative Gaussian kernel amplitude, α). At the end of the first iteration using IEnSRF, the mean of the analysed (barcode stripe parameterisation of the) realisations are corrected toward one side of the 0 to provide the estimated barcode, while the analysed uncertainty is greatly reduced compared to the initial prior. This agree with the design of the analysis step of the IEnSRF. The estimated barcode is converged towards the truth, however realisations around the 15th and between the 65th and 75th barcode stripes are still quite close to 0 compared to the realisations at the other locations. The uncertainty at these places is preserved and needs to be processed further. The signal matching has been improved with removed unrealistic negative Gaussian kernel amplitude and reduced uncertainty. During the second iteration, the estimation improvement mainly takes place around the 15th and in between the 60th and 70th barcode stripes where the estimation is not perfect from the previous iteration. The uncertainties of all the barcode stripes are further reduced compared to the previous iteration, because of the convergence property of the IEnSRF. At the end of this iteration, with the true barcode being recovered, the IEnSRF is terminated. Theoretically, the conventional IEnSRF should take 2500 iterations with the

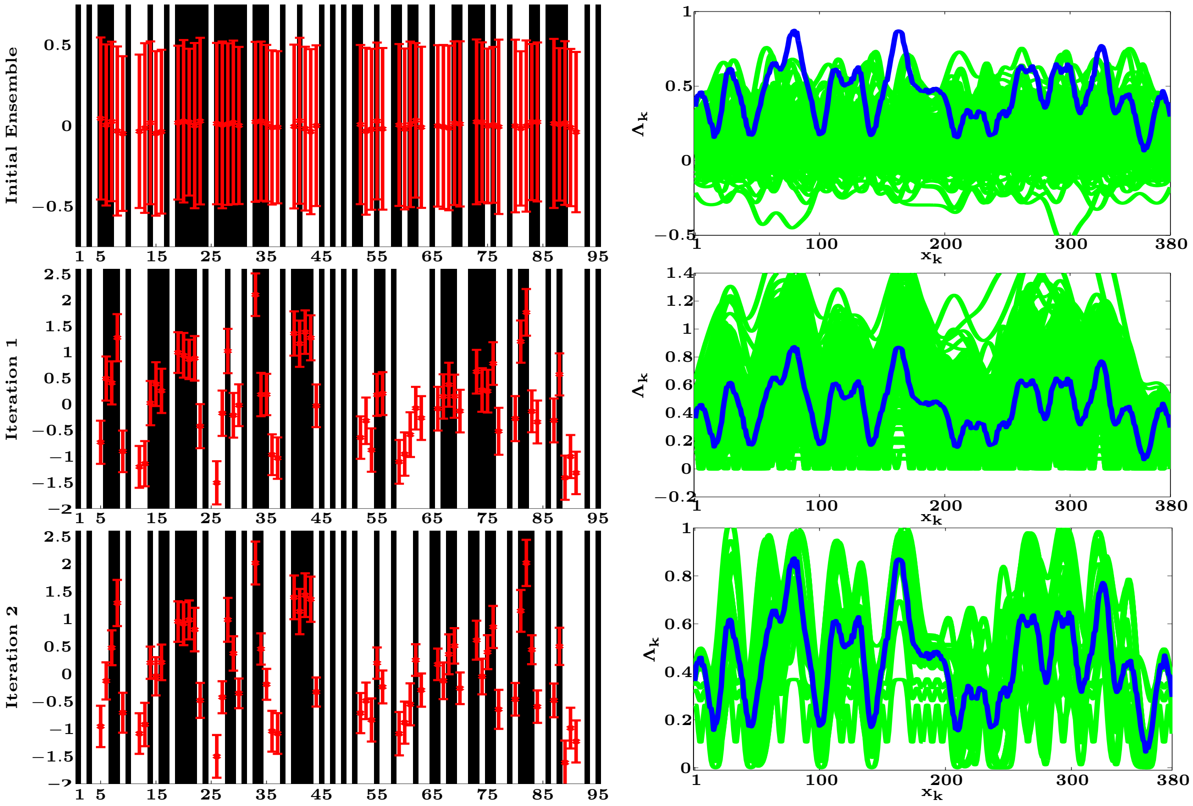

Figure 5.3: The barcode (left column) as estimated from the mean of the barcode stripe parameterisation (red crosses) and signal matching (right column) using the barcode signal of the full-size barcode image in synthetic experiment 5.4.1. Results are shown at the initial prior (top) and the end of the 1st (middle row) and 2nd iteration (bottom row). The barcode estimation plots show the mean (red crosses) and standard deviation (red horizontal bars) of the barcode stripe parameterisation. The measurement matching plots shows the measured signal (blue) and the simulations using the analysed ensemble (green).

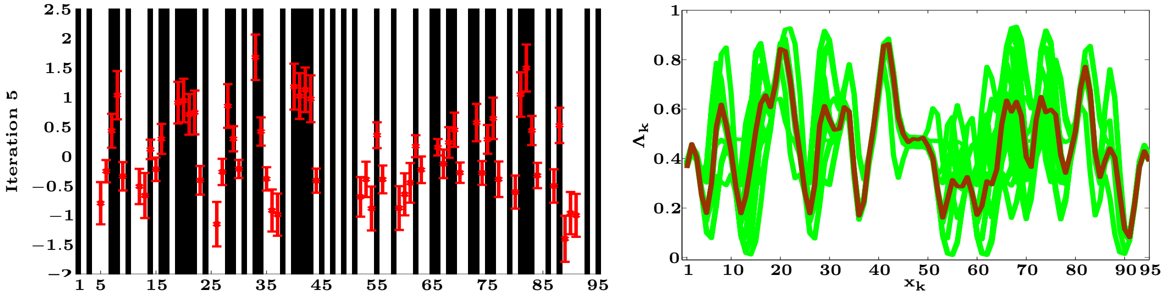

Figure 5.4: The barcode (left) as estimated from the mean of the barcode stripe parameterisation (red crosses) and signal matching (right) using the barcode signal of the low-resolution barcode image in synthetic experiment 5.4.1. The barcode estimation plots show the mean (red crosses) and standard deviation (red horizontal bars) of the barcode stripe parameterisation. The signal matching plots shows the measured signal (brown) and the simulations using the analysed ensemble (green).

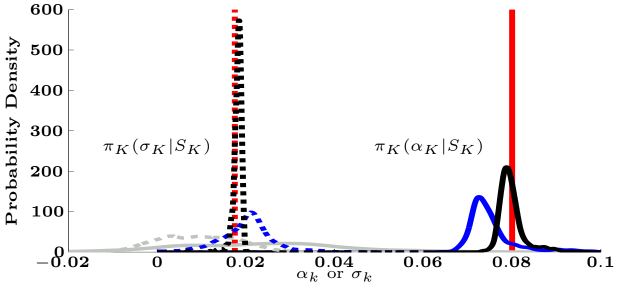

Figure 5.5: The marginal pdfs of the Gaussian kernel amplitude $\pi_K(\alpha_K|S_K)$ (solid lines) and standard deviation $\pi_K(\sigma_K|S_K)$ (dashed lines) in the initial prior (gray) and at the end of the 1st (blue) and 2nd iterations (black) using the full-size barcode image in the synthetic experiment 5.4.1. The true states (red lines).

Exp. 5.4.1		α	σ
Exact		0.08	0.175
FS	Mean	0.08	0.181
	SD	0.003	0.001
LR	Mean	0.079	0.177
	SD	0.004	0.001

Table 5.3: Estimation provided by the analysed ensembles of Gaussian kernel amplitude α and standard deviation σ using IEnSRF with 500 realisations.

Exp. 5.4.1		FS	LS
Computational Time (Sec)	Mean	2.93	1.91
	SD	0.98	0.88
	Esedoglu	12.0	5.6
Iterations	Mean	4	6
	SD	1	2

Table 5.4: Measures of the computational time and number of iterations as they result from 100 trials of IEnSRF using 500 realisations or from the method proposed by Esedoglu in [55].

inflated measurement uncertainty ($\sigma_I = 0.05$) to provide the posterior estimate as it should be resulted using the exact measurement uncertainty ($\sigma_s = 0.001$). The estimated uncertainty (also in all our numerical experiments where the same initial prior and inflated measurement uncertainty are applied) is thus overestimated (as the terminating iteration is much less than the designed 2500 iterations).

As shown in Fig. 5.5, both the marginal posterior pdfs of the Gaussian kernel amplitude $\pi_K(\alpha_K|S_k)$ and SD $\pi_K(\sigma_K|S_k)$ converge to their true states quite rapidly even starting with very poor initial priors. More specifically, as summarised in Tables 5.3 and 5.4, the IEnSRF provides excellent estimation of the true states within only a few iterations. These results verify that for the purpose of barcode and shooting-related parameters estimation or barcode detection, running the IEnSRF to the designed number of iterations is not compulsory and might be surprising to those readers, who believed the conclusions and experiment experience reported in [55, 174].

Similar conclusions can be made from the results for the LR barcode image case as can be seen from Table 5.3 and Fig. 5.4 which is plotted in the same spirit as Fig. 5.3. At the end of the terminating iteration, starting with the same initial ensemble as in the FS image case, the barcode stripe parameterisation estimation using the LR image. Table 5.3 further demonstrates that the Gaussian kernel parameter estimations are also excellent.

In Fig. 5.4, the estimation uncertainties for the LR image case is smaller compared to the results in Fig. 5.3 for the FS image case. Even starting with the same initial ensemble as in the FS image case, more iterations must be performed to achieve successful detection using the less-informative LR image (5 iterations in this case rather than 2 for the FS image case, average number of iterations is presented in Table 5.4) . The uncertainties of the barcode stripe parameterisation estimation are thus further reduced during the additional iterations due to the convergence property of the IEnSRF. On the other hand, in Table 5.4, it might be surprising to some readers that although taking more iterations to process the LR image, its computational time is less than the FS image case. This is because the dimension of the measurement vector and matrix operation in the analysis step of the IEnSRF for the LR image case is significantly reduced compared to the FS image case (see eqs. (2.9c), (5.2a,b)).

5.4.2 Poorly Printed Barcode Image Detection

This experiment took place at 11am on 24 October 2011. We print the (artificially generated) FS barcode image (left panel in the second row of Fig. 5.2) in synthetic experiment 5.4.1 on A4 paper. As shown in the top left panel of Fig. 5.1, the image of this barcode print (black rectangle) is taken under natural daylight through the window (red rectangle). Although, the image (bottom left panel of Fig. 5.1) was taken using the correct focus, the barcode print itself is poorly convoluted and thus considered as an example of a poorly printed barcode.

We select an area from the original image (red rectangle in Fig. 5.1) to generate

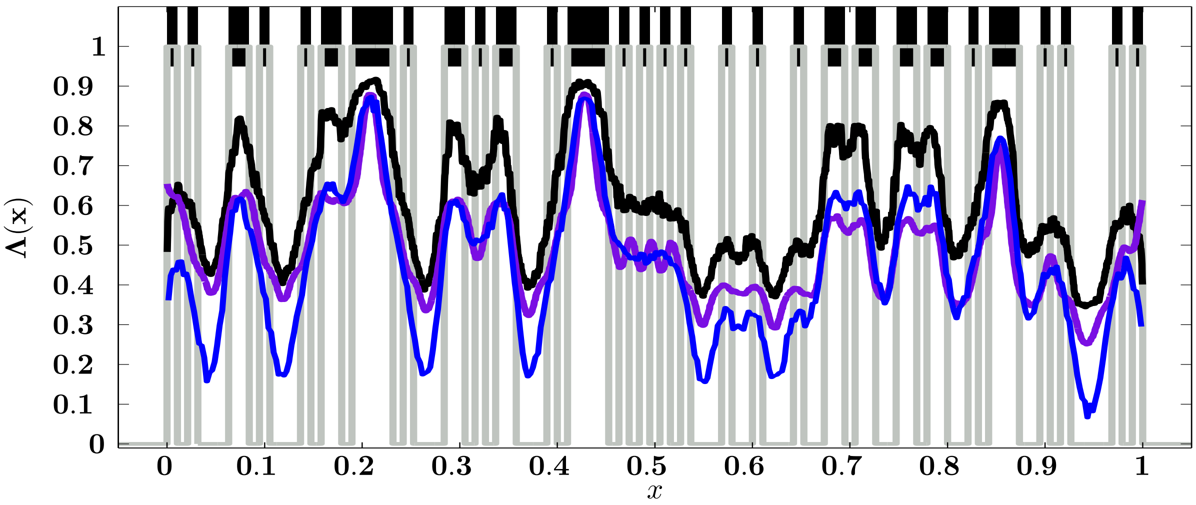

Figure 5.6: The idealised signal (gray) generated by the idealised barcode (stripes on the top), signals generated using the FS barcode images (in Fig. 5.2) for synthetic experiment 5.4.1 (blue) and real experiments 5.4.2 (black) and 5.4.3 (purple).

the FS barcode image (left panel in the third row of Fig. 5.2). The dimension of the FS image is 3082×51, of which the first pixel in every 8 consecutive pixels across the barcode direction is sampled to generate the LR image (right panel in the third row of Fig. 5.2) which is of dimension 385×51 and more noisy

By averaging the image vertically, the barcode signal using the FS image is generated and summarised in Fig. 5.6. Compared to the (exact) signal generated using the FS image in the synthetic experiment, the signal generated using the FS image in this experiment is not only shifted positively (due to the ambient light) with an attenuated signal around 0.2, 0.45 and 0.85, but also polluted by noise.

Fig. 5.7 presents the estimated barcode using the IEnSRF on the FS and LR images. Starting with the same initial ensemble, at the terminating iteration, the barcode stripe parameterisation estimation using both the FS and LR images are quite similar, from which the true barcode was able to be recovered successfully. Excellent results are also verified in the signal matching plots for both cases. As presented in Fig. 5.7 and Table 5.6, based on the 100 trials, it takes more iterations and longer computational times to achieve detections using the LR image compared to using the FS image due to the degraded measurement signal in the LR image.

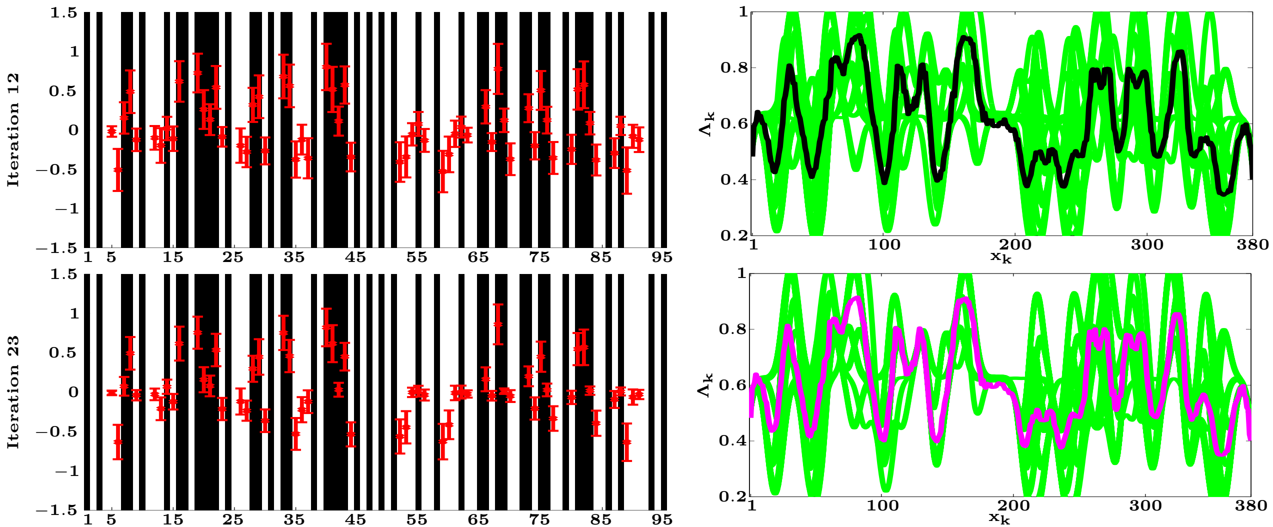

Figure 5.7: The barcode (left column) as estimated from the mean of the barcode stripe parameterisation (red crosses) and signal matching (right column) using IEnSRF on the barcode signal of the full-size (top row) and low-resolution (bottom row) barcode image in real experiment 5.4.2. The barcode estimation plots show the mean (red crosses) and standard deviation (red horizontal bars) of the barcode stripe parameterisation. The signal matching plots show the resampled measured signal (black and magenta) and the simulations using the analysed ensemble (green).

Exp. 5.4.2		α	σ	E_s
Exact		0.08	0.175	N/A
FS	Mean	0.080	0.181	0.14
	SD	0.001	0.002	0.008
LR	Mean	0.079	0.173	0.16
	SD	0.002	0.003	0.013

Table 5.5: Estimation provided by the analysed ensembles of Gaussian kernel amplitude α and standard deviation σ using IEnSRF with 500 realisations.

Exp. 5.4.2		FS	LS
Computational Time (Sec)	Mean	6.72	10.6
	SD	4.05	5.44
	Esedoglu	110	14.6
Iterations	Mean	9	15
	SD	5	8

Table 5.6: Measures of the computational time and number of iterations as they result from 100 trials of IEnSRF using 500 realisations or from the method proposed by Esedoglu in [55].

It can be seen in Table 5.5, the IEnSRF provides excellent estimation of the model parameters. For the image brightness due to ambient light, the estimation using both FS and LR images are found to be consistent. The uncertainties in the estimates are bigger using the LR image than using the FS image due to the larger signal simulation uncertainty requirement for matching the less-informative LR barcode signals.

5.4.3 Out-of-focus Barcode Image Detection

The FS and LR barcode images under investigation are shown in the left and right panels in the bottom row of Fig. 5.2, respectively. As demonstrated in the top right panel of Fig. 5.1, the image of the barcode print (in the bottom right panel of Fig. 5.1) was taken at 22:12 under lamp light (indicated by red rectangles) on 24 October 2011. The true barcode in the top panel of Fig. 5.1 is printed on A4 paper, the image of which is taken with a incorrect focus (for a clear image).

The FS barcode image (indicate by blue rectangle) select from the original image in the bottom right panel of Fig. 5.1, has dimensions 2988 × 101, while the LR image is generated by sampling the first pixel in every 7 consecutive pixels across the barcode direction in the FS barcode image and is thus of dimension 427 × 101.

In the original barcode image, the color of the red frame on the left side is darker than on the right side, which indicates a possible ambient light variation across the barcode. As shown in the top right panel of Fig. 5.1, this is likely caused by the print being placed closer to the overhead lamp on the right. Furthermore, in Fig. 5.6, the barcode signal has unrealistic peaks at the beginning (0-0.02) and the end (0.98-1), which are caused by the convolution of the barcode and the frames. These highlight the real-world imperfectness[14] and provide a challenging test environment for examining the robustness and real-world applicability of our proposed method. Due to strong convolution effect, as can be seen from Fig. 5.8, the (high-frequency) measurement noise is almost negligible in this experiment.

The results of the barcode estimation and signal matching are presented in Fig. 5.8 which is plotted in the same spirit as Fig. 5.7. The barcode and barcode stripe parameterisation estimates are similar in both FS and LR image cases and both successfully recovered the true barcode. In the signal matching plots, in both cases, the measured barcode signals fall within the uncertainty of the simulations using the

---

[14] Assumptions 2 and 3 in the mathematical modelling (§2.3) have been violated.

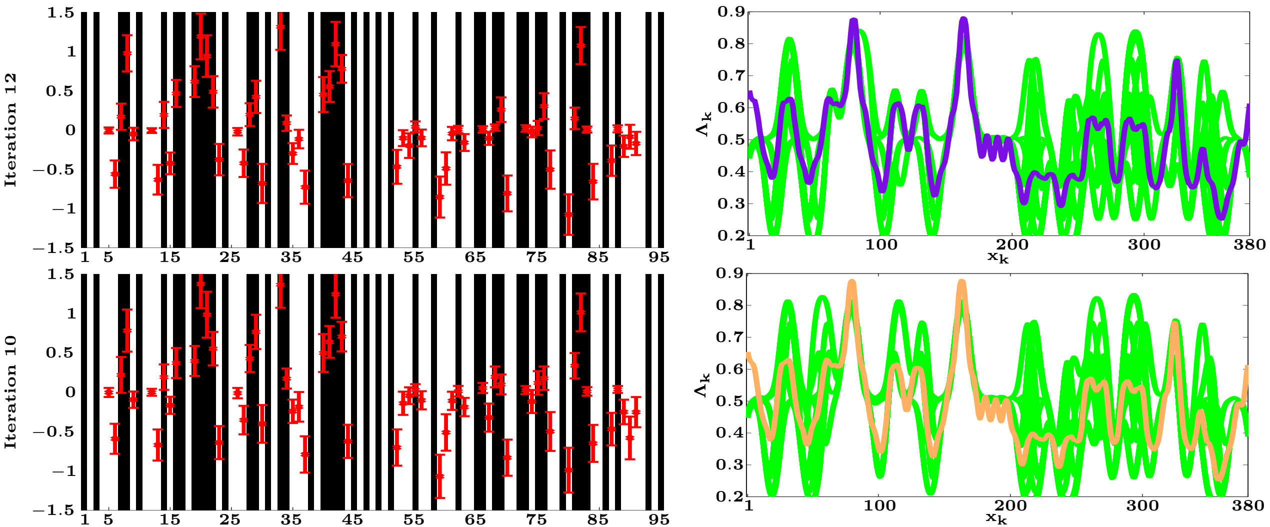

Figure 5.8: The barcode (left column) as estimated from the mean of the barcode stripe parameterisation (red crosses) and signal matching (right column) using IEnSRF on the barcode signal of the full-size (top row) and low-resolution (bottom row) barcode image in real experiment 5.4.3. The barcode estimation plots show the mean (red crosses) and standard deviation (red horizontal bars) of the barcode stripe parameterisation. The signal matching plots show the resampled measured signal (purple and gold) and the simulations using the analysed ensemble (green).

Exp. 5.4.3		α	σ	E_s
Exact		0.08	0.175	N/A
FS	Mean	0.066	0.153	0.17
	SD	0.0005	0.001	0.003
LR	Mean	0.063	0.154	0.18
	SD	0.0006	0.001	0.004

Table 5.7: Estimation provided by the analysed ensembles of Gaussian kernel amplitude α and standard deviation σ using IEnSRF with 500 realisations.

Exp. 5.4.3		FS	LS
Computational Time (Sec)	Mean	8.16	9.52
	SD	4.06	7.10
	Esedoglu	86.8	14.3
Iterations	Mean	11	13
	SD	6	9

Table 5.8: Measures of the computational time and number of iterations as they result from 100 trials of IEnSRF using 500 realisations or from the method proposed by Esedoglu in [55].

analysed ensemble everywhere except at the places where the convolution over the guard bars is carried out due to the inadequate frame placement. However, because the reliable guard bars information has been used in constructing the initial prior, the IEnSRF reliably provides good matching for the part of the signal with adequate information, but not for the inadequate part at both ends. Indeed, from Table 5.8, based on the result of 100 detection trials, the computational iterations and time on average for both the FS and LR image cases are quite similar. For the estimations of Gaussian kernel parameters and the image brightness due to ambient light, the results are found to be consistent in both the FS and LR image cases in Table 5.7.

5.4.4 Comparison Against an Existing Method and Commercial Software

As a comparison of performance and computational time, our numerical experiments are repeated using Esedoglu's method in [54, 55][15].

Following [55], the results are presented in Fig. 5.9. In the top panel, using the FS barcode signal in synthetic experiment 5.4.1, the method provides a reasonable overall estimate, but fails to estimate the guard bars at the beginning and provides a nonexistent barcode stripe estimate at around $x = 0.67$ and 0.79. In fact, the incapability of estimating the guard bars is observed in all the experiments and is partially because of lack of explicit prior knowledge regarding the guard bars[16].

Besides the described problems[17], Esedoglu's method failed to provide any solution when using the LR barcode signal in our synthetic experiment 5.4.1 (The results are not explicitly plotted). Indeed, as commented in [116, 165], Esedoglu's method cannot work well for heavily distorted signals.

Even worse estimates are found for signals in our real experiments 5.4.2 and 5.4.3. Generally, the estimation is worse when the LR signal is processed. The poor performance of Esedoglu's method in real applications might partially be caused by the fact that the image brightness due to ambient light is not considered.

For the computational time comparison, the computational time of one trial is recorded[18] and summarised in tables 5.4, 5.6 and 5.8 for each experiment, respectively.

---

[15] Total number of time steps is 30000 (to guarantee convergence). The recommended time step of 0.0004 for the gradient flow of the variational model is used

[16] In the experiments of [55], estimation of the guard bars was never considered.

[17] While one may argue that the nonexistent barcode stripe estimation at around $x = 0.67$ can be filtered by applying a threshold filter, the nonexistent barcode stripes estimation at around $x = 0.79$ is impossible to attenuate using simple filters.

[18] This is because the computational time of Esedoglu's method only depends on the dimension of

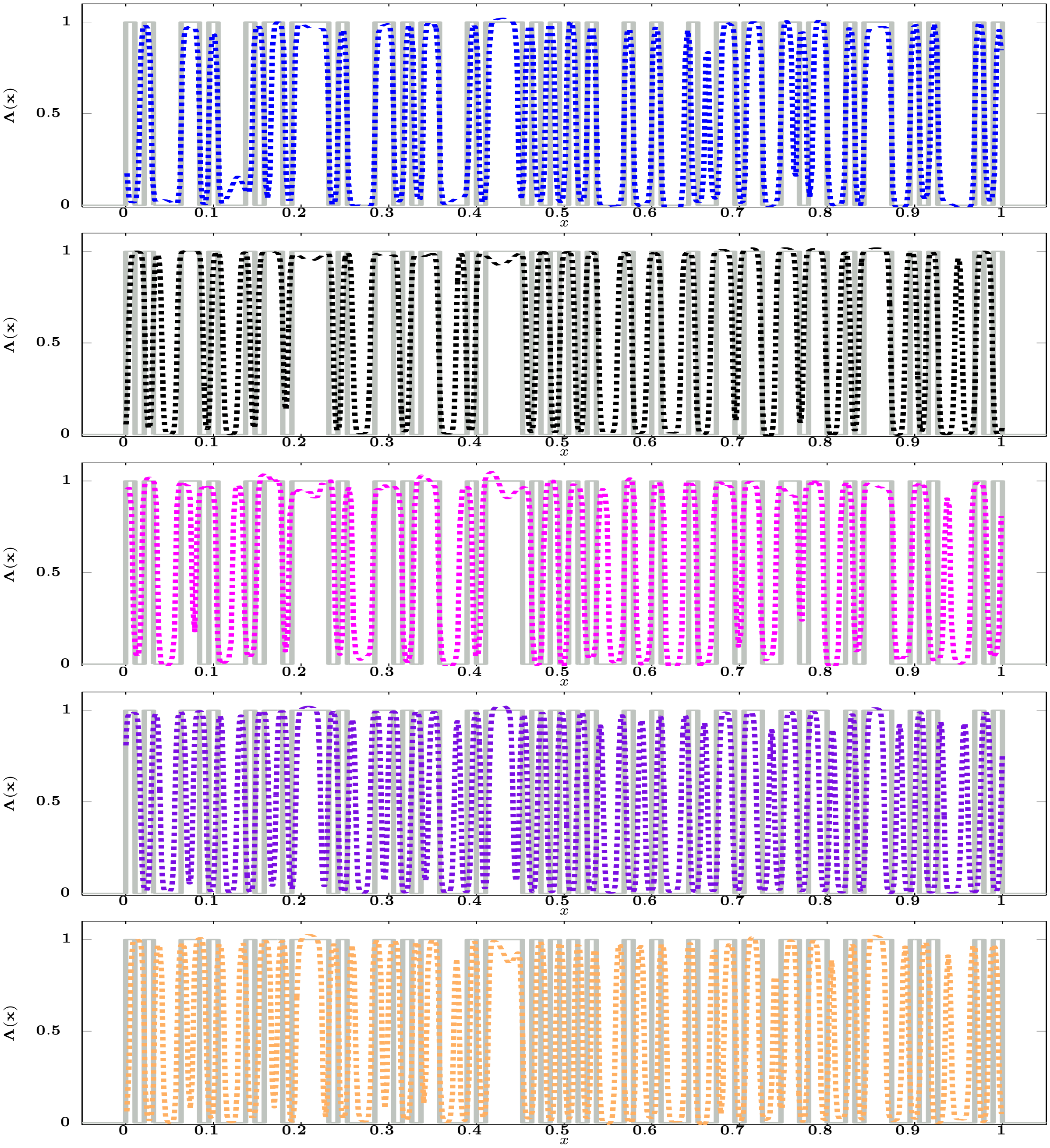

Figure 5.9: True barcode signal (solid gray) and signals as estimated using the method proposed by Esedoglu in [54, 55] (dashed lines) for the synthetic experiment 5.4.1 with the full-size barcode signal (blue, first row), real experiment 5.4.2 with the full-size (black, second row) and low-resolution (magenta, third row) barcode signals, and real experiment 5.4.3 with the full-size (purple, fourth row) and low-resolution (gold, bottom row) barcode signals.

Read any barcode from an image online with GMSE Imaging.

Try our samples for GMSE Imaging online:

Upload your own image and let GMSE Imaging detect the barcodes:

No file chosen

GMSE Imaging has detected the following barcodes:

1	EAN 13	0093053772246

No barcodes detected on this image.

No barcodes detected on this image.

No barcodes detected on this image.

Figure 5.10: Detection results using the commercial software, GMSE imaging [72], for the idealised (left) and full-size barcode images in synthetic experiment 5.4.1 (first right) and real experiments 5.4.2 (middle right) and 5.4.3 (bottom right).

Our proposed method using IEnSRF is superior to Esedoglu's method. Furthermore, the actual digits are provided by our proposed method (rather than an estimated barcode signal as in Esedoglu's method).

A comparison is also conducted using commercial software called GMSE imaging [72]. The results are shown in Fig. 5.10. The GMSE imaging detects the idealised barcode successfully, but fails to detect any of the original (not explicitly presented), FS and LR (not explicitly presented) images in all experiments.

5.5 Summary

The aim of this chapter is to develop an efficient and robust Bayesian method for the real-world problem of blurry barcode image detection which is ubiquitous and yet still lacks reliable approaches. Because the barcode stripes are discrete variables, and hence non-differentiable and non-Gaussian, seeking estimates directly using (say) the EnSRF is not appropriate. Using a level set parameterisation, these variables were transferred into a continuous variables which can be estimated using the IEnSRF.

Numerical experiments have been conducted in both synthetic and real-world situations using poorly-printed and out-of-focus barcode images in FS or LR forms.

---

the barcode signal if the same prior and stopping criteria is used.

Starting from vague priors without prior digit information, the IEnSRF estimates the logic of each barcode stripe by adjusting its parameterisation along the real number set and substantially reduces its uncertainty at each iteration. With a greatly reduced number of iterations using the modified stopping criterion (compared to the conventional setting), the IEnSRF provides excellent estimates and accurate detections for both the FS and LR images in all experiments with average computational times between 1.9 to 10.6 secs, while the posterior uncertainty is overestimated[19]. Great efficiency and robustness is demonstrated.

As a comparison of performance, we also repeated the same numerical experiments using Esedoglu's method [55] and the commercial software, GMSE imaging [72]. In all experiments, both methods failed to provide satisfactory results. In particular, the computational time of Esedoglu's method depends on the signal dimension, while the computational time of our proposed method depends on the quality of the information embedded in the image, in accord with the Bayesian framework.

As demonstrated in synthetic experiment 5.4.1, the theoretical minimum resolution of the input barcode image for using our proposed method is 95×1. However, when detecting the real barcode images (such as in experiments 5.4.2 and 5.4.3), the minimum resolution of image to guarantee successful detection and stability when using our proposed method is recommended to be 380×1 (i.e. the default setting in the forward simulator and our proposed method).

---

[19] It has been proved that in the absence of any measurement noise, the convolved signals contain enough information to determine the barcode uniquely [55]. With the presence of some insignificant measurement noises (as in our experiments), the IEnSRF, which is designed to converge to a single Gaussian posterior estimate, is thus capable to achieve successful detection in just a few iterations.

Chapter 6

An Iterative Deconvolution Method for Well-Test Data

6.1 Introduction

There are more than 40,000 oil and gas reservoirs of all sizes in the world. A single reservoir typically contains oil from a few hundred to over one hundred billion barrels (e.g. the Ghawar field in Saudi Arabia) and gas from a few hundred to over 1 trillion cubic feet (e.g. the South Pars/North Dome field in Iran and Qatar), ranging from a few inches to more than 1,500 feet (e.g. the Burgan field in Kuwait) in deposit thickness, from the surface of the earth to over 30,000 feet (e.g. the Blackbeard site in the Gulf of Mexico) in depth, from a few square miles to more than 3,000 square miles (e.g. the Ghawar field in Saudi Arabia) [Schlumberger World Energy Atlas].

Well testing is a useful tool for obtaining reservoir/well configuration and reservoir geometry and productivity in the early stage and optimising production during all stages in the reservoir life. A test well is normally drilled soon after the discovery of the reservoir. In the well testing literature, the reservoir/well system is characterised by the response function: the Pressure Type Curve (PTC), which is the wellbore pressure behaviour in response to flowing the hydrocarbon at a unit flow rate (FR), and the Log-Log Derivative Type Curve (LLDTC), the derivative of the PTC on a log-log scale. These curves depend on reservoir and well properties such as permeability, large-scale reservoir heterogeneity, well damage (skin factor[1]) and the reservoir flow geometry defined by the geometry of the well completions and by reservoir boundaries [75, 103]. Hence, some of these reservoir and well characteristics may potentially be recovered from the type curves through type curve analysis.

Measuring the PTC directly is not an option, not only because of great difficulties in controlling the FRs accurately using the conventional equipment, but also because the wellbore pressure is sensitive to FR variations. For this reason, typical well tests are operated in several flow periods (FPs) with variable FRs, where the FRs are typically measured by single-phase flow meters installed on each of the fluid (gas, oil and water) outlets of standard separators and tanks. The pressure measurements acquired during the production period do not normally yield good quality data, because of poor meter calibration, well control and monitoring. Hence, the well normally has one or more shut-in periods, during which the data acquired are used for pressure-transient analysis. Conventional methods analyse the pressure behaviour during an individual FP and are thus unable to access the full potential information content. Deconvolution, a more recent well-test-analysis method, is proposed to extract the type curves which the reservoir would exhibit when subjected over any period of time up to the entire well test duration [163]. The deconvolution problem is a well known and long-standing inverse problem which was first formulated within the field in 1959 [84] and has received sporadic, but recurring attention [75, 105, 131].

The deconvolution problem is ill-posed, meaning that small changes in the measured pressure and FR data lead to large changes in the deconvolved type curves. The ill-posed nature of the deconvolution problem, combined with noise always present in the

---

[1] A measure of the obstruction of the flow due to the well construction effects.

pressure and/or FR data, makes the problem very challenging. A variety of different deconvolution algorithms have been proposed in the literature [62, 134, 155, 164]. However, none of them is robust enough to provide satisfactory estimates to meet industrial needs. It is common for large oil companies to purchase all the commercial well-test-analysis software application in order to meet their needs by comparing and analysing the estimates from each software application.

An efficient and widely-used deconvolution method was first introduced by von Schroeter *et al.* in 2001 [163]. The deconvolution problem is reformulated as a separable nonlinear total least-squares problem with piecewise linear parameterisation of the LLDTCs, which accounts for uncertainties in both FR and pressure data. A curvature regularisation term is also introduced to incorporate a priori knowledge of the smooth LLDTC trend. The variations of this method [34, 52, 103] have been implemented in several well-known commercial software, such as Saphir, TLSD, Interpret$^{\mathrm{TM}}$ and Fekete, and tested on many synthetic and real-world problems, because of its stable performance and ease of implementation.

However, the piecewise-linear approximation is not accurate for the highly-nonlinear LLTDCs except with large numbers of pieces [76]. A more realistic and robust parameterisation with lower requirements on the number of discrete pieces is proposed by Ilk *et al.* [85] in 2005 using nonparametric B-spline functions.

By parameterising the impulse response function (the derivative of the PTC, see eq. (2.26) on page 18) using a nonparametric B-spline, a linear least-squares problem[2] with respect to the B-spline control point weights can be formulated, in which the sensitivities of the observed pressure response are calculated by numerical inversion of the Laplace transform after the Laplace domain convolution. The robustness of this method is claimed due to the use of the high reliability of the numerical Laplace transform inversion [2, 161] and demonstrated on various synthetic and real examples.

---

[2] A first order non-smoothness penalising term similar to [163] is included.

However, to our best knowledge, this method is computationally demanding and has not been investigated further or implemented in any commercial software.

Deconvolution is a technical “masterpiece” when it comes to the assessment and exploitation of complex reservoir architectures and productivity. Yet, the existing methods fail to deliver satisfactory solutions and reliable performance and have been observed to have three major drawbacks when applied to real problems: (i) The estimation result is sensitive to regularisation terms [75, 103, 164][3]. For example, in Fig. 6.1, two different LLDTC estimates[4] found using existing methods with different regularisation parameters provide the same pressure simulations[5][6]. (ii) A single deterministic estimate is insufficient for risk and uncertainty analysis in reservoir characterisation and proactive field management. To the best of our knowledge, this problem has been only considered in [164], where the data uncertainty and confidence interval of the estimation were quantified statistically using cross validation techniques based on linearisation assumptions. The specified statistics are thus sensitive to the regularisation term. (iii) Incapability of providing accurate estimation for initial pressure. In [104, 164], the authors concluded that inclusion of the initial pressure in the list of deconvolution parameters often causes the existing algorithms to fail.

A Bayesian method, which overcomes these challenges, is indeed the goal of this chapter. Our proposed method, the Interactive Deconvolution Method (IDM), is based on one-dimensional unclamped cubic parametric B-spline parameterisation of the LLDTC and utilises the Iterative Ensemble Square Root Filter (IEnSRF) to provide estimates for the type curves, FRs, initial pressure, cumulative production and corresponding posterior densities. This chapter is organised as follows: §6.2 recalls the state-space formulation for conventional measurements and derives the modified state-

---

[3] The optimal level of regularisation is suggested to be found using trail-and-error tests [164].

[4] The blue LLDTC indicates a single vertical well with constant skin factor in a closed homogeneous reservoir while the late-time behaviour of the dashed-red LLDTC is uninterpretable.

[5] Another example using real gas data is presented in Fig. E.1 in Appendix E.

[6] As a convention and for the easiness of analysis, both the PTC and its natural derivative, LLDTC, are always presented on the same type curve figure [19].

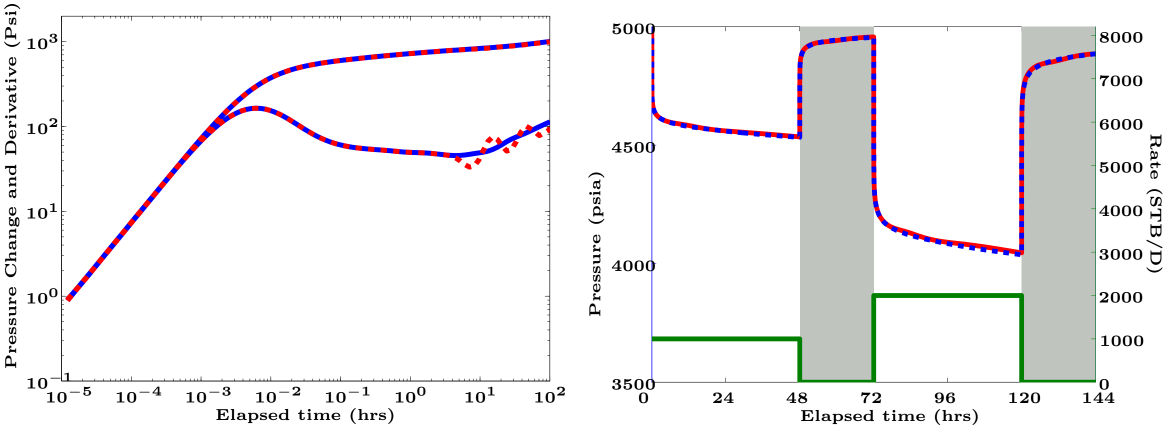

Figure 6.1: The pressure simulations (right panel) using two estimated LLDTCs (left panel) found by existing methods with different regularisation paramater (value). The pressure simulation plot presents the flow rate (green), the pressure simulations (blue and dashed red) using the blue and dashed red LLDTCs in the LLDTC plot.

space formulation when the cumulative production measurement is incorporated. The assumptions and initial ensemble generation for the use of the IEnSRF are summarised in §6.3. §6.4 presents and discusses the results of one synthetic and two real numerical experiments. Finally, we conclude the work in §6.5.

6.2 The State-Space System and Practical Implementation

As defined in Chapter 1, the deconvolution problem in well testing is to estimate the LLDTC using the pressure and FR data. Deconvolution is the reverse of the (nonlinear) convolution process (2.33) of the LLDTC and FRs, which is modified from the well-known Duhamel's principle (2.26), and is a long standing inverse problem to be solved using priors based on realistic and practical assumptions.

In §4.3, to capture the high-nonlinearity and smoothness of the analytical LLDTCs, against which the engineers match the estimates in the well test analysis, we construct our prior by parameterising the LLDTC using parametric B-splines (eq. (4.3a)). It is demonstrated through comprehensive numerical experiments that the proposed parameterisation is capable of representing the LLDTC using a few knots and is computationally superior to the existing parameterisation methods.

We recall the state-space system for solving the considered problem with the proposed parametric B-spline parameterisation is summarised in eqs. (4.4a,b) in §4.3.3. It is modified from the state-space system (2.35a,b) on page 22.

The State-Space System with the Cumulative Production Measurement

Following [52], the incorporation of an extra measurement, namely the cumulative production data, can help to obtain an improved LLDTC estimate and a more realistic FR estimate[7]. It is found that the calculation using the estimated FRs in the existing methods often leads to a great inconsistency in the cumulative measurement of hydrocarbon in the storage tank, yet the cumulative production is normally measured most accurately (compared to the wellbore pressure and FR measurements).

With a modification of the state-space system (4.4a,b), the state-space system with an additional cumulative production measurement can be summarised as follows:

$$\begin{aligned} x_1 = f(x_0) = [\mathbf{a}_0, \mathbf{b}_0, p_0^0, \mathbf{Q}_0, \gamma_1(p_0^0, \mathbf{m}_0^z(\mathbf{a}_0, \mathbf{b}_0), \mathbf{Q}_0), \ldots, \\ \gamma_N(p_0^0, \mathbf{m}_0^z(\mathbf{a}_0, \mathbf{b}_0), \mathbf{Q}_0), \sum_{j=1}^{J} Q^j(F_e^j - F_e^{j-1})]^T, \qquad (6.1\text{a}) \\ s_1 = Hx + v. \qquad (6.1\text{b}) \end{aligned}$$

Here, the superscript T denotes the matrix transpose, $x_0 = [\mathbf{a}_0, \mathbf{b}_0, p_0^0, \mathbf{Q}_0, \mathbf{p}, D]^T \in \mathcal{R}^{n_x \times 1}$, where $D \in \mathcal{R}^+$ is the cumulative production measurement. $H = [0^{(N+J+2)\times(n_x-N-J-2)}, I^{N+J+2}]$ is the measurement operator, where $0^{(N+J+2)\times(n_x-N-J-2)}$ is an $(N+J+2) \times (n_x - N - J - 2)$ zero matrix, I^{N+J+2} is an $(N+J+2) \times (N+J+2)$ identity matrix and used to take the initial pressure, FR, pressure and cumulative production mea-

---

[7] The inspiration and request for incorporating such measurements came from the industry companies: Ente Nazionale Idrocarburi and Paradigm.

surements, v is the measurement noise and is assumed to be independent and drawn from a Gaussian distribution: $v \sim \mathcal{N}(0, R)$, where the covariance matrix

$$R = \begin{pmatrix} \sigma_{p^0}^2 & 0 & 0 & 0 \\ 0 & \sigma_Q^2 \mathcal{D}^J & 0 & 0 \\ 0 & 0 & \sigma_P^2 I^N & 0 \\ 0 & 0 & 0 & \sigma_D^2 \end{pmatrix}, \tag{6.1c}$$

σ_{p^0}, σ_Q, σ_P and σ_D are the standard deviations (SDs) of the initial pressure, the FR data, the pressure data and the cumulative production data noise, respectively; and $\mathcal{D}^J$ is the $J \times J$ diagonal matrix defined in eq. (2.36).

6.3 Iterative Deconvolution Method using the Iterative Ensemble Square Root Filter

The core of the proposed IDM is to update the parametric B-spline parameterisation of the LLDTC using the IEnSRF derived in §3.3. To adapt the IEnSRF, the state-space system (6.1a,b) is transformed into the iterative formation as in eqs (3.19a,b) of §3.4.3. A typical realisation of the ensemble is therefore of the form:

$$\begin{aligned} x_{K,i} = [&a_{K,i}^0, ..., a_{K,i}^{n_z-1}, b_{K,i}^0, ..., b_{K,i}^{n_z-1}, p_{K,i}^0, \\ &Q_{K,i}^1, \ldots, Q_{K,i}^J, p_{K,i}^1, \ldots, p_{K,i}^N, D_{K,i}]^T \in \mathcal{R}^{(N+J+2n_z+2)}. \end{aligned} \tag{6.2}$$

In all experiments, as discussed in the conclusion of §4.3.3, the number of control points, n_z, is chosen to be 10. To mitigate the potential problem of ensemble collapse, ensembles with 500 realisations are used in the experiments [59, 135, 136].

The initial prior pdf, $\pi(p_0^0, \mathbf{Q}_0, \mathbf{b}_0)$, for the initial pressure, FRs and LLDTC are constructed as Gaussian distributions with means at $p_s^0 \in \mathcal{R}$, $\mathbf{Q}_s \in \mathcal{R}^J$ and $\mathbf{b}_s \in \mathcal{R}^{n_z}$

and SDs of $\sigma^I_{p^0} \in \mathcal{R}$, $\sigma^I_Q \in \mathcal{R}$ and $\sigma^I_{\mathbf{b}_s} \in \mathcal{R}$, respectively, as follows[8]:

$$\begin{pmatrix} p^0_0 \\ \mathbf{Q}_0 \\ \mathbf{b}_0 \end{pmatrix} \sim \mathcal{N}\left(\begin{pmatrix} p^0_s \\ \mathbf{Q}_s \\ \mathbf{b}_s \end{pmatrix}, \begin{pmatrix} {\sigma^I_{p^0}}^2 & 0 & 0 \\ 0 & {\sigma^I_Q}^2 \mathcal{D}^J & 0 \\ 0 & 0 & {\sigma^I_{\mathbf{b}_s}}^2 I^{n_z} \end{pmatrix}\right). \tag{6.3}$$

For the initial pressure and FRs, we use the measurements as the mean of their initial priors. In experiments where comparison against the existing methods is carried out, the initial pressure is assumed exact (not to be estimated) and SD $\sigma^I_{p^0}$ is set to be 0. For the initial LLDTC prior, it is widely accepted that most useful LLDTC information can be extracted from the pressure derivative data in the longest shut-in flow period (FP) available[9] [20, 75, 163]. The mean of the initial LLDTC prior, $\mathbf{b}_s$, is taken as the optimal B-spline approximation to the pressure derivative on the log-log scale[10] and the SD, $\sigma^I_{\mathbf{b}_s}$, is taken as 3 times the L_2 norm residual of this B-spline approximation. The SD parameter is chosen according to the relationship between SD and confidence intervals of the Gaussian distributions and aims to cover a realistic initial uncertainty. Note that since the B-spline control nodes are located uniformly across the logarithmic well test duration axis, the exact position of the control points, $\mathbf{a}$, is assigned in all realisations of the initial ensemble.

6.4 Numerical Experiments

One synthetic and two real-world numerical experiments are performed to test the proposed IDM and to evaluate its performance. Both real-world examples are artificial industrial dataset generated by the professional engineers. The second real example, in particular, is used as a benchmark dataset due to the poor and inconsistent results

---

[8] D^J is (again) specified as in eq. (2.36).

[9] If there is one. Otherwise, production data also can be used.

[10] i.e. The pressure derivative calculated using the pressure data in the specified shut-in period which is normalised against the FR difference between the current and previous FPs.

given by the commercial software applications using existing methods [6].

In the synthetic experiment, we simulate the 'true' pressure sequence and cumulative production. Synthetic measurements are then extracted from the true states and perturbed with (known) random noise to test the IDM in the Perfect Model Scenario. In the real experiments, the IDM is performed under the Imperfect Model Scenarios with inadequate information regarding the measurement noise. The means and SD of the type curves, FRs, initial pressure and cumulative production in the analysed ensemble are used to quantify their estimates and uncertainty.

6.4.1 Synthetic Experiment

This synthetic example is a modification of the benchmark deconvolution problem for Interpret$^{\text{TM}}$ 2010. The considered reservoir is a homogeneous oil reservoir with constant wellbore storage and impermeable channel boundaries. A vertical well is drilled and located 2000 ft from either side of the reservoir boundaries. The well, reservoir and oil properties are summarised in Table 6.1. In the 6 days well testing duration, two, two-day production and two one-day shut-in periods are performed. The FRs are 1000 stb/D in FP1 and 2000 stb/D in FP3.

Using the true reservoir model and FRs, we simulate the true pressure data and added random noise to produce the pressure measurements in Fig. 6.2. Similarly, the FRs for FP1 and FP3, the initial pressure and cumulative production measurement are 800 stb/D, 2200 stb/D, 4500 psia and 5400 stb[11], respectively. The detailed acquisition parameters are summarised in Table 6.2. Note that the accurate pressure measurements and relatively poor FR, initial pressure and cumulative production measurements are deliberately chosen to highlight the real-world difficulties. For the initial prior of the initial pressure and FR, we use the mean and SD of the measurement as their mean and SD, respectively. To increase the estimation difficulties even

---

[11] Based on the exact cumulative production 6000 stb at the end of this well test.

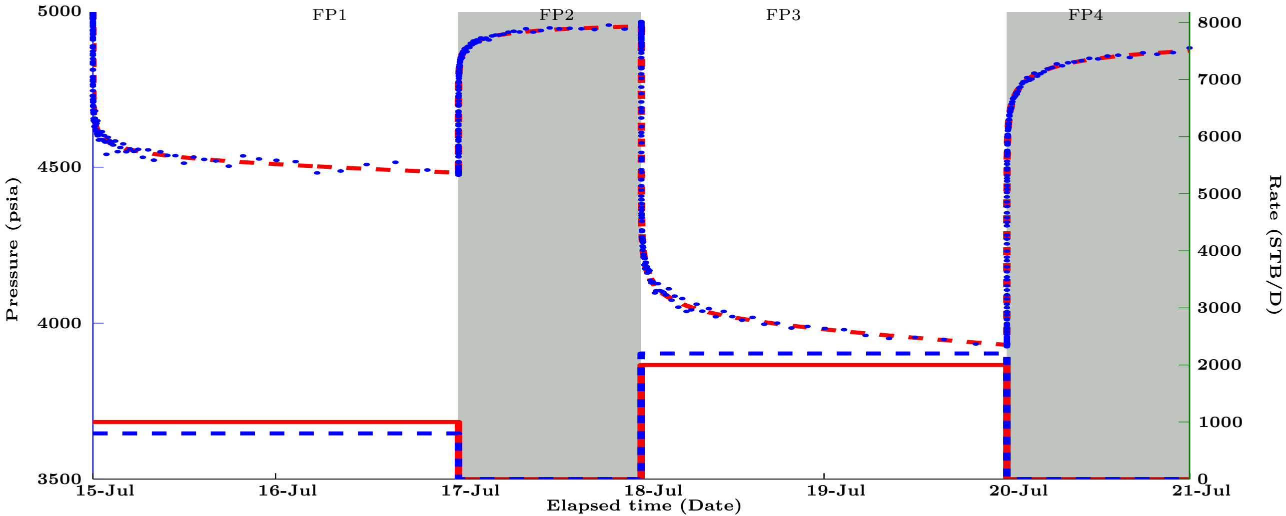

Figure 6.2: Well test data for synthetic experiment 6.4.1. Pressure data (blue), exact pressure simulation (red), measured flow rates (dashed blue), exact flow rates (red) and two well shut-in periods (gray).

Wellbore radius	Formation volume factor	Net reservoir thickness	Matrix porosity	Total compressibility	Viscosity
4.25 ft	1 rb/stb	100 ft	30%	10^{-5}/psi	1.0 cP

Table 6.1: The well, reservoir and oil properties for experiment 6.4.1.

Durations (days)	Initial pressure (psia)	Reservoir temperature (°F)	σ_{P^0} (psia)	σ_P (psia)	σ_Q (stb/D)	σ_D (stb)
6	5000	150	250	3	200	600

Table 6.2: The well testing acquisition parameters for experiment 6.4.1.

more, the realisations of the initial LLDTC ensemble, have been modified to have an unrealistic downward late-time trend.

Two tests are performed to estimate the FRs, LLDTC, initial pressure and cumulative production with consistent initial ensembles using 5 iterations of the IDM on measurements including the pressure data in both shut-in periods and FR data (MECPD[12]) and measurements including the pressure data in both shut-in periods, FR data and cumulative production data (MICPD[13]), respectively.

Fig. 6.3 presents the type curve estimates and the pressure matches[14]. In both

---

[12] Measurements Excluding Cumulative Production Data.

[13] Measurements Including Cumulative Production Data.

[14] As a convention and for the easiness of analysis, both the PTC and its natural derivative, LLDTC, are always presented on the same type curve figure [19].

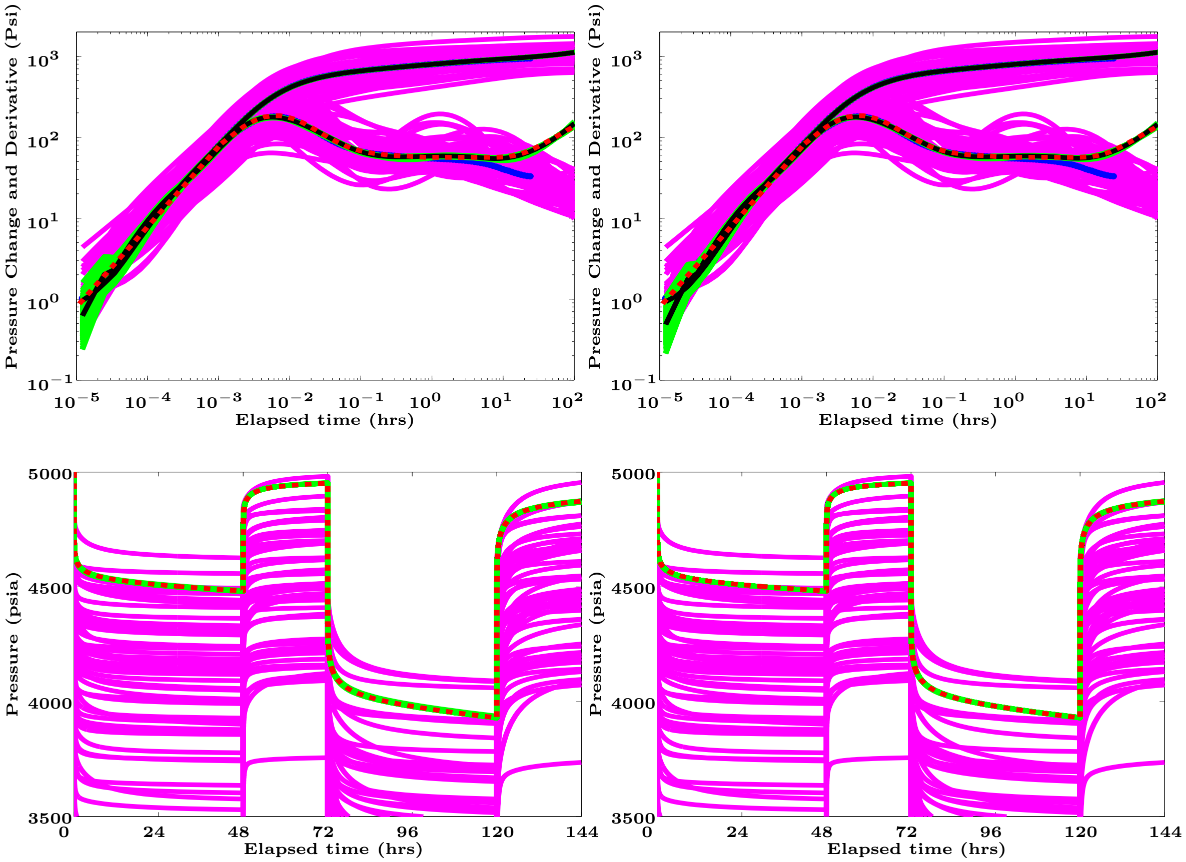

Figure 6.3: The type curve estimates (top row) and pressure matches (bottom row) for synthetic experiment 6.4.1 using IDM on MECPD (left column) and MICPD (right column). The type curve estimation plots show the modified pressure derivative data (blue), the estimated type curve (black), the true LLDTC (red dashed) and the type curves in the initial (magenta) and analysed (green) ensembles. The pressure matching plots show the pressure simulations using the true states (dashed red), and initial (magenta) and analysed (green) ensembles.

tests, because of the lack of complete knowledge and poor initial prior, our initial realisations of the LLDTC are quite unrealistic (i.e. contain humps and downward late-time trends) and are considered to be quite different from the true LLDTC. Consistently, the pressure simulations using the initial LLDTC realisations are biased below the simulation using the true states. After the process of deconvolution, the LLDTC estimates concentrate around the true LLDTC with a very small uncertainty which is significantly reduced compared to the initial ensemble. However, the LLDTC estimate in the domain $[10^{-5}, 10^{-4}]$ is biased slightly negatively compared to the truth with an relatively large uncertainty compared to elsewhere. This is due to the

	p^0 (psia)			D (stb)			Q^1 (stb/D)			Q^3 (stb/D)		
	True	Mean	SD	True	Mean	SD	True	Mean	SD	True	Mean	SD
MECPD	5000	5000.0	5.1	6000	6287.0	104.1	1000	1050.5	17.4	2000	2093.0	34.7
MICPD		5000.0	6.7		5848.8	98.9		977.3	16.6		1947.0	32.9

Table 6.3: The true states and the mean and standard derivations (SD) of the marginal pdfs estimated using IDM for the initial pressure, cumulative production and flow rates in the first and second production periods.

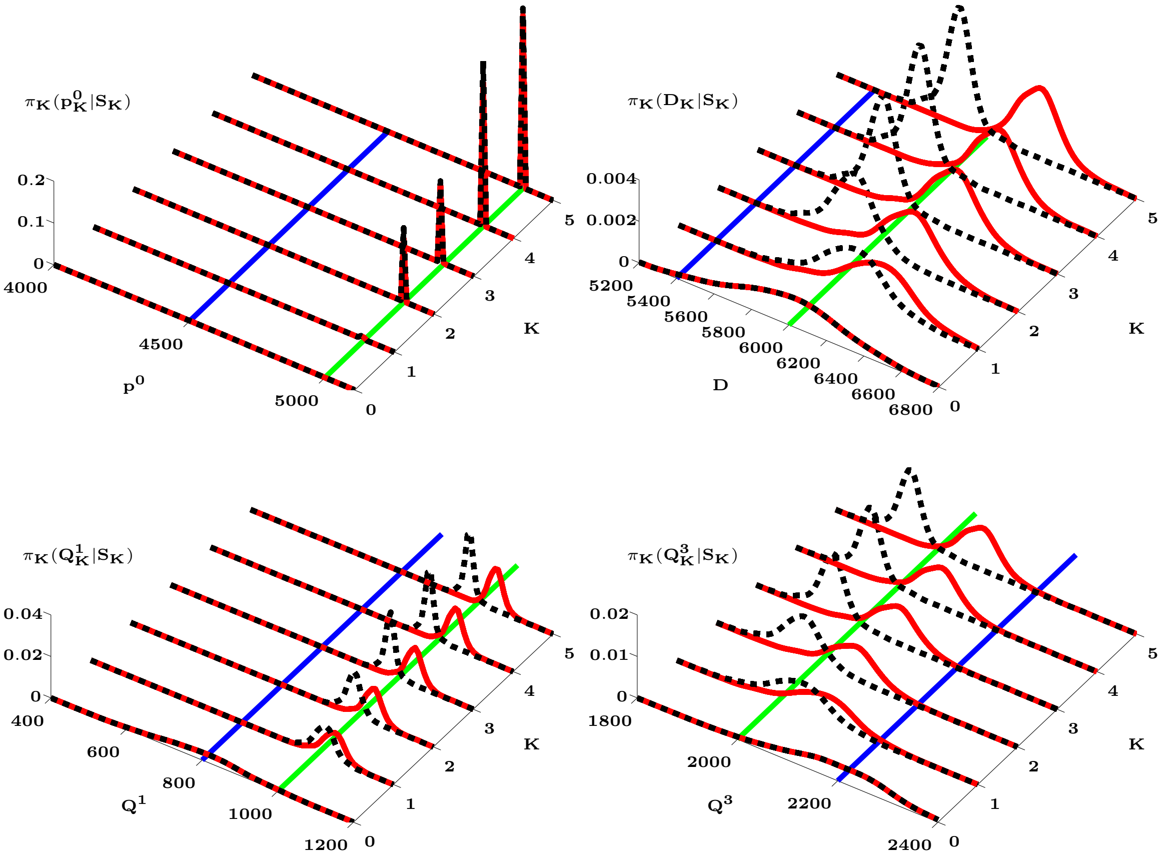

Figure 6.4: The marginal pdf of the initial pressure (top left), cumulative production (top right) and flow rates of the first (bottom left) and second (bottom right) production period for the synthetic experiment 6.4.1. The 0^{th} iteration denotes the initial prior. These plots show the true states (green lines), the measured states (blue lines) and the marginal pdfs conditioned on MEPCD (red) and MICPD (dashed black).

relatively small number pressure data point presented within this given time interval (on both the absolute and superposed time scale).

Fig. 6.4 presents the iteration-evolution of the marginal pdfs of the initial pressure ($\pi_K(p_K^0|S_K)$), cumulative production ($\pi_K(D_K|S_K)$) and FRs ($\pi_K(Q_K^1|S_K)$ and

$\pi_K(Q_K^3|S_K))$, while the detailed analysis of these marginal pdfs at the terminating iteration are summarised in Table 6.3. For the estimation of initial pressure, even starting with a very poor initial prior, the convergence of the marginal pdfs conditioned on MECPD or MICPD is rather rapid. Excellent and consistent estimates are found using either of the marginal pdfs as shown in Table 6.3.

For the estimation of the cumulative production, starting with a Gaussian initial prior with mean the same as the truth and a large uncertainty, the marginal pdf conditioned on the MECPD and the MICPD are biased in the opposite direction. This is due to incorporation of the cumulative production data which is significantly smaller than the truth. The reduction of pdf uncertainty is the greatest during the first few iterations and quite gradual in later iterations. This agrees with the formulation of the IEnSRF. As shown in Table 6.3, the IDM conditioned on the MICPD provides an improved estimate compared to just conditioning on the MECPD.

Similar conclusions for the FR estimates can be made. Using the MECPD, the true FRs fall at the left tail of the marginal pdfs, while, using MICPD (with additional cumulative production information), they fall at the right tail. As shown in Table 6.3, IDM using MICPD provides improved estimates to the truth than using MECPD.

In Fig. 6.3, as the result of excellent parameter estimates in both tests, the simulated pressure using the analysed ensembles well (re)produce the pressure simulation using the exact parameters with a very small estimation uncertainty (much smaller than the initial uncertainty). This, indeed, confirms the success of our IDM.

6.4.2 Real Gas Field Experiment

The reservoir under investigation is a multilayered natural gas reservoir, which consists of two 43 ft thick layers. The reservoir, well and gas properties are summarised in Table 6.4 and 6.5. This well test was carried out to identify the reservoir boundary, the measurement data of which is presented in Fig. 6.5. Over a six-day period, a total

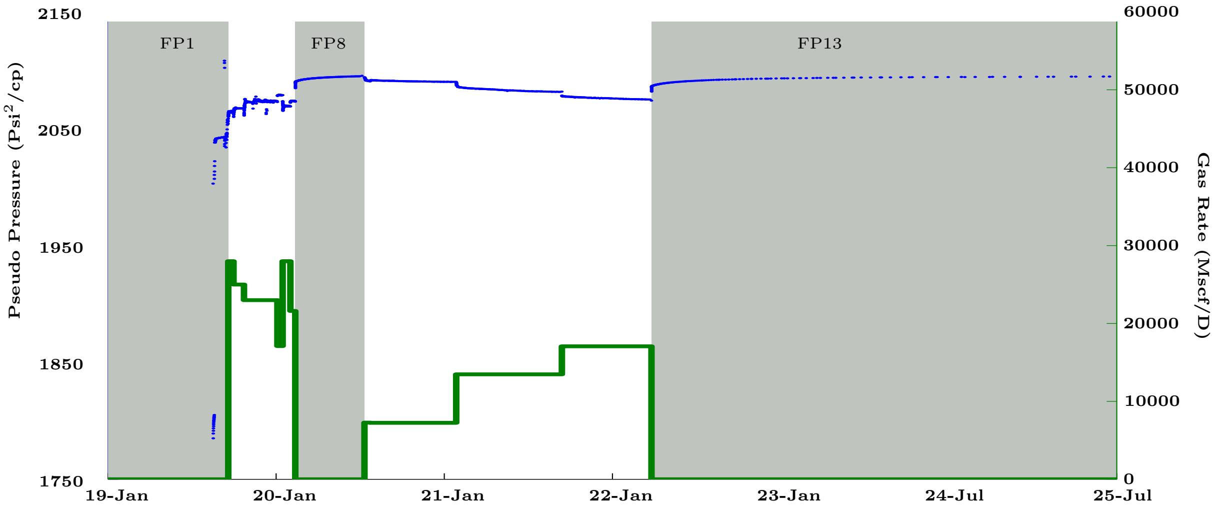

Figure 6.5: Well test data for real gas field experiment 6.4.2. Pseudo pressure data (blue), flow rate data (green) and the initial cleaning and two shut-in periods (gray).

Wellbore radius	Formation volume factor	Net reservoir thickness	Matrix porosity
6.25 ft	0.004 cf/scf	160 ft	26.9%

Table 6.4: The well and reservoir for experiment 6.4.2.

Total compressibility	Viscosity	Gas gravity	Z-factor
4.35×10^{-5}/psi	0.02 cP	0.57	0.89

Table 6.5: The gas properties for experiments 6.4.2.

Durations (days)	Initial pressure (psia^2/cp)	Reservoir temperature (°F)	σ_P (psi^2/cp)	σ_Q (Mscf/D)	σ_D (Mscf)
7	2098	140	2	3000	2000

Table 6.6: The well testing acquisition parameters for experiment 6.4.2.

of 13 FPs were operated, consisting of an initial well cleaning period (7:00, 19 Jan - 00:10, 20 Jan; duration: 17.2 hrs), two shut-in periods: FP8 (09:43 - 19:27, 20 Jan; duration: 9.9 hrs) and FP13 (12:35, 22 Jan - 13:00, 24 Jan; duration: 72.4 hrs) and 10 production periods (total duration: 50.5 hrs)[15]. Fluctuations in the pressure and FR data are observed between FP2 and FP7 and likely to be caused by water loading up in the well. The pressure and FR data after FP7 are reasonably correlated. The initial pseudo pressure and the cumulative production are 2089 psi^2/cp and 29437 Mscf, respectively. The acquisition parameters are summarised in Table 6.6.

---

[15] Fig. E.2 in Appendix E presents the detailed pressure data plots in FP8, FP12 and FP13.

Two tests are performed to estimate the FRs, LLDTC and cumulative production with the same initial ensemble using 5 iterations of the IDM with measurements including the pressure in FP13 and FRs (MECPD) or measurements including the pressure data in FP13, FRs and cumulative production (MICPD). The initial pseudo pressure is considered to be exact and not to be estimated. The initial LLDTC realisations are generated using the pressure derivative data in the FP13. The FR realisations are constructed to be drawn from a Gaussian distribution with mean being the measured FRs and SD being 30% of the measured FRs[16] due to the large fluctuations in pressure and FR data between FP2 and FP7.

Fig. 6.6 presents the type curve estimates and the pressure matches. The pressure derivative data between 0.03 hrs and 0.2 hrs and after 65 hrs are particularly poor. This leads to large uncertainty in the initial LLDTC realisations and corresponding pressure simulations. However, even with such a large pressure simulation uncertainty, the majority of the pressure data in the first three FPs falls outside this uncertainty. This agrees with our earlier comments on the potential causes and quality of this portion of the data, and confirms the need for a special way of generating the initial FR realisations. After the process of deconvolution, both tests provide almost identical LLDTC estimates with reduced uncertainty (compared to the initial ensemble), while the uncertainty of the LLDTC estimation found using MICPD is slight smaller than using MECPD. The late-time part (after 0.1 hrs) of the LLDTC estimate (in both tests) has been significantly corrected positively and formed the shape of a straight line (with slope of 0.5), which indicates an impermeable reservoir boundary [75].

Table 6.7 presents the FR estimates. For both tests, while the estimates are similar to the measurements, the analysed uncertainty is reduced significantly compared to the uncertainty in the initial ensemble. In particular, incorporating the cumulative production data, the FR estimation uncertainties using MICPD is further reduced

---

[16] This special way of generating the initial ensemble was suggested by the engineers in Paradigm.

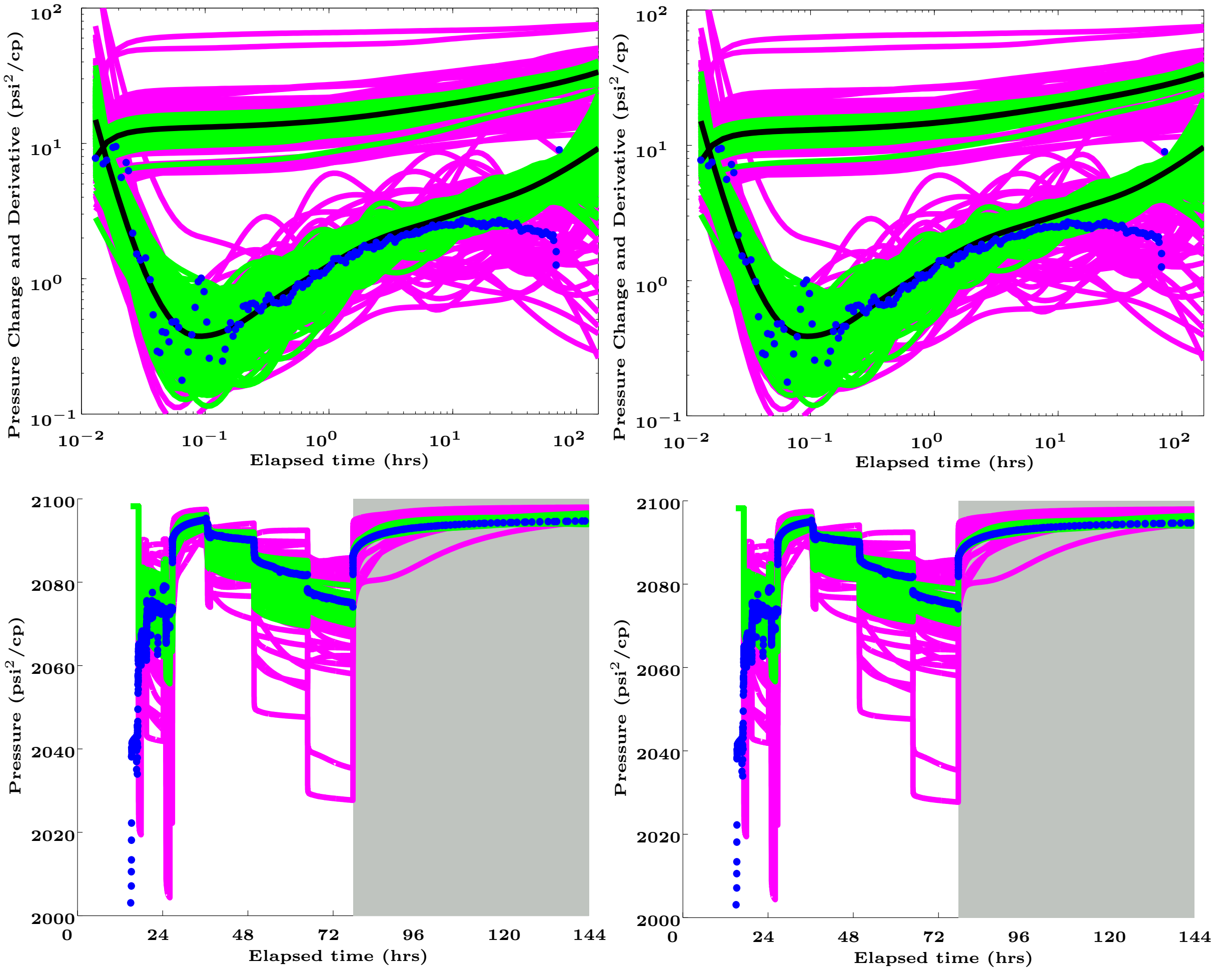

Figure 6.6: The LLDTC estimates (top row) and pressure matches (bottom row) for real gas field experiment 6.4.2 using MECPD (left column) and MICPD (right column). The type curve estimation plots show the pressure derivative data (blue), estimated type curves (black) and type curves in the initial (magenta) and analysed (green) ensembles. The pressure matching plots show the pressure data (blue), pressure data selected for deconvolution (gray shadow) and pressure simulation using initial (magenta) and analysed (green) ensembles.

compared to the estimated uncertainty using MECPD.

The FR estimation improvement using MICPD over MECPD is further demonstrated in Table 6.8 with the results of cumulative production estimation. Together with the FP intervals, using the estimated FRs in each realisation, we calculate the cumulative production for each realisation and summarise the result using the mean and SD of the realisations as the description of estimation and uncertainty. The cu-

FP(Msc/D)		2	3	4	5	6	7	9	10	11	12
Measurement		28000	25000	23000	17100	28000	21600	7275	7237	13467	17065
MECPD	Mean	27989	25084	23068	17050	27986	21635	7251	7246	13728	17050
	SD	2394	2365	2350	2247	2397	2341	1597	1632	2101	1844
MICPD	Mean	27951	25004	22864	17044	27932	21589	7241	7243	13168	16703
	SD	2158	2135	2104	2049	2159	2119	1520	1488	1754	1608

Table 6.7: The production rate measurements and estimates after deconvolution using IDM with MECPD and MICPD in real gas field experiment 6.4.2.

Measurement	Initial mean	Initial SD	MECPD mean	MECPD SD	MICPD mean	MICPD SD
29437	30957	4316	31287	1903	30545	1383

Table 6.8: The cumulative production in the initial prior and estimates after deconvolution using IDM with MECPD and MICPD in real gas field experiment 6.4.2.

mulative production estimate found using MICPD is reduced compared to the mean in the initial ensemble to indicate some reasonable amount of lost in transition, while the estimate found using MECPD increases from the mean of the initial ensemble and can be difficult to interpret.

As shown in the pressure matching plots in Fig. 6.6 and the enlarged plots in Fig. E.3 in Appendix E, the quality data in FP8 to FP13 are better matched (within the uncertainty (the vertical width of the green lines)) and the poor data in FP1 to FP7 are better distinguished (fall outside the uncertainty) using the estimates found by IDM with MICPD than with MECPD. Hence, although consistent and excellent LLDTC estimates are found using both MECPD and MICPD, the IDM with MICPD provides a more reliable FR and cumulative production estimates.

6.4.3 Real Oil Field Experiment

The considered reservoir is an oil and gas reservoir formed by sandstone with basic well, reservoir and oil properties being summarised in Table 6.9. The well test is carried out to verify the presence of a barrier (impermeable reservoir boundary) around

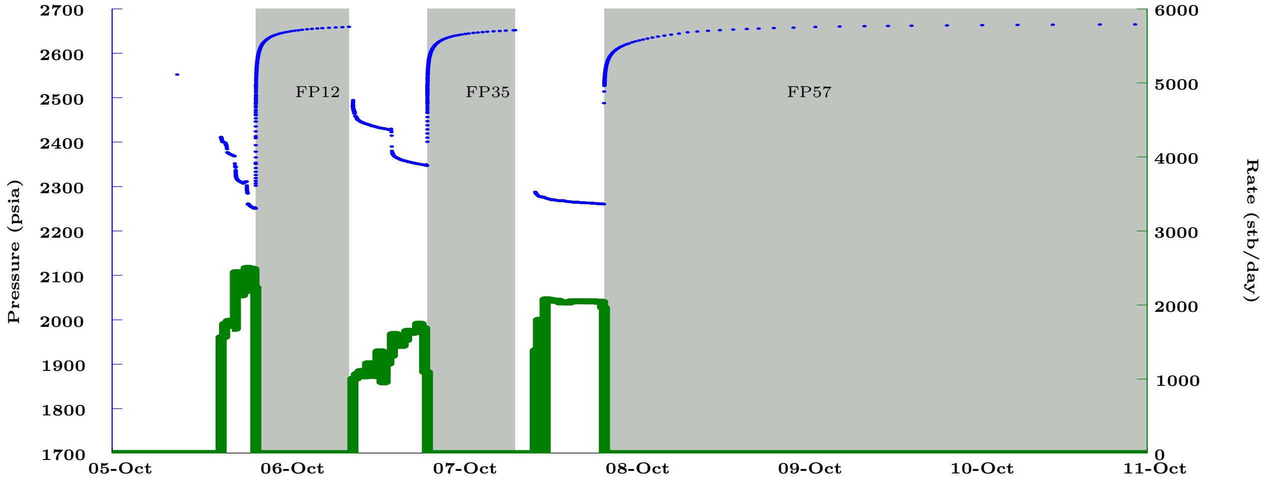

Figure 6.7: Well testing data for real oil field experiment 6.4.3. Pressure data (blue), flow rate history (green) and three well shut-in periods (gray).

Wellbore radius	Formation volume factor	Net reservoir thickness	Matrix porosity	Total compressibility	Viscosity
4.25 ft	1.3 rb/stb	86 ft	22.7%	1.3×10^{-5}/psi	1.3 cP

Table 6.9: The well, reservoir and oil parameters for experiment 6.4.3.

Durations (days)	Initial pressure (psia)	Reservoir temperature (°F)	σ_P (psia)	σ_Q (stb/D)
6	2670	156	5	100

Table 6.10: The well testing acquisition parameters for experiment 6.4.3.

400 ft from the position of the vertical test well [6], the measurement data of which is presented in Fig. 6.7. Over a six day period, a total of 57 FPs have been operated, which consist of an initial well cleaning period (7:00-22:10, 05-Oct; duration: 15.2 hrs), three shut-in periods: FP12 (3:00-16:00, 06-Oct; duration: 13 hrs), FP35 (2:52-15:05, 07-Oct; duration: 12.2 hrs) and FP57 (03:30, 08-Oct - 19:00, 11-Oct, duration: 87.5 hrs) and 53 individual (approximate half-hour) production periods. The detailed FRs can be found in Table 6.12. The initial pressure is 2670 psia. The acquisition parameters and measurement uncertainties are summarised in Table 6.10.

Two tests are carried out to repeat the benchmark experiments in [6] and are designed to compare the performance (deconvolved type curves and predictability of the barrier) of different deconvolution algorithms in the commercial applications:

Interpret$^{\text{TM}}$ 2009, Saphir and TSLD, with the assumption of an exact initial pressure. The deconvolution is first performed on measurements including the pressure data in and FR data before FP12. This is denoted as test 6.4.3.1 for ease of presentation. In the second test (denoted as test 6.4.3.2), the deconvolution is then performed on measurements including the pressure data in both the FP12 and FP35 and FR data before FP35. The derivative of the pressure data in FP12 and FP35 are used for the initial LLDTC ensemble construction in test 6.4.3.1 and 6.4.3.2, respectively. The FR realisations in the initial ensemble are constructed to be drawn from a Gaussian distribution with mean being the measured FRs and SD being 400 stb/D. In each test, the estimated LLDTC and barrier distance found using IDM (5 iterations), Interpret, Saphir and TSLD are presented and compared[17].

In both tests, the posterior pdfs of the barrier distance, $\pi_K(d_b|x_K)$, is found by calculating the barrier distance for each realisation of the analysed LLDTC ensemble (procedure described in [1]) from IDM and using density reconstruction in Appendix D. As a comparison, the barrier distance is also calculated deterministically using the estimated LLDTCs from Interpret, Saphir and TSLD.

Fig. 6.8 presents the pressure matches, the type curve estimates and the pdfs of the estimated barrier distance from the well for both tests. In test 6.4.3.1, our initial realisations of the LLDTC consist of only the wellbore storage ($[10^{-3}, 10^{-2}]$ hrs elapsed time) and the infinite acting radial flow (horizontal line). After the deconvolution process, the uncertainty has been greatly reduced. The late-time behaviour of the LLDTC estimate is corrected positively, and indicates the existence of a barrier. Note that the estimated LLDTCs using IDM, TLSD and Saphir are quite similar, while the estimated LLDTC using Interpret is very different and there is a lack of physical

---

[17] One may note that the pressure data in the longest build-up, FP57, is surprisingly not used. In fact, during the initial benchmark test, only the first 35 FPs were initially performed to verify the barrier distance. However, the existing commercial software applications fail to provide satisfactory and consistent results through the described tests. A much longer well shut-in period (FP57) is then used to provide extra information to further investigate the existence of the barrier.

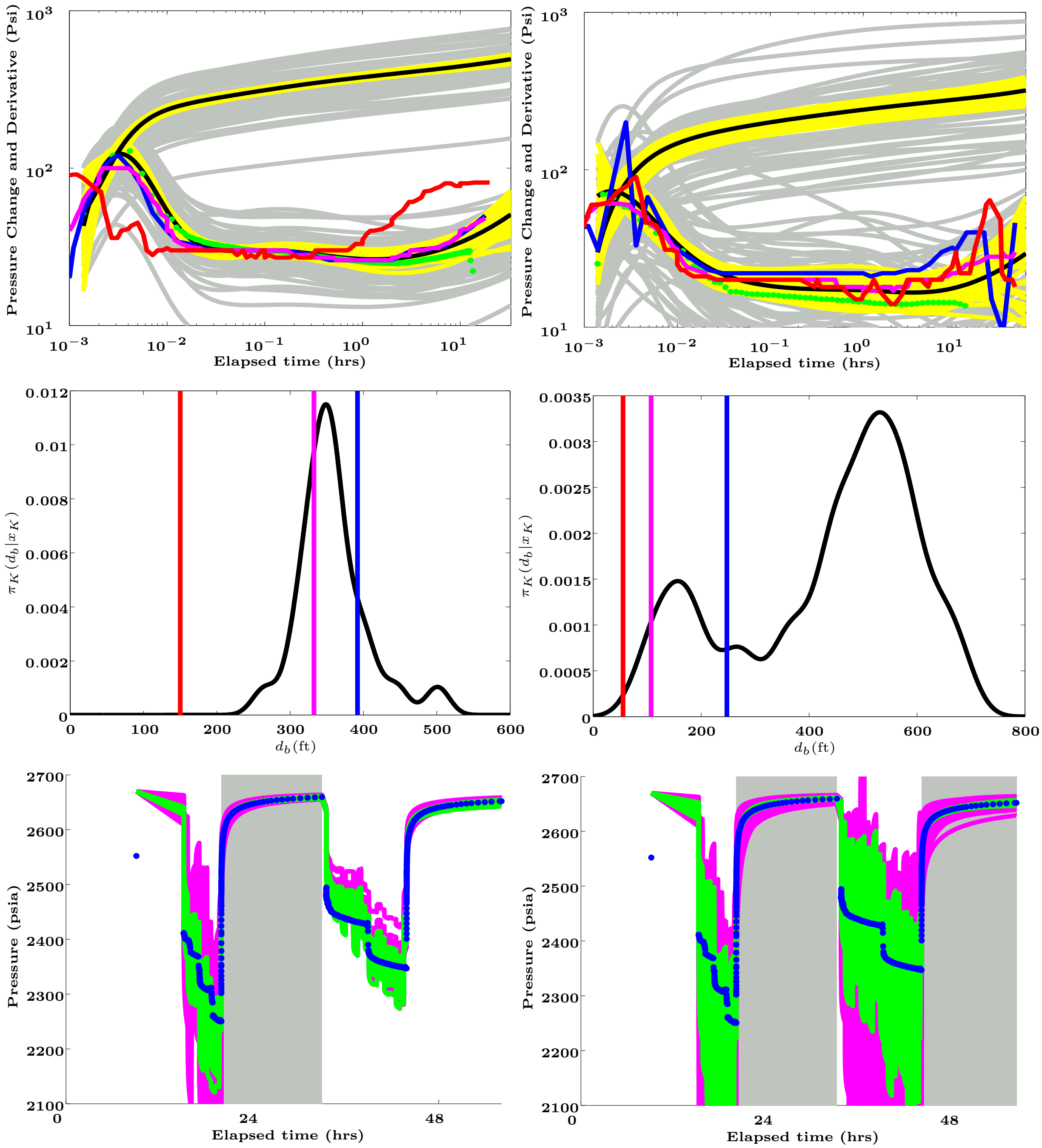

Figure 6.8: The LLDTC estimates (top row), barrier distance estimates (second row) and pressure matches (bottom row) for test 6.4.3.1 (left column) and 6.4.3.2 (right column). The type curve estimation plots show the pressure derivative data (green), the deconvolved type curves using IDM (black), Interpret (red), TSLD (blue) and Saphir (magenta) and type curves in the initial (gray) and analysed (yellow) ensembles of the IDM estimation. The barrier distance plots show the approximate pdf using IDM (black) and estimated distance using Interpret (red), TSLD (blue) and Saphir (magenta). The pressure matching plots show the pressure data (blue), pressure data selected for deconvolution (gray shadow) and pressure simulations using initial (magenta) and analysed (green) ensembles of IDM.

Barrier Distance (ft)	Interpret$^{\text{TM}}$ 2009	TLSD	Saphir	IDM Mean	IDM SD
Test 6.4.3.1	150.1	391.9	332.5	358.5	47.7
Test 6.4.3.2	55.4	247.7	107.3	435.8	168.1

Table 6.11: The estimated barrier distances using Interpret, TLSD, Saphir and IDM in real oil field experiment 6.4.3.

Rate (stb/D)		Q^2	Q^3	Q^4	Q^5	Q^6	Q^7	Q^8	Q^9	Q^{10}	Q^{11}
Measurement		1566	1746	1785	1678	2444	2131	2184	2501	2487	2239
Test 6.4.3.1	Mean	1568	1748	1787	1679	2444	2134	2184	2500	2480	2233
	SD	160.3	160.3	160.3	160.3	160.3	160.3	160.3	160.3	160.1	152.7
Test 6.4.3.2	Mean	1563	1739	1768	1657	2414	2099	2124	2402	2238	2033
	SD	330.6	330.3	329.9	329.3	329.1	328.5	326.9	323.1	297.6	265.3

Table 6.12: The production rate measurements and estimates in FP2 to FP11 after the deconvolution using IDM in real oil field experiment 6.4.3.

meaning at the early time. For the same reason, in the barrier distance plot and statistics in Table 6.11, the estimated barrier distance found by TLSD and Saphir are quite consistent (within 1 SD) with the mean of the barrier distance pdf found by IDM, while Interpret fails to meet the well test objective. With clear evidence that a barrier exists between 310.2ft to 406.2ft (one SD on either side of the mean which equivalent to 68% of the probability) away from the well using IDM, the well test objective can be considered accomplished. However, such a conclusion cannot be made with the inconsistent deterministic estimates if the existing methods were used.

The result of FR estimation is presented in Table 6.12. For test 6.4.3.1, although the estimates are quite similar to the measurements, in the pressure matching plot of Fig. 6.8, the success of estimation is verified as the pressure data in FP2 to FP12 fall within the uncertainty (vertical width of the green lines) of the pressure simulation (generated using these estimates). However, note that the pressure data after FP12 fall at the tail of simulation uncertainty, which indicates that further FR adjustments for FP2 to FP12 are required to improve the matching for these data.

The results of test 6.4.3.2 are presented in the right column of Fig. 6.8, the estimated LLDTCs found by commercial software are only of 0th order smooth and are inconsistent with each other and with their results found in test 6.4.3.1, while the LLDTC estimate found by IDM is consistent and yields a slightly bigger uncertainty compared to the estimate in test 6.4.3.1. Indeed, this is also confirmed by the result in the barrier distance plot and the analysis in Table 6.11. In particular, in the barrier distance plot, all the estimated barrier distances found by commercial software are distributed around the less probable mode of the bimodal pdf estimated using IDM. This is caused by the ill-posedness of the inverse problem and indicates that the non-Bayesian conventional methods lack accuracy and practicality.

In fact, compared to the results in test 6.4.3.1, the bimodal distribution and increment of the barrier distance estimation uncertainty is caused by the dimensional increment of the FR estimation. One can see from Table 6.12 that the adjustments[18] of the FR in test 6.4.3.2 are generally more significant compared to the adjustments in test 6.4.3.1 (e.g. FP4 to FP11), which agrees with our earlier conclusion regarding the need for further FR adjustments for pressure matching in FP35. However it is, perhaps, surprising to some non-Bayesian readers that using twice the amount of pressure data (test 6.4.3.2) approximately doubles the FR estimation uncertainties in the first 11 FPs. This is because by incorporating pressure data in FP35 (test 6.4.3.2) in addition to the pressure data in FP12 (test 6.4.3.1), the non-uniqueness of the inverse problem is greatly enhanced by the requirement of estimating significantly more FRs. In the pressure matching plot of Fig. 6.8, the pressure data in FP2 to FP35 fall within the uncertainty of the pressure simulations using the realisations of the analysed ensemble, which verifies the success of the deconvolution using IDM.

6.5 Conclusion

The aim of this chapter is to develop a general, efficient and robust Bayesian method for solving the deconvolution problem in well testing and overcoming the problems

---

[18] Difference between the estimated and measured FRs.

with the existing methods. The proposed IDM based on the IEnSRF is demonstrated to achieve: (i) Physical and interpretable estimates with uncertainty quantification. (ii) The capability of estimating the initial pressure. (iii) The capability of incorporating the cumulative production data. The IDM also outperforms the existing methods under both synthetic (PMS) and real (IMS) scenarios.

In both synthetic oil field experiment 6.4.1 and real gas field experiment 6.4.2, by incorporating the cumulative production data, the FR estimate is improved and better agrees with the real-world situation and engineering expect. The estimates can thus be interpreted and analysed with better confidence. In particular, in experiment 6.4.1, the IDM is shown to be capable of estimating the initial pressure. By deliberately assigning a nonphysical and poor initial prior, the IDM is tested under an extreme scenario and demonstrates great robustness and performance in estimating the exact underlying physics with reliable uncertainty quantification.

In real oil field experiment 6.4.3, under very challenging conditions and with an ambitious goal, the estimates found using IDM are compared against the estimates found using existing commercial software: Interpret$^{\mathrm{TM}}$ 2009, TSLD and Saphir. Both the LLDTC and barrier distance estimates using IDM are found to be physical and interpretable and meet the industrial needs with reliable uncertainty quantification for the propose of target verification and risk management, while the solutions found using existing commercial software are inconsistent (as the error estimates are never available to these results) and (sometimes) uninterpretable. The FR estimates and the corresponding uncertainty quantifications using the IDM are also shown (through the experiment with the pressure data in an additional FP) to be reliable and accord with Bayesian principles for solving inverse problems.

Chapter 7

History Matching of Geological Facies Patterns using Warp Ensemble Square Root Filters

7.1 Introduction

History matching is the art of adjusting reservoir models until they closely reproduce the past reservoir behaviour, consisting of historical production and injection data. Once a model has been history matched, it is often assumed that it can then be used to simulate future reservoir behaviour with a higher degree of confidence, particularly if the model estimation is constrained by known geological properties [89]. In the most general case, the reservoir parameters, which are required to be history matched and used in the production prediction, include the porosity, permeability, density of the fractures, capillary pressure and so on. Generally speaking, retaining a high-dimensional parameterisation of all possible reservoir properties and parameters provides enhanced ability for the production prediction and better flexibility for history matching. Indeed, as shown in [30], with additional global parameters such as relative permeability curve and initial oil/water contact parameters, the history matching of the permeability and porosity of the Brugge field - a large-scale SPE (Society of Petroleum Engineers) benchmark study, was able to be further improved.

However, because of the limited observation locations and diffusive nature of the flow, information regarding the reservoir parameters contained in the production data is generally low [120]. In the Bayesian framework, retaining a high-dimensional parameterisation of all reservoir parameters means that the estimation will be strongly influenced by the initial prior. In [119], through a one-dimensional single-phase history matching exercise, only 3 out of 80 model parameters can be determined by the data, and the remaining variables are determined by prior information [120]. Similar conclusions have also been made in [126, 162]. These, indeed, highlighted the ill-posed nature of the history matching problem. That is, different parameter sets can lead to an equivalent fit to the available measurements [153].

One way to ease the ill-posedness is to introduce regularisation, while another way is to replace the original set of parameters to be estimated with a set of reduced dimension which still captures the most important underlying physics. In the petroleum engineering literature, the first approach inspired the formulation of the history matching problem of facies patterns[1], in which, all model parameters are assumed known and only the structure of facies pattern is to be estimated. Due to its strong connection to realistic earth models, it has became an important area of study in a number of research projects [27, 44, 107, 108, 117] and is indeed the problem considered in this thesis. The latter approach is known as parameterisation and is classified as a prior construction process in the Bayesian framework.

The parameterisation approach can be utilised for solving general history matching problems and is thus popularly used by reservoir engineers. In general, the application of this approach approximates the spatial reservoir properties using different basis

---

[1] Facies are a body of rock with specified characteristics such as permeability, porosity, etc [127].

functions based on (i) the piecewise constant function with zonation [71, 86, 90, 140], (ii) pilot point method [40, 106, 170, 171, 178], (iii) spline methods [42, 101, 111], (iv) spectral decomposition [68, 87, 88, 89, 130, 137] and (v) data sensitivity [66, 133].

The parameterisation method based on these basis functions normally works well for reservoir properties that are continuous and approximately Gaussian, but not for geological models with discrete facies or repetitive shapes [120] as in the considered problem, without additional regularisation. Nielsen *et al.* [117] and Dorn *et al.* [44] applied the level set method to model the facies bodies and performed history matching by minimising a misfit function between the simulated and observed data with Tikhonov regularisation. This approach was found to be robust, but is generally more computationally expensive than, say an Ensemble Kalman Filter (EnKF) method, because it requires integrating the model adjoint to determine the gradient descent directions. More importantly, this method only provides a deterministic estimation (without uncertainty), which might be insufficient for reservoir management.

Sequential ensemble-based data assimilation techniques, based on the work of the EnKF in [56, 57], appear to offer attractive features and powerful capabilities. The EnKF actually provides an efficient approach to estimate a large number of variables and is based on a simple conceptual formulation and relative ease of implementation[2]. It furthermore computes estimates of the solution uncertainties as part of its algorithm at reasonable computational cost. However, because all Kalman-based ensemble filters are only designed for the estimation of continuous variables, the main challenge in applying these filters to the considered problem is to transform the discrete facies variables into continuous variables through an appropriate parameterisation.

Liu *et al.* [107, 108] used a threshold truncation map to parameterise the facies in each cell, and thus transformed the estimation of the geostatistical model in the considered problem into a level estimation problem on a threshold truncation map.

---

[2] It does not need the linearisation of the reservoir model nor the development of its adjoint and only requires forward integrations of the reservoir model.

However, when applying the ensemble-based filter to estimate the level of parameterisation on the threshold truncation map, the initial ensemble is required to be generated using truncated pluri-Gaussian models[3] to optimise the performance of the filters, which may not be able to meet easily in a real problem[4].

Chang [27] combined the level set method and the traditional EnKF. The domain of the discrete facies body variable is extended to be defined on a continuous real set with several subsets which represent the number and probability of facies types. The EnKF is then utilised to estimate the described level set parameterisation during the history matching process. The proposed method demonstrated good performance through the synthetic experiments, but as a cell-based parameterisation, when applied to a large-scale history matching problem, it is normally not very efficient, because the estimation is not directly performed on the desired geological structures as in [48].

More recently, in [48], it is proposed to estimate the location of the feature (boundaries) directly. It can be viewed as a parameterisation using data sensitivity, because the matching of production data can be adjusted significantly by varying the width and shape of the feature. This parameterisation works well in a reservoir with simple reservoir features, but may fail to provide satisfactory results in large-scale complicated reservoir models, because explicit prior information regarding the number of features and complexity of the features is required to optimise the performance.

Inspired by the work in [48], in this chapter, the Warp Ensemble Square Root Filter (WEnSRF) is developed and proposed as a method for solving the considered problem. This chapter is organised as follows. §7.2 recalls the state-space formulation based on the WEnSRF. §7.3 discusses the typical form of filter realisations, the detailed WEnSRF implementation and the incorporation of the prior permeability field library for the numerical experiments. §7.4 and §7.5 present and discuss the results for solving

---

[3] Which is primarily used as a geostatistical method for producing geological facies maps conditioned on facies proportions and hard data [70, 100].

[4] Because the information of the facies proportions (required as the parameters in the truncated pluri-Gaussian models) is almost always absent without costly investigation.

the history matching problem of simple facies patterns and large-scale complicated facies patterns, respectively. A summary and a discussion conclude the work in §7.6.

7.2 The State-Space System

Defined mathematically in §4.4.2, the considered history matching problem of facies patterns assumes exact knowledge of all reservoir properties except the (absolute) permeability field and aims to estimate the geological structure of a two dimensional horizontal rectangular oil reservoir formed from two types of rock: the large shale area with low permeability κ_l and some sandstone with high permeability κ_h.

The reservoir is initially fully saturated with water and oil. Using the water flooding experiment[5] [23] demonstrated in Fig. 2.3, pressure measurements in the injection wells (along the east boundary) and the water saturation measurement in the production wells (along the west boundary) are used as the production data for automatic history matching in real time.

As a new ensemble-based Bayesian method for solving the considered problem, the WEnSRF, which combines the warping transformation and EnSRF, is derived in §3.5. The warping transformation transforms the estimation of the discrete permeability variables (in the original formulation) into estimation of continuous warping transformation variables and optimises the performance of the EnSRF. However, without any restriction, it enlarges the dimension of the model variables to be estimated. To make the WEnSRF practicable for large-scale reservoir models, in §4.4, the prior information is constructed by parameterising the warping transformation mapping in each direction using a B-spline surface.

We recall that the state-space system for solving the considered problem using WEnSRF with the proposed B-spline surfaces parameterisation is summarised in eqs.

---

[5] A secondary oil recovery strategy where water is injected at the west boundary of the reservoir at a constant rate and oil is produced from the east boundary with a constant bottomhole pressure.

(4.8a,b) in §4.4.2, which is modified from the eqs (3.26a,b) on page 52.

7.3 Updating Facies with the Warp Ensemble Square Root Filter

To perform history matching using the WEnSRF, based on the formulation of the input in (4.7) for the state-space system (4.8a,b), a typical realisation is: $x_{k,i} = [\Phi^1_{k,i}, \ldots, \Phi^N_{k,i}, \lambda^1_{k,i}, \ldots, \lambda^N_{k,i}, \kappa^{0^1}_{k,i}, \ldots, \kappa^{0^N}_{k,i}, b^0_{k,i}, \ldots, b^{G_x-1}_{k,i}, \mathrm{b}^0_{k,i}, \ldots, \mathrm{b}^{G_y-1}_{k,i}, P^1_{k,i}, \ldots, P^N_{k,i}, S^1_{k,i}, \ldots, S^N_{k,i}]^T$, where the subscript k and $i \in [1, r]$ denote the time and realisation indices, respectively; and r is the total number of realisations. Note that the control net dimension (G_x and G_y) is normally small compared to the dimension of the discretised permeability field (N) (e.g. see Fig. 4.3 on Page 68).

In addition, with clear evidence presented in [7], it is desirable to history match with realisations of greater heterogeneity. While history matching small-scale reservoir models with simple features is possible with the WEnSRF using a single prior permeability field, to include a more varied heterogeneity for large-scale history matching with complicated features such that the prior information of the reservoir structure is better constructed, we propose to history match using the WEnSRF with a prior permeability field library (or an ensemble of prior permeability fields) consisting of l realisations: $\{\mathbf{K}^0_1, \ldots, \mathbf{K}^0_l\}$.

For each realisation of the prior permeability field library, we use r realisations to perform history matching. Hence, a total $r_l = r \times l$ realisations are used. The utilised scheme can be viewed as a parallel WEnSRF or an (equal-weighted) ensemble of WEnSRFs [83]. At the end of each data assimilation cycle, we reconstruct the permeability fields using the prior permeability field and the warping transformation in each realisation (for all r_l realisations). The realisations of these estimated permeability fields are then analysed to quantify the estimation and uncertainty.

As commented in [83], the main issue with running an ensemble of WEnSRFs is the computational burden associated, knowing that running a WEnSRF in high dimensional systems may already be a challenge. To reduce computational cost, we conducted a sensitivity test in §7.4.3 to obtain the empirical optimal number of realisations for a single WEnSRF with acceptable performance on estimating both the reservoir properties and the associated uncertainties.

All experiments adapt the cubic B-spline surfaces with control point nets of dimension $G_x = G_y = 8 \times 6$ (i.e. 8 control points along the x direction and 6 control points along the y direction for the parameterisation of both $\mathcal{T}_x$ and $\mathcal{T}_y$). Using the prior knowledge, the initial ensemble is generated with the exact porosity, mobility and initial pressure and saturation.

7.4 Numerical Experiments on Simple Synthetic Reservoir Models with a Single Feature

Following [48], three numerical experiments were performed to test the WEnSRF and to evaluate its performance. The test cases are a curved channel (Fig. 7.1), a disconnected channel (Fig. 7.5), and a two-dimensional closed feature (Fig. 7.8).

The relative permeability functions are defined by the Corey models:

$$\kappa_{rw} = \hat{\kappa}_{rw} \left(\frac{S_w - S_{wr}}{1 - S_{wr} - S_{or}} \right)^{e_w}, \qquad \text{and} \qquad \kappa_{ro} = \hat{\kappa}_{ro} \left(\frac{S_o - S_{or}}{1 - S_{or} - S_{wr}} \right)^{e_o}. \quad \text{(7.1a,b)}$$

where the Corey exponents, e_w and e_o, the residual saturations, S_{wr} and S_{or}, and the endpoint permeabilities, $\hat{\kappa}_{rw}$ and $\hat{\kappa}_{ro}$, are assumed to be known. The numerical values of the reservoir properties are listed in Table 7.1.

For each reference permeability field, we simulate the ‘true’ values of saturation and pressure for the applied time steps by integrating the reservoir model forward in

Reservoir dimensions:	$1000m \times 1000m \times 40m$	
Simulation grid:	$16 \times 16 \times 1$ cells	
Facies Permeability (mD):	$\kappa_h = 10000$	$\kappa_l = 500$
Porosity:	0.2	
Viscosity:	$\mu_w = 0.5 \cdot 10^{-3}$ Pa·s	$\mu_o = 0.5 \cdot 10^{-3}$ Pa·s
Endpoint relative permeability:	$\hat{\kappa}_{rw} = 0.1$	$\hat{\kappa}_{ro} = 1$
Residual saturations:	$S_{wr} = 0.2$	$S_{or} = 0.2$
Corey exponents:	$e_w = 2$	$e_o = 3$
Initial saturations:	$S_w = 0.2$	$S_o = 0.8$
Injection wells:	8% of total pore volume per year	
Production wells:	constant pressure of 200.0 bar	
Number of timesteps:	100	
Total production time:	1600 days	

Table 7.1: Key properties in the reservoir simulator.

time. Synthetic measurements are then extracted from the true states and perturbed with random noise drawn from an uncorrelated Gaussian distribution with zero mean. The standard deviations (SDs) of the pressure measurement noise in the injection wells and the water saturation measurement noise in the production wells are $\sigma_P = 2$ bar and $\sigma_S = 0.002$, respectively. History matching of facies patterns then uses these measurements every 16 days and over an 800 day period. The estimated permeability field ensemble is then used to predict the reservoir behaviour of another 800 days. To mitigate the problem of ensemble collapse, large ensembles with $r = 600$ members are used in the experiments. For the estimation quality check of transformation mappings and log permeability field, we use the following approaches:

1. *Take the mean (MTX and MTY) and SD (SDTMX and SDTY) of the transformations in both the x and y directions of the analysed ensemble*: (i) compute the cell-based transformation mappings (in both the x and y directions) associated with the B-spline control point nets in each realisation (ii) calculate the mean (MTX) and SD (SDTX) of the transformation mapping in the x direction cell-by-cell. (iii) Similarly, for the estimation of the transformation in the y direction, MTY and SDTY are computed.

2. *Take the mean (MLP) and SD (SDLP) of the estimated log permeability fields found using the analysed ensemble*: (i) compute the log permeability fields associated with the prior permeability field and the transformation mapping in each realisation. (ii) calculate the mean (MLP) and SD (SDLP) of the estimated log permeability fields cell-by-cell. During this process, artificial rock types might be generated.

3. *Misfit figure of the facies:* Following [48], we adapt the facies transformation for the prior permeability field using a level-set parameterisation (i.e. replacing permeabilities k_h and k_l by facies value -1 and 1, respectively) and process the analysed ensemble in the same way as for MLP and SDLP to get the mean and SD of the estimated facies. The misfit figure presents the exact discontinuous curve, the estimated discontinuous curve, and the cells with large facies uncertainty. The discontinuous curve is plotted along the boundary of the cells where a sign change of the facies occurs. We define the cells with facies SD greater than 0.8 as the cells with large facies uncertainty, and label these with black dots in their cell centers.

In each of the above approaches and the considered estimation aspects, the calculated means and SDs using the realisations are used as the measures for describing the quality of estimation and estimation uncertainty, respectively.

7.4.1 Curved and Disconnected Channels

In the case that the permeability field has a curved or disconnected channel, Fig. 7.1 presents the evolution of the log permeability and facies pattern estimates over the history matching period for the curved channel case.

Because of a lack of complete knowledge of the initial state of the reservoir (on day 0), the initial prior permeability field is considered to be quite different from the truth. One can see from Fig. 7.1 that convergence toward the true permeability field is rather slow and after 192 assimilation days (12 assimilation cycles) the facies esti-

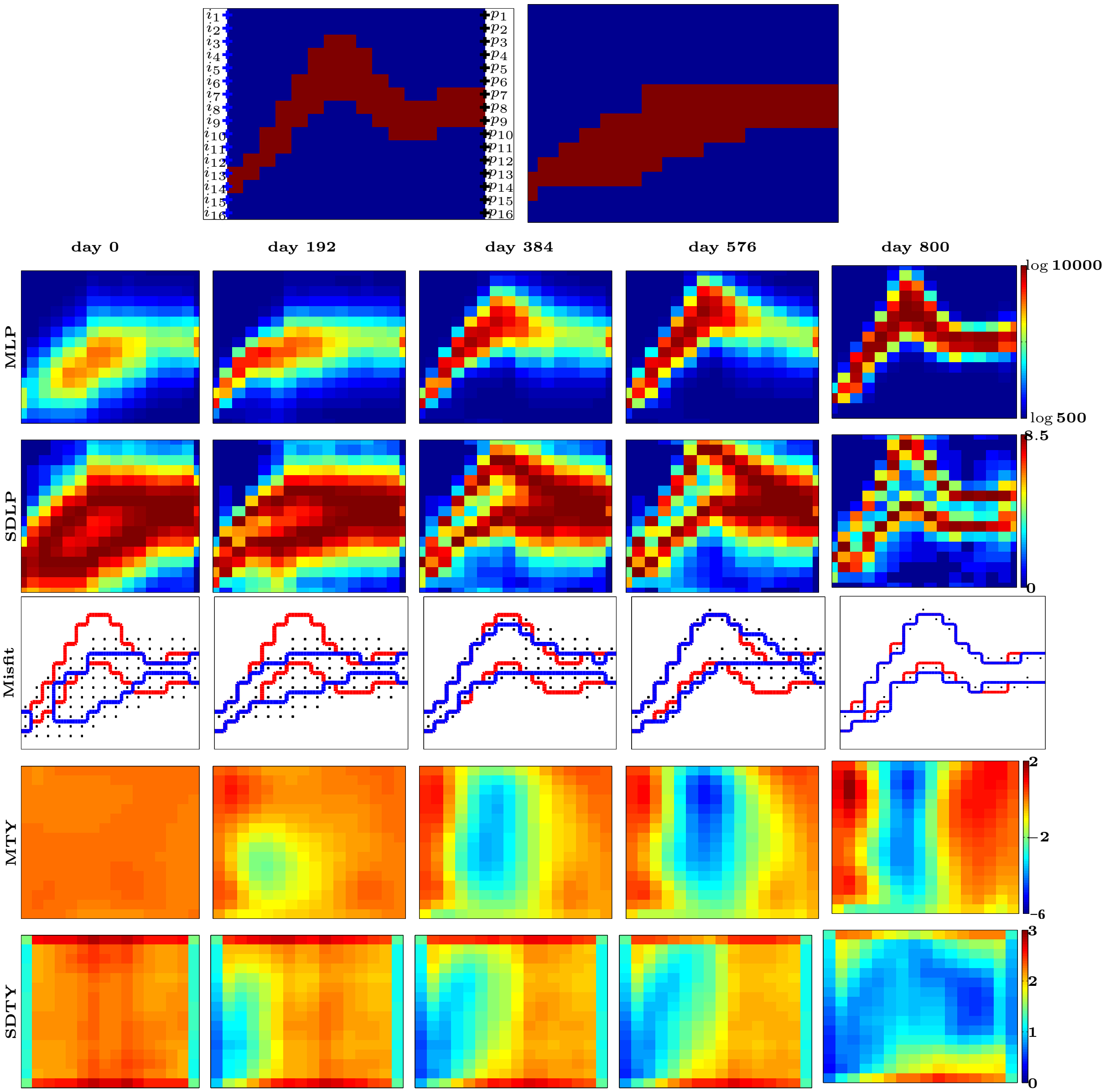

Figure 7.1: The true log permeability field (left panel, first row), the prior log permeability field (right panel, first row), the mean (second row) and SD (third row) of the log permeability field estimates, the misfit of facies pattern (fourth row) and the mean (fifth row) and SD (sixth row) of the transformation estimates in the y direction for the curved channel case. Results are shown at the end of 0^{th}, 192^{nd}, 384^{th}, 576^{th} and 800^{th} days with 600 realisations. The true log permeability field plot presents the cells which the indexed injection (blue pluses) and production (black pluses) wells. The misfit figures show the true (red) and estimated (blue) facies patterns, and the cells with large facies uncertainties (black dots).

mates are still quite different from the true facies. This is due to the limited amount of information (the number of observations) that has been used in the estimation process. The filter however preserves SDs thus indicating large uncertainties on the estimates during that period. As more information becomes available over time, the estimation gradually improves. At the end of the history matching period, the estimated permeability field and facies pattern are almost identical to the true fields. There are only 11 cells showing a mismatch between the estimation and truth, but the truth lies within the estimated uncertainties.

Fig. 7.3 shows typical data assimilation processes in an injection well (no. 7), and three production wells (no. 3, 14 and 16) over time. One can see that the history match is such that the pressures in the injection well and saturations in the production wells have been well reproduced. The uncertainty level (the vertical width of the green lines) provided by the WEnSRF, can be seen to be much smaller than the initial uncertainty level (the vertical width of the magenta lines). Water breakthroughs are not observed in all production wells during the history matching period, but well-predicted in the forecasting period. The true reservoir pressure and saturation behaviour are well predicted and within the uncertainty level for all the other injection and production wells including the ones not explicitly present here.

Similar conclusions can be made from the results in the disconnected channel case as can be seen from Figs. 7.2 and 7.4, which are plotted in the same spirit as Figs. 7.1 and 7.3. During the first 192 days, the estimated log permeability field and facies pattern indicate a disconnected channel, but with a quite large uncertainty. WEnSRF efficiently recovers the true fields in the next 608 days. The corresponding uncertainties further decrease over time and become much smaller than the initial uncertainties. Again, the estimated permeability field and facies pattern are almost identical to the truth at the end of the history matching period, and the truth falls within the estimated uncertainties. Fig. 7.4 further demonstrates that the estimated production data and state of the disconnected channel reservoir are also quite good.

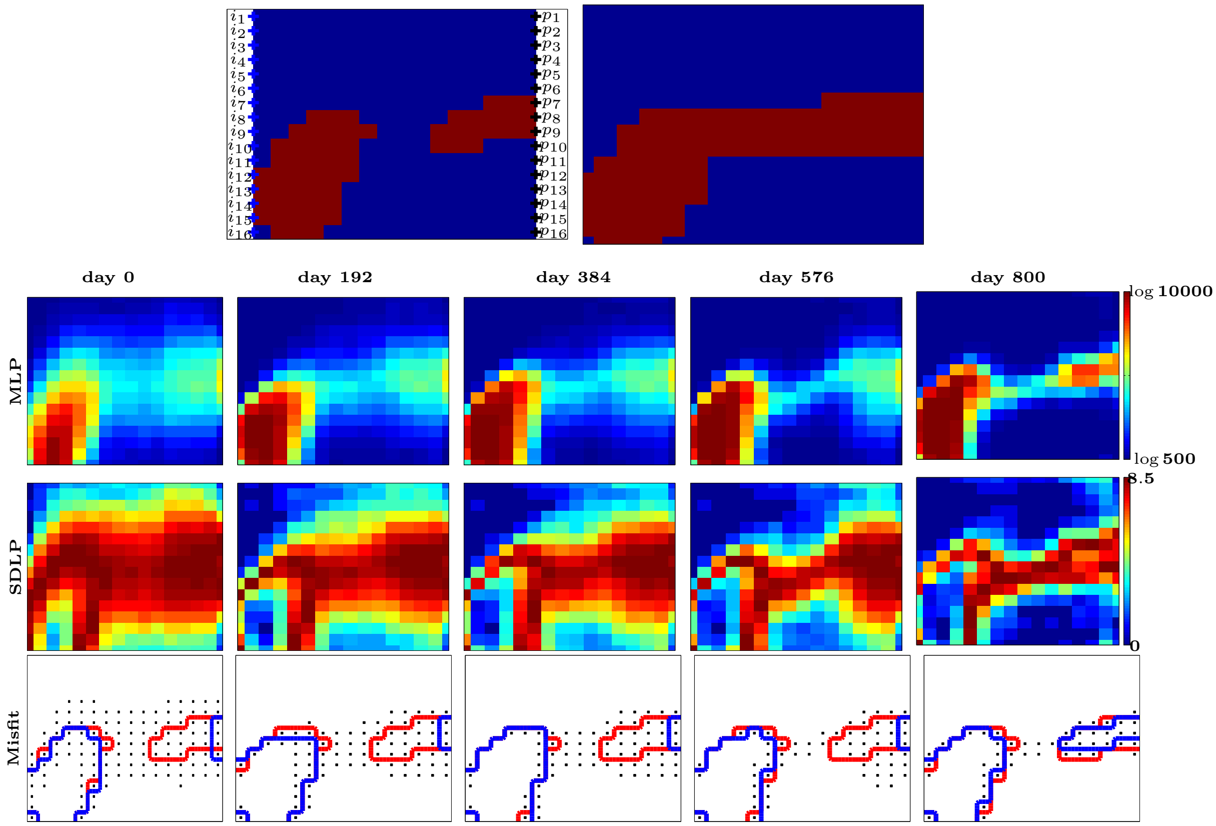

Figure 7.2: The true log permeability field (left panel, first row), the prior log permeability field (right panel, first row), the mean (second row) and SD (third row) of the log permeability field estimates and the misfit of facies pattern (fourth row) for the disconnected channel case. Results are shown at the end of 0^{th}, 192^{th}, 384^{th}, 576^{th} and 800^{th} days with 600 realisations. The true log permeability field plot presents the indexed injection (blue pluses) and production (black pluses) wells. The misfit figures show the true (red) and estimated (blue) facies patterns, and the cells with large facies uncertainties (black dots).

7.4.2 Two-Dimensional Closed Feature

Here, we consider the permeability field with a two-dimensional closed feature (i.e. without any channel feature appearing along the reservoir boundaries). In practical applications, perhaps, some prior information about the existence of a closed feature[6] is available, but not about its shape and location. We therefore deliberately generate a very poor[7] initial ensemble that reflects the reality of these problems.

---

[6] In real application, such information is often found by the core samples in the injection, production or testing wells.

[7] The prior is dogmatic and far from the truth with a large variance.

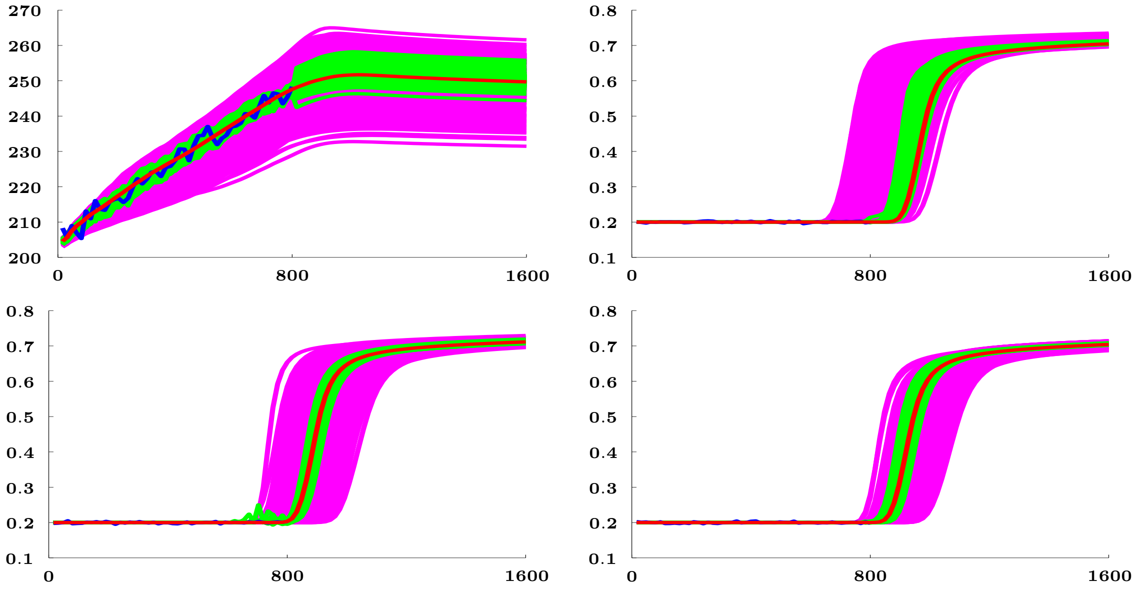

Figure 7.3: Time-evolution of the estimated pressure in injection well no.7 (top left) and the (water) saturation (top right and bottom row) of production well nos. 3, 14 and 16 over the production period for the case of a curved channel with 600 realisations. The figure shows the true states (red), measurements (blue), simulations of the initial ensembles (magenta) and history matched ensembles (green).

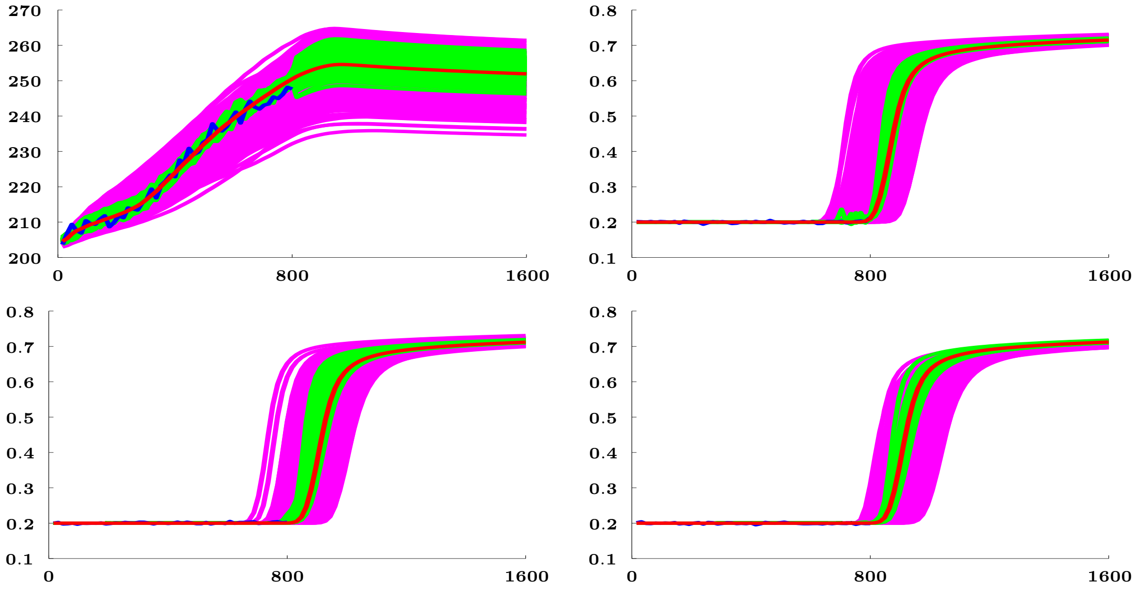

Figure 7.4: Time-evolution of the estimated pressure in injection well no.7 (top left) and the (water) saturation (top right and bottom row) of production well nos. 3, 14 and 16 over the production period for the case of a disconnected channel with 600 realisations. The figure shows the true states (red), measurements (blue), simulations of the initial ensembles (magenta) and history matched ensembles (green).

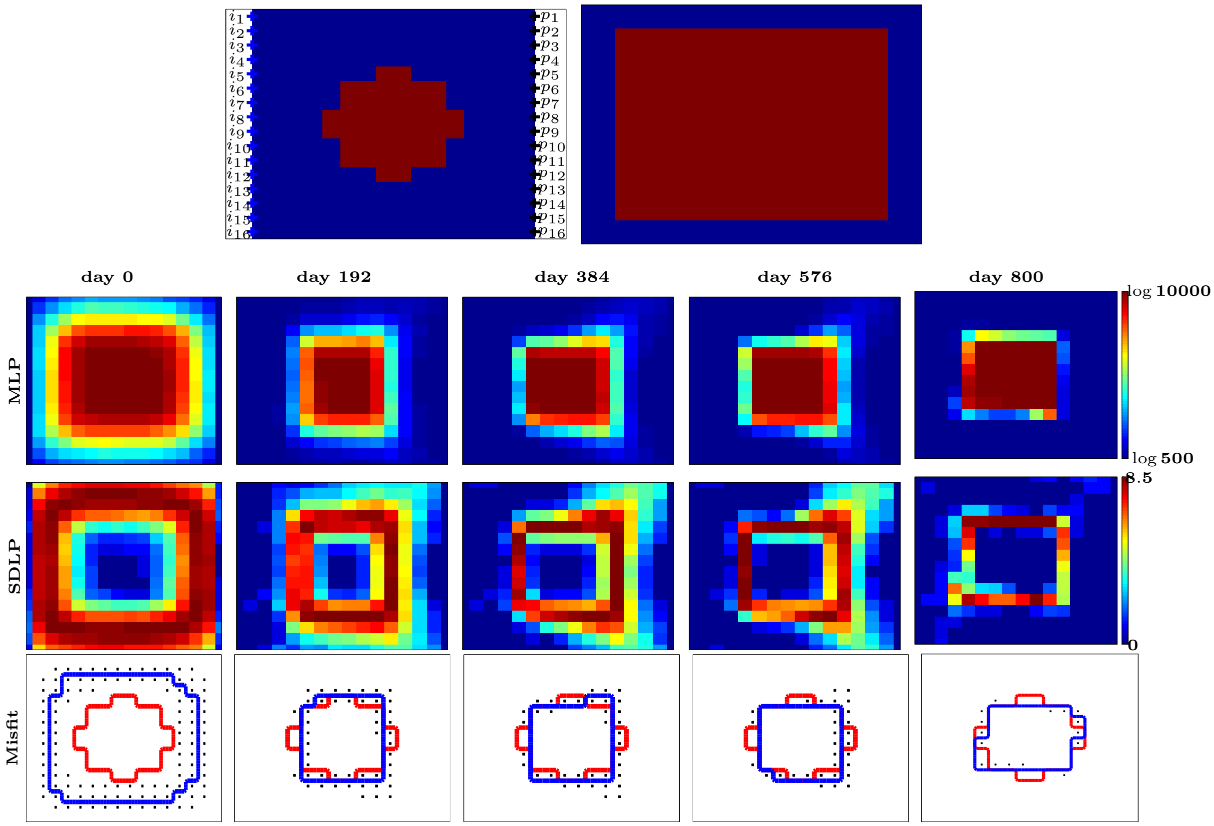

Figure 7.5: The true log permeability field (left panel, first row), the prior log permeability field (right panel, first row), the mean (second row) and SD (third row) of the log permeability field estimates and the misfit of facies pattern (fourth row) for the case of a two-dimensional closed feature. Results are shown at the end of 0^{th}, 192^{nd}, 384^{th}, 576^{th} and 800^{th} days with 600 realisations. The true log permeability field plot presents the indexed injection (blue pluses) and production (black pluses) wells. The misfit figures show the true (red) and estimated (blue) facies patterns, and the cells with large facies uncertainties (black dots).

As in the channel cases, Fig. 7.5 shows that the WEnSRF is capable of recovering the structure of the true fields just after 192 days. Compared to the rapid convergence of the estimates, the uncertainties of the permeability, facies pattern and transformation mapping estimates are quite large in the first 192 days and are continuously reduced as more data becomes available over time. Towards the end of the history matching period, the transformation estimation in Fig. 7.6 and the permeability and facies pattern estimates in Fig. 7.5 further improve and converge. The final estimated permeability is quite similar to the true one. However, there are 9 mismatch

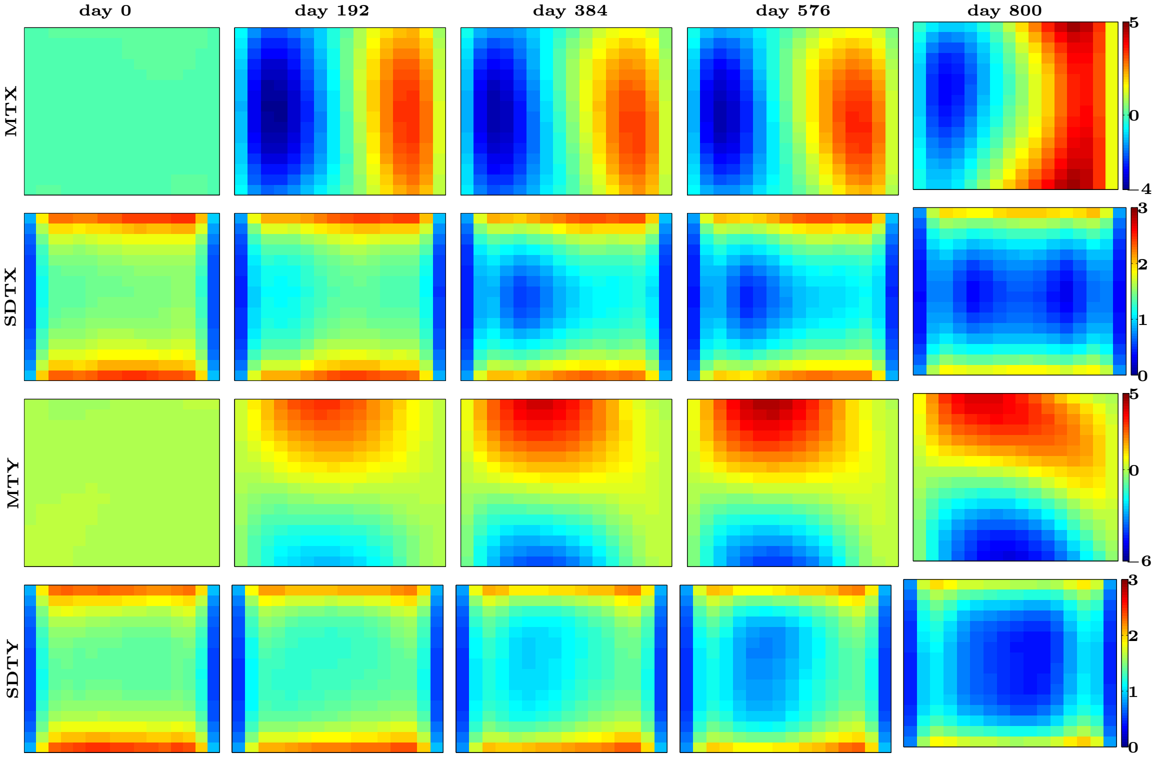

Figure 7.6: The transformation estimates at the end of 0^{th}, 192^{nd}, 384^{th}, 576^{th} and 800^{th} days with 600 realisations for the case of a two-dimensional closed feature. The mean (first row) and standard derivation (second row) of the transformation estimates in the x direction and the mean (third row) and standard derivation (fourth row) of the transformation estimates in the y direction.

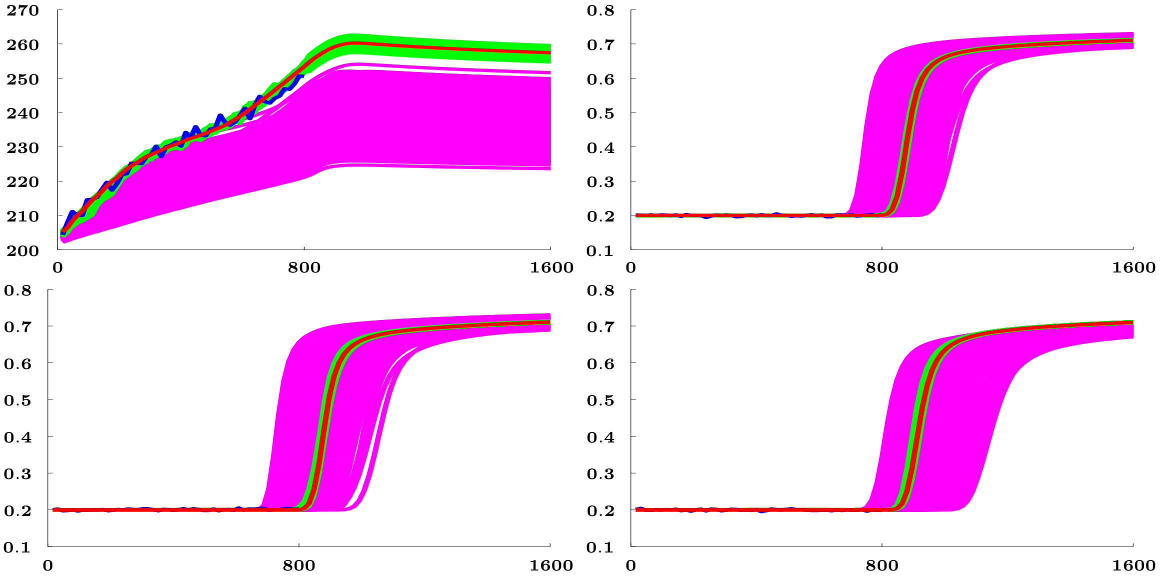

Figure 7.7: Time-evolution of the estimated pressure in injection well no.7 (top left) and the (water) saturation (top right and bottom row) of production well nos. 3, 14 and 16 over the production period for the case of a two-dimensional closed feature with 600 realisations. The figure shows the true states (red), measurements (blue), simulations of the initial ensembles (magenta) and history matched ensembles (green).

cells between the estimated and true fields, in 5 of which the truth is different from the estimate and falls outside the estimation uncertainty. As we have emphasised in many places, the history matching problem is ill-posed, i.e. many different permeability estimates may fit the production data equally well. Indeed, this is the biggest challenge in estimating the detailed shape (four prominences along the feature boundaries) of this considered feature. Similar results (with one mismatch cell) have also been reported for a similar experiment using B-spline parameterisation on the feature boundaries directly and EnSRF in [48].

Fig. 7.7 shows the time-evolution of the assimilated processes in the injection well no. 7 and three production wells nos. 3, 14 and 16. Despite the facies mismatch in some cells, history matching has been achieved very well. The typical behavior of the sequential assimilation system is again observed (as in the channel cases) with an uncertainty increase after every prediction step before it gets corrected with the new observations in the analysis step of WEnSRF. Similarly good results are obtained for the other injection and production wells.

7.4.3 Sensitivity to Ensemble Size

As we have stated in the introduction of this chapter, estimating the facies pattern of a large-scale real reservoir is one of the desirable goals for the proposed WEnSRF. Application of the WEnSRF incurs demanding computational costs for integrating the ensemble forward in time. This sets severe limits on the size of the ensemble that can be used in practice. However, an ensemble with few realisations can impair the performance of the filter analysis. Balance between the quality of the estimate and acceptable computing resources should therefore be found. Here, we test the assimilation system with a smaller ensemble size, conducting the same experiments as in §7.4.1 and §7.4.2 but using only 100 ensemble realisations. Note that it takes a laptop with an Intel duo processor P8800 and 2 gigabytes of memory around 4 hours to complete the history matching process when the WEnSRF is implemented with 100 realisations and around 24 hours with 600 realisations in Matlab.

Figs. 7.8 and 7.9 present the misfit figures and history matching results of the well data, respectively. One can see from Fig. 7.8 that although the structure and the uncertainty of the initial ensemble are similar to the corresponding processes with 600 realisations, the evolution of the estimation is very different. In contrast with the assimilation process with 600 realisations, the number of cells with larger facies uncertainty are reduced faster using 100 realisations over the time. At the end of the history matching period, the estimated permeability fields (Fig. E.4-E.9 in Appendix E) contain more mismatch cells compared to the estimates obtained with 600 realisations. In Fig. 7.9, the uncertainty level resulting using 100 realisations is also much smaller than the one resulting using 600 realisations. The true pressure and saturation, however, lie within the uncertainty level in each well.

We consider the following three measures to compare the results of the two runs:

1. *Permeability Mismatch*:

   The number of permeability cells that fall outside the estimated uncertainty range.

2. *Pressure/Saturation Coverage*:

   The normalisation (percentage) of the number of time steps for which the true pressure in all injection wells (or saturation in all production wells) falls within the estimated uncertainty range over the total number of time steps and the total number of injection (or production) wells.

3. *Pressure/Saturation Average Uncertainty*:

   The SD of the pressure in injection wells (or saturation in production wells) averaged over all time steps and all injection wells (or production wells).

Comparison results of these measures for the WEnSRF assimilation with 100 and 600 realisations are presented in Table 7.2. In terms of predicting the reservoir

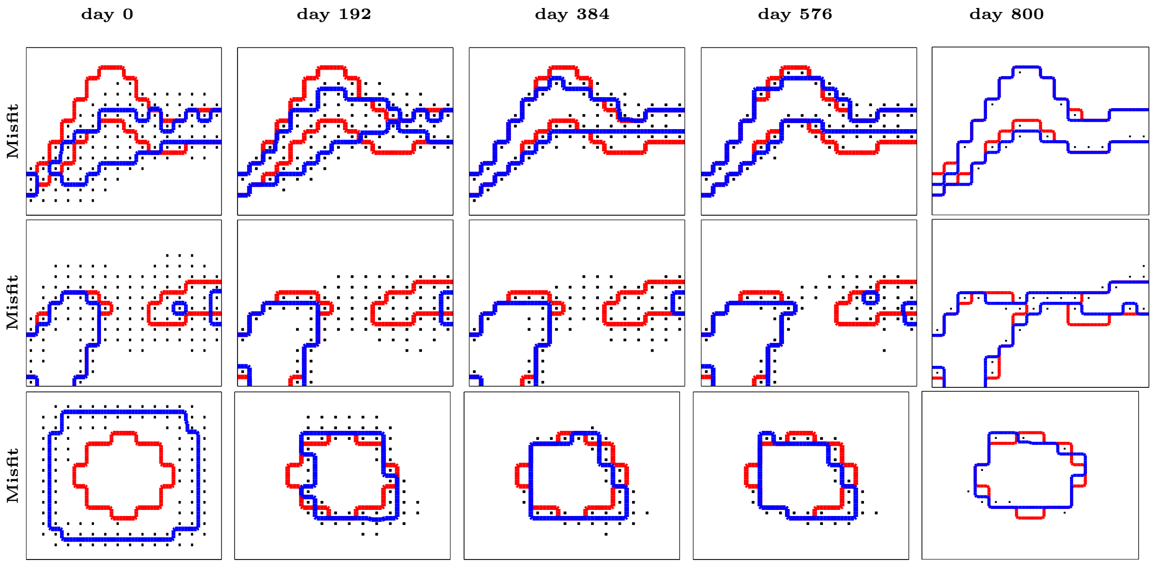

Figure 7.8: The misfits of facies pattern for cases of a curved channel (top row), a disconnected channel (middle row) and a two-dimensional closed feature (bottom row). Results are shown at the end of 0^{th}, 192^{nd}, 384^{th}, 576^{th} and 800^{th} days with 100 realisations. The true facies pattern (red), the estimated facies pattern (blue), and the cells with facies standard deviation greater than 0.8 (black dots).

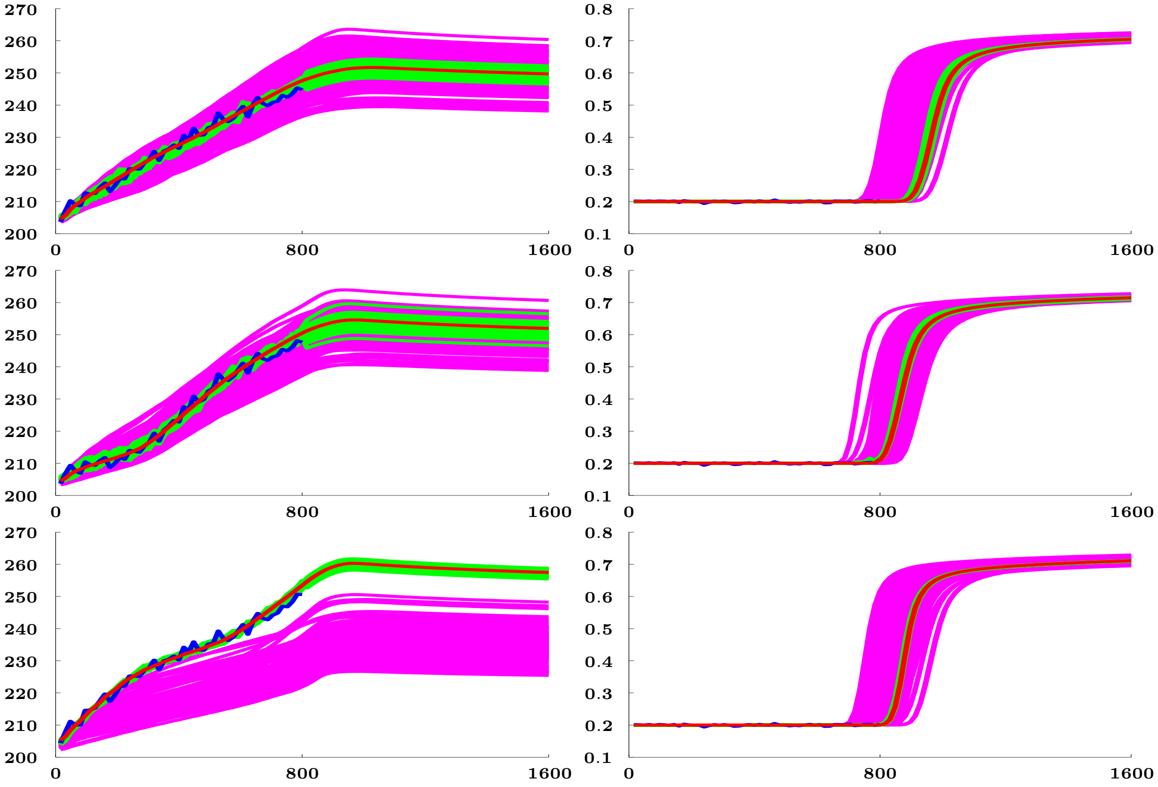

Figure 7.9: Time-evolution of the pressure simulation in injection well no.7 (left) and the (water) saturation simulation (right) of production well nos. 3 over the production period for the cases of a curved channel (top row), a disconnected channel (middle row) and a two-dimensional closed feature (bottom row) with 100 realisations. The figure shows the true states (red), measurements (blue), simulations of the initial ensembles (magenta) and history matched ensembles (green).

		Reservoir Type					
		Connected Channel		Disconnected Channel		Closed Feature	
Number of realisations		600	100	600	100	600	100
Permeability Mismatch		0	4	0	6	5	7
Coverage	Pressure	100%	99.2%	100%	99.2%	100%	98.9%
	Saturation	100%	94.8%	100%	97.1%	100%	100%
Average Uncertainty	Pressure (Bar)	7.5	4.0	7.6	6.1	4.1	2.6
	Saturation	0.046	0.015	0.043	0.002	0.012	0.006

Table 7.2: Measures of the permeability mismatch, production data coverages, and average uncertainties as they result from the WEnSRF using 600 or 100 realisations.

behaviour, both runs lead to very similar (almost perfect) results with data coverages above 94%. However, in terms of reservoir risk and management, WEnSRF with 100 realisations significantly underestimates the average uncertainties. Concerning the quality of the permeability estimates, more mismatched cells are obtained using the WEnSRF with 100 realisations.

To conclude, by reducing the ensemble size containing 600 realisations in the initial tests to only 100 realisations, both the quality of the permeability estimation and the uncertainty quantification degraded slightly. However, achieving only one sixth of the computational time compare to assimilation using WEnSRF with 600 realisations and almost equivalent estimation results, WEnSRF with 100 realisations is preferable for the application to large-scale history matching problem of facies patterns.

7.5 Numerical Experiments on Large-Scale Complicated Reservoir Models with Complicated Features

Two numerical experiments are carried out to test the performance of the WEnSRF in history matching production data from large-scale reservoir models and to evaluate the potential applicability of WEnSRF to real-world reservoir models.

The reservoir is square and horizontal with constant thickness and no-flow outer boundaries. Again, the coordinate system is set up with the origin located at the south-west corner where the x–axis is pointing east and the y-axis is pointing north. The water flooding experiment is adapted. The pressure data in the injection wells and the saturation data in the production wells are used for history matching.

Follow the same experiment setup in §7.4, indices of the injection and production wells are labelled increasingly (1-45) from north to south at the cell centres along the west and east boundaries of the reservoir, respectively. The relative permeability functions are defined by the Corey models in eqs. (7.1a,b). The numerical values of the reservoir properties are listed in Table 7.10. Note that the dimension of the state vector[8] is 10221 and is much larger compared to the state vector in the last section.

Prior to history matching, we assume a training image as shown in Fig. 7.11, which consists of two distinct facies types and describes the reservoir (channel) structure and (complicated) geometry, has been provided. The permeability along the west and east boundaries of the reservoir (where the wells are drilled) is assumed known and is conditioned to generate the true permeability field and realisations of the prior permeability field library by applying the Single Normal Equation SIMulation (SNESIM) [36, 63, 64, 151] to the given training image. The test cases utilise permeability fields with a rotated H (the left realisation in the top row) or Z shaped channel (the right realisation in the top row) as the reference 'true' permeability fields and the (five) test realisations as the realisations of the prior permeability field library.

For each reference permeability field we simulate the 'true' values of saturation and pressure for each time step going forward in time. Synthetic measurements are made by perturbing the true states with random noise drawn from an uncorrelated Gaussian distribution with zero mean. The SDs of the pressure measurement noise

---

[8] $2 \times 45 \times 45$ for the pressure and saturation discretisation, $2 \times 6 \times 8$ for the B-spline control nets and $3 \times 45 \times 45$ for the exact porosity, mobility and initial permeability field.

Reservoir dimensions:	450m × 450m × 10m	
Simulation grid:	45 × 45 × 1 cells	
Facies permeability (mD):	$\kappa_h = 10000$	$\kappa_l = 500$
Porosity:	0.2	
Viscosity (cP):	$\mu_w = 1$	$\mu_o = 10$
Density (kg/m^3):	$\mu_w = 1000$	$\mu_o = 700$
Endpoint relative permeability:	$\hat{\kappa}_{rw} = 1$	$\hat{\kappa}_{ro} = 1$
Residual saturations:	$S_{wr} = 0$	$S_{or} = 0$
Corey exponents:	$e_w = 2$	$e_o = 2$
Initial saturations:	$S_w = 0$	$S_o = 1$
Injection rate (m^3/D):	270 (24% of total pore volume per year)	
Production wells:	constant pressure of 1 bar	
Number of timesteps:	100	
Total production time:	200 days	

Figure 7.10: Key properties in the reservoir simulator.

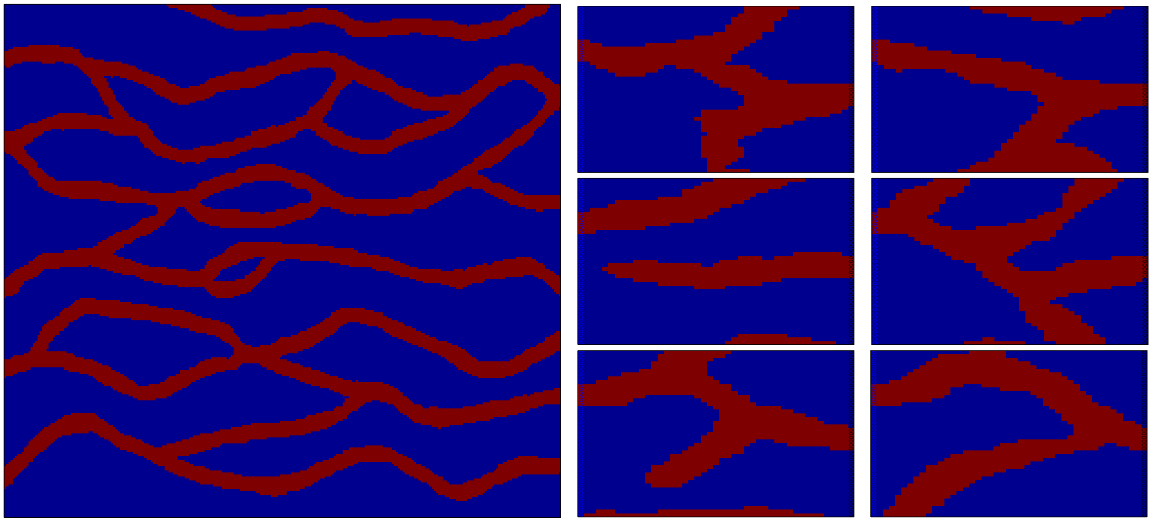

Figure 7.11: The training image (large figure in the left panel) and six simulated realisations (small figures in the right panel) using the SNESIM and conditioned on the permeability along the west and east boundaries of the reservoir.

in the injection wells and the water saturation measurement noise in the production wells are 20 bar and 0.01, respectively. History matching is then performed every 2 days and over a 100 day period. The realisations of the estimated permeability field are then used to predict the reservoir behaviour for another 100 days.

Using the conclusion and results from the sensitivity test of the ensemble size in §7.4.3 and considering the significant dimensional increment of reservoir model (compare to the reservoir model in §7.4), it is appropriate to utilise an ensemble of 100 realisations for each realisation of the permeability field library and assimilate the measurements on each ensemble of realisations. This is equivalent to 5 parallel WEnSRF runs with 100 realisations in each one.

We (again) adapt the MLP and SDLP for quantifying the log permeability estimation and estimation uncertainty, respectively, and the misfit figures for the facies pattern estimation and uncertainty as in the last section. When calculating the described measures and quantifying the reservoir state uncertainties, the realisations of all the (500) reconstructed fields must be used.

Fig. 7.12 presents the evolutions of the permeability field and facies pattern estimates over the history matching period for the case of a Z shaped channel. Because of the lack of knowledge of the spatial reservoir properties (on day 0), all realisations of the prior permeability field library are considered to be quite different from the true one. The convergence toward the true permeability field is more rapid in the first 76 days (38 assimilation cycles) and then becomes gradual in the last 24 days of the history matching period. This is because water cut and more informative saturation measurements in some of the production wells (see Fig. 7.14) occur between day 24 to 76 (and does not occur in any production well in the last 24 days). During the history matching period, the Z shaped channel is not only estimated by the MLP, but also confirmed by the SDLP which is gradually reduced and becomes small in most of the low permeability shale-rock cells. At the end of history matching, the estimated permeability field and facies pattern are very similar to the true fields. Only 8 cells show significant mismatch between the estimated and true permeability.

Fig. 7.14 shows the typical data assimilation process in one injection wells (no. 13) and three production wells (nos. 13, 28 and 40) over time. The reservoir behaviour have been well reproduced and predicted with greatly reduced uncertainties compared to simulations uncertainty using the initial ensemble. Similar good results are also

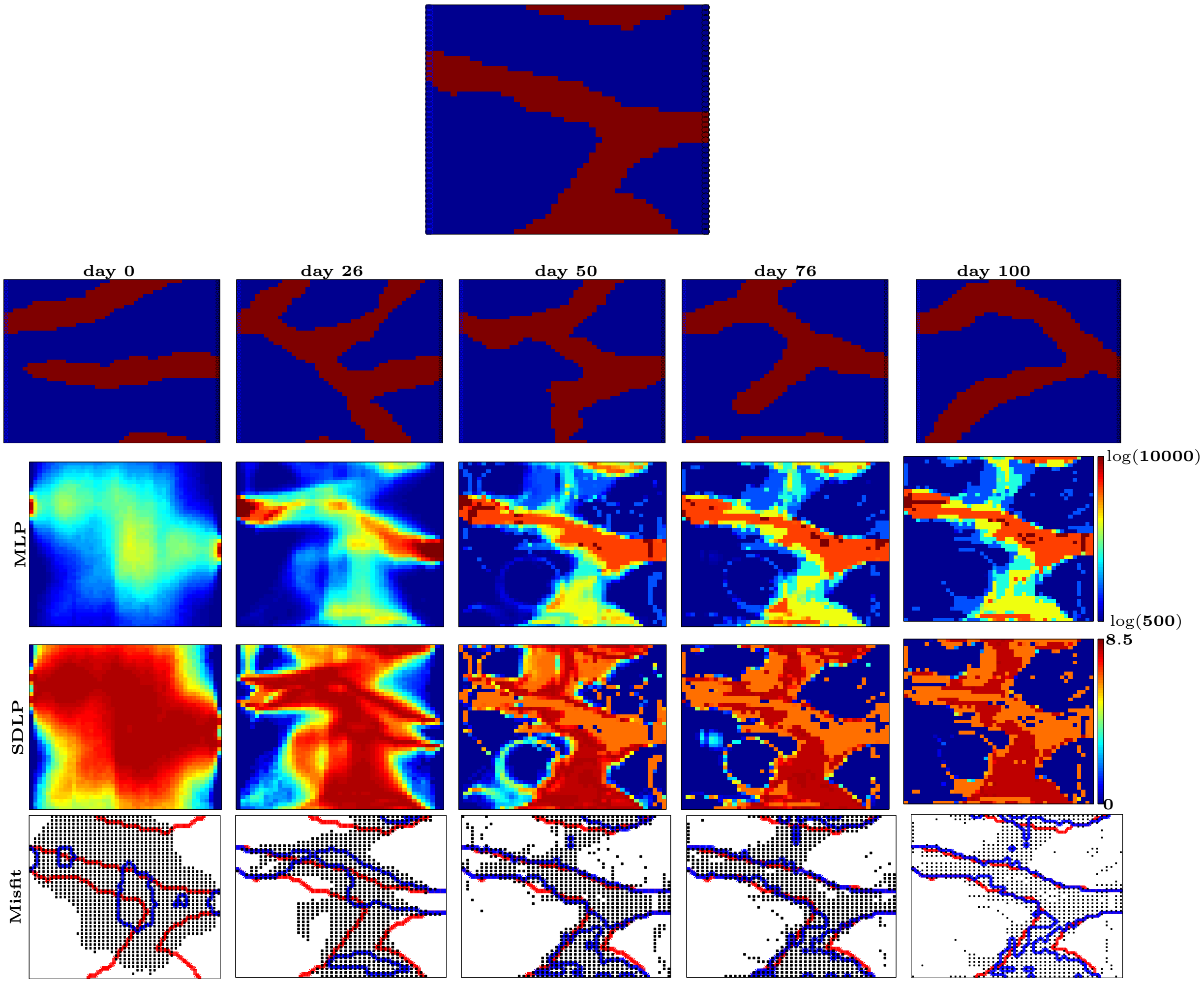

Figure 7.12: The true permeability field (top), realisations of the initial prior permeability library (second row), mean (third row) and SD (fourth row) of the log permeability field estimates and misfit of facies pattern (fifth row) for the case of a Z-shaped channel. Results are shown at the end of 0^{th}, 26^{th}, 50^{th}, 76^{th} and 100^{th} days using WEnSRF with 100 realisations for each realisation of the prior permeability library. The true permeability field plot presents the injection (blue circles) and production (black circles) wells. The misfit figures show the true (red) and estimated (blue) facies patterns, and the cells with large facies uncertainties (black dots).

obtained for the other injection and production wells.

Similar conclusions can be made from the results in the case of a rotated H shaped channel as can be seen from Figs. 7.13 and 7.15 (plotted in the same spirit as Figs. 7.12 and 7.14). During the first 50 days, the estimated log permeability field and facies pattern indicate a rotated H shaped channel, but with quite large uncertainties. The

WEnSRF efficiently recovers the true fields in the rest of the history matching period. The corresponding uncertainties further decrease over time and are much smaller than the initial uncertainties. Compare to the case of a Z shaped channel, the convergence toward the true permeability field is more rapid in the first 50 days due the early water cut (see the number of cells with large facies uncertainties in the misfit figure plot in Figs. 7.12 and 7.13) and more informative saturation measurements in some of the production wells (see Fig. 7.15). Again, the history matched permeability field and facies pattern are very similar to the truth at the end of the history matching period with only 5 cells fall outside the estimation uncertainty. Fig. 7.15 further demonstrates that the reservoir states is well reproduced and predicted.

7.6 Conclusion

The aim of this chapter is to develop a general, efficient and robust method based on the newly-developed Warp Ensemble Square Root Filter (WEnSRF) for history matching facies patterns - a problem for which an approach such as a conventional ensemble Kalman filter, is not immediately applicable. This is because the variable representing the facies is a discrete variable, and hence non-differentiable and non-Gaussian. By a proper representation of the warping transformation between the prior and true permeability fields using a continuous B-spline surface parameterisation, the WEnSRF transformed the history matching problem for facies patterns into an estimation problem with continuous variables parameterising the warping transformation which can then be solved using an ensemble-based Kalman filter.

We conducted numerical experiments using reservoirs, with two facies types, various scales and both simple and complicated structures. Starting from vague priors, the WEnSRF efficiently recovered the true facies pattern at the end of the history matching period. The uncertainties in the estimated state and model variables condi-

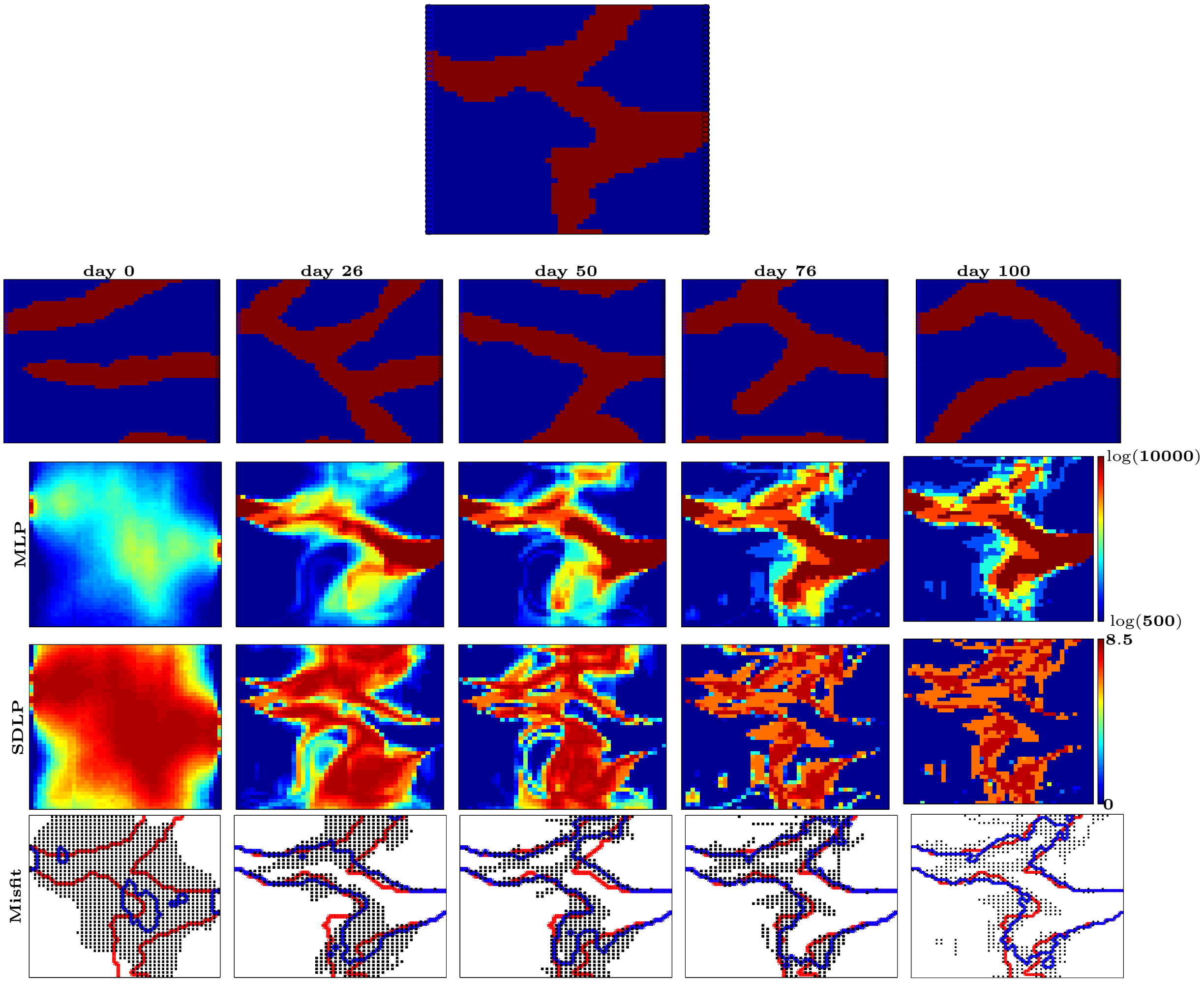

Figure 7.13: The true permeability field (top), realisations of the initial prior permeability library (second row), mean (third row) and SD (fourth row) of the log permeability field estimates and misfit of facies pattern (fifth row) for the case of a rotated H-shaped channel. Results are shown at the end of 0^{th}, 26^{th}, 50^{th}, 76^{th} and 100^{th} days using WEnSRF with 100 realisations for each realisation of the prior permeability library. The true permeability field plot presents the injection (blue circle) and production (black circles) wells. The misfit figures show the true (red) and estimated (blue) facies patterns, and the cells with large facies uncertainties (black dots).

tioned on the data are also substantially reduced compared to the initial uncertainties. The results of the different experiments demonstrate that the proposed method is efficient, robust and applicable to large-scale real-world problems, and is able to provide accurate and improved estimates of the reservoir structure and behaviour.

The WEnSRF requires prior permeability fields to provide the prior information

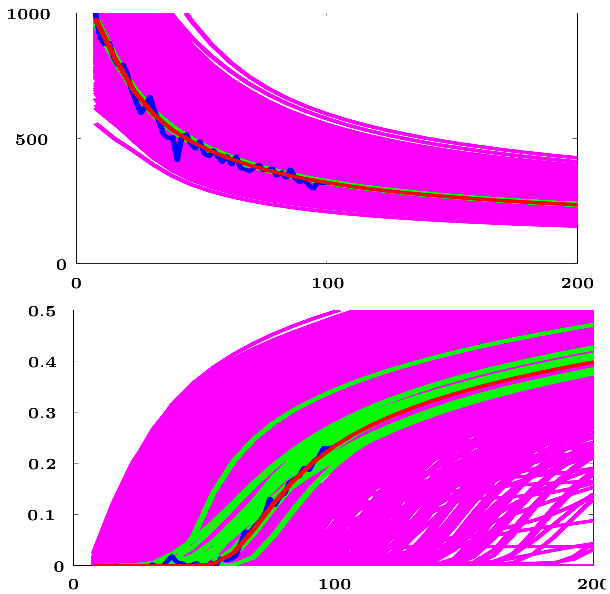

Figure 7.14: Time-evolution of the estimated pressure in injection wells no. 13 (top left) and the (water) saturations of production well nos. 13, 28 and 40 (top right, bottom left and right) over the entire production period for the case of a Z-shaped channel. The figure shows the true states (red), measurements (blue) and simulations of the initial ensembles (magenta) and history matched ensembles (green).

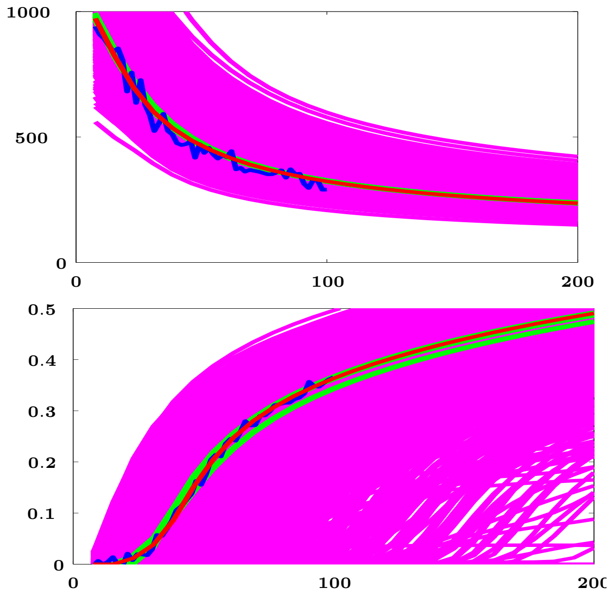

Figure 7.15: Time-evolution of the estimated pressure in injection wells no. 13 (top left) and the (water) saturation of production wells nos. 13, 28 and 40 (top right, bottom left and right) over the entire production period for the case of a rotated H-shaped channel. The figure shows the true states (red), measurements (blue) and simulations of the initial ensembles (magenta) and history matched ensembles (green).

for the exact number of facies types and the geological structure and to quantify the structural uncertainty (if a prior permeability fields library is used). The WEnSRF might not be able to provide reliable estimate if the prior permeability fields fail to reasonably capture the exact underlying physics or geological features due to the smooth transformation constraints between the estimated and prior permeability field imposed by warping using B-spline surfaces.

Chapter 8

Conclusions and Future Work

As we have introduced in Chapter 1, inverse problems are ubiquitous. Yet, the solution methods for many of them still lack efficiency and robustness. With so many open questions in real world applications, research in this field has been very attractive for at least the last two decades as forward simulation methods have matured. The main objective of this thesis is to develop ensemble-based Bayesian filters with a low computational cost for the barcode detection problem, the deconvolution problem in well testing and the history matching problem of facies patterns. This final chapter summarises the main results that we have obtained before highlighting some of the outstanding problems which require further work.

8.1 Review of Thesis

In this thesis, we have formalised three inverse problems: the barcode detection problem, the deconvolution problem in well testing and the history matching problem of facies patterns. Our work on the barcode detection problem in Chapter 5 was carried out with inspiration from Wittman and Esedoglu [54, 55, 173]. It was demonstrated that the inverse-problem-based barcode detection approach, as proposed in their papers, lacks robustness and computational efficiency for real applications. Our work on the deconvolution problem in well testing in Chapter 6 was carried out with inspiration from industrial companies: Paradigm and Ente Nazionale Idrocarburi. In particular, clear and strong evidence in [6] has been presented to demonstrate that the non-Bayesian methods in commercial software fail to meet industrial needs. Our work on history matching of facies patterns using the Warping Ensemble Square Root Filter (WEnSRF) in Chapter 7 is inspired by our earlier research [48] with focus on the applicability and performance for real-world problems.

Chapter 1 began with a general description and formulation of inverse problems before a summary of the Bayesian approach for solving inverse problems. The non-technical backgrounds of the three considered inverse problems and brief description of the Bayesian approaches for solving them were introduced.

The mathematical modelling and formulation of the considered inverse problems are derived in Chapter 2. The state-space system, which summaries the model and measurement processes of a considered physical system, is first introduced and used to rigorously formulate the inverse problems. For the formulation of the barcode detection problem, we modified the existing barcode signal model from barcode laser scanning to model blurry barcode images. For the deconvolution problem in well testing, we derived Duhamel's principle, which describes the convolution relationship between the wellbore pressure, flow rate and type curves, and extended it to based on the Log-Log Derivative Type Curve (LLDTC). For the history matching problem of facies patterns, we started with mathematical modelling of two phase flow in porous media under the considered configuration and then derived the Finite Volume reservoir simulator (Appendix A) in seeking a numerical solution.

Chapter 3 provided the foundations of the Bayesian filtering methods in this thesis. We started with the recursive Bayesian filter which defines the exact posterior pdf and derived its well-studied approximation using ensemble of realisations: the Ensemble Square Root Filter (EnSRF). The EnSRF is not directly adaptable to our considered problems. For the barcode detection problem and the deconvolution problem in well testing, accurate measurements and less-informative or biased initial prior in real applications lead to practical difficulties in approximating the posterior pdf using a feasible number of realisations, because of the insufficient likelihood weights associated with the predictive prior realisations. To overcome this difficulty, the Iterative Ensemble Square Root Filter (IEnSRF) - an approximation to the iterative Bayesian filter, is derived. It is essentially an iterative formulation of the EnSRF. For the history matching problem of facies patterns, the Warp Ensemble Square Root Filter (WEnSRF) is designed specifically to overcome the incompatibility in estimating the non-Gaussian discrete facies variable with the direct EnSRF implementation and to provide efficient updates of the features by estimating the warping transformation between the prior and estimated permeability field using the EnSRF.

Chapter 4 formed the foundations of the prior construction and the parameterisation of the model variables in solving the considered inverse problems. For solving the barcode detection problem, assuming the barcode is black-and-white only, the level set parameterisation of the barcode stripes is first introduced. The concept of B-splines formed the core of prior construction and parameterisation. The unclamped B-spline function is proposed to parameterise the LLDTC in the deconvolution problem in well testing using the prior information of the smoothness of the analytical LLDTC, while the B-spline surfaces are proposed for parameterising the warp transformation mapping in the WEnSRF with the assumption of a smooth transformation between the prior and estimated permeability field.

In Chapter 5, we studied the barcode detection problem using the blurry image (due to both out-of-focus shooting and poor printing) in both synthetic and real scenarios. The problem is solved using the IEnSRF with a level set parameterisation of the barcode stripes. Comprehensive numerical experiments were carried out and the results using IEnSRF were compared against some of the well-known existing methods and commercial software. At the expense of overestimating the posterior uncertainty for real-world applicability, the IEnSRF efficiently achieves successful detections with very challenging real barcode images which the other considered methods and commercial software fail to detect. It also demonstrates great reliability and robustness in detecting low-resolution images under poor ambient light conditions.

In Chapter 6, the deconvolution problem for well-test data was solved using the Iterative Deconvolution Method (IDM). The IDM utilises the IEnSRF as the core to update the B-spline parameterisation of the LLDTC and thus is capable of quantifying estimation uncertainty, incorporating the cumulative production data and estimating the initial pressure, which were thought to be unachievable in the existing well testing literature. The capabilities, performance and robustness of IDM were demonstrated using numerical experiments with well-test data from one synthetic oil reservoir, one real gas reservoir and one real oil/gas reservoir, and were shown to significantly outperform the existing methods in the commercial software.

In Chapter 7, the WEnSRF was utilised for solving the history matching problem of facies patterns. The WEnSRF requires explicit prior information[1] regarding the existence of a feature and the structural complexity and uncertainty. (Failing to enclose reliable prior information can lead to degraded estimates.) Its performance is thus superior in estimating the large-scale complicated facies patterns. Through numerical experiments with three small-scale representative reservoirs and two large-scale complicated reservoirs, the WEnSRF is shown to be robust and efficient and is able to provide accurate estimates of the reservoir properties.

8.2 Future Research

Several important research questions are raised in the review of this thesis. Some of these lead to future research directions. In general, a Bayesian solution for the inverse

---

[1] Such information is often absent in real application. It is a great challenge to build such prior.

problem is achieved in three steps: prior construction, taking realistic observations, and merging the prior with the observations using Bayes' rule. We briefly discuss the research directions addressing various aspects of each of these steps.

8.2.1 Prior Construction

It is believed by many researchers that a robust Bayesian method should provide reliable variable estimation and adequate posterior approximation even if the prior is general and non-informative. However, in our opinion, such a goal often requires infeasible computational resources and amounts of measurements in real applications[2]. It is important to appreciate that reliable and informative priors help variable estimation to be achieved more efficiently and the posterior to be more informative.

In the deconvolution problem in well testing, the initial prior of LLDTC is extracted from data. In the history matching problem of facies patterns, both the prior permeability field and the initial prior for the transformation mappings of the WEnSRF must be specified based on our knowledge about the reservoir. For both problems, it can be seen that the initial priors generated using the described procedures are quite different from the underlying true model and with a significant inherent uncertainty. Significant calibration is required using the measurements. Further work is needed to find a systematic way of constructing improved priors for solving these problems.

Prior construction involves specifying the prior information and incorporating the knowledge of the characterisation of the underlying model physics. Although representing all the model physics is important for reliable simulation and prediction, it normally increases the non-uniqueness of the inverse problem and the computational requirements. Instead, only the important model characterisation should be used in the inverse problem for a more realistic and well-structured sampling strategy for the posterior estimation. It is crucial that this characterisation captures the true physics.

---

[2] The underlying mathematical model is normally complicated and highly nonlinear.

In the barcode detection problem, although the key model characteristic such as the guard bars, the code indicators and the logic of the barcode stripes have already been incorporated, further work is required to merge the information of the product-digit-to-code mapping into the prior to achieve better efficiency and accuracy. In history matching problems of facies patterns, the exact information of facies and configuration of features are key, and have to be well-captured. However, when solving the history matching problem in general, the key characterisation is normally not easily identified without a time-consuming sensitivity test. Further work is needed to seek an efficient and robust way to sift and weigh the key model characteristics and find a reliable and systematic way of incorporating them in the prior.

8.2.2 Observation Uncertainties and Model Accuracy

In the oil industry, it has been a major area of research to develop more accurate devices for both the bottomhole pressure and multi-phase flux monitoring. However, from a Bayesian point of view, starting from the same prior, the posterior resulting from incorporating a single very accurate measurement can be the same as the one resulting from incorporating a few less accurate measurements (as shown in the derivation of the Iterative Bayesian Filter in §3.4.1). With the consideration of the cost of introducing and maintaining newly-developed devices for more accurate measurements, future research is required to develop an optimal measuring scheme to minimise the cost of making (accurate and less accurate) measurements while collecting information for the required quality from the investigated system.

In real applications, several sources of uncertainty are observed in the description of inverse problems. An inappropriate mathematical model, which is incapable of presenting these uncertainties, can harm the filtering method and estimation results severely. As demonstrated by the out-of-focus barcode image taken under lamps in Fig. 5.1, the image brightness due to ambient light is clearly non-uniform which was not considered in the mathematical model[3]. Similarly, as discussed in §2.5, there are several sources of uncertainty present in reservoir description which might not be considered in our simple reservoir model (2.38a-f). Future research is required to develop more adequate mathematical models for blurry barcode images under real-world conditions and more-capable reservoir models to ensure the performance of the filtering method and the quality of the estimation and prediction.

8.2.3 Ensemble-based Filtering Method

All the filtering methods introduced and utilised in this thesis are based on the Kalman update equation which only involves matrix operations and is thus computationally superior to the more rigorous filtering methods (such as the Iterating or Regularised Particle Filter)[4]. It is discussed and showed in [59], although the rank of the analysed ensemble covariance can be preserved using n_x+1 (i.e. one more than the dimension of the state variable) realisations (at minimum) in the Kalman update (if the forecast ensemble covariance is full-rank), with nonlinear model, there is no guarantee that the nonlinear transformations will preserve the rank of the forecast ensemble covariance. Without a sensitivity test, the number of realisations required for quantifying the uncertainty is yet unclear[5]. A large ensemble might provide a good uncertainty quantification, but might also require impracticable computational times or resources (e.g. for the barcode detection problem, detection time is important for practical applicability). On the other hand, too small an ensemble results in uncertainty underestimation and even filter divergence. Further research is required to uncover the relationship between the number of realisations required in an ensemble-based filter and the dimension (or nonlinearity) of the state-space system.

---

[3] In this uncomplicated case, a simple linear modification accounting the considered real-world situation to the mathematical model or a simple bandpass filter preprocessing to the data without modifying the mathematical model can be used to solve the problem.

[4] The randomised maximum likelihood method [31] is able to take the computational advantage of EnKF (when computing the descent direction) and rigorously sample the posterior [60].

[5] The required ensemble size seems to vary from one physical system to another.

Although the Kalman update equation is computationally efficient, it relies entirely on the prior sample covariance to provide a Gaussian approximation of the posterior and estimate the unobserved states and parameters (using correlations). The Kalman update equation is derived assuming a Linear-Gaussian state-space system, which is clearly not the case for the considered inverse problems. Yet, as demonstrated here and in a variety of applications (as referenced throughout), ensemble-based filtering methods using the Kalman update equation work surprisingly well. This leads to the question "Is there a better analysis equation than Kalman update equation, such that improved estimation performance or better computational efficiency arises." or "Could we find a rigorous filtering method that provides results as good as the ensemble-based methods with a similar computational cost?"[6].

8.2.4 Other Industrial Applications

The IEnSRF and WEnSRF proposed in this thesis, are general and shown to be robust and efficient for the considered inverse problem. The state-space formulation for the considered inverse problem are also used in a variety of industrial applications. The proposed methods are thus able to provide Bayesian solutions which are not presented in the existing literature. Here, we highlight two important inverse problems:

Deconvolution Problem in Seismic Processing

The nature of transitions in the subsurface is estimated by measuring the time, location and magnitude of the reflected waves at the surface, which were sent out with a known form by a source (e.g. a thumper truck on land or an air gun at sea) at a given location. The reflected seismic waves sample regions of geological [81], geophysical and rock-physical interest [82]. However, when seismic waves travel in the subsurface, they are not only reflected at transitions, but they also deform, attenuate

---

[6] The recent and significant development for this question can be found in [64, 149].

and are polluted by the surface ghost[7] (in a simple scenario). Traditionally, this is modelled as a convolution process and the simplest deconvolution/deghosting[8] problem in seismic processing is to estimate the underlying exact seismic record using the observed seismic data. Will the Bayesian solutions using IEnSRF overcome the challenges generated by wave deformation and attenuation? Will the performance of IEnSRF outperform the existing engineering deconvolution/deghosting methods.

Full Waveform Inversion (FWI)

Continuing in the seismic applications, it is well-known that the seismic waves travel with different speeds in different rock types. An adequate velocity model of the underlying subsurface is crucial for the migration process in seeking the reflectivity [180]. The inverse problem, which infers the subsurface velocity, by matching the simulated (using the forward subsurface wave travelling model) and recorded data at the surface, is known as FWI [181]. It is shown in the literature to provide a significant improvement in reflectivity and velocity model resolution and is particularly useful for capturing small-scale features [22, 148]. With a formulation similar to the considered history matching problem (and increasing computational power), can we use the WEnSRF or IEnSRF as a FWI algorithm for the estimation of the subsurface velocity model?

---

[7] Due to the high density contrast, the surface is (of the ocean or the desert) acts as an almost acoustic mirror, causing ghost effects in recorded seismic data [179].

[8] The deghosting problem can also be formulated as a deconvolution problem [53].

Appendix A

Derivation of the Numerical Reservoir Simulator

In the numerical (reservoir) simulator, with known reservoir behaviour (i.e. pressure and saturation of each fluid phase: $S_w(\underline{x}, t)$, $S_o(\underline{x}, t)$ and $P(\underline{x}, t)$) at a given time t, our goal is to find the reservoir behaviour (i.e. $S_w(\underline{x}, t+\delta t)$, $S_o(\underline{x}, t+\delta t)$ and $P(\underline{x}, t+\delta t)$) at time $t + \delta t$ by solving the reservoir model equations (2.38a-e). This appendix introduces the spatial assumptions, grid setup and discretisation for the state and model variables before providing a derivation of an implicit Finite Volume scheme.

A.1 Spatial Discretisation and Grid Setup

Before deriving the numerical scheme which propagates the state variables forward from one time to another, their spatial (Finite Volume) numerical approximation is formulated. For ease of presentation and derivation, the reservoir domain Ω is normalised to a unit square. As shown in Fig. A.1, we divide the north and south boundaries of the reservoir $\Omega : \{0 \leq x \leq 1; 0 \leq y \leq 1\}$ into segments with length $h_x = 1/(N_x - 1)$ such that $0 = x_0 < x_1 < \cdots < x_i < \cdots < x_{N_x} = 1$ for $N_x \geq 2$ and $x_i = ih_x - h_x/2$ for $i \in [1, N_x - 1]$. Similarly, we divide the east and west boundaries

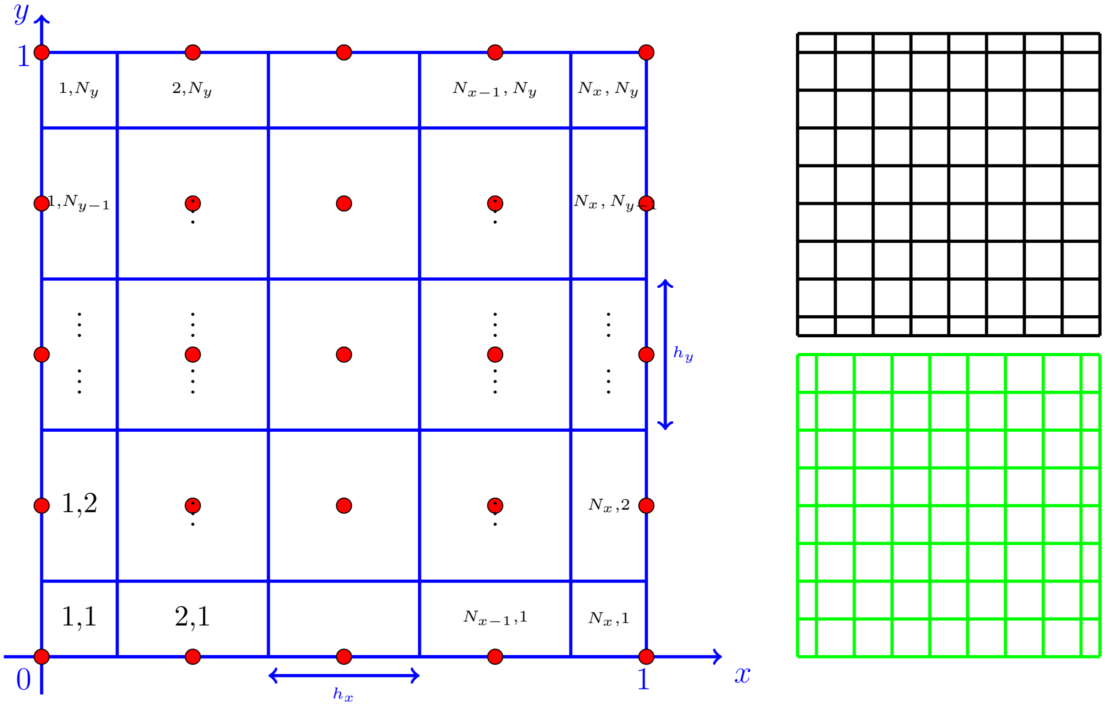

Figure A.1: The standard (left, blue), staggered-x (right top, black) and staggered-y (right bottom, green) discretisation grids. The standard grid plot shows the coordinate system, cell index ($1, 1$ to N_x, N_y), cell dimension (h_x and h_y) and node for each cell which the variable constant is taken from (red dots).

into segments with length $h_y = 1/(N_y - 1)$ such that $0 = y_0 < y_1 < \cdots < y_j < \cdots < y_{N_y} = 1$ for $N_y \geq 2$ and $y_j = jh_y - h_y/2$ for $j \in [1, N_y - 1]$. By connecting $(x_i, 0)$ and $(x_i, 1)$ with latitudes for all i and $(0, y_j)$ and $(1, y_j)$ with longitudes for all j, the reservoir domain Ω can be divided into $N_x \times N_y$ identical cells (subdomains), where the domain and boundaries of each cell (with corners at (x_{i-1}, y_{j-1}), (x_{i-1}, y_j), (x_i, y_j) and (x_i, y_{j-1})) are denoted by $\Omega_{i,j}$ and $\partial\Omega_{i,j}$, respectively, and the subscript i and j denote the cell index in the x and y direction, respectively. We define the described grid for discretisation as the standard grid.

For the propose of having a constant (Finite Volume) variable approximation across all the boundaries of a given cell on the standard grid, we further define the staggered-x and staggered-y grids, which are the half-cell shifts of the standard grid in the x and y directions, respectively, as show in Fig. A.1. Each cell of the staggered-x

grid has corners at $(x_i - h_x/2, y_{j-1})$, $(x_i - h_x/2, y_j)$, $(x_i + h_x/2, y_j)$ and $(x_i + h_x/2, y_{j-1})$ for $i \in [1, N_x - 1]$ and $j \in [1, N_y]$ and is denoted by $\Omega_{i+1/2,j}$. Similarly, each cell of the staggered-y grid has corners at $(x_{i-1}, y_j - h_y/2)$, $(x_i, y_j - h_y/2)$, $(x_i, y_j + h_y/2)$ and $(x_{i-1}, y_j + h_y/2))$ for $i \in [1, N_x]$ and $j \in [1, N_y - 1]$ and is denoted by $\Omega_{i,j+1/2}$. As a result, the east, west, north and south boundaries of $\Omega_{i,j}$ will locate in the middle of the cells $\Omega_{i+1/2,j}$, $\Omega_{i-1/2,j}$, $\Omega_{i,j+1/2}$ and $\Omega_{i,j-1/2}$, respectively.

A.2 Implicit Finite Volume Scheme

At a given time t_k, we assume the state variables: pressure $(P(\underline{x}, t_k))$, saturation for oil $(S_o(\underline{x}, t_k))$ and water $(S_w(\underline{x}, t_k))$ are constant inside each cell. (i) For cells which are not located at the reservoir boundaries, we take the variable value at each cell centre as the constant value inside these cells. (ii) For cells located along the boundaries but not at the four corners, we take the variable value at the middle point of each cell on the reservoir boundaries as the constant value inside these cells. (iii) For cells at the reservoir corners, we take the variable value at the corner of the reservoir domain as the constant value inside these cells. These nodes, which the variable constant for each cell is taken from, are denoted as red dots in the left panel of Fig. A.1. One may note that, in this setting, two consecutive nodes are consistently distanced h_x along the x direction or h_y along the y direction. The state variables, therefore, can be expressed in the following Finite Volume approximation form:

$$P(\underline{x}, t_k) = \sum_{i=1}^{N_x} \sum_{j=1}^{N_y} H_{i,j} P_{i,j}^k, \quad S_o(\underline{x}, t_k) = \sum_{i=1}^{N_x} \sum_{j=1}^{N_y} H_{i,j} S_{o,i,j}^k, \quad S_w(\underline{x}, t_k) = \sum_{i=1}^{N_x} \sum_{j=1}^{N_y} H_{i,j} S_{w,i,j}^k, \quad \text{(A.1)}$$

where both the subscript and superscript k denotes the time index,

$$H_{i,j}(\underline{x}) = \begin{cases} 1, & \text{if } \underline{x} \in \Omega_{i,j} \\ 0, & \text{if } \underline{x} \notin \Omega_{i,j} \end{cases}, \quad \text{(A.2)}$$

is the Heaviside function step function for cell $\Omega_{i,j}$ and $P^k_{i,j}$, $S^k_{o,i,j}$ and $S^k_{w,i,j}$ are the constant pressure and oil and water saturations inside $\Omega_{i,j}$, respectively. For consistency, the model variables: mobilities for oil ($\lambda_o(\underline{x}, t_k)$) and water ($\lambda_w(\underline{x}, t_k)$), porosity ($\phi(\underline{x})$), absolute permeability ($\kappa(\underline{x})$) are also assumed to be constant inside each cell of the standard grid in the same form as (A.1), but not explicitly specified.

Using assumption 20 in the described experiment setup and the proposed standard grid, we assume the number of injection and production well pairs is N_y. The wells are placed at the centre of each cell along the east and west boundaries of the reservoir (i.e. $\omega \in [1, N_y]$, $\underline{\varsigma}_{\omega,I} = (0, (\omega-1)h_y)$ and $\underline{\varsigma}_{\omega,P} = (1, (\omega-1)h_y)$. Hence, the boundary conditions imposed by the wells are assumed to be constraints for the variables inside the cells where they are placed. That is the oil and water production rates of the j^{th} production well are denoted by $q_{P,o,N_x,j}$ and $q_{P,w,N_x,j}$, respectively; the water injection rate of the j^{th} injection well is denoted by $q_{I,w,1,j}$ and the bottomhole pressure of the j^{th} production is denoted by $P_{N_x,j}$.

As will be showed next, for a given cell (i, j), one could see that the numerical approximation of the second terms (Laplace operator) of eqs (2.38a,b) involves approximating the mobilities and absolute permeability across the boundaries of cells on the standard grid. In this case, we must interpolate the approximate mobilities and (absolute) permeability on the staggered grids (using the approximations of the discrete variables on the standard grid). Here, we approximate and interpolate the oil mobility $\lambda_o(\underline{x}, t_k)$ using single-point upstream weighting, as follows:

$$\lambda_o(\underline{x}, t_k) = \sum_{i=1}^{N_x}\sum_{j=1}^{N_y} H_{i,j}\lambda^k_{o,i,j} = \sum_{i=1}^{N_x-1}\sum_{j=1}^{N_y} H_{i+1/2,j}\lambda^k_{o,i+1/2,j} = \sum_{i=1}^{N_x}\sum_{j=1}^{N_y-1} H_{i,j+1/2}\lambda^k_{o,i,j+1/2},$$

where

$$\lambda_{o,i+1/2,j}(\underline{x}) = \begin{cases} \lambda_{o,i,j}, & \text{if } P_{i,j} \geq P_{i+1,j} \\ \lambda_{o,i+1,j}, & \text{if } P_{i,j} < P_{i+1,j} \end{cases}, \quad \lambda_{o,i,j+1/2}(\underline{x}) = \begin{cases} \lambda_{o,i,j}, & \text{if } P_{i,j} \geq P_{i,j+1} \\ \lambda_{o,i,j+1}, & \text{if } P_{i,j} < P_{i,j+1} \end{cases},$$

and $H_{i+1/2,j}$ and $H_{i,j+1/2}$ are Heaviside step functions for cells $\Omega_{i+1/2,j}$ and $\Omega_{i,j+1/2}$ on the staggered grids as defined in eq. (A.2), respectively.

In the same way, the approximation and interpolation of the water mobility $\lambda_w(\underline{x}, t_k)$ for water can be performed. For the approximation of absolute permeability on the staggered grids, we use the harmonic mean of two adjacent cells on the standard grid as follows:

$$\kappa(\underline{x}) = \sum_{i=1}^{N_x}\sum_{j=1}^{N_y} H_{i,j}\kappa_{i,j} = \sum_{i=1}^{N_x-1}\sum_{j=1}^{N_y} H_{i+1/2,j}\kappa_{i+1/2,j} = \sum_{i=1}^{N_x}\sum_{j=1}^{N_y-1} H_{i+1/2,j}\kappa_{i,j+1/2},$$

where

$$\kappa_{i+1/2,j} = \frac{\kappa_{i+1,j}\kappa_{i,j}}{\kappa_{i+1,j}+\kappa_{i,j}} \qquad \text{and} \qquad \kappa_{i,j+1/2} = \frac{\kappa_{i,j}\kappa_{i,j+1}}{\kappa_{i,j}+\kappa_{i,j+1}}.$$

A.2.1 Derivation of an Implicit Finite Volume Scheme

First, we introduce the discrete approximation of the diffusive term in eq. (2.38a,b). For a cell Ω_{ij} which is not on the boundary $\partial\Omega$ (i.e. $i\in[2, N_x-1]$ and $j\in[2, N_y-1]$), applying the divergence theorem, the diffusive term of eqs (2.38a,b) must satisfy:

$$\iint_{\Omega_{i,j}} \nabla\cdot(\kappa(\underline{x})\lambda(\underline{x},t)\nabla P(\underline{x},t))\,dx\;dy = \oint_{\partial\Omega_{i,j}} (\kappa(\underline{x})\lambda(\underline{x},t)\nabla P(\underline{x},t))\cdot\mathbf{n}\;ds, \quad \text{(A.5a)}$$

where for simplicity of derivation, we drop the time and fluid phase indices and the vector $\mathbf{n}$ denotes the normal vector perpendicular to the cell boundaries and pointing outwards. Using the discretisation assumption, the volume integral on the left-hand side of eq. (A.5a) can be expressed in the Finite Volume formulation as:

$$\iint_{\Omega_{i,j}} \nabla\cdot(\kappa(\underline{x})\lambda(\underline{x},t)\nabla P(\underline{x},t))\,dx\;dy = h_x h_y\left[\nabla\cdot(\kappa(\underline{x})\lambda(\underline{x},t)\nabla P(\underline{x},t))\right], \quad \text{(A.5b)}$$

while using a first order numerical derivative approximation, the surface integral on the right-hand side of eq. (A.5a) can be approximated as:

$$\begin{aligned}
&\oint_{\partial\Omega_{i,j}} (\kappa(\underline{x})\lambda(\underline{x},t)\nabla P(\underline{x},t))\cdot\mathbf{n}\; ds \\
&= \kappa_{i-\frac{1}{2},j}\lambda_{i-\frac{1}{2},j}\frac{P_{i-1,j}-P_{i,j}}{h_x}h_y + \kappa_{i+\frac{1}{2},j}\lambda_{i+\frac{1}{2},j}\frac{P_{i+1,j}-P_{i,j}}{h_x}h_y \\
&\quad + \kappa_{i,j-\frac{1}{2}}\lambda_{i,j-\frac{1}{2}}\frac{P_{i,j-1}-P_{i,j}}{h_y}h_x + \kappa_{i,j+\frac{1}{2}}\lambda_{i,j+\frac{1}{2}}\frac{P_{i,j+1}-P_{i,j}}{h_y}h_x \\
&= \frac{h_y}{h_x}\kappa_{i-\frac{1}{2},j}\lambda_{i-\frac{1}{2},j}P_{i-1,j} + \frac{h_y}{h_x}\kappa_{i+\frac{1}{2},j}\lambda_{i+\frac{1}{2},j}P_{i+1,j} + \frac{h_x}{h_y}\kappa_{i,j-\frac{1}{2}}\lambda_{i,j-\frac{1}{2}}P_{i,j-1} \\
&\quad + \frac{h_x}{h_y}\kappa_{i,j+\frac{1}{2}}\lambda_{i,j+\frac{1}{2}}P_{i,j+1} - \left[\frac{h_y}{h_x}\left(\lambda_{i-\frac{1}{2},j}+\lambda_{i+\frac{1}{2},j}\right) + \frac{h_x}{h_y}\left(\lambda_{i,j-\frac{1}{2}}+\lambda_{i,j+\frac{1}{2}}\right)\right]P_{i,j}. \qquad \text{(A.5c)}
\end{aligned}$$

Using eqs. (A.5a-c), the discrete approximation of the diffusive term inside a cell not along the reservoir boundary can be derived:

$$\begin{aligned}
&\nabla\cdot(\kappa(\underline{x})\lambda(\underline{x},t)\nabla P(\underline{x},t)) \\
&= \frac{1}{h_x^2}\kappa_{i-\frac{1}{2},j}\lambda_{i-\frac{1}{2},j}P_{i-1,j} + \frac{1}{h_x^2}\kappa_{i+\frac{1}{2},j}\lambda_{i+\frac{1}{2},j}P_{i+1,j} + \frac{1}{h_y^2}\kappa_{i,j-\frac{1}{2}}\lambda_{i,j-\frac{1}{2}}P_{i,j-1} \\
&\quad + \frac{1}{h_y^2}\kappa_{i,j+\frac{1}{2}}\lambda_{i,j+\frac{1}{2}}P_{i,j+1} - (\frac{1}{h_x^2}\lambda_{i-\frac{1}{2},j} + \frac{1}{h_x^2}\lambda_{i+\frac{1}{2},j} + \frac{1}{h_y^2}\lambda_{i,j-\frac{1}{2}} + \frac{1}{h_y^2}\lambda_{i,j+\frac{1}{2}})P_{i,j}. \qquad \text{(A.6)}
\end{aligned}$$

Following the same procedure, this diffusive term of the model system (2.38a,b) can also be approximated for the rest of cells. The differences between the cells along the boundaries and the interior cells are the cell size and the imposition of the no-flow boundary condition along the reservoir domain (i.e. the pressure gradient through the cell boundary which is on the reservoir boundary is taken to be zero[1]). The equations, which are used to approximate the diffusive term of the model system (2.38a,b) in each cell of the standard grid, are summarised in table A.1.

Hereafter, the Finite Volume approximation of the diffusive term $\nabla\cdot(\kappa\lambda\nabla P)$ for oil and water in $\Omega_{i,j}$ at time t_k are denoted as $\Upsilon^k_{o,i,j}$ and $\Upsilon^k_{w,i,j}$, respectively. With known reservoir properties at time t_k, using an implicit scheme, at time $t_{k+1} = t_k + \delta t$,

---

[1] For example, for cell $(1,1)$, the pressure gradient though the east and south cell boundaries are both zeros.

i	j	$\Upsilon_{i,j}$ or $\nabla\cdot(\kappa(\underline{x})\lambda(\underline{x},t)\nabla P(\underline{x},t))$ at cell (i,j)
1	1	$\frac{2}{h_x^2}\kappa_{\frac{3}{2},1}\lambda_{\frac{3}{2},1}P_{2,1}+\frac{2}{h_y^2}\kappa_{1,\frac{3}{2}}\lambda_{1,\frac{3}{2}}P_{1,2}-(\frac{2}{h_x^2}\kappa_{\frac{3}{2},1}\lambda_{\frac{3}{2},1}+\frac{2}{h_y^2}\kappa_{1,\frac{3}{2}}\lambda_{1,\frac{3}{2}})P_{1,j}$
1	$[2, N_y-1]$	$\frac{2}{h_x^2}\kappa_{\frac{3}{2},j}\lambda_{\frac{3}{2},j}P_{2,j}+\frac{1}{h_y^2}\kappa_{1,j-\frac{1}{2}}\lambda_{1,j-\frac{1}{2}}P_{1,j-1}+\frac{1}{h_y^2}\kappa_{1,j+\frac{1}{2}}\lambda_{1,j+\frac{1}{2}}P_{1,j+1}$ $-(\frac{2}{h_x^2}\kappa_{\frac{3}{2},j}\lambda_{\frac{3}{2},j}+\frac{1}{h_y^2}\kappa_{1,j-\frac{1}{2}}\lambda_{1,j-\frac{1}{2}}+\frac{1}{h_y^2}\kappa_{1,j+\frac{1}{2}}\lambda_{1,j+\frac{1}{2}})P_{1,j}$
1	N_y	$\frac{2}{h_x^2}\kappa_{\frac{3}{2},N_y}\lambda_{\frac{3}{2},N_y}P_{2,N_y}+\frac{2}{h_y^2}\kappa_{1,N_y-\frac{1}{2}}\lambda_{1,N_y-\frac{1}{2}}P_{1,N-1}$ $-(\frac{2}{h_x^2}\kappa_{\frac{3}{2},N}\lambda_{\frac{3}{2},N_y}+\frac{2}{h_y^2}\kappa_{1,N_y-\frac{1}{2}}\lambda_{1,N_y-\frac{1}{2}})P_{1,N_y}$
$[2, N_x-1]$	N_y	$\frac{1}{h_x^2}\kappa_{i-\frac{1}{2},N_y}\lambda_{i-\frac{1}{2},N_y}P_{i-1,N_y}+\frac{1}{h_x^2}\kappa_{i+\frac{1}{2},N_y}\lambda_{i+\frac{1}{2},N_y}P_{i+1,N_y}$ $+\frac{2}{h_y^2}\kappa_{i,N_y-\frac{1}{2}}\lambda_{i,N_y-\frac{1}{2}}P_{i,N_y-1}-(\frac{1}{h_x^2}\kappa_{i-\frac{1}{2},N_y}\lambda_{i-\frac{1}{2},N_y}$ $+\frac{1}{h_x^2}\kappa_{i+\frac{1}{2},N_y}\lambda_{i+\frac{1}{2},N_y}+\frac{2}{h_y^2}\kappa_{i,N_y-\frac{1}{2}}\lambda_{i,N_y-\frac{1}{2}})P_{i,N_y}$
N_x	N_y	$\frac{2}{h_x^2}\kappa_{N_x-\frac{1}{2},j}\lambda_{N_x-\frac{1}{2},j}P_{N_x-1,j}+\frac{2}{h_y^2}\kappa_{N_x,N_y-\frac{1}{2}}\lambda_{N_x,j-\frac{1}{2}}P_{N_x,N_y-1}$ $-(\frac{2}{h_x^2}\kappa_{N_x-\frac{1}{2},j}\lambda_{N_x-\frac{1}{2},j}+\frac{2}{h_y^2}\kappa_{N_x,N_y-\frac{1}{2}}\lambda_{N_x,N_y-\frac{1}{2}})P_{N_x,j}$
N_x	$[2, N_y-1]$	$\frac{2}{h_x^2}\kappa_{N_x-\frac{1}{2},j}\lambda_{N_x-\frac{1}{2},j}P_{N_x-1,j}+\frac{1}{h_y^2}\kappa_{N_x,j-\frac{1}{2}}\lambda_{N_x,j-\frac{1}{2}}P_{N_x,j-1}$ $+\frac{1}{h_y^2}\kappa_{N_x,j+\frac{1}{2}}\lambda_{N_x,j+\frac{1}{2}}P_{N_x,j+1}-(\frac{2}{h_x^2}\kappa_{N_x-\frac{1}{2},j}\lambda_{N_x-\frac{1}{2},j}$ $+\frac{1}{h_y^2}\kappa_{N_x,j-\frac{1}{2}}\lambda_{N_x,j-\frac{1}{2}}+\frac{1}{h_y^2}\kappa_{N_x,j+\frac{1}{2}}\lambda_{N_x,j+\frac{1}{2}})P_{N_x,j}$
N_x	1	$\frac{2}{h_x^2}\kappa_{N_x-\frac{1}{2},1}\lambda_{N_x-\frac{1}{2},1}P_{N_x-1,1}+\frac{2}{h_y^2}\kappa_{N_x,\frac{3}{2}}\lambda_{N_x,\frac{3}{2}}P_{N_x,2}$ $-(\frac{2}{h_x^2}\kappa_{N_x-\frac{1}{2},1}\lambda_{N_x-\frac{1}{2},1}+\frac{2}{h_y^2}\kappa_{N_x,\frac{3}{2}}\lambda_{N_x,\frac{3}{2}})P_{N_x,1}$
$[2, N_x-1]$	1	$\frac{1}{h_x^2}\kappa_{i-\frac{1}{2},1}\lambda_{i-\frac{1}{2},1}P_{i-1,1}+\frac{1}{h_x^2}\kappa_{i+\frac{1}{2},1}\lambda_{i+\frac{1}{2},1}P_{i+1,1}+\frac{2}{h_y^2}\kappa_{i,\frac{3}{2}}\lambda_{i,\frac{3}{2}}P_{i,2}$ $-(\frac{1}{h_x^2}\kappa_{i-\frac{1}{2},1}\lambda_{i-\frac{1}{2},1}+\frac{1}{h_x^2}\kappa_{i+\frac{1}{2},1}\lambda_{i+\frac{1}{2},1}+\frac{2}{h_y^2}\kappa_{i,\frac{3}{2}}\lambda_{i,\frac{3}{2}})P_{i,1}$
$[2, N_x-1]$	$[2, N_y-1]$	$\frac{1}{h_x^2}\kappa_{i-\frac{1}{2},j}\lambda_{i-\frac{1}{2},j}P_{i-1,j}+\frac{1}{h_x^2}\kappa_{i+\frac{1}{2},j}\lambda_{i+\frac{1}{2},j}P_{i+1,j}$ $+\frac{1}{h_y^2}\kappa_{i,j-\frac{1}{2}}\lambda_{i,j-\frac{1}{2}}P_{i,j-1}+\frac{1}{h_y^2}\kappa_{i,j+\frac{1}{2}}\lambda_{i,j+\frac{1}{2}}P_{i,j+1}$ $-(\frac{1}{h_x^2}\lambda_{i-\frac{1}{2},j}+\frac{1}{h_x^2}\lambda_{i+\frac{1}{2},j}+\frac{1}{h_y^2}\lambda_{i,j-\frac{1}{2}}+\frac{1}{h_y^2}\lambda_{i,j+\frac{1}{2}})P_{i,j}$

Table A.1: The Finite Volume Approximation of the diffusive term in the model system (2.38a,b) for each cell $\Omega_{i,j}$ with omitted fluid phase and time indices.

the numerical scheme for the model system (2.38a-e) can be summarised as:

$$\phi_{i,j}(S^{k+1}_{o,i,j}-S^{k}_{o,i,j})\ -\delta t\Upsilon^{k+1}_{o,i,j}-\delta t q^{k+1}_{P,o,N_x,j}\ =0, \tag{A.7a}$$

$$\phi_{i,j}(S^{k+1}_{w,i,j}-S^{k}_{w,i,j})-\delta t\Upsilon^{k+1}_{w,i,j}-\delta t q^{k+1}_{I,w,1,j}-\delta t q^{k+1}_{P,w,N_x,j}=0, \tag{A.7b}$$

$$S^{k+1}_{w,i,j}+S^{k+1}_{o,i,j}=1, \tag{A.7c}$$

$$P^{k+1}_{N_x,j}=p_P, \qquad \forall j\in[1,N_y], \tag{A.7d}$$

$$\sum_{j=1}^{N_y}(q^{k+1}_{P,o,N_x,j}+q^{k+1}_{P,w,N_x,j})=-\sum_{j=1}^{N_y}q^{k+1}_{I,w,1,j}=-q_I. \tag{A.7e}$$

where $q^{k+1}_{I,w,i,j}$, $q^{k+1}_{P,o,i,j}$ and $q^{k+1}_{p,w,i,j}$ are the volumetric flow rates for water injection due to the j^{th} injection well and the oil and water production due to the j^{th} production well in $\Omega_{i,j}$ at time t_{k+1}, respectively[2]. To model the flow rates in the wells, we introduce the fractional flow using the mobility of fluid [124] as follows:

$$q^k_{I,w,1,j} = \frac{q_I \lambda^k_{w,1,j}}{\sum_{j=1}^{N_y} \lambda^k_{w,1,j}},\ q^k_{P,o,N_x,j} = \frac{-q_I \lambda^k_{o,N_x,j}}{\sum_{j=1}^{N_y} \lambda^k_{o,N_x,j} + \lambda^k_{w,N_x,j}},\ q^k_{P,w,N_x,j} = \frac{-q_I \lambda^k_{w,N_x,j}}{\sum_{j=1}^{N_y} \lambda^k_{o,N_x,j} + \lambda^k_{w,N_x,j}}. \quad \text{(A.8)}$$

Note that the proposed fractional flow equations satisfy the boundary condition (A.7e) exactly and accord to physical principle between the fluid mobility and production.

With the Finite Volume approximation of all terms in model system (A.7a-e) derived for every cell on the standard grid for time t_k and t_{k+1}, we can rewrite the model system in a matrix form for all cells using the function $\varpi(\cdot)$ as follows:

$$\varpi\left(\mathbf{P}^k, \mathbf{S}^k_w, \mathbf{P}^{k+1}, \mathbf{S}^{k+1}_w, \mathbf{\Phi}, \mathbf{K}, \mathbf{\Lambda}\right) = 0, \quad \text{(A.9)}$$

where $\mathbf{\Phi} = [\phi_{1,1}, \ldots, \phi_{N_x,N_y}]^T$, $\mathbf{K} = [\kappa_{1,1}, \ldots, \kappa_{N_x,N_y}]^T$, $\mathbf{\Lambda} = [\lambda_{1,1}, \ldots, \lambda_{N_x,N_y}]^T$, $\mathbf{S}_w = [S_{w,1,1}, \ldots, S_{w,N_x,N_y}]$ and $\mathbf{P} = [P_{1,1}, \ldots, P_{N_x,N_y}]$ are the porosity, permeability, mobility and water saturation and pressure for all reservoir cells presented in vectors of dimension N, respectively[3], the superscript T denotes the matrix transpose and $N = N_x N_y$ is the total number of cells.

With the known reservoir model $(\mathbf{\Phi}, \mathbf{K}, \mathbf{\Lambda})$ and state $(\mathbf{P}^k,\ \mathbf{S}^k_w)$ at time t_k and to find out the reservoir state at time t_{k+1} $(\mathbf{P}^{k+1}, \mathbf{S}^{k+1}_w)$, we minimise the cell residues of system (A.9) by applying Newton iterations in which the Generalised Minimal RESidual (GMRES) method is adapted as the linear solver at each time step. For ease of presentation, we denote the reservoir solver of the described process as:

$$\left[\mathbf{P}^{k+1}, \mathbf{S}^{k+1}_w\right]^T = \varpi_s\left(\mathbf{P}^k, \mathbf{S}^k_w, \mathbf{\Phi}, \mathbf{K}, \mathbf{\Lambda}\right). \quad \text{(A.10)}$$

---

[2] They are zeros for almost all is and js expect in the cells where the wells are drilled (i.e. $i = 1$ or N_x and $j \in [1, N_y]$).

[3] One may notice that the oil saturations in the reservoir cells are not included in eq. (A.9), because they can be easily derived using eq. (A.7c) and either $\mathbf{S}^k_w$ or $\mathbf{S}^{k+1}_w$.

Appendix B

Derivation of the Ensemble Kalman Filter

The traditional Ensemble Kalman Filter (EnKF) [56, 57] is the first well-studied and widely-used filter which samples the posterior pdf in eq. (3.9) stochastically. It processes each ensemble member using the analysis eq. (3.10a):

$$x^a_{k,i} = x^f_{k,i} + K_k(s_k + v_{k,i} - H_k x^f_{k,i}), \qquad i = 1, ..., r, \tag{B.1}$$

where $v_{k,i} \sim \mathcal{N}(0, R)$ is the synthetic perturbation[1] of the observation s_k. Hence, the ensemble average of (B.1) yields the analysis eq. (3.10a), provided that the ensemble average of $v_{k,i}$ is zero. To calculate the analysed error covariance, we subtract the analysis equation (B.1) from (3.10a) and rewrite the function in terms of an ensemble anomaly:

$$A^a_{k,i} = A^f_{k,i} + K_k(v_{k,i} - H_k A^f_{k,i}), \qquad i = 1, ..., r.$$

---

[1] This synthetic perturbation is required for matching the theoretical value of the approximate posterior pdf using Kalman filter in the Linear-Gaussian case.

In matrix form, this is

$$A_k^a = A_k^f + K_k(V_k - H_k A_k^f), \tag{B.2}$$

where $V_k = [v_{k,1}, ..., v_{k,N}]$. The analysed error covariance carried by the ensemble can be calculated by eq. (3.7c):

$$\begin{aligned} P_k^a &= \frac{1}{r-1} A_k^a A_k^{aT} = \frac{1}{r-1}[A_k^f + K_k(V_k - H_k A_k^f)][A_k^f + K_k(V_k - H_k A_k^f)]^T \\ &= P_k^f - P_k^f H_k^T K_k^T - K_k H_k P_k^f + K_k H_k P_k^f H_K^T K_k^T + \frac{1}{r-1} K_k V_k V_k^T K_k^T \\ &+ \frac{1}{r-1}(I - K_k H_k) A_K^f V_k^T K_k^T + \frac{1}{r-1} K_k V_k A_k^{f^T}(I - H_k^T K_k^T). \end{aligned} \tag{B.3}$$

To match this to the theoretical value of the approximate posterior pdf in eq. (3.10b), the synthetic perturbation V_k has to be the solution of the following conditions [25, 115]:

$$\frac{1}{r-1} V_k V_k^T = R, \tag{B.4a}$$

$$A_k^f V_k^T K_k^T = 0. \tag{B.4b}$$

However, such a solution does not generally exist. Consequently, the traditional EnKF only satisfies these conditions approximately, in a statistical sense[2]. The $O(r^{-1/2})$ sampling error [25] makes the traditional EnKF systematically in error, particularly for small ensembles, which tends to underestimate the analysed error covariance and can cause ensemble collapse[3]. Particularly satisfying EnKF (and thus EnSRF) derivations are provided in [64, 149].

---

[2] If V_k contains random normally distributed elements such that eq. (B.4a) are satisfied in a statistical sense, then, if rows of V_k are not correlated with rows of A_k^f, eq. (B.4b) is also satisfied in a statistical sense [56].

[3] The ensemble spread reduces too rapidly in the analysis step in one time step, which leads to insufficient pdf approximations in the subsequent time step [25].

Appendix C

Barcode Signal Averaging Resample Algorithm

Given a one-dimensional barcode signal with a total number of N uniform samples $[y_1, \ldots, y_N]$, a signal with a total number of $n(< N)$ uniform samples, $[Y_1, \ldots, Y_n]$, is resampled from the original signal using the following algorithm:

1. Place the samples y_i on a unit length interval, such that the x-coordinate of sample y_i is $1/2N+i/(N-1)$ for all $i = 1, \ldots, N$, where subscript i denote sample index of the original signal.

2. Generate the samples Y_j of the resampled signal by averaging the samples of signal $[y_1, \ldots, y_N]$ in each of the n uniform intervals: $Y_j = \frac{1}{K_j} \sum_{k=1}^{k=K_j} y_{k,j}$ for all $j = 1, \ldots, n$, where the subscripts j and k are the index of the reconstructed sample and index of the samples in the original signal in the j^{th} resample interval, $((j-1)/n, j/n]$, respectively; and $y_{k,j}$ and K_j are the k^{th} sample and the total number of samples of the original signal in the j^{th} resampling interval, respectively.

Appendix D

Density Reconstruction using Ensemble and Gaussian Kernels

The density reconstruction method presented here is based on Section 2.4 of [145] with Gaussian kernels. The goal is to reconstruct the probability density using an ensemble of realisations. Assuming the ensemble available for the density construction consists of r realisations: $X = [x_1, ..., x_r] \in \mathcal{R}^{n_x \times r}$, a Gaussian kernel function is found using the covariance matrix of the realisations [59, 60]: $K(x, w) = \mathcal{N}(x, R/w)$, where w is a scaler called the 'window width', $R = [X - X\mathcal{U}^{r \times n_x}/n][X - X\mathcal{U}^{r \times n_x}/n]^T/(n-1)$, $\mathcal{U}^{r \times n_x}$ denotes a $r \times n_x$ unit matrix (matrix of 1s). The probability density is computed as $\pi(x) = \frac{1}{n} \sum_{i=1}^{n} K(x_i, w)$ with appropriate window width w.

The proposed method is known as the 'traditional kernel density estimation method'. When the window size w varies from one kernel to another (for the purpose of capturing a specified uncertainty or a specified probability at the tail), the purposed method is extended to the so-called 'variable kernel density estimation'. For our applications in this thesis, the traditional kernel density estimation is used and provides satisfactory results. Unless otherwise stated, the default value of the window width w is chosen to be 10 throughout this thesis.

Appendix E

Additional Figures

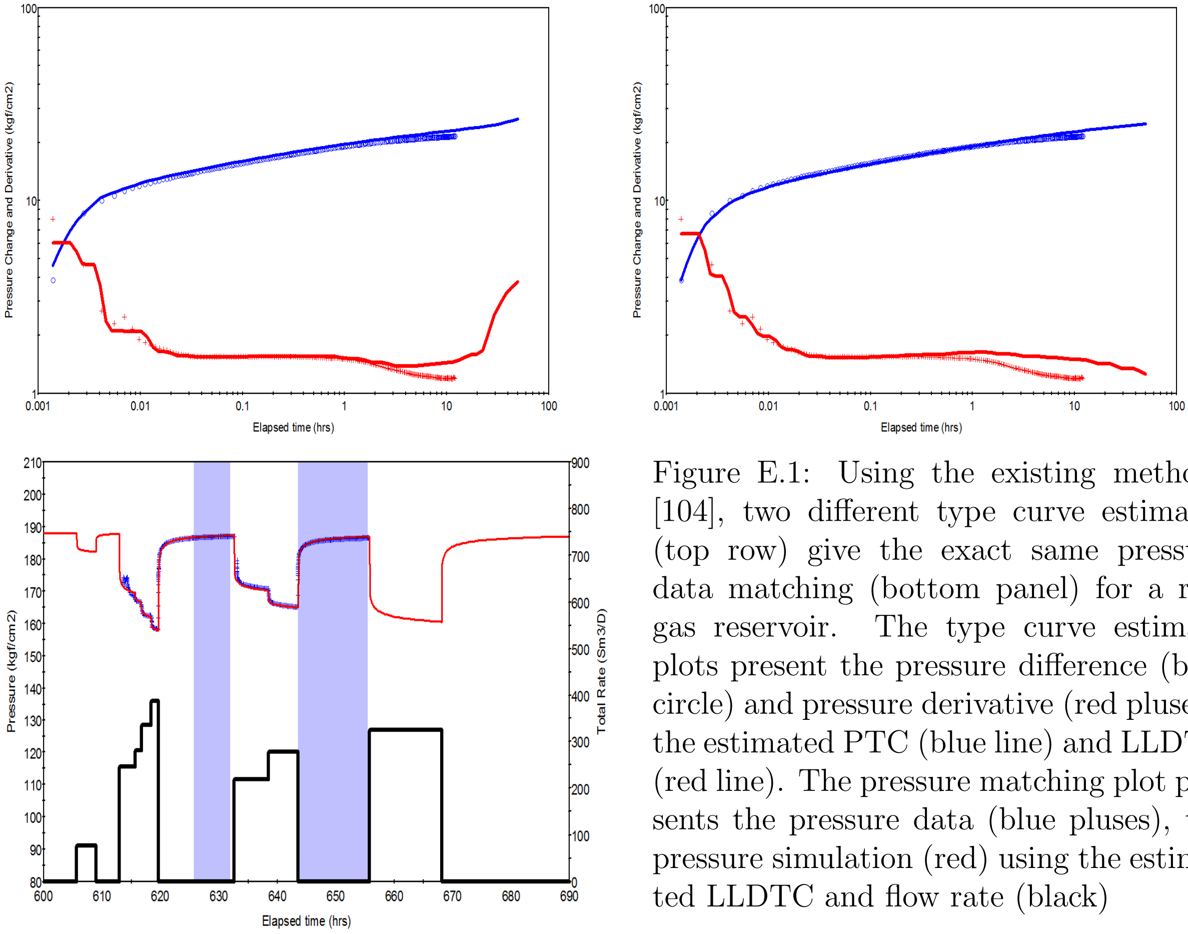

Figure E.1: Using the existing methods [104], two different type curve estimates (top row) give the exact same pressure data matching (bottom panel) for a real gas reservoir. The type curve estimate plots present the pressure difference (blue circle) and pressure derivative (red pluses), the estimated PTC (blue line) and LLDTC (red line). The pressure matching plot presents the pressure data (blue pluses), the pressure simulation (red) using the estimated LLDTC and flow rate (black)

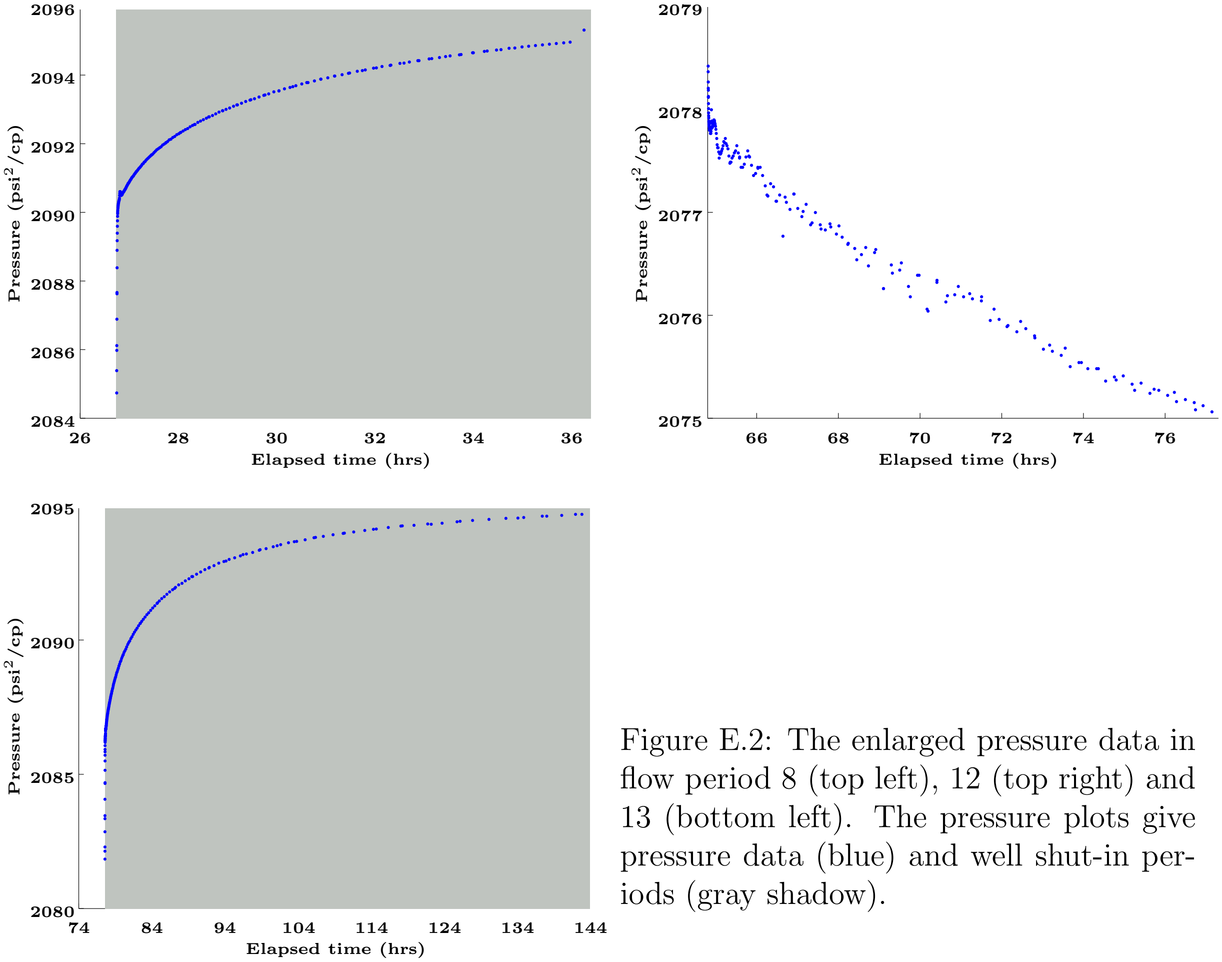

Figure E.2: The enlarged pressure data in flow period 8 (top left), 12 (top right) and 13 (bottom left). The pressure plots give pressure data (blue) and well shut-in periods (gray shadow).

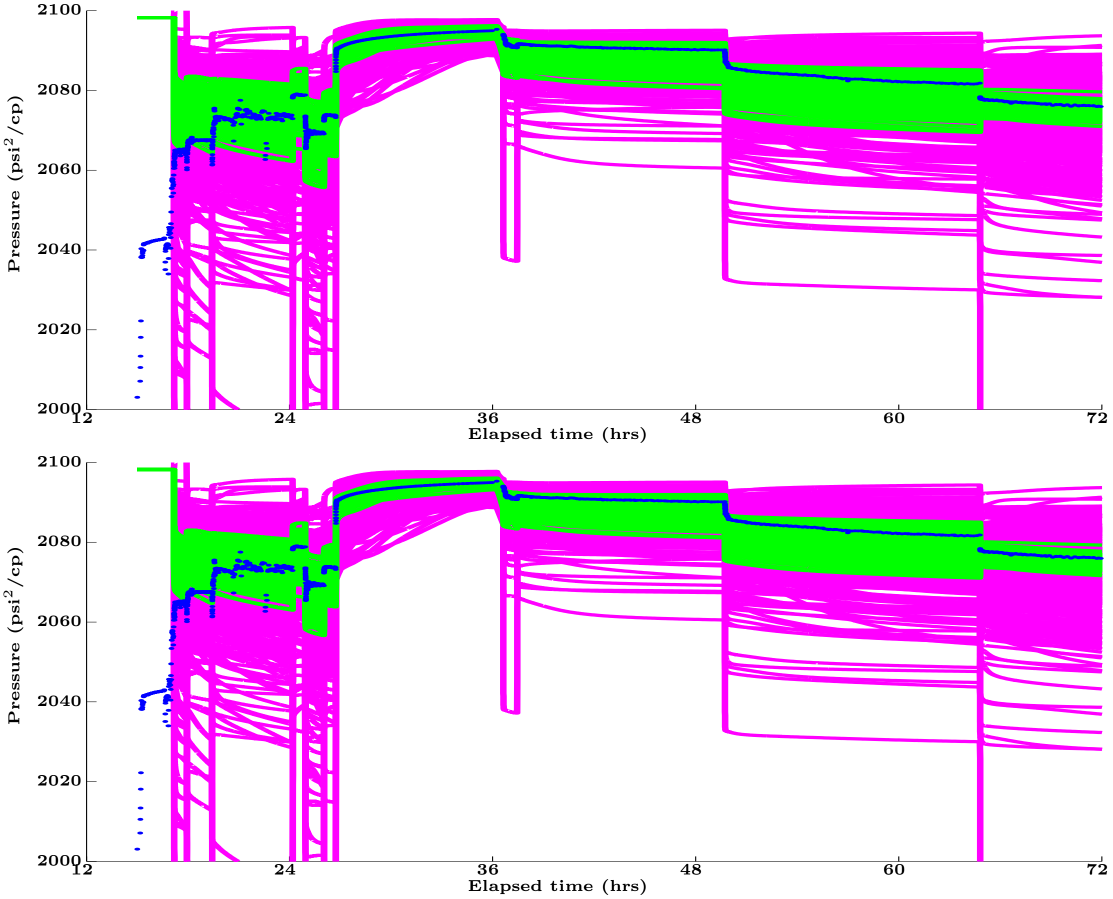

Figure E.3: The enlarged pressure match for real experiment 6.4.2 using IEnSRF with MECPD (top) and MICPD (bottom) in Fig. 6.6. The pressure data (blue) and pressure simulation using initial (magenta) and analysed (green) ensembles.

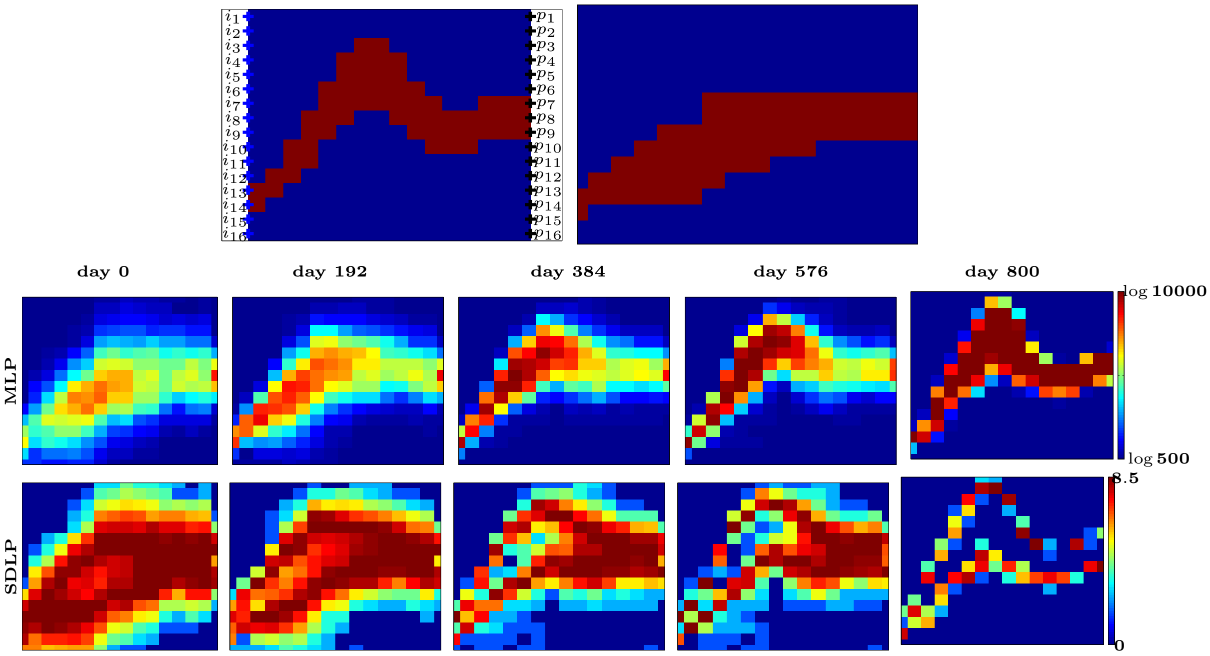

Figure E.4: The true log permeability field (left panel, first row), the prior log permeability field (right panel, first row) and the mean (second row) and SD (third row) of the log permeability field estimates, for the curved channel case. Results are shown at the end of 0^{th}, 192^{nd}, 384^{th}, 576^{th} and 800^{th} days with 100 realisations. The true log permeability field plot presents the cells which the indexed injection (blue pluses) and production (black pluses) wells. The misfit figures show the true (red) and estimated (blue) facies patterns, and the cells with large facies uncertainties (black dots).

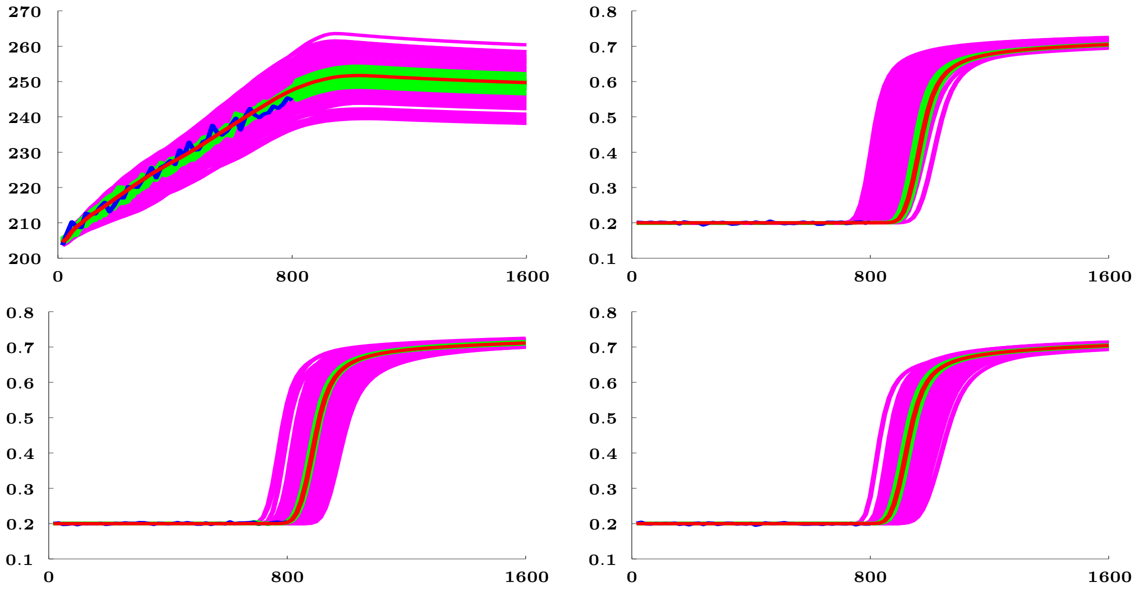

Figure E.5: Time-evolution of the estimated pressure in injection well no.7 (top left) and the (water) saturation (top right and bottom row) of production well nos. 3, 14 and 16 over the production period for the case of a curved channel with 100 realisations. The figure shows the true states (red), measurements (blue), simulations of the initial ensembles (magenta) and history matched ensembles (green).

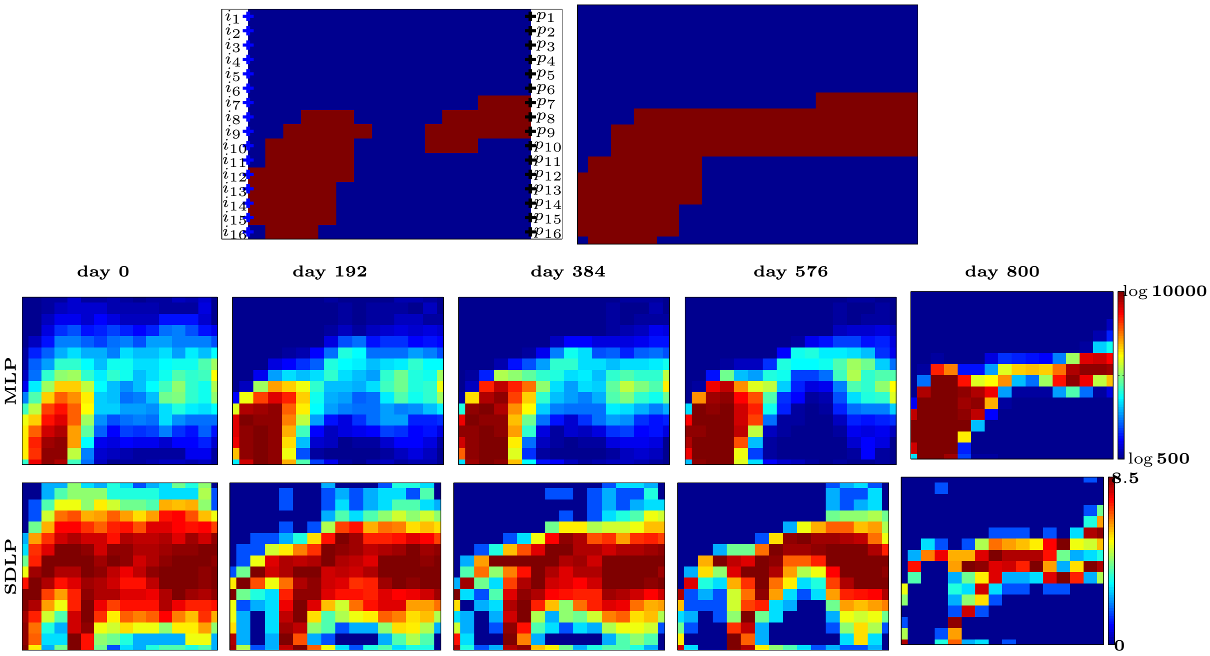

Figure E.6: The true log permeability field (left panel, first row), the prior log permeability field (right panel, first row) and the mean (second row) and SD (third row) of the log permeability field estimates for the disconnected channel case. Results are shown at the end of 0^{th}, 192^{th}, 384^{th}, 576^{th} and 800^{th} days with 100 realisations. The true log permeability field plot presents the indexed injection (blue pluses) and production (black pluses) wells.

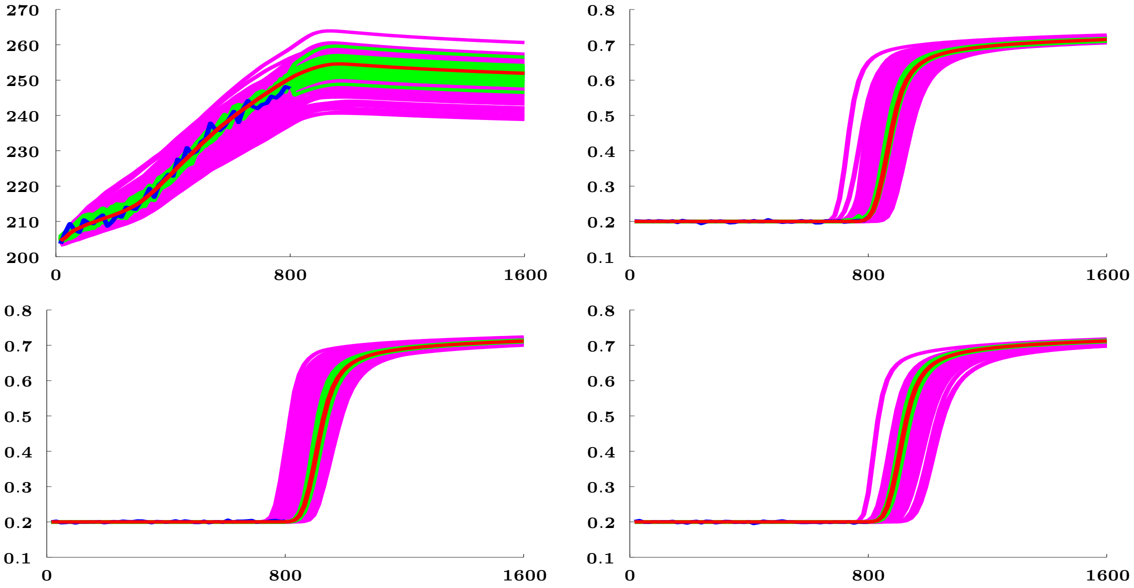

Figure E.7: Time-evolution of the estimated pressure in injection well no.7 (top left) and the (water) saturation (top right and bottom row) of production well nos. 3, 14 and 16 over the production period for the case of a disconnected channel with 100 realisations. The figure shows the true states (red), measurements (blue), simulations of the initial ensembles (magenta) and history matched ensembles (green).

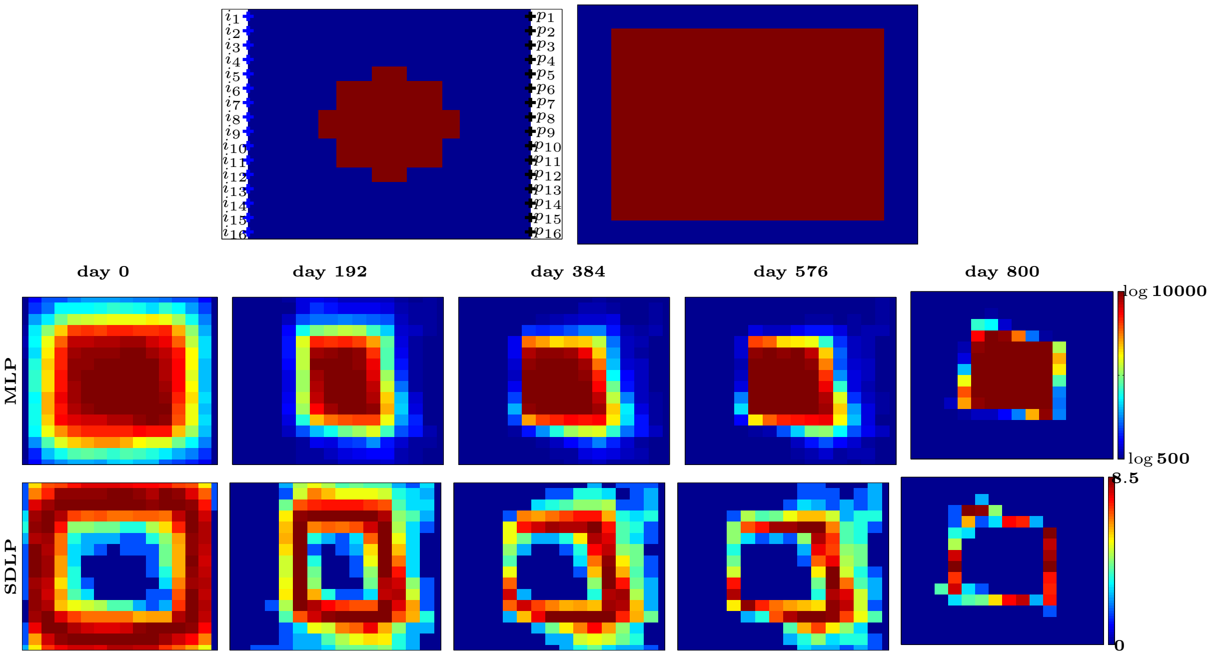

Figure E.8: The true log permeability field (left panel, first row), the prior log permeability field (right panel, first row) and the mean (second row) and SD (third row) of the log permeability field estimates for the case of a two-dimensional closed feature. Results are shown at the end of 0^{th}, 192^{nd}, 384^{th}, 576^{th} and 800^{th} days with 100 realisations. The true log permeability field plot presents the indexed injection (blue pluses) and production (black pluses) wells.

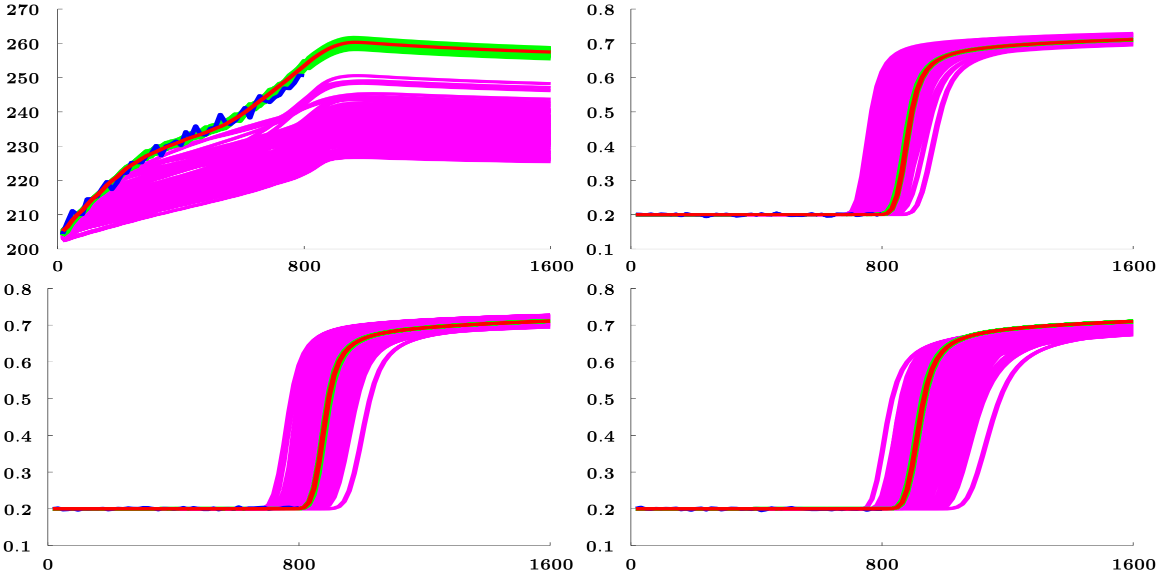

Figure E.9: Time-evolution of the estimated pressure in injection well no.7 (top left) and the (water) saturation (top right and bottom row) of production well nos. 3, 14 and 16 over the production period for the case of a two-dimensional closed feature with 100 realisations. The figure shows the true states (red), measurements (blue), simulations of the initial ensembles (magenta) and history matched ensembles (green).

Bibliography

[1] Department of Petroleum Engineering, Heriot-Watt University. Leture notes on 'well test analysis', 2005. Available online at: http://people.maths.ox.ac.uk/duan/semi-infinite_system_late_transient_analysis.pdf.

[2] J. Abate and P. Valko. Multi precision Laplace transform inversion. *International Journal for Numerical Methods in Engineering*, 60(5):979–993, 2004.

[3] R. Agarwal and R. Al-Hussainy. An investigation of wellbore storage and skin effect in unsteady liquid flow: I. analytical treatment. *SPE Journal*, 10(3):279–290, 1970.

[4] R. Al-Hussainy, H. Ramey, and P. Crawford. The flow of real gases through porous media. *Journal of Petroleum Technology*, 18(5):624–636, 1966.

[5] J. Anderson. An ensemble adjustment Kalman filter for data assimilation. *Monthly Weather Review*, 129:2884–2903, 2001.

[6] Anonymity. Deconvolution: Software comparison, 2009. Available online at: https://docs.google.com/file/d/0B9TdyzcyS8KERTh0N3lIaHFpMEU/edit.

[7] M. Armstrong and P. Dowd. *Geostatistical Simulations (Quantitative Geology and Geostatistics)*. Kluwer Academic Publishers, 1994.

[8] J. Aronofsky. Effect of gas slip on unsteady flow of gas through porous media. *Journal of Applied Physics*, 25(1):48–53, 1954.

[9] J. Aronofsky and O. Ferris. Transient flow of non-ideal gases in porous solids one-dimensional case. *Journal of Applied Physics*, 25(10):1289–1293, 1954.

[10] J. Aronofsky and R. Jenkins. A simplified analysis of unsteady radial gas flow. *Journal of Petroleum Technology*, 6(7):23–28, 1954.

[11] S. Arulampalam, S. Maskell, N. Gordon, and T. Clapp. A tutorial on Particle filters for online nonlinear/non-Gaussian Bayesian tracking. *IEEE Transactions on Signal Processing*, 50(2):174–188, 2002.

[12] K. Aziz and A. Settari. *Petroleum Reservoir Simulation*. Chapman and Hall, 1979.

[13] A. Bain and D. Crisan. *Fundamentals of Stochastic Filtering (Stochastic Modelling and Applied Probability)*. Springer, 2008.

[14] E. Barkan and J. Swartz. System design considerations in bar-code laser scanning. *Optical engineering (Bellingham. Print)*, 23(4):413–420, 1984.

[15] T. Bengtsson, P. Bickel, and B. Li. *Curse-of-dimensionality revisited: Collapse of the particle filter in very large scale systems*, pages 316–334. Institute of Mathematical Statistics, 2008.

[16] A. Bennett. *Inverse methods in physical oceanography*. Cambridge university press, 1992.

[17] P. Bidaux, T. Whittle, P. Coveney, and A. Gringarten. Analysis of pressure and rate transient data from wells in multilayered reservoirs: Theory and application. In *SPE Annual Technical Conference and Exhibition, Washington, D.C., 4-7 October 1992*. Society of Petroleum Engineers. Document ID: 24679-MS, DOI:10.2118/24679-MS.

[18] C. Bishop, B. Etherton, and S. Majumdar. Adaptive sampling with the ensemble transform Kalman filter. part i: theoretical aspects. *Monthly Weather Review*, 129:420–436, 2001.

[19] D. Bourdet, J. Ayoub, V. Kniazeff, Y. Pirard, and T. Whittle. Interpreting well tests in fractured reservoirs. *World Oil*, 197:5:77–78, 1983.

[20] D. Bourdet, J. Ayoub, and Y. Pirard. Use of pressure derivative in well test interpretation. *SPE Formation Evaluation*, 4(2):293–302, 1989.

[21] M. Brosnan and R. Quan. Digital bar code slot reader with threshold comparison of the differentiated bar code signal. US (Patent) 4740675 A, 1988.

[22] R. Brossier, S. Operto, and J. Virieux. Seismic imaging of complex onshore structures by 2D elastic frequency-domain full-waveform inversion. *Geophysics*, 74(6):WCC105–WCC118, 2009.

[23] D. Brouwer, G. Naedal, J. Jansen, E. Vefring, and C. van Kruijsdijk. Improved reservoir management through optimal control and continuous model updating. In *SPE Annual Technical Conference and Exhibition, Houston, Texas, 26-29 September 2004*. Society of Petroleum Engineers. Document ID: 90149-MS, DOI: 10.2118/90149-MS.

[24] L. Brown. A survey of image registration techniques. *ACM computing surveys (CSUR)*, 24(4):325–376, 1992.

[25] G. Burgers, P. van Leeuwen, and G. Evensen. Analysis scheme in the ensemble Kalman filter. *Monthly Weather Review*, 126:1719–1724, 1998.

[26] F. Cantelli. Sulla determinazione empirica delle leggi di probabilita. *Giornale dell'Istituto Italiano degli Attuari*, 4(421-424), 1933.

[27] H. Chang, D. Zhang, and Z. Lu. History matching of facies distribution with the EnKF and level-set parameterization. *Journal of Computational Physics*, 229(20):8011–8030, 2010.

[28] A. Chaudhry. *Gas well testing handbook*. Gulf professional publishing, 2003.

[29] A. Chaudhry. *Oil well testing handbook*. Gulf professional publishing, 2004.

[30] Y. Chen and D. Oliver. Ensemble-based closed-loop optimization applied to Brugge field. *SPE Reservoir Evaluation and Engineering*, 13(1):56–71, 2010.

[31] Y. Chen and D. S. Oliver. Ensemble randomized maximum likelihood method as an iterative ensemble smoother. *Mathematical Geosciences*, 44(1):1–26, 2012.

[32] Z. Chen. Bayesian filtering: From Kalman filters to Particle filters, and beyond. *Adaptive Systems Lab., McMaster University, Hamilton, Ontario, Canada*, 2003. Available Online at: http://www.mendeley.com/research/bayesian-filtering-from-kalman-filters-to-particle-filters-and-beyond-1/.

[33] W. Cheney and D. Kincaid. *Numerical Mathematics and Computing*. Brooks/Cole Pub Co, 2007.

[34] M. Cinar, D. Ilk, M. Onur, P. Valko, and T. Blasingame. A comparative study of recent robust deconvolution algorithms for well-test and production-data analysis. In *SPE Annual Technical Conference and Exhibition, San Antonio, Texas, 24-27 September 2006*. Society of Petroleum Engineers. Document ID: 102575-MS, DOI: 10.2118/102575-MS.

[35] T. Coleman and Y. Li. An interior trust region approach for nonlinear minimization subject to bounds. *SIAM Journal on Optimization*, 6(2):418–445, 1996.

[36] N. Cressie. Statistics for spatial data. *Terra Nova*, 4(5):613–617, 1992.

[37] F. Daum. Nonlinear filters: beyond the Kalman filter. *Aerospace and Electronic Systems Magazine, IEEE*, 20(8):57–69, 2005.

[38] F. Daum and J. Huang. Curse of dimensionality and Particle filters. In *Aerospace Conference, Big Shq, Montana, 8-15 March, 2003*, volume 4, pages 1979–1993. IEEE.

[39] C. De Boor. *A Practical Guide to Splines.* Springer Verlag, 2001.

[40] G. De Marsily, G. Lavedan, M. Boucher, and G. Fasanino. Interpretation of interference tests in a well field using geostatistical techniques to fit the permeability distribution in a reservoir model. *Geostatistics for Natural Resources Characterization*, 2:831–849, 1984.

[41] C. Deutsch. *Geostatistical Reservoir Modeling.* Oxford University Press, New York, 2002.

[42] N. Distefano and A. Rath. An identification approach to subsurface hydrological systems. *Water Resources Research*, 11(6):1005–1012, 1975.

[43] L. Dong, Y. Wang, K. Ni, and K. Lu. Facial animation system based on image warping algorithm. In *International Conference on Electronics, Communications and Control, Ningbo, China, 9-11 September 2011*, pages 2648–2653. DOI:10.1109/ICECC.2011.6066515.

[44] O. Dorn and R. Villegas. History matching of petroleum reservoirs using a level set technique. *Inverse Problems*, 24(3):035015, 2008.

[45] L. Doublet, P. Pande, T. McCollum, and T. Blasingame. Decline curve analysis using type curves–analysis of oil well production data using material balance time: Application to field cases. In *International Petroleum Conference and Ex-*

hibition of Mexico, Veracruz, Mexico, 10-13 October 1994. Society of Petroleum Engineers. Document ID: 28688-MS, DOI: 10.2118/28688-MS.

[46] A. Doucet, N. de Freitas, and N. Gordon. *Sequential Monte Carlo Methods in Practice*. Springer New York, USA, 2001.

[47] A. Doucet and A. Johansen. A tutorial on Particle filtering and smoothing: fifteen years later, December 2008. Available online at: http://people.cs.ubc.ca/~arnaud/doucet_johansen_tutorialPF.pdf.

[48] L. Duan, C. Farmer, I. Hoteit, X. Luo, and I. Moroz. Data assimilation using Bayesian filters and B-spline geological models. *Journal of Physics: Conference Series*, 290:012004, 2011.

[49] L. Duan, C. Farmer, and I. Moroz. Regularized Particle filter with langevin resampling step. *AIP Conference Proceedings*, 1281:1080–1083, 2010.

[50] L. Duan, C. Farmer, and I. Moroz. Sequential inverse problems Bayesian principles and the logistic map example. *AIP Conference Proceedings*, 1281:1071–1074, 2010.

[51] L. Duan, C. Farmer, and I. Moroz. History matching using deformation ensemble square root filter and geological facies models. To Be Submitted, 2011.

[52] L. Duan and R. Stadie. Iterative deconvolution method for well test data with a cumulative production constraint. To Be Submitted, 2011.

[53] L. Duan, Y. Zhang, and G. Roberts. True amplitude reverse time migration-from reflectivity to velocity and impedance perturbations. In *75th EAGE Conference and Exhibition, London, 10-13 June 2013*.

[54] S. Esedoglu. Barcode reconsturction code, 2004. Available online at: http://www.math.lsa.umich.edu/~esedoglu/Research/code/code.html.

[55] S. Esedoglu. Blind deconvolution of barcode signals. *Inverse Problems*, 20:121, 2004.

[56] G. Evensen. Inverse methods and data assimilation in nonlinear ocean models. *Physica D*, 77:108–128, 1994.

[57] G. Evensen. Sequential data assimilation with a nonlinear quasi-geostrophic model using Monte Carlo methods to forecast error statistics. *Journal of Geophysical Research*, 99(C5):10,143–10,162, 1994.

[58] G. Evensen. The ensemble Kalman filter: theoretical formulation and practical implementation. *Ocean Dynamics*, 53:343–367, 2003.

[59] G. Evensen. Sampling strategies and square root analysis schemes for the EnKF. *Ocean Dynamics*, 54(6):539–560, 2004.

[60] G. Evensen. *Data assimilation: the ensemble Kalman filter.* Springer, 2009.

[61] R. Ewing, M. Pilant, J. Wade, and A. Watson. Estimating parameters in scientific computation: A survey of experience from oil and groundwater modeling. *IEEE Computational Science and Engineering*, 1(3):19–31, 1994.

[62] P. Fair and J. Simmons. Novel well testing applications of Laplace transform deconvolution. In *SPE Annual Technical Conference and Exhibition, Washington, D.C., 4-7 October 1992.* Society of Petroleum Engineers. Document ID: 24716-MS, DOI: 10.2118/24716-MS.

[63] C. Farmer. *Numerical Rocks.* Oxford University Press, Oxford, 1992.

[64] C. Farmer. An ensemble Bayesian filter for state estimation. *OCCAM Preprint Number 12/47*, 2013. Available online at: https://www.maths.ox.ac.uk/system/files/attachments/finalOR47.pdf.

[65] C. Farmer. An introduction to Bayesian filtering for inverse problems. *Background notes for a lecture*, January 2009.

[66] M. Fienen, C. Muffels, and R. Hunt. On constraining pilot point calibration with regularization in pest. *Ground Water*, 47(6):835–844, 2009.

[67] C. Fishman. The killer app - bar none. Available online at: http://www.americanwaymag.com/so-woodland-bar-code-bernard-silver-drexel-university.

[68] F. Floris, M. Bush, M. Cuypers, F. Roggero, and A. Syversveen. Methods for quantifying the uncertainty of production forecasts: a comparative study. *Petroleum Geoscience*, 7(S):S87–S96, 2001.

[69] M. Fox. Alan haberman, who ushered in the bar code, dies at 81, 2011. Available online at: http://www.nytimes.com/2011/06/16/business/16haberman.html?_r=2&hp.

[70] A. Galli, H. Beucher, G. Le Loch, and B. Doligez. *The pros and cons of the truncated Gaussian method*. Geostatistical simulations. 1994.

[71] G. Gavalas, P. Shah, and J. Seinfeld. Reservoir history matching by Bayesian estimation. *SPE Journal*, 16(6):337–350, 1976.

[72] GMSE. *GMSE Imaging*. GMSE GmbH, Germany, 2011. Available online at: http://imaging.gmse.net.

[73] N. Gordon, D. Salmond, and A. Smith. Novel approach to nonlinear/non-Gaussian Bayesian state estimation. *In Radar and Signal Processing, IEE Proceedings F*, 140(2):107–113, 1993.

[74] A. Gringarten. Interpretation of tests in fissured and multilayered reservoirs with double-porosity behavior: theory and practice. *Journal of Petroleum Technology*, 36(4):549–564, 1984.

[75] A. Gringarten. From straight lines to deconvolution: The evolution of the state of the art in well test analysis. *SPE Reservoir Evaluation and Engineering*, 11(1):41–62, 2008.

[76] A. Gringarten, D. Bourdet, P. Landel, and V. Kniazeff. A comparison between different skin and wellbore storage type-curves for early-time transient analysis. In *SPE Annual Technical Conference and Exhibition, Las Vegas, Nevada, 23-26 September 1979*. Society of Petroleum Engineers. Document ID:8205-MS, DOI: 10.2118/8205-MS.

[77] A. Gringarten and H. Ramey. An approximate infinite conductivity solution for a partially penetrating line-source well. *SPE Journal*, 15(2):140–148, 1975.

[78] F. Gustafsson and P. Hriljac. Particle filters for prediction of chaos. *Proceedings of SYSID, Rotterdam, NL*, 2003.

[79] J. Hadamard. Sur les problémes aux dérivées partielles et leur signification physique. *Princeton University Bulletin*, 13(49-52):28, 1902.

[80] R. Hebert and J. Ekstrand. Signal processor method and apparatus. 1976. US (Patent) 4642678, 1987.

[81] F. Herrmann. Singularity characterization by monoscale analysis: Application to seismic imaging. *Applied and Computational Harmonic Analysis*, 11(1):64–88, 2001.

[82] F. Herrmann and Y. Bernab. Seismic singularities at upper-mantle phase transitions: a site percolation model. *Geophysical Journal International*, 159(3):949–960, 2004.

[83] I. Hoteit, X. Luo, and D. Pham. Particle Kalman filtering: A nonlinear Bayesian framework for ensemble Kalman filters. *Monthly Weather Review*, 140:528–542, 2011.

[84] T. Hutchinson and V. Sikora. A generalized water-drive analysis. *Petroleum Transactions, AIME*, (216):169–178, 1959.

[85] D. Ilk, P. Valko, and T. Blasingame. Deconvolution of variable rate reservoir performance data using B-splines. *SPE Reservoir Evaluation and Engineering*, 9(5):582–595, 2006.

[86] P. Jacquard and C. Jain. Permeability distribution from field pressure data. *SPE Journal*, 5(4):281–294, 1965.

[87] B. Jafarpour. *Oil Reservoir Characterization Using Ensemble Data Assimilation (Massachusetts Institute of Technology)*. PhD thesis, 2008.

[88] B. Jafarpour and D. Mclaughlin. Efficient permeability parameterization with the discrete cosine transform. In *SPE Reservoir Simulation Symposium, Houston, Texas, 26-28 February 2007*. Society of Petroleum Engineers. Document ID: 106453-MS, DOI: 10.2118/106453-MS.

[89] B. Jafarpour and D. McLaughlin. History matching with an ensemble Kalman filter and discrete cosine parameterization. *Computational Geosciences*, 12(2):227–244, 2008.

[90] H. Jahns. A rapid method for obtaining a two-dimensional reservoir description from well pressure response data. *SPE Journal*, 6(4):315–327, 1966.

[91] A. Jazwinski. *Stochastic Processes and Filtering Theory*. Academic Press, 1970.

[92] E. Joesph and T. Pavlidis. Peak classifier for barcode waveforms. In *11th IAPR International Conference on Pattern Recognition, Hague, Holland, 30 August-3 September 1992*, volume 2, pages 238–241.

[93] E. Joseph and T. Pavlidis. Deblurring of bilevel waveforms. *IEEE Transactions on Image Processing*, 2(2):223–235, 1993.

[94] E. Joseph and T. Pavlidis. Barcode waveform recognition using peak locations. *IEEE Transactions on Pattern Analysis and Machine Intelligence*, 16(6):630–640, 1994.

[95] J. Kaipio and E. Somersalo. *Statistical and Computational Inverse Problems.* Springer, Berlin, 2004.

[96] G. Kallianpur. *Stochastic Filtering Theory.* Springer Verlag, 1980.

[97] R. Kalman. A new approach to linear filtering and prediction problems. *Journal of Basic Engineering*, 82 (1):35–45, 1960.

[98] R. King. A review of Bayesian state-space modelling of capture-recapture-recovery data. *Interface Focus*, 2(2):190–204, 2012.

[99] M. Krymskaya, R. Hanea, and M. Verlaan. An iterative ensemble Kalman filter for reservoir engineering applications. *Computational Geosciences*, 13(2):235–244, 2009.

[100] G. Le Loch, H. Beucher, A. Galli, and B. Doligez. Improvement in the truncated Gaussian method: combining several Gaussian functions. In *4th European Conference on the Mathematics of Oil Recovery, Roros, Norway, 7-10 June 1994.*

[101] T. Leo, C. Kravaria, and J. Seinfeld. History matching by spline approximation and regularization in single-phase areal reservoirs. *SPE Reservoir Engineering*, 1(5):521–534, 1986.

[102] J. Levine and G. Pignie. Exact finite dimensional filters for a class of non-linear discrete-time systems. *Stochastics An International Journal of Probability and Stochastic Processes*, 18:97–132, 1986.

[103] M. Levitan. Practical application of pressure-rate deconvolution to analysis of real well tests. *SPE Reservoir Evaluation and Engineering*, 8(2):113–121, 2005.

[104] M. Levitan, G. Crawford, and H. Andrew. Practical considerations for pressure-rate deconvolution of well test data. In *SPE Annual Technical Conference and Exhibition, Houston, Texas, 26-29 September 2004*. Society of Petroleum Engineers. Document ID: 90680-MS, DOI: 10.2118/90680-MS.

[105] M. Liu and R. Taylor. A consistent nonparametric density estimator for the deconvolution problem. *Canadian Journal of Statistics*, 17(4):427–438, 1989.

[106] N. Liu and D. Oliver. Evaluation of Monte Carlo methods for assessing uncertainty. *SPE Journal*, 8(2):188–195, 2003.

[107] N. Liu and D. Oliver. Critical evaluation of the ensemble Kalman filter on history matching of geologic facies. *SPE Reservoir Evaluation and Engineering*, 8(6):470–477, 2005.

[108] N. Liu and D. Oliver. Ensemble Kalman filter for automatic history matching of geologic facies. *Journal of Petroleum Science and Engineering*, 47:147–161, 2005.

[109] R. J. Lorentzen and G. Naevdal. An iterative ensemble Kalman filter. *IEEE Transactions on Automatic Control*, 56(8):1990–1995, 2011.

[110] X. Luo, I. Hoteit, L. Duan, and W. Wang. *Review of Nonlinear Kalman, Ensemble and Particle Filtering with Application to the History Matching Problem.* Nonlinear Estimation and Applications to Industrial Systems Control. Nova, 2011.

[111] E. Makhlouf, W. Chen, M. Wasserman, and J. Seinfeld. A general history matching algorithm for three-phase, three-dimensional petroleum reservoirs. *SPE Advanced Technology Series*, 1(2):83–92, 1993.

[112] C. Mattax and R. Dalton. *Reservoir Simulation SPE Monograph 13.* Society of Petroleum Engineers. 1990.

[113] C. Matthews and D. Russell. *Pressure buildup and flow tests in wells*, volume 1 of *SPE Monograph Series Vol. 1.* Society of Petroleum Engineers of AIME Dallas, Texas, 1967.

[114] R. McKinley. Wellbore transmissibility from afterflow-dominated pressure buildup data. *Journal of Petroleum Technology*, 23(7):863–872, 1971.

[115] H. Mitchell, P. Houtekamer, G. Pellerin, M. Buehner, and B. Hansen. Assimilation of AMSU-A microwave radiances with an Ensemble Kalman Filter (EnKF). Available online at: http://collaboration.cmc.ec.gc.ca/science/arma/enkf/itsc-13.pdf.

[116] D. Nguyen, T. Bui, and T. Le. *Blur estimation for barcode recognition in out-of-focus images*, volume 6744 of *Pattern Recognition and Machine Intelligence.* Springer Berlin / Heidelberg, 2011.

[117] L. Nielsen, H. Li, X. Tai, S. Aanonsen, and M. Espedal. Reservoir description using a binary level set model. *Computing and visualization in science*, 13(1):41–58, 2010.

[118] M. Nixon and A. Aguado. *Feature Extraction and Image Processing*. Academic Press, 2008.

[119] D. Oliver. Incorporation of transient pressure data into reservoir characterization. *In Situ*, 18:243–243, 1994.

[120] D. Oliver and Y. Chen. Recent progress on reservoir history matching: a review. *Computational Geosciences*, 15(1):185–221, 2010.

[121] D. Oliver, A. Reynolds, Z. Bi, and Y. Abacioglu. Integration of production data into reservoir models. *Petroleum Geosciences*, 7(SUPP):65–73, 2001.

[122] M. Onur, M. Cinar, D. Ilk, P. Valko, T. Blasingame, and P. Hegeman. An investigation of recent deconvolution methods for well-test data analysis. *SPE Journal*, 13(2):226–247, 2008.

[123] N. Otsu. A threshold selection method from gray-level histograms. *Automatica*, 11(285-296):23–27, 1975.

[124] D. Peaceman. *Fundamentals of numerical reservoir simulation*, volume 6. Elsevier, 1977.

[125] H. Prautzsch, W. Boehm, and M. Paluszny. *Bèzier and B-spline techniques*. Springer Verlag, 2002.

[126] B. Rao and S. Mishra. Adjoint sensitivity analysis for mathematical models of coupled nonlinear physical processes. *International Association of Hydrological Sciences*, pages 483–490, 1996.

[127] H. Reading. *Sedimentary Environments: Processes, Facies, and Stratigraphy*. Wiley-Blackwell, 1996.

[128] E. Reinhard, W. Heidrich, S. Pattanaik, P. Debevec, G. Ward, and K. Myszkowski. *High Dynamic Range Imaging: Acquisition, Display, and Image-based Lighting*. Morgan Kaufmann, 2010.

[129] H. Ren, Y. Wu, and X. Zhu. The quadratic B-spline curve fitting for the shape of log cross sections. *Journal of Forestry Research*, 17(2):150–152, 2006.

[130] A. Reynolds, N. He, L. Chu, and D. Oliver. Reparameterization techniques for generating reservoir descriptions conditioned to variograms and well-test pressure data. *SPE Journal*, 1(4):413–426, 1996.

[131] S. Riad. The deconvolution problem: An overview. *Proceedings of the IEEE*, 74(1):82–85, 1986.

[132] B. Ristic, S. Arulampalam, and N. Gordon. *Beyond the Kalman Filter: Particle Filters for Tracking Applications*. Artech House Publishers, 2004.

[133] C. Romero and J. Carter. Using genetic algorithms for reservoir characterisation. *Journal of Petroleum Science and Engineering*, 31(2-4):113–123, 2001.

[134] A. Roumboutsos and G. Stewart. A direct deconvolution or convolution algorithm for well test analysis. In *SPE Annual Technical Conference and Exhibition, Houston, Texas, 2-5 October 1988*. Society of Petroleum Engineers. Document ID: 18157-MS, DOI: 10.2118/18157-MS.

[135] P. Sakov and P. Oke. A deterministic formulation of the ensemble Kalman filter: an alternative to ensemble square root filters. *Tellus A*, 60(2):361–371, 2008.

[136] P. Sakov and P. Oke. Implications of the form of the ensemble transformation in the ensemble square root filters. *Monthly Weather Review*, 136(3):1042–1053, 2008.

[137] P. Sarma, L. Durlofsky, A. Khalid, and W. Chen. Efficient real-time reservoir manangement using adjoint management using adjoint-based optimal control and model updating. *Computational Geosciences*, 10:3–26, 2006.

[138] T. Sederberg and S. Parry. Free-form deformation of solid geometric models. *ACM Siggraph Computer Graphics*, 20(4):151–160, 1986.

[139] J. Sethian. *Level Set Methods and Fast Marching Methods: Evolving Interfaces in Computational Geometry, Fluid Mechanics, Computer Vision, and Materials Science*. Cambridge University Press, Cambridge, 1999.

[140] S. Shah, G. Gavalas, and J. Seinfeld. Error analysis in history matching: The optimum level of parameterization. *SPE Journal*, 18(3):219–228, 1978.

[141] R. Shams and P. Sadeghi. Barcode recognition in highly distorted and low resolution images. In *IEEE International Conference on Acoustics, Speech and Signal Processing, Honolulu, Hawaii, 15-20 April 2007*, volume 4, pages IV–49–IV–52.

[142] L. Shapiro and G. Stockman. *Computer Vision*. Prentice Hall, 2001.

[143] S. Shellhammer, D. Goren, and T. Pavlidis. Novel signal-processing techniques in barcode scanning. *Robotics and Automation Magazine, IEEE*, 6(1):57–65, 1999.

[144] C. Shene. Lecture notes on 'CS3621 computing with geometry'. Fall, 2005. Available online at: http://www.cs.mtu.edu/~shene/COURSES/cs3621/NOTES/surface/bspline-construct.html.

[145] B. Silverman. *Density Estimation for Statistics and Data Analysis*. Chapman and Hall, 1986.

[146] M. Simandl. Lecture notes on 'state estimation of nonlinear non Gaussian stochastic systems', 2006. Available online at: http://math.tut.fi/~piche/topics/simandl/nonlinearfilteringnotes.pdf.

[147] D. Simon. *Optimal State Estimation: Kalman, H-Infinity, and Nonlinear Approaches*. Wiley Blackwell, 2006.

[148] L. Sirgue, O. Barkved, J. Gestel, O. Askim, and J. Kommedal. 3D waveform inversion on Valhall wide-azimuth obc. In *71st EAGE Conference and Exhibition, Amsterdam, Holland, 8-11 June 2009.*

[149] A. Stordal, H. Karlsen, G. Nvdal, H. Skaug, and B. Valls. Bridging the ensemble Kalman filter and Particle filters: the adaptive Gaussian mixture filter. *Computational Geosciences*, 15(2):293–305, 2011.

[150] S. Strebelle. Conditional simulation of complex geological structures using multiple-point statistics. *Mathematical Geology*, 34(1):1–21, 2002.

[151] S. Strebelle and A. Journel. Sequential simulation drawing structures from training images (stanford university). PhD, 2000.

[152] X. Tai and C. Yao. Image segmentation by piecewise constant Mumford-Shah model without estimating the constants. *International Journal of Computer Mathematics*, 24(3):435–443, 2006.

[153] Z. Tavassoli, J. Carter, and P. King. Errors in history matching. *SPE Journal*, 9(3):352–361, 2004.

[154] C. Theis. The relation between the lowering of the Piezometric surface and the rate and duration of discharge of a well using ground-water storage. *Transaction, American Geophysical Union*, 16(2):519–524, 1935.

[155] L. Thompson and A. Reynolds. Analysis of variable-rate well-test pressure data using Duhamel's principle. *SPE Formation Evaluation*, 1(5):453–469, 1986.

[156] A. Tikhonov and V. Arsenin. *Methods for Solving Ill-posed Problems*, volume 15. Nauka, Moscow, 1979.

[157] M. Tippett, J. Anderson, C. Bishop, T. Hamill, and J. Whitaker. Ensemble square-root filters. *Monthly Weather Review*, 131:1485–1490, 2003.

[158] R. Tsai and S. Osher. Level set methods and their applications in image science. *Communications in Mathematical Sciences*, 1(4):623–656, 2003.

[159] W. Turin and R. Boie. Barcode recovery via the EM algorithm. *IEEE Transactions on Signal Processing*, 46(2):354–363, 1998.

[160] N. Tustison, B. Avants, and J. Gee. Improved FFD B-spline image registration. In *11th International Conference on Computer Vision, Rio de Janeiro, Brazil, 14-21 October 2007*, pages 1–8. IEEE.

[161] P. Valko and J. Abate. Comparison of sequence accelerators for the Gaver method of numerical Laplace transform inversion. *Computers and Mathematics with Applications*, 48(3-4):629–636, 2004.

[162] J. Van Doren, P. Van den Hof, J. Jansen, and O. Bosgra. Determining identifiable parameterizations for large-scale physical models in reservoir engineering. In *17th International Federation of Automatic Control World Congress, Seoul, R.Korea, 6-11 June, 2008*, volume 17, pages 6–11.

[163] T. von Schroeter, F. Hollaender, and A. Gringarten. Deconvolution of well test data as a nonlinear total least squares problem. In *SPE Annual Technical Conference and Exhibition, New Orleans, Louisiana, 30 September - 3*

October 2001. Society of Petroleum Engineers. Document ID: 71574-MS, DOI: 10.2118/71574-MS.

[164] T. von Schroeter, F. Hollaender, and A. Gringarten. Deconvolution of well-test data as a nonlinear total least-squares problem. *SPE Journal*, 9(4):375–390, 2004.

[165] K. Wang, Y. Zou, and H. Wang. Barcode reading from images captured by camera phones. In *2nd International Conference on Mobile Technology, Applications and Systems, Guangzhou, China, 15-17 November, 2005*, pages 6 pp.–6.

[166] K. Wang, Y. Zou, and H. Wang. 1D bar code reading on camera phones. *International Journal of Image and Graphics*, 7(3):529–550, 2007.

[167] D. Watkins. *Fundamentals of Matrix Computations*. LibreDigital, 2002.

[168] A. Watson, J. Wade, and R. Ewing. Parameter and system identification for fluid flow in underground reservoirs. In *Inverse Problems and Optimal Design in Industry, Philadelphia, Pennsylvania, 1994*, pages 8–10.

[169] X. Wen and W. Chen. Real-time reservoir model updating using ensemble Kalman filter with confirming option. *SPE Journal*, 11(4):431–442, 2006.

[170] X. Wen, C. Deutsch, and A. Cullick. High-resolution reservoir models integrating multiple-well production data. *SPE Journal*, 3(4):344–355, 1998.

[171] X. Wen, S. Lee, and T. Yu. Simultaneous integration of pressure, water cut, 1 and 4-D seismic data in geostatistical reservoir modeling. *Mathematical Geology*, 38(3):301–325, 2006.

[172] J. Whitaker and T. Hamill. Ensemble data assimilation without perturbed observations. *Monthly Weather Review*, 130:1913–1924, 2002.

[173] T. Wittman. Barcode reading, 2002. Available online at: http://www.ima.umn.edu/~wittman/barcode/index.html.

[174] T. Wittman. Lost in the supermarket: Decoding blurry barcodes. *SIAM News*, 37(7):16, 2004.

[175] G. Wolberg. *Digital Image Warping.* Wiley-IEEE Computer Society Press, 1990.

[176] G. Wolberg. Image morphing: a survey. *The Visual Computer*, 14(8):360–372, 1998.

[177] www.nationalbarcode.com. History of barcode scanners, 2012. Available online at: http://www.nationalbarcode.com/History-of-Barcode-Scanners.htm.

[178] G. Xue and A. Datta-Gupta. Structure preserving inversion: An efficient approach to conditioning stochastic reservoir models to dynamic data. In *SPE Annual Technical Conference and Exhibition, San Antonio, Texas, 5-8 October 1997.* Society of Petroleum Engineers. Document ID:38727-MS, DOI: 10.2118/38727-MS.

[179] Y. Zhang and L. Duan. *Predicting multiples using a reverse time demigration*, pages 1–5. Society of Exploration Geophysicists, 2012.

[180] Y. Zhang, L. Duan, and Y. Xie. A stable and practical implementation of least-squares reverse time migration. In *83rd Annual Meeting and Exhibition, Houston, Taxas, 22-27 September 2013.* Society of Exploration Geophysicists.

[181] Y. Zhang, A. Ratcliffe, L. Duan, and G. Roberts. Velocity and impedance inversion based on true amplitude reverse time migration. In *83rd Annual Meeting and Exhibition, Houston, Taxas, 22-27 September 2013.* Society of Exploration Geophysicists.